DISSERTATION

NEW OPTIMALITY THEORIES OF DYNAMIC VEGETAL RESPONSES TO CLIMATE VARIABILITY: ECO-HYDROLOGIC AND WATER SUPPLY VULNERABILITY IMPLICATIONS

Submitted by:

Jonathan A. Quebbeman

Department of Civil and Environmental Engineering

In partial fulfillment of the requirements

For the Degree of Doctor of Philosophy

Colorado State University

Fort Collins, Colorado

Spring 2016

Doctoral Committee:

Advisor: Jorge A. Ramirez

Neil S. Grigg
William L. Bauerle
Thomas C. Brown

ABSTRACT

NEW OPTIMALITY THEORIES OF DYNAMIC VEGETAL RESPONSES TO CLIMATE VARIABILITY: ECO-HYDROLOGIC AND WATER SUPPLY VULNERABILITY IMPLICATIONS

A major challenge for water and land resource managers over the coming decades is understanding how vegetation changes due to climate change will affect the water, energy and carbon budgets in our biosphere. In this dissertation, we implement new optimality theories for stomatal control and photosynthetic capacities in order to understand and describe dynamic vegetation responses to climatic changes. The resulting optimal dynamic vegetation models are then applied to project eco-hydrologic responses that incorporate explicitly the feedbacks between vegetation, hydrology, and climate.

Plants adjust their stomatal openings in response to changes in environmental conditions. Optimal stomatal control theories are based on the assumption that plants adjust their stomatal openings in such a way that carbon assimilation is maximized while minimizing transpiration. Here, we formulate the optimal stomatal control theory fully, bringing to the forefront a rarely discussed implication of current formulations, which is the implicit statement of a fixed volume of transpiration over the period of analysis. We offer an alternative solution procedure using *dynamic programming* that explicitly accounts for the constraint on the total transpiration volume, and eliminates the need of estimating the marginal water use efficiency, λ. In addition to the advantage of a more realistic decreasing volume of water for transpiration, we posit that the proposed dynamic programming solution offers other important advantages over solutions based on the calculus of variations including, the replacement of λ with an actual transpiration volume, and the potential to model stochastic behavior not possible with the calculus of variations solution. The new dynamic programming approach may also be easily extended to more complicated eco-hydrologic and plant physiologic questions.

The maximum rate of carboxylation, V_{cmax}, and the maximum rate of electron transport, J_{max}, describe leaf-level capacities of the photosynthetic system, and are critical in determining the net fluxes of carbon dioxide and water vapor in the terrestrial biosphere. Both V_{cmax} and J_{max} ex-

hibit high spatial and temporal variability. However, many models of photosynthesis employed in terrestrial biosphere models assume constant values for V_{cmax} and J_{max} at a reference temperature ignoring intra-seasonal, inter-annual, and water stress-induced variations. Although general patterns of variation of V_{cmax} and J_{max} have been correlated with groups of species, climates, and nitrogen concentrations, scant theoretical support has been provided to explain these variations. We present a new approach to determine V_{cmax} and J_{max} based on the assumption that a limited amount of leaf nitrogen is allocated optimally among the various components of the photosynthetic system in such a way that expected carbon assimilation is maximized. The optimal allocation is constrained by available nitrogen, and responds dynamically to the near-term environmental conditions of light and water supply. We then demonstrate that the resulting optimal allocations of a finite supply of nitrogen replicate observed relationships in nature, including the commonly referenced ratio of J_{max}/V_{cmax}, the relationship of leaf nitrogen to V_{cmax}, and the changes in nitrogen allocation under varying water availability and light environments. This optimal allocation approach provides a mechanism to describe the response of leaf-level photosynthetic capacity to varying environmental and resource supply conditions that can be incorporated into terrestrial biosphere models.

Vegetation is responding to our rapidly changing climate resulting in species compositional shifts, changes to growing seasons, and changes in biomass amount and distribution. These changes can be observed in the seasonal phenology of leaf area indices (LAI). Magnitudes of LAI are indicative of the biomass and growing capacity of a system - regions with low precipitation or other poor growing conditions (cold, low light, etc.) will exhibit low LAI values, whereas ideal climatic growing conditions will show higher values of LAI. There is a clear connection between climate and the magnitude and timing (i.e., phenology) of LAI, which we exploit in a harmonic regression model based on a space-for-time substitution approach. Coefficients of a linear harmonic regression model are fit to 30-years of bi-weekly observations (i.e. remotely sensed reanalysis) of LAI over a large domain (the Colorado River Basin). Fitted harmonics, which are considered observations of seasonal phenology, are then regressed against climate covariates; only natural vegetation points are considered. As a result, harmonic coefficients describing seasonal phenology are directly related to climate, allowing for the prediction of annual phenology in novel climates. The resulting models are used to compare predicted LAI against observations over a historical period, in addition to a study

of predicted phenology using projected GCM data. The former shows high skill in comparing the reanalysis to observations, whereas the latter indicates the true power and significance of including a dynamic model of annual LAI phenology in macro-scale modeling applications, with direct effects on the surface water balance.

Individually, these components are extremely powerful and informative, but an application framework is required to deploy these systems in practice. A new dynamic vegetation model utilizing these optimality theories was developed (VIC-VEO), which allows testing of macro-scale hydrologic responses across large spatial domains, and under a range of projected climate scenarios. VIC-VEO utilizes an optimal stomatal model to estimate conductance and the associated transpiration rates. Optimal stomatal conductance is directly linked to vapor pressure deficits, CO_2 concentrations, irradiance levels, ambient temperatures and soil moisture status. To assess deployment of the optimal stomatal model in a macro-scale framework, canopy integrated evapotranspirative (ET) fluxes are compared to estimated fluxes using a traditional stomatal model, in addition to observations of Fluxnet canopy ET. This comparison indicates improved skill. Impacts to the hydrologic cycle, considering longer-term phenologic changes, are also tested over a projected century. This process is compared to 'static' phenologic responses for two diverse climates, helping to highlight the range of potential vegetation changes, in addition to the magnitudes of *partitioned* changes to the hydrologic cycle. Using the new macro-scale hydrologic framework, these comparisons are then completed for multiple sub-basins across the Colorado River Basin, indicating the potential diverse responses of vegetation and yield - specifically, highlighting the conclusion that disparate vegetation responses are possible across large regions with significant effects on the hydrologic cycle and aggregated yields.

Finally, the VIC-VEO model is applied in a study of Water-Supply vulnerability across the Colorado River Basin. A range of Global Circulation Models (GCMs) and Representative Concentration Pathways (RCPs, CMIP5) are used to estimate projected yield to year 2100. VIC-VEO is a spatially distributed hydrologic model, thus yield is routed and aggregated at 41 sub-catchments across the basin. Monthly projected consumptive use demand data was supplied to year 2100 at the HUC4 level. A water management and routing model (WEAP) was used to model yield, diversions, trans-basin diversions, minimum flows, storage reservoir routings, and the consumptive use at the HUC4 level for each of the GCM and RCP scenarios. This procedure indicated gross

changes to the projected yield under most GCM-RCP scenarios, with some scenarios indicating extreme vulnerability of water supply in the coming decades. Accounting for dynamic vegetation processes increased the potential aggregated yield compared to static vegetation responses, but still estimates large potential future supply vulnerabilities.

ACKNOWLEDGMENTS

A dissertation is a comprehensive document of ideas, theories, proofs, and conclusions developed from countless hours of effort and late evenings - it doesn't document all of the sacrifices made and the gifts given over these many years of effort. I can only begin to note my appreciation to all of those who have helped shape this research effort, and also shape who I have become today.

I want to thank my committee members, Tom, Neil, Bill and Jorge, for review and support of these research efforts. I also fully appreciate their individual wealth of knowledge over an extremely broad spectrum of research interests, encapsulating many aspects of my dissertation.

All of these efforts have been generously supported through research grants from the United States Bureau of Reclamation (USBR) and the United States Forest Service (USFS). Thank you for helping to support this research, and my family.

I would also like to thank Tom Brown for providing invaluable projected consumptive use demand data that was used for the Vulnerability Analysis of this dissertation.

Personally, I also need to acknowledge the support of many friends, including Joel Sholtes and Mikell Warms, who have unselfishly lent ears, beers, and tears over the years. Your words of support and encouragement, stress relieving bike rides, or simply a laugh have helped make this process both a success and that much more memorable.

I am also eternally indebted to my advisor, mentor, and friend, Jorge Ramirez. I know there could have been an easier advisor, a less challenging advisor, one who pushed me a little lighter, but I doubt I could have had anyone teach me more about academia, writing, critical thinking, challenging theories, life, and respect, over such a short period of time. The value Jorge has added goes well beyond a degree, and has shaped my personal, academic, and professional future.

None of this would have been possible without the extremely generous support of my parents – I doubt I can ever fully express my emotional (and financial) indebtedness. This includes everything from support of this doctorate, from our time in Maine, before my Bachelors degree in Iowa, and all the way through my childhood; you have shown me continuous support, encouragement, challenge, and love, making me who I have become today. As I now start to see with my own two little girls,

parenting can appear as a thankless job, but please know, it is certainly not an unappreciated job. For all those times, all that you have given, for all of your support, for everything, thank you, I love you.

And finally, I owe a world of gratitude to my loving, supportive, and patient family: my amazing wife Renee, and two beautiful girls, Avery and Pace. They have made many sacrifices over the years, financially and emotionally, allowing this degree to become reality. This journey has been so much more than just an education, but a fun journey through this Chapter of life adding more meaning to the titles of 'dad' and 'husband'. We've all grown together over the years in so many ways. Soon, I hope missed weekend hikes, too infrequent date nights, and late nights working are merely a distant memory, and we can all celebrate our path forward together in the next Chapter of life. Thank you for everything – I love you to the moon... and back.

Jonathan A. Quebbeman

Fort Collins, Colorado

DEDICATION

In memory of my brother, Eddie Quebbeman, who has inspired us all to 'live in the now', and appreciate all we have every day of our too-short lives.

TABLE OF CONTENTS

LIST OF TABLES

LIST OF FIGURES

Chapter 1

Introduction

> *I like to define biology as the history of the earth and all its life – past, present, and future. To understand biology is to understand that all life is linked to the earth from which it came; it is to understand that the stream of life, flowing out of the dim past into the uncertain future, is in reality a unified force, though composed of an infinite number and variety of separate lives.*
>
> – **Rachel Carson**

The field of ecohydrology brings together the study of ecology, including vegetation growth, response, and interaction with the environment, and hydrology, the interaction of water with the biosphere. Vegetation, water and energy are inextricably linked in a continual system of feedbacks and responses creating an extremely dynamic system at a wide range of spatial and temporal scales. The dynamic nature of vegetation makes reliable prediction of system responses extremely challenging, even without considering uncertain climatic variability on the future of vegetation and its influence on the water cycle.

Single or multiple year droughts can result in large scale mortality of vulnerable vegetation species changing both the ecological landscape and hydrologic response for decades. Less extreme than mortality, vegetation can exhibit other responses such as leaf and branch senescence during periods of stress, or even rapid growth during favorable periods. Further, vegetation acclimates to climates and based on growing conditions potentially resulting in a wide range of potential vegetation species compositions, growth states, biomass, and forms.

Developing an improved understanding of vegetation dynamics, especially given our rapidly changing climate and changing supplies of water (e.g. precipitation patterns, evaporation, transpi-

ration, etc.), is extremely important to scientists and engineers in estimating landscape vegetation changes and the associated impact on hydrologic yield [20, 54, 92].

At no point in contemporary history has the future supply of water been so uncertain and simultaneously critically important as we cross thresholds of decreasing supply and increasing demand. To help model and develop future predictions of water supply, scientists and engineers use Global Circulation Models (GCMs), which provide estimates of meteorologic data, with Terrestrial Biosphere Models (TBMs), which estimate the respones of the land-surface to meteorologic forcings. Although there is gross consensus in the direction of mean temperature changes among GCMs, the magnitude, spatial, and temporal patterns of projected responses varies significantly across climate models and Representative Concentration Pathways (RCPs). Further complicating the predictive skill of TBMs in water supply forecasting is the uncertainty of modeling methods translating climatic and meteorologic data into a hydrologic response, partly moderated by vegetation. With a fixed vegetation system, this uncertainty would be minimized, although in reality vegetation is highly dynamic at several spatial and temporal scales, even under 'typical' climates. Attempting to predict vegetation responses under extreme and novel climates is a great challenge to contemporary scientists.

Researchers have been attempting for decades to explain vegetation processes, find patterns, and develop predictive frameworks, all with a range of success, but generalized mechanistic frameworks sufficiently flexible and scalable for applications in long-term dynamic modeling still remain elusive. Individual components for specific spatial and temporal scales may be explainable, or at least display consistent patterns, but extrapolation to a range of species, climates, or temporal periods is made with great uncertainty.

Regardless, engineers still require a comprehensive system that can be used for planning and design, even when vegetation dynamics are not completely defined and explainable. As such, approximations of system processes are made, such as assuming constant vegetation types, using generalized plant functional types with fixed responses, or when responses are assumed to follow constant rules over time.

The research community attempts to address these challenges with tools such as Dynamic Global Vegetation Models (DGVMs) using a range of mechanistic and/or regression approaches. These tools are currently considered the best available for estimation of vegetation responses for

coupling GCMs and Terrestrial Biosphere Models (TBMs), but many processes are still founded on gross simplifications, assume stationarity of certain processes, or assume similarity in temporal responses, for example.

Let us use the ubiquitous Jarvis [62] approach for stomatal response as a specific example - this model includes a series of response functions to determine how stomata adjust to the environment. For a set of correctly parameterized response functions, this approach can work well in replicating observed stomatal behavior, but is it appropriate to assume these response functions will remain constant for a given species over a season, years, decades or centuries? We can make similar statements regarding the more contemporary Leuning Model [78] for stomatal response, which uses two empirical parameters - they can be fit to observations and used to reasonably replicate observed stomatal behavior, but how should those empirical parameters adjust over shorter seasonal periods or longer years or decades of time in relation to a changing climate? Similar statements can be made regarding photosynthetic system parameterization, biomass production, leaf area phenologic sequences, or any response of the vegetal system for that matter.

An alternative to fixed mechanistic processes or regression is to assume a system is responding in an optimal manner maximizing or minimizing a given objective function. This is relevant here, as assuming that a system is following an optimal state reduces the degrees of freedom and allows unknown system parameters to become emergent outcomes [93]. This dissertation presents several new approaches for considering optimal vegetation states at a range of spatial and temporal scales, and also explores how they can be applied in a macro-scale TBM for use in long-term climate projection modeling. Although studies of optimal vegetation response theories are not new, further improvements in understanding optimal approaches are required [102]. Further, implementation and testing of optimal theories within macro-scale TBMs for long-term simulations is limited.

The power and fitness of Terrestrial Biosphere Models has progressed greatly over recent decades, but there still remains many unexplained or unaccounted for processes of vegetation response. Modelers try to minimize the influence and error from commonly required assumptions where insufficient knowledge or data prevail, but still require constant values where they should be variable, aggregate parameters across multiple species or climates, or use fixed response relationships. The field of ecohydrology has extensive room for growth, linking mechanistic responses with longer term growth and allocation processes, coupled with the hydrologic cycle.

Mechanistic processes are typically modeled using short-term and/or small-scale, and are commonly assumed to scale directly to longer-term or larger-scale processes [29, 45, 61]. Integrating these mechanistic responses over a season, multiple decades, centuries, or millenia, can lead to gross accumulated errors in estimated assimilation, net primary production, and transpiration.

For this dissertation, we attempt to address several critical aspects of vegetation dynamics, over a range of temporal and spatial scales by proposing alternative and novel approaches using optimality theories. Chapter 2 considers short-term leaf-level stomatal control using an optimality theory. Although optimal stomatal control has been studied for well over 50-years, we solve this problem using a novel approach: *Dynamic Programming*. This solution procedure opens several new and unexplored pathways utilizing optimal control theory, including stochastic processes, to characterize stomatal control. This new solution procedure to the classic optimal stomatal control problem is also shown to use measurable quantities for constraining the problem that are more easily incorporated into a soil-plant-atmospheric continuum modeling framework.

We then continue in Chapter 3 considering leaf-level photosynthetic capacity and evaluate the resources required to develop and maintain such capacity. Plants have access to limited resources that we postulate are utilized optimally to maximize the expected value of assimilation over a fixed period of time. This approach allows the system to respond dynamically to a changing environment as light, temperature or water deficits change. As such, we explain and replicate variable responses of photosynthetic system capacity observed in nature, and develop a solution procedure that can be used to parameterize photosynthetic capacity dynamically, rather than relying on biome-based or literature averaged static values.

Chapter 4 considers longer-term responses of climatically-based canopy level leaf area phenology. This approach utilizes a set of new space-for-time empirical climatic relationships that allow for a dynamic leaf area phenology using a Fourier series. Commonly, leaf area phenology is either prescribed based on a given vegetation type, or defined based on set rules (e.g. degree days). That approach can work well for short-term (a few years) response, but may present significant predictive errors for longer term simulations (decades to centuries). We explore climatic based relationships of leaf area phenology, a re-analysis of observed leaf area phenology in a range of climates using these relationships, and potential differences in hydrologic response for long-term prediction under a changing climate.

Bringing these elements together into a comprehensive macro-scale modeling framework called VIC-VEO is discussed in Chapter 5. We explore the response of stomata through the canopy and compare the integrated flux of water vapor against observations of canopy level evapotranspiration. We evaluate the skill of this optimal stomatal model in macro-scale applications by also comparing to a ubiquitous alternative stomatal model approach. Hydrologic responses from a long-term dynamic vegetation model are then compared against a static vegetation model highlighting potential changes in water partitioning. This comparison is completed at two different locations with different climates, using a single global climate projection model, which show disparate vegetation responses. Finally, we integrate the hydrologic yield over multiple subcatchments across the Colorado River Basin and evaluate long-term spatial and temporal changes. This is a critical assessment highlighting the potential differences in projected yield when considering a dynamic vegetatal response. Further, it reinforces an understanding that generalized comments regarding 'global' changes in projected yield should be made with extreme caution, if at all. For example, an aggregated watershed level response may show a reduction in yield, but certain locations within the watershed may actually still show an increase in yield.

Finally, in Chapter 6 we consider the utility of this new TBM, VIC-VEO, in a macro-scale hydrologic modeling and operating network framework for assessment of long-term water supply vulnerability using a range of climate projections. This approach shows the wide range of potential responses that are highly sensitive to climate data. Although we observe great variability in water supply vulnerability among climate models, a macro-scale dynamic vegetation system allows flexibility in potential vegetation responses affecting hydrology, directly related to the projected climate, affecting the yield for any individual scenario.

Incorporation of vegetation responses into long-term simulation models is undergoing rapid development and changes. Many different modeling approaches are available, but maintaining a system with sufficient predictive power in our rapidly changing climate is of paramount importance. Optimality theories are an efficient and flexible approach aiding in parameter reduction, and help to explain the complex dynamics and interactions of vegetation in earth's biosphere.

Chapter 2

Solution of the Optimal Stomatal Control Calculus of Variations Problem using Dynamic Programming

> *Owing to this struggle for life, any variation, however slight, and from whatever cause proceeding, if it be in any degree profitable to an individual of any species, in its infinitely complex relations to other organic beings and to its physical conditions of life, will tend to the preservation of that individual, and will generally be inherited by its offspring.*
>
> – **Charles Darwin, Origin of Species**

2.1 Introduction

Plant communities constantly compete for limited resources, including light, nutrients, and water, by adjusting different strategies for growth, resource allocation and morphology. Many of these adjustments may occur at times scales of months to years. However, on shorter timescales, plants can control the rates of *photosynthesis* (conversion of atmospheric carbon into stored forms of energy, also referred to as carbon assimilation) and *transpiration* (loss of water vapor into the atmosphere) through regulation of stomatal aperture. Stomata adjust their aperture over time to regulate the leaf internal CO_2 concentration for carbon assimilation, and the rate of water loss – in economic terms, these may be thought of as benefit and cost, respectively.

Water is commonly a limiting resource in natural systems – it may be scarce because of a combination of factors including low precipitation, high evaporation, high seepage, and competition by other plants. Regardless of the reason, it is evolutionarily advantageous for plants to use limited resources efficiently (e.g., maximize carbon assimilation per unit transpiration) [52].

Here, we consider plant responses in the form of stomatal control at the leaf level that regulates the CO_2 supply limiting photosynthetic assimilation rates, and also the inevitable loss of water vapor in the form of transpiration. A traditional procedure solving the calculus of variations problem using the Euler-Lagrange equation is discussed, followed by an alternative solution procedure using dynamic programming. Both of these solution procedures are then compared using published data from a case-study. Finally, we discuss problem formulations that may be more efficient using dynamic programming, or even impossible to solve with the traditional Euler-Lagrange solution procedure.

2.2 Optimal Stomatal Control

Stomata are small epidermal pores, usually on the abaxial side of leaves, that allow the exchange of gases into and out of the leaves, including CO_2, H_2O and O_2, during photosynthesis [105]. For a given set of leaf photosynthetic capacities and environmental conditions, photosynthesis cannot be increased by adjusting the supply rate of CO_2 (*e.g.*, by increasing the stomatal conductance, g, through increasing stomatal aperture) without concurrently increasing transpiration. This trade-off between carbon gain and water loss is the basis of optimal stomatal control theories [28, 56, 71]. Optimal stomatal control assumes that stomata operate in a manner such that assimilation is maximized for a given set of constraints, for example water, light and nitrogen limitations. Here, we consider optimal stomatal function constrained only by water supply. As applied here for stomatal control, we are interested in the rate of net assimilation (A, $\mu mol CO_2\ m^{-2}s^{-1}$) integrated over a period of time (an hour, a day, or potentially longer). Assimilation is a function of stomatal conductance (g, $mol\ CO_2\ m^{-2}s^{-1}$), which is itself a function varying over the period of integration. Assimilation, stomatal conductance, and transpiration depend on time-varying exogenous environmental variables (Θ), which vary with time (τ) creating set $\Theta(\tau)$, including irradiance, temperature, etc.

The total assimilation over a period of time, T, is given by the following general integral of a functional,

$$F(g) = \int_T A(\tau, g(\tau), g'(\tau))\ \mathrm{d}\tau \tag{2.1}$$

where A is the rate of assimilation. For notational convenience, the dependence of A and g on $\Theta(\tau)$ is not explicitly indicated. Here, we want to determine the optimal stomatal variation, $g^*(\tau)$, such that the net assimilation is maximized over a period of time, T. That is,

$$F^* = F(g^*(\tau)) = \int_T A(\tau, g^*(\tau), g^{*'}(\tau))\ \mathrm{d}\tau = extremum \tag{2.2}$$

In this form, the extremum (maximum) value is simply found by maximizing the stomatal conductance, which would maximize the integrated assimilation. However, this ignores the constraint of water limitation. A water limitation constraint for integrated transpiration takes the following general form,

$$J(g) = \int_T E_t(\tau, g(\tau), g'(\tau))\ \mathrm{d}\tau = E_T \tag{2.3}$$

where E_t is the rate of transpiration ($mol\ H_2O\ m^{-2}s^{-1}$), and E_T ($mol\ H_2O\ m^{-2}$) is a constant constraint on the cumulative volume of transpiration for the period of integration.

2.2.1 Calculus of Variations

The solution to the optimal stomatal control problem has been approached using the *Calculus of Variations* for many decades [17, 28, 52, 53]. The calculus of variations may be used to find stationary points of *functionals*, which are functions of functions.

Using a Lagrange multiplier, λ, the problem of solving (3.2) subject to the constraint of (2.3) is equivalent to solving,

$$H^* = H(g^*(\tau)) = \int_T G(\tau, g^*(\tau), g^{*'}(\tau))\mathrm{d}\tau \tag{2.4}$$

where

$$G(\tau, g(\tau), g'(\tau)) = A(\tau, g(\tau), g'(\tau)) - \lambda E_t(\tau, g(\tau), g'(\tau)) \tag{2.5}$$

Here, the solution of (2.4) can be obtained by solving the generalized Euler-Lagrange partial differential equation,

$$\frac{\partial G}{\partial g} - \frac{\mathrm{d}}{\mathrm{d}\tau}\frac{\partial G}{\partial g'} = 0 \tag{2.6}$$

which expanded and restating the constraint is,

$$\frac{\partial (A - \lambda E_t)}{\partial g(\tau)} - \frac{\mathrm{d}}{\mathrm{d}\tau}\frac{\partial (A - \lambda E_t)}{\partial g'(\tau)} = 0 \tag{2.7a}$$

$$\int_T E_t \mathrm{d}\tau = E_T \tag{2.7b}$$

where for notational convenience explicit dependence on τ, $g(\tau)$, and $g'(\tau)$ has been omitted.

Because A and E_t do not depend on the first derivative of g, the second term in Eq.(2.7a) is equal to zero. Therefore, Eq.(2.7a) reduces to,

$$\frac{\partial (A - \lambda E_t)}{\partial g(\tau)} = 0 \tag{2.8}$$

Or equivalently,

$$\frac{\partial A}{\partial g(\tau)} - \lambda \frac{\partial E_t}{\partial g(\tau)} = 0 \tag{2.9}$$

where the system is constrained by,

$$\int_T E_t(\tau, g(\tau))\ \mathrm{d}\tau = E_T \tag{2.10}$$

Obtaining an analytical solution of Eqs.(2.9) and (2.10) is not trivial and may not be feasible. The typical approach is to assume a value for the unknown marginal water use efficiency λ (also known as a Lagrange parameter), and then solve equation Eq.(2.9) without addressing (2.10). This approach is generally applied using a biome based approximation of λ [84]. However, because the resulting amount of total transpiration may exceed the capacity to transpire such volume (e.g. low soil matric potentials), empirical relationships can be used to estimate λ against soil moisture, soil water potential, or leaf water potential [89]. Increased λ, or higher values of efficiency, will reduce result in reduced assimilation and transpiration rates, inevitably decreasing the volume of transpiration over the period of integration.

2.2.2 Dynamic Programming

An alternative approach is to solve the constrained calculus of variations problem of Eqs. (3.2) and (2.3) using *Dynamic Programming*. Dynamic programming (DP) is a numerical solution procedure that divides complicated continuous problems into smaller discrete subproblems [9]. Here, the period of integration in Eq.(3.2) can be divided into T discrete stages (indexed by t) with a width of Δt (seconds), and the constraint on the total volume of transpiration (E_T) Eq.(2.10) may be divided into K discrete states (indexed by k), each of width ΔE_T ($moles\ H_2O\ m^{-2}$). The question becomes,"*How do the stomata operate over the choices of discrete states such that total transpiration over all stages is equal to (or less than) the constrained volume, while maximizing assimilation?*".

State Dynamics In the non-inverted form, the state dynamics equation can be written as,

$$S_{t+1,j} = f(S_{t,k}, g_t, \Theta_t) \tag{2.11}$$

where, the state variable $S_{t,k}$ is the starting cumulative transpiration at stage t and state k, $S_{t+1,j}$ is the cumulative transpired volume at the following stage $t+1$ and state j, g_t is the stomatal conductance to CO_2, and Θ_t is the exogenous time-varying environmental parameters set.

This can be rearranged into the inverted state dynamics equation,

$$g_t = f(S_{t,i}, S_{t+1,j}, \Theta_t) \tag{2.12}$$

In this form, knowing the state of cumulative transpired volume between two stages, and the environmental conditions, allows solution of the stomatal conductance as a continuous variable for any stage t.

Using a simple Fickian diffusive approach for transpiration (Eq. (A.10)), the stomatal conductance can be solved as,

$$g_t = \frac{S_{t+1,j} - S_{t,k}}{\Delta t a D_t} = \frac{(j-k)\Delta E_T}{\Delta t a D_t} \tag{2.13}$$

where Δt is the discrete timestep length (seconds), a is a constant for the ratio of conductance

of water vapor to CO_2, $(j-k)$ is the number of discrete intervals change of cumulative storage (where, $j \geq k$), and D_t is the vapor pressure deficit at stage t.

Cost-to-go Objective For a given stomatal conductance and environmental parameter set Θ_t (for this study, only including irradiance and vapor pressure deficit), the estimated assimilation rate (or total assimilated carbon when integrated over Δt), may be found using the Farquhar, von Caemmerer, Berry biochemical (FvCB) model of photosynthesis (Appendix A.1).

Therefore, knowing the stomatal conductance and the environmental conditions, we can find the 'benefit' of assimilation for any cumulative transpiration states between stage t to $t+1$.

Recursive Backward Dynamic Programming Backward dynamic programming is a procedure that can solve these combinatorial options for discrete cumulative transpiration over all stages. In Backward DP, the final stage ($t = T$) is assessed first. For every possible state ($\forall k \in K$), all feasible cumulative transpiration volume states $S_{(t+1,j)}$ from state k are considered. Feasible actions (movement between states) require the total cumulative transpiration state $0 \leq S_t \leq S_{t+1} \leq E_T$ (or, $j \geq k$), otherwise implying a positive transpiration rate, $E_t \geq 0$.

With the calculated stomatal conductance from a selected action and environmental parameter set, the assimilation (benefit) is determined (Eq. (A.9)); this is otherwise known as the *cost-to-go*. The total benefit ($F_{t,k}$) for any selected action is the sum of the cost-to-go (A) and the future total benefit ($F_{t+1,j}$) at decision $S_{t+1,j}$. From all feasible actions, the maximum total benefit and the associated action is recorded, described as,

$$F_{t,k} = max(A_{t,\forall k} + F_{t+1,\forall j}) \tag{2.14}$$

For the last stage ($t = T$), it is assumed that all future benefits are 0, or $F_{t+1,\forall j} = 0$. This process is illustrated for a given stage t and state k in Figure 2.1.

The procedure is repeated for the next state $k+1$ at time t, considering all actions to state j at $t+1$, until all states are considered over the final stage t. Then, the solution procedure steps 'backward' in time to the previous stage, and repeats the process moving backward until the first stage, where $t = 0$.

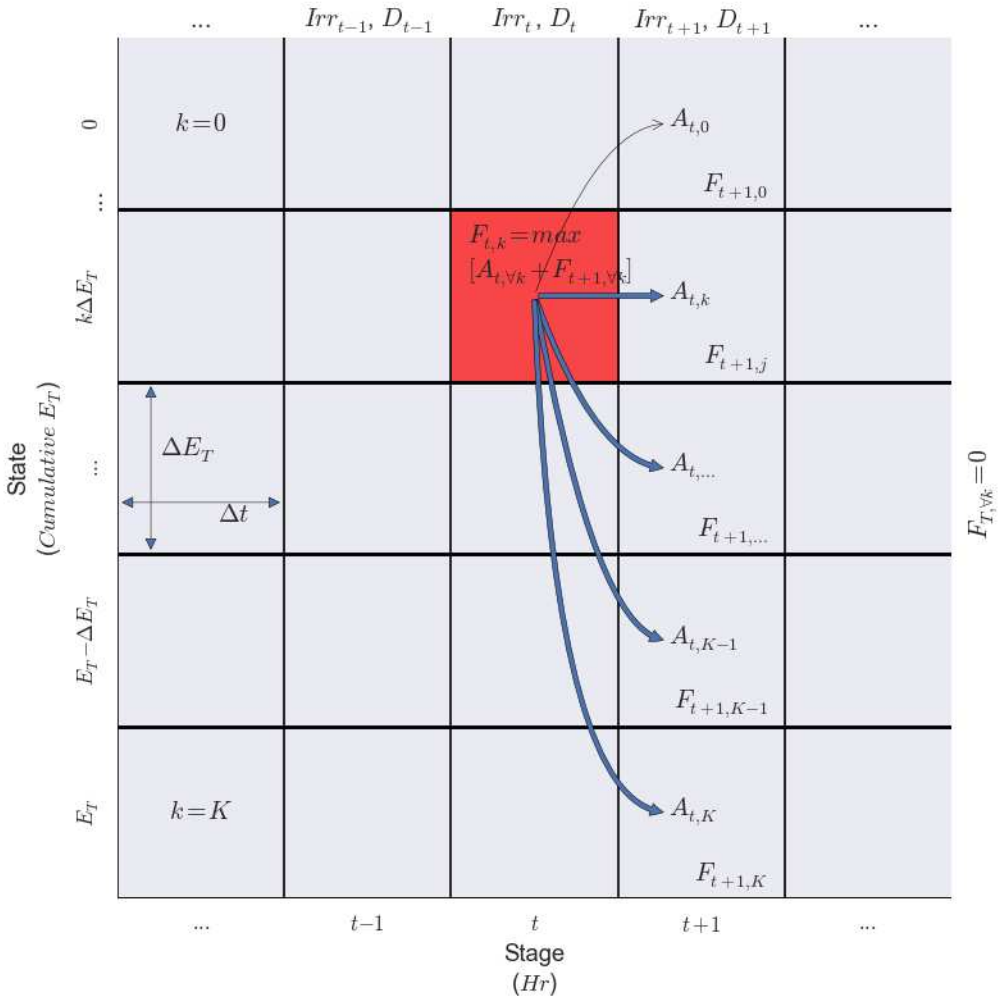

Figure 2.1: Discrete Dynamic Programming Decision Space - Backward DP feasible options are shown as thick arrows, infeasible option shown as light arrow. Objective function for current stage-state (t,k) is maximum of the sum of cost-to-go and future benefits.

Once the states and stages have been populated with optimal policies, a *traceback* is performed moving forward in time from any initial state; in other words, the optimal decision for all discrete states and times is now known. For this problem, the cumulative transpiration over the period of integration will always be starting with zero cumulative transpiration ($S_{0,k} = 0$). As recorded during the recursive backward dynamic programming process, the optimal policy is fully known from the starting stage - from each optimal stage, the next optimal stage (action) has also already been determined.

As a result, the stomatal conductance function over time is determined from a traceback that maximizes the accumulated net assimilation, constrained by a prescribed (known) total amount of available transpiration over the period of integration.

2.3 Case Study

To demonstrate and compare the procedure using the two optimal solution procedures (Euler-Lagrange and Dynamic Programming), we consider data from a study of C3 grasses [99] that presented detailed temporal data on environmental conditions and stomatal conductance. Observed field data allows for a direct comparison to observations of the predicted responses by the optimal stomatal control assumption, as well as a comparison between the two solution procedures.

The Monson study includes data collected during day-light periods, over two different summer sampling days (mid June, and mid July), for *Agropyron Smithii*, or wheatgrass. Data include vapor pressure deficit ($mmol\ H_2O\ (moleair)^{-1}$), leaf temperature (C), air temperature (C), irradiance ($W\ m^{-2}$), assimilation ($\mu moles\ CO_2\ m^{-2}s^{-1}$), and transpiration ($mmoles\ H_2O\ m^{-2}s^{-1}$). Data from the Monson study was digitized into 1-hour increments ($\Delta t = 3600\ s$) for this demonstration.

For the Euler-Lagrange solution, the value of λ is unknown and cannot be calculated directly. Therefore, using the temporally varying environmental data measurements, the value of λ was tested iteratively using the solution from Eq. (2.9) where the calculated stomatal conductance values were compared to observations. This approach does not address the volume of transpiration explicitly, but simply was a calibration of the unknown λ parameter.

For the Dynamic Programming solution, rather than needing to estimate a constant λ parameter over the period of integration, the constraint on the total volume of transpiration over the period of

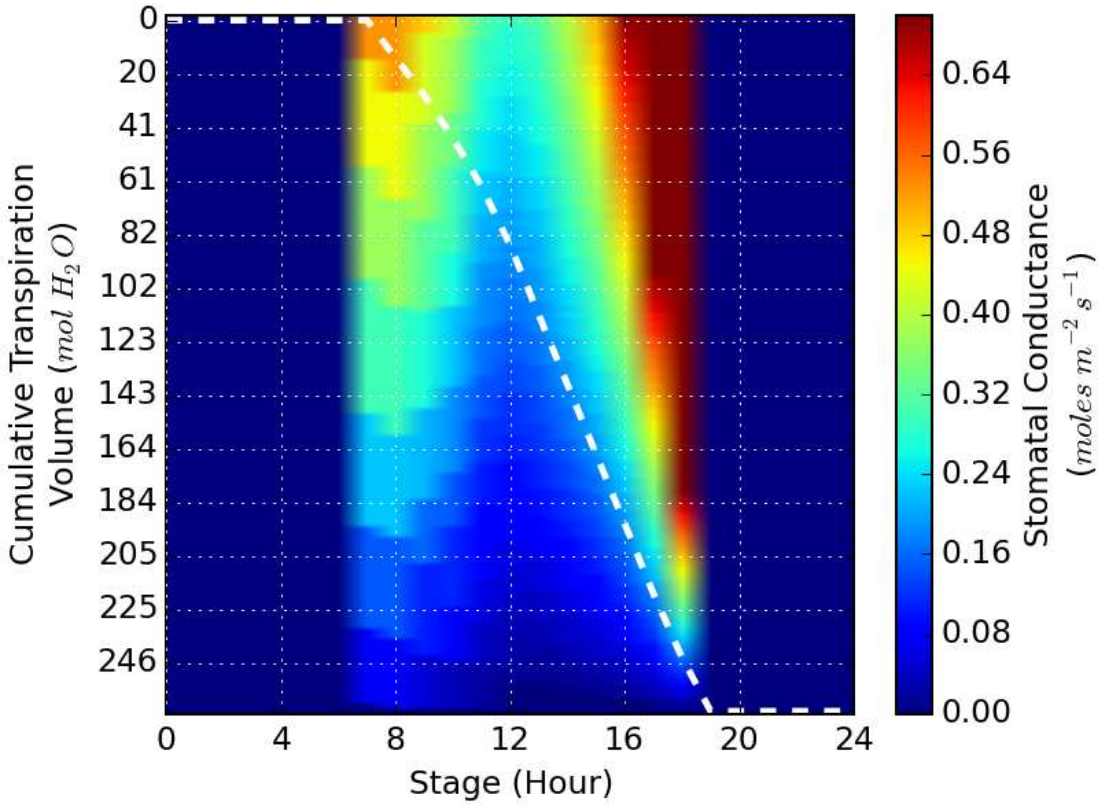

Figure 2.2: Sample State-Stage Decision Policy Matrix. Dashed line shows the optimal traceback path starting from zero cumulative transpiration at $t = 0$.

integration (E_T) is required. Although transpiration rates were reported in the study by Monson, our approach assumes a simple Fickian diffusive transpiration rate, thus requiring a calibration adjustment of the total transpirative volume, E_T.

Following the DP procedure, the optimal stomatal conductance values were determined for each state and stage, and are shown in Figure 2.2. Starting at midnight with no cumulative transpiration, the optimal policy traceback over the period of integration was determined (shown as the white dashed line). The stages begin at midnight, where the traceback shows no transpiration until daylight periods (as would be expected). Cumulative transpiration increases through the day, reaching the peak cumulative value E_T (the constraint) by the end of day-light hours. During the day, the rate of transpiration varies, as does the associated optimal stomatal conductance at each stage. The stomatal conductance values along the optimal traceback policy line are extracted from this surface.

Comparisons of stomatal response to Monson data during two separate sampling periods are shown in Figures 2.3 and 2.4. Also included on these figures is the solution using the Euler-Lagrange approach with the calibrated estimates of λ (a different value for each day).

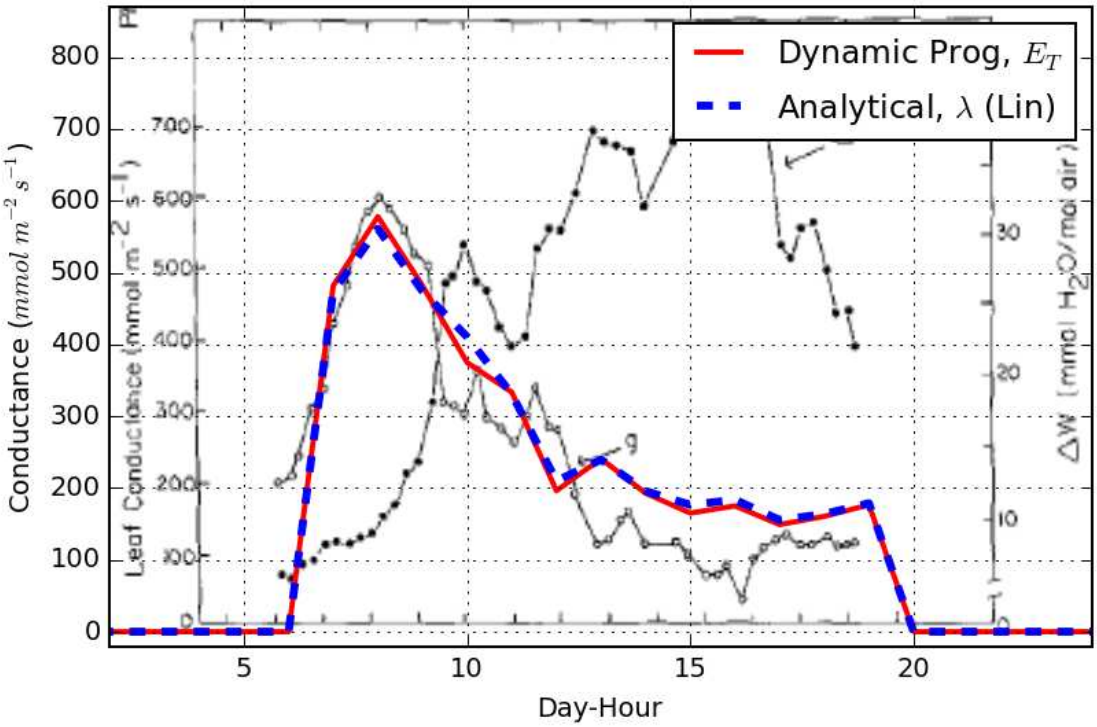

Figure 2.3: Hourly Optimal Stomatal Responses with Original Observed Data (July 17, 1983) [99]

2.4 Discussion

The temporal response of the optimal stomatal policy compares well to the observations considering the coarse environmental data and gross simplification of many plant physiological and soil-root processes. The mid-morning peak assimilation rate is well captured, while vapor pressure deficits are low, and depression of stomatal conductance through the course of the day is captured. Inclusion of a more robust transpiration scheme, including leaf energy balances, micro-climate variability, leaf boundary layer resistances, and coupling to soil moisture dynamics may further improve the performance of the model.

As can be seen in Figures 2.3 and 2.4, the optimal policies between the dynamic programming and the Euler-Lagrange solution procedure are nearly identical. This shouldn't be a surprise,

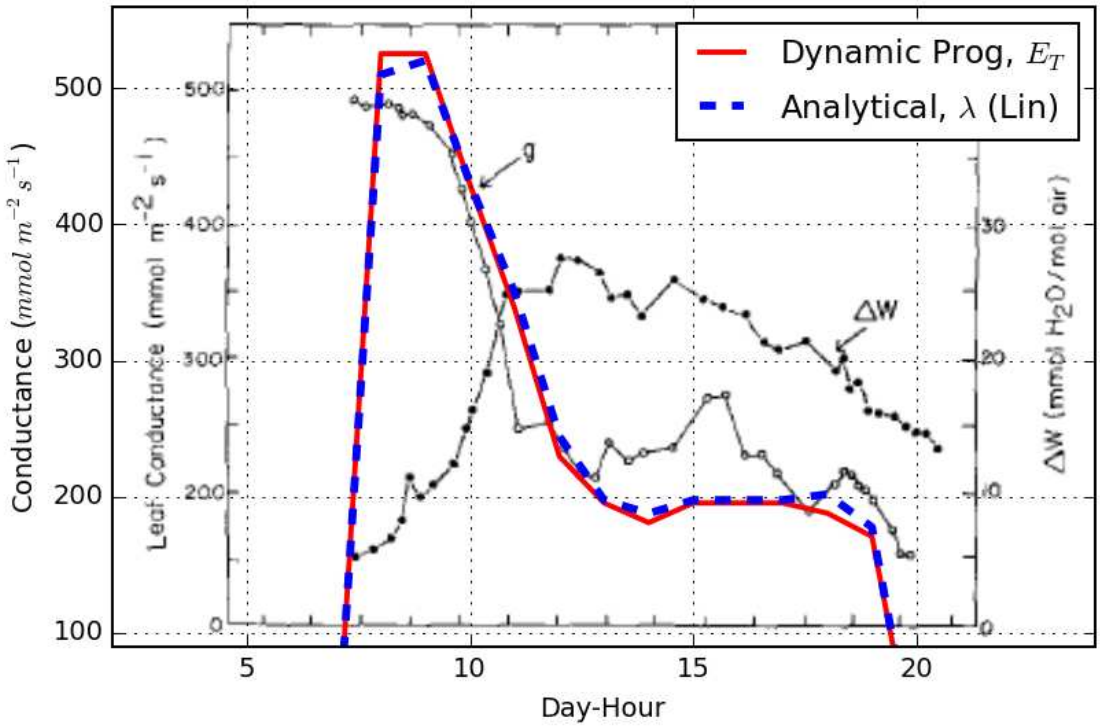

Figure 2.4: Hourly Optimal Stomatal Responses with Original Observed Data (June 14, 1983) [99]

considering that if both methods are providing the optimal policy, they should be equivalent. Note, the Euler-Lagrange solution is a 'continuous' solution, whereas the Dynamic Programming solution is 'discrete', thus there may be small differences between states and stages.

This detailed derivation and solution of the calculus of variations problem using either the Euler-Lagrange equation, or dynamic programming, highlight an important consideration - regardless of solution procedure when using an optimal stomatal control approach, a statement regarding total transpiration volume over the period of integration must be made. This occurs either implicitly through the selection of λ, or explicitly as an upper limit state constraint in dynamic programming. Therefore, models utilizing an estimate of λ through empirical relationships should consider adding further environmental covariates – as the value of λ is related directly to the total transpiration volume, soil moisture status, root structure, vapor pressure deficit, wind speed, leaf shape and size, canopy structure and micro-climate, and many other factors can affect an appropriate estimate - it is not simply a constant based on species or biome, and should instead be considered a dynamic environment dependent variable.

There are potentially gross errors through selection of a single value of λ (even for well-watered conditions) without considering the plant physiology and environmental affects on the constraint explicitly. Dynamic programming may be a more direct solution procedure, where estimating a value of daily integrated transpiration can be related to well established soil-plant-atmosphere processes. Whereas the meaning of the marginal water use efficiency parameter (λ) is well-defined analytically, estimation of the parameter beyond observational or regressive means is difficult or even impossible.

A simple recursive backward DP solution procedure has been presented here - the approach of utilizing DP to solve this problem opens further avenues of research and opportunity. For example, the problem can easily be adapted as a stochastic-dynamic programming problem, rather than using fully explicit environmental values as shown in this study. Further, multi-dimensional states can be defined, such as including soil moisture dynamics, or even possibly canopy level processes (rather than single leaf states as used in this study).

The advantage of DP is the ability to solve a wide array of complicated problems by dividing them into smaller discrete problems, and the potential applications in plant physiology and ecohydrology are unlimited.

2.5 Conclusions

Optimal stomatal conductance has been studied and applied for decades, but the traditional solution procedure, using the Euler-Lagrange equation without explicit consideration of the constraint for selection of λ may result in stomatal conductance errors as physiologic or environmental conditions change. We offer an alternative solution procedure to the original calculus of variations problem while explicitly considering the integrated transpiration volume using DP, rather than requiring an estimate of the marginal water use efficiency λ.

The final solution shows virtually no difference between procedures, assuming the integrated transpiration depth equals the resulting transpiration for a given MWUE.

Numerically, λ is well defined, although relating the magnitude of this parameter directly to a physical constraint of a system is difficult. Conversely, specifying the transpirative volume of a system (e.g. over the period of a day) can more easily be related to environmental conditions, soil

moisture status, and xylem conductance from roots to leaves. As such, for an optimal stomatal model, the DP approach can be integrated into a modeling framework where the volume used for transpiration is specified based on resource limitations and physical constraints of a system, rather than utilizing either a constant marginal water use efficiency or increasing the MWUE through empirical relationships.

Further, extensions of the DP approach into stochastic processes, or multi-state problem formulations, opens many avenues for assessing optimality in ecohydrology and plant physiology not possible using the traditional Euler-Lagrange solution procedure.

Chapter 3

Optimal Allocation of Leaf-Level Resources

It is not the strongest of the species that survives, not the most intelligent that survives. It is the one that is the most adaptable to change.

– **Charles Darwin, Origin of Species**

3.1 Introduction

Photosynthesis uses atmospheric carbon dioxide (CO_2), water, nitrogen, and other molecules to transform solar energy (i.e., from photons) into chemical energy (i.e., glucose, ATP, and other forms of chemical energy), a process also termed *carbon assimilation*. Photosynthesis occurs in the leaf chloroplasts and involves light-dependent and light-independent biochemical reactions. The former reactions produce O_2, ATP and NADPH and are constrained by the maximum rate of electron transport, J_{max} ($\mu mol\ e^-\ m^{-2}s^{-1}$), whereas the latter reactions use the products of the light-dependent reactions to produce glucose from CO_2, and are constrained by the maximum rate of carboxylation, V_{cmax} ($\mu mol\ CO_2\ m^{-2}s^{-1}$).

CO_2 enters the leaf through *stomata*, small pores on the epidermis of leaves (most abundant on the abaxial side) whose aperture varies depending on environmental and biochemical factors. The flux of CO_2 is the product of the stomatal conductance and the concentration gradient of CO_2

between the leaf pore spaces and the atmosphere. However, the rate of carbon assimilation depends also on the biochemical capacity of the photosynthetic system defined by V_{cmax} and J_{max}.

Carboxylation includes the reaction of CO_2 with Ribulose-1,5-Bisphosphate (RuBP), which is catalyzed by the enzyme Ribulose-1,5-Bisphosphate Carboxylase-Oxygenase (RuBisCO); V_{cmax} is the maximum rate of RuBP carboxylation. RuBP and RuBisCO are essential in the light-independent reactions leading to the production of glucose (i.e., of the Calvin-Benson cycle) [105]. J_{max} is the maximum rate of electron transport in the light-dependent reactions that limits the supply of energy (i.e., ATP and NADPH) for carboxylation and for regeneration of RuBP in the Calvin-Benson cycle. Therefore, both V_{cmax} and J_{max} are critical in determining the rate of carbon assimilation.

The biochemical model of photosynthesis of Farquhar, von Caemmerer and Berry [40], hereafter referred to as the FvCB model, is widely employed to describe C3 and C4 photosynthesis over a range of climates and species (see Appendix A for details about the FvCB model). Typically, V_{cmax} and J_{max} are estimated by fitting the FvCB model to gas-exchange measurements [120]. This has resulted in a plethora of published values varying between species, climates and environmental conditions [79, 95, 129, 136, 146]. Furthermore, V_{cmax} and J_{max} also vary with depth in the canopy [101, 104], and through the season [15, 98, 108, 142, 147]. However, a general approach for describing variable V_{cmax} and J_{max} dependent on environmental and biochemical conditions has not been developed. As a result, many photosynthesis models currently used in terrestrial biosphere models (TBMs) assume constant values for V_{cmax} and J_{max} normalized to a reference temperature (usually 25 deg.C, referenced as $V_{cmax_{25}}$ or $J_{max_{25}}$).

Here, we propose a new *optimal allocation* approach for C3 photosynthesis such that V_{cmax} and J_{max} vary with mean environmental and biochemical conditions so as to make optimal use of a finite supply of resources (i.e., light, nitrogen and water). Optimal use is that which maximizes the expected value of carbon assimilation over appropriate timescales (e.g., seasonal, inter-annual, climatic).

3.2 Approach

3.2.1 Optimality

Many optimality hypotheses describing photosynthetic responses to varying environmental conditions have been proposed and studied for well over 50-years, including optimal stomatal responses [28, 81], optimal nitrogen partitioning in a canopy [21, 33, 117], optimal partitioning of leaf level nitrogen [59], optimal leaf area indices [4], and mutually dependent (i.e., coordinated) optimality of plant hydraulic traits (i.e., water transport) and photosynthesis [90, 111].

Here, we consider a novel optimal allocation approach for partitioning leaf-level nitrogen between the two photosynthetic sub-systems associated with light-dependent and light-independent reactions that maximizes the expected value of assimilation, and leads to optimal values for carboxylation and electron transport capacities for a given light environment and mean stomatal conductance. As opposed to previous approaches that either fix the magnitude of one of the systems at a reference temperature, or constrain the ratio of $J_{max_{25}}$ to $V_{cmax_{25}}$, this approach allows both V_{cmax} and J_{max} to vary in a coordinated manner.

The photosynthetic system includes a series of inter-operating sub-systems where solar energy is used for converting atmospheric carbon and water into active and stored forms of energy [40, 131]. This includes sub-systems for light harvesting and electron transport, and for the development and maintenance of RuBisCO, critical for carboxylation. Larger values of V_{cmax} or J_{max} represent greater photosynthetic capacities of each sub-system, although at a cost of increased requirements for limited resources (primarily nitrogen) [113].

Stomata adjust to environmental and biotic conditions on short time scales on the order of minutes [62,76,124], whereas V_{cmax} and J_{max} adjust seasonally on longer time scales [108]. Approximately 2-5% of biomass proteins (e.g., RuBisCO, etc.) are turned over and regenerated daily [123], which is approximately 100% turnover every 30 days. This is a more appropriate time scale for assessment of adaptation of V_{cmax} and J_{max}.

If most nitrogen resources were invested primarily in the development and maintenance of RuBisCO, the leaf would have a relatively high maximum rate of carboxylation (V_{cmax}), but limited resources remaining for investment in the electron transport system resulting in a relatively low

J_{max}. Under this condition, the assimilation rate will remain limited by J_{max} regardless of irradiance level – clearly not an optimal allocation of nitrogen. Conversely, the system could have a high value of J_{max}, but no capacity for RuBP carboxylation with limited investment in RuBisCO. An optimal allocation is likely closer to a state of co-limitation between both photosynthetic systems [132]. We posit that there exists an optimal nitrogen allocation strategy that maximizes expected assimilation over a given time scale for V_{cmax} and J_{max} variation. In the case of natural vegetation, this can be approximated as a period of one month.

For a given concentration of leaf-level organic nitrogen, N_{org}, we define the optimal values of V_{cmax} and J_{max} corresponding to the optimal allocation of organic nitrogen by the following expression,

$$\begin{aligned} V^*_{cmax}, J^*_{max} &= argmax \\ &\int_t A_n(V_{cmax}, J_{max}, g_s; \Theta)\ \mathrm{d}t \mid N_{org} \end{aligned} \tag{3.1}$$

where A_n is the net rate of assimilation (gross assimilation minus leaf respiration), g_s is the stomatal conductance, and Θ is a vector of exogenous time-dependent variables including irradiance, soil moisture, and vapor pressure. The period of integration, t, corresponds to the time scale of variation of V_{cmax} and J_{max} (e.g., a month). In the above expression, N_{org}, V_{cmax} and J_{max} are constant for the given t, but A_n, g_s, and Θ vary continuously.

For a given period of integration, the values of V_{cmax} and J_{max} that solve Eq. 3.1 also maximize the expectation of A_n. Therefore, we can similarly restate the above as,

$$\begin{aligned} V^*_{cmax}, J^*_{max} &= argmax \\ &\mathbf{E}\left[A_n(V_{cmax}, J_{max}, g_s; \Theta)\right] \mid N_{org} \end{aligned} \tag{3.2}$$

which is analogous to,

$$\begin{aligned} V^*_{cmax}, J^*_{max} &= argmax \int_\Theta f(\Theta) \\ &A_n(V_{cmax}, J_{max}, g_s; \Theta)\ \mathrm{d}\Theta \mid N_{org} \end{aligned} \tag{3.3}$$

where $f(\Theta)$ is the joint probability density function (PDF) of variable(s) in set Θ for the given time period t.

3.2.2 Nitrogen and Photosynthetic Capacity

Nitrogen is critical for development and maintenance of all components of the photosynthetic system [114] and is allocated to its various components as follows, [37],

$$N_{org} = N_P + N_E + N_R + N_S + N_O \tag{3.4}$$

where, N_P is the nitrogen invested in pigment proteins such as chlorophyll a and b, N_E is nitrogen allocated to the electron transport system including cytochrome f and coupling factor, N_R is the nitrogen allocated to RuBisCO, N_S is nitrogen in soluble proteins other than RuBisCO, and N_O is additional organic leaf nitrogen not invested in photosynthetic functions such as in cell walls (all terms in Eq. 3.4 are in units of $mmol\ N\ m^{-2}$.)

In order to solve Eq.3.1 through Eq.3.3, constrained by leaf-level nitrogen, an explicit link relating leaf nitrogen concentration to V_{cmax} and J_{max} is required, although this does not specify any fixed relationship between nitrogen and mean/max photosynthetic capacity. Several researchers have assessed these relationships for C3 species using observations, including Hikosaka and Terashima in 1995 [58], and Evans and Poorter in 2001 [36].

Following Evans and Poorter, the non-soluble thylakoid nitrogen, equal to the sum $N_P + N_E$, may be estimated as [36, 149],

$$N_P + N_E = 0.079 J_{max} + 0.0331\chi \tag{3.5}$$

where J_{max} is in $(\mu mol\ e^-)\ m^{-2}\ s^{-1}$, χ is the concentration of chlorophyll per unit area $(\mu mol\ Chl\ m^{-2})$, 0.079 is in $mmol\ N\ s\ (\mu mol\ e^-)^{-1}$, and 0.0331 is in $mmol\ N\ (\mu mol\ Chl)^{-1}$.

The soluble nitrogen excluding that allocated to Rubisco is,

$$N_S = \nu J_{max} \tag{3.6}$$

where $\nu \approx 0.3\ (mmol\ N\ s\ (\mu mol\ e^-)^{-1})$.

To make the connection between V_{cmax} and RuBisCO, we utilize relationships from Niinemets et al. [101, 103],

$$N_R = V_{cmax}/(6.25 \times V_{cr} \times \xi) \tag{3.7}$$

where V_{cmax} is in $\mu mol\ CO_2\ m^{-2}\ s^{-1}$, V_{cr} is the specific activity of RuBisCO, that is, the maximum rate of RuBP carboxylation per unit Rubisco
($\approx 20.5\ \mu mol\ CO_2\ (g\ RuBisCO)^{-1}\ s^{-1}$), 6.25 is grams RuBisCO per gram nitrogen in RuBisCO, and ξ is the mass of one millimole of nitrogen in grams equal to 0.014 $gN\ (mmol\ N)^{-1}$.

Finally, the term N_O is a constant of 'extra' organic leaf nitrogen allocated to non-photosynthetic resources.

Therefore, substituting Eqs. 3.5, 3.6, and 3.7 into Eq. 3.4, leads to,

$$\begin{aligned} N_{org} = 0.079 J_{max} + 0.0331\chi \quad &+ \quad V_{cmax}/(6.25 V_{cr} \xi) \\ &+ \nu J_{max} + N_O \end{aligned} \tag{3.8}$$

which directly relates leaf organic nitrogen N_{org} to V_{cmax} and J_{max}.

3.2.3 Assimilation and Stomatal Control

We implement the FvCB model to determine the rate of net assimilation in Eqs.3.1 - 3.3 for a given V_{cmax} and J_{max}, (see Appendix A for details about the FvCB model). However, the FvCB model does not explicitly include stomatal function regulating the internal concentration of CO_2 and the supply of CO_2 into the leaf. There are several models describing the relationship between assimilation and stomatal conductance, including the Ball-Woodrow-Berry model [5] and its variant the Leuning model [78], as well as optimality based models including the seminal work of Farquhar and Cowan [28], and more recent adaptations of optimal stomatal control by Katul et al. [70] and Manzoni et al. [89].

In order to determine the variations of stomatal conductance and the associated rate of assimilation, we implement an optimality based approach similar to that of Manzoni et al. (2011) (see Appendix A for the derivation of the optimal stomatal control model).

3.3 Results

3.3.1 Optimization

A closed form analytical solution of Eq. 3.3 is not feasible, therefore we implemented a numerical procedure as described in detail in Appendix A. The maximum expected value of assimilation is determined by using a gridded-search in the feasible decision space of V_{cmax} and J_{max}.

For a given N_{org} and distribution of irradiance, the numerical procedure leads to a decision surface as shown in Figure 3.1. The figure shows that there exists a unique pair of carboxylation and electron transport capacities that maximize the expected assimilation; that is, there exists an optimal pair (V^*_{cmax}, J^*_{max}) that solves Eq.3.3.

Suboptimal values occur for alternate allocations of nitrogen between N_P, N_R, N_S and N_E. For example, holding the optimal value of J_{max}, while increasing allocation of nitrogen in chlorophyll (N_P) and concurrently decreasing nitrogen in RuBisCO (N_R) to maintain a constant N_{org}, would decrease the expected value of assimilation. Even as the absorptance fraction (solid white lines) increases from higher levels of Chlorophyll, the system would become increasingly carboxylation-limited due to lower investment of nitrogen in RuBisCO. This condition is demonstrated by moving along the dashed line, which represents constant J_{max}, with lower values of V_{cmax} than the optimal value in Figure 3.1.

3.3.2 Variable Leaf-Level Nitrogen

The process of finding optimal allocations was repeated for a number of leaf organic nitrogen levels, holding all other parameters constant, resulting in an optimal response function. The optimal V_{cmax} values over a typical range of observed nitrogen levels were then compared to regressed relationships by Kattge et al. (2009) [69], who used a collection of observations from a number of different studies and plant functional types. This comparison is shown in Figure 3.2.

For temperate broadleaf trees, shrubs and herbaceous groups, Figure 3.2 shows that the optimal allocation approach leads to relationships between N_{org} and V_{cmax} that are nearly identical to the relationships of Kattge et al. (2009), supporting the hypothesis that nitrogen is allocated between various photosynthetic systems to maximize net expected assimilation.

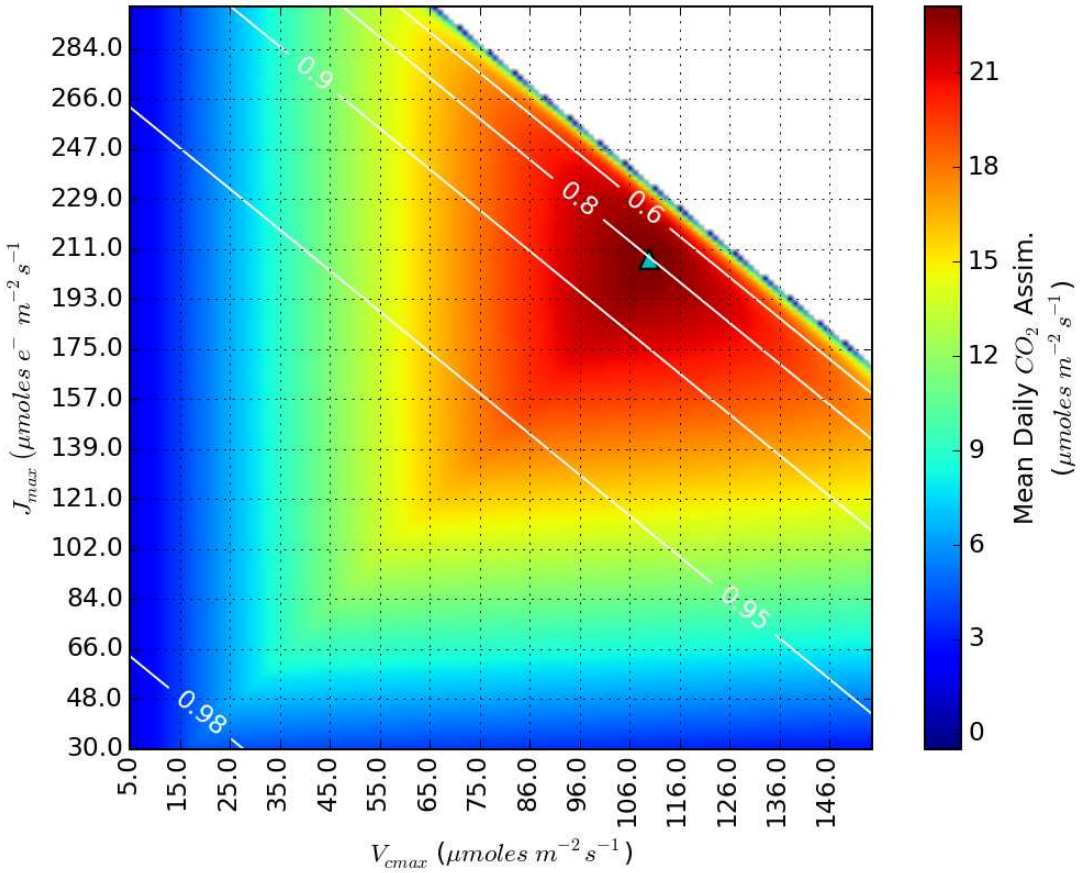

Figure 3.1: Photosynthetic Parameter Decision Space - Leaf level photosynthetic parameters and the expected value of daily assimilation. White contours represent the irradiance absorptance fraction. Optimal allocation with maximum expected assimilation marked with a small triangle. [The graph shown corresponds to $N_{org} = 2.7g\ m^{-2}$, $K_m = 450\ \mu mol\ mol^{-1}$, and a scaled beta-distributed irradiance with parameters: $Irr_{max} = 1000W\ m^{-2}$, Irradiance density parameters: $\beta_a = 1.2$, $\beta_b = 1.5$]

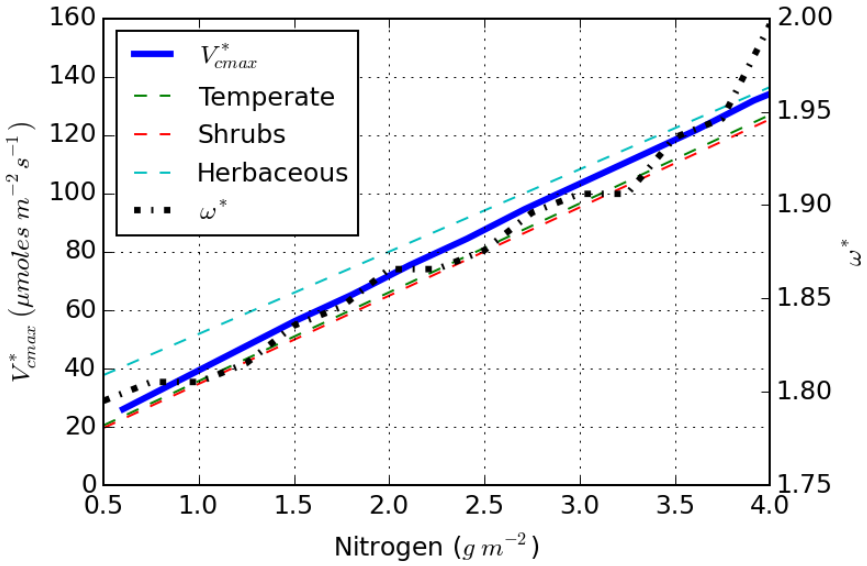

Figure 3.2: Comparison of optimal V_{cmax} values with regressed relationships for different biomes (Regressions from Kattge, 2009, Table 2, using just V_{cmax} regressions) [$K_m = 450\ \mu mol\ mol^{-1}$, $Irr_{max} = 1000W\ m^{-2}$, $\beta_a = 1.2$, $\beta_b = 1.5$]

3.3.3 Variable Light Environment

Variability in the characteristics of the light environment (i.e., changes in the distribution of irradiance) may result from seasonal effects [8], from canopy closure [142], or both.

For a given amount of N_{org}, the optimal allocation approach for variable irradiance levels leads to results as those shown in Figure 3.3. Reduction of irradiance leads to a reduction in V^*_{cmax} (and an increase in the ratio $J^*_{max}/V^*_{cmax} = \omega^*$), representing an optimal solution with greater investment of organic nitrogen in chlorophyll a and b for light harvesting as compared to that invested in carboxylation systems.

The predicted pattern of change in ω^* shown in Figure 3.3 is similar to observations in nature [142], and is explained by the optimal allocation approach. Thus, the optimal allocation of nitrogen between photosynthetic sub-systems also explains why the ratio of J^*_{max}/V^*_{cmax}, (i.e., ω^*), is commonly observed to equal 2.1 +/- 0.6 across a wide range of biomes and species [7,68,79,95,108,146].

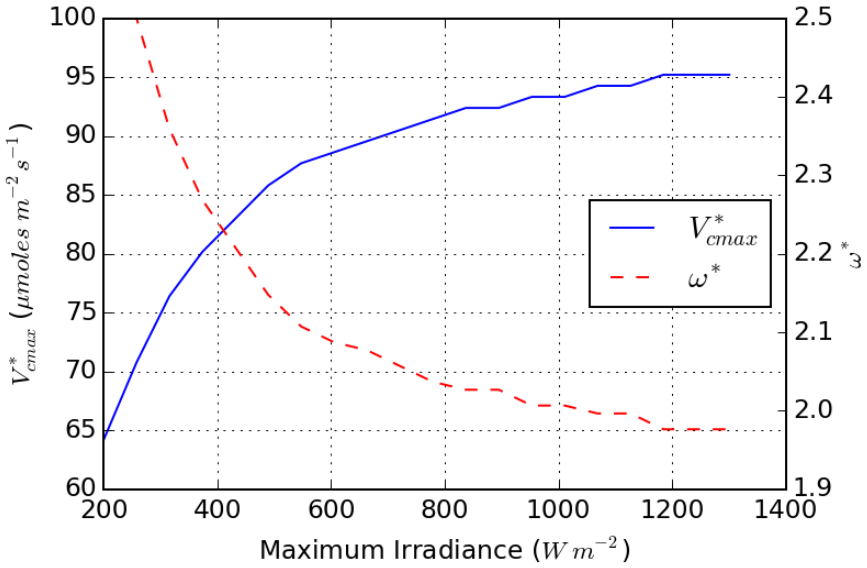

Figure 3.3: Optimal values of V_{cmax} and ω with variable light environment [$N_{org} = 2.7g\ m^{-2}$, $K_m = 450\ \mu mol\ mol^{-1}$, $Irr_{max} = variable$, $\beta_a = 1.2$, $\beta_b = 1.5$, $R_d = 0.015 \times V_{cmax}$]

3.3.4 Photosynthetic Down-Regulation

During periods of low soil moisture supply (i.e., periods of moisture stress), stomata may partially or fully close to prevent excessive negative leaf, shoot or root water potentials causing xylem embolism [66, 86, 128]. Closure of stomata reduces transpiration and the flux of CO_2 into the leaf resulting in inhibited assimilation – rates below the maximum potential for well-watered capacity (i.e., no moisture stress). This available but unused photosynthetic capacity incurs continued maintenance costs from respiration and protein re-synthesis.

Rather than maintaining this unused capacity, the photosynthetic system may be down-regulated (sometimes referred to as a non-stomatal response), resulting in a reduction of V_{cmax} and J_{max} from well-watered values [43]. The down-regulation process requires modification of the photosynthetic system and potentially translocation of resources. For a given N_{org}, light, and temperature, reduction of V_{cmax} and J_{max} from the optimum values should occur in a coordinated manner that maximizes the assimilation at reduced photosynthetic capacity.

In terms of V_{cmax} and J_{max}, an optimal down-regulated state is where the reduction in expected assimilation is minimum for a unit change in photosynthetic capacity (i.e., unit changes in V_{cmax}, J_{max}), implying a reallocation of the maximum amount of N_{org} to other biochemical uses.

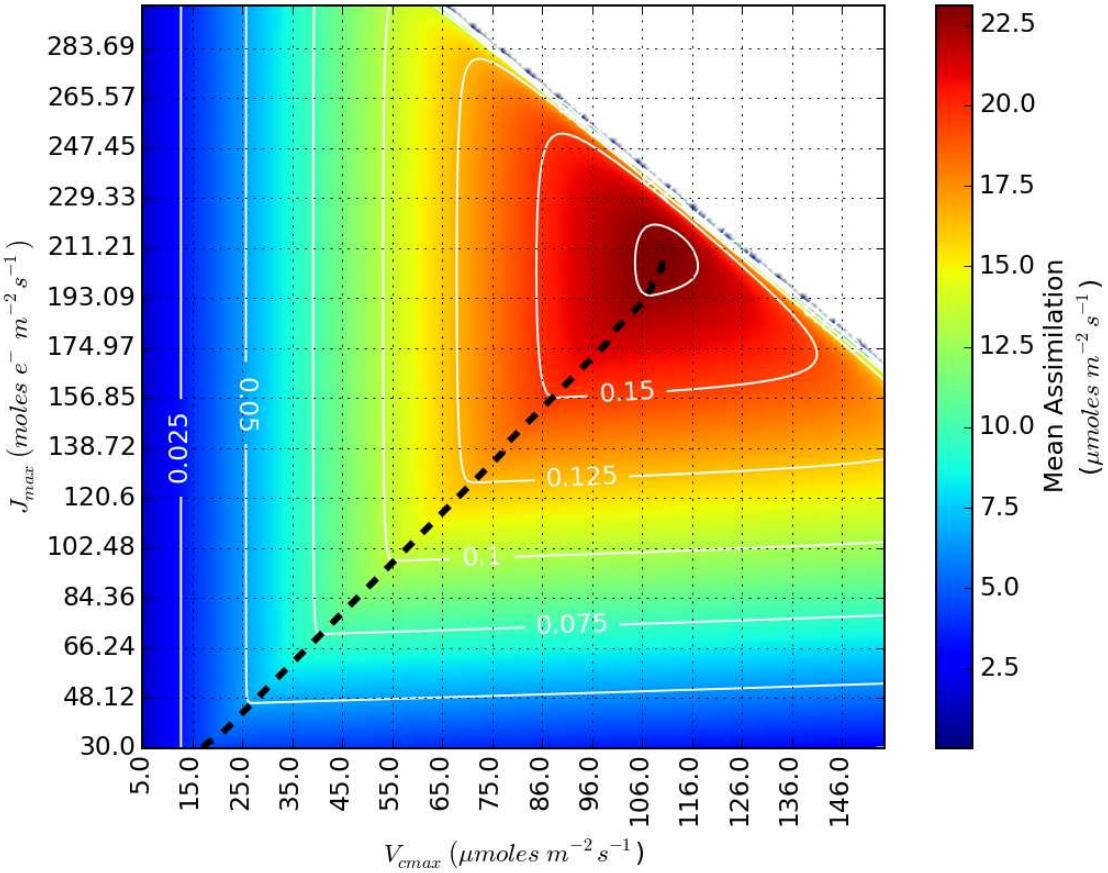

Figure 3.4: Most efficient non-stomatal down-regulation pathway (dashed black line) for V_{cmax} and J_{max}. Contours of mean stomatal conductance (white solid lines) $(mol\ m^{-2}s^{-1})$.

Mathematically, the optimal down-regulation path is the *locus* of (V_{cmax}, J_{max}), starting from the (V^*_{cmax}, J^*_{max}), satisfying the condition that the magnitude of the gradient is minimum, that is, $|\nabla A_n(V_{cmax}, J_{max})| = minimum.$

Figure 3.4 shows the path of down-regulation on the assimilation decision surface. The optimal down-regulation path represents a path of optimal reallocation of nitrogen – this is also an allocation strategy that closely follows a state of co-limitation between the photosynthetic systems. Chen et al.,(1993) proposed the *Coordination Theory* describing nitrogen allocation through a canopy where photosynthetic systems are co-limited [21]. More recently, Maire et al., (2012) assessed 293 observations from 31 different species under a range of environmental conditions, and found that under mean environmental conditions during the preceding month, RuBP carboxylation equaled RuBP regeneration [88]. Our results further support these ideas from an optimality perspective.

The path of down-regulation provides a direct link between the expected value of assimilation and the optimal values of V^*_{cmax} and J^*_{max}. Therefore, knowing the leaf-level N_{org} and the irradiance density distribution, the optimal allocation resulting in the stomatal-constrained values of V^*_{cmax} and J^*_{max} can be found for any A_n lower than the maximum value. However, a relationship between expected A_n (or equivalently g_s) and soil moisture status is required. Generally, these relationships can be estimated using linear-step functions similar to maximum stomatal conductance responses [42, 127], or any other available species-specific approach.

3.3.5 Optimal Allocation Down-Regulation against Observations

The optimal down-regulation procedure postulated here was tested against reported seasonal values of J_{max} and V_{cmax} in a summer semi-arid environment. We utilized data reported by Xu and Baldocchi [147], who studied an oak savanna system in California exposed to extended summer dry periods. Their study provided detail of temperatures, vapor pressure deficits, and soil moisture throughout the growing season. Additionally, they measured stomatal conductance and carbon assimilation, which were used to determine the seasonally variable V_{cmax} and J_{max}.

The study by Xu and Baldocchi represents a system whose moisture stress is slowly increased through a season – a condition allowing photosynthetic system down-regulation compared to solely regulating assimilation with stomatal control.

Using the reported values of total leaf nitrogen (where total leaf nitrogen is organic nitrogen plus nitrate nitrogen), with an estimated fraction as organic nitrogen, in addition to temperature adjusted estimates of the Michaelis-Menten half-rate constant, K_m, [96] and an irradiance density distribution (assumed constant during the growing season), the down-regulation path was determined starting from the unstressed optimum as postulated above, resulting in optimal down-regulated values of V^*_{cmax} and J^*_{max} at a range of stomatal conductances and expected assimilation rates. Finally, using only the stomatal conductance values reported over the season, the corresponding optimal values of V^*_{cmax} and J^*_{max} were returned from the optimal path. Figure 3.5 compares the resulting optimal values of V^*_{cmax} and J^*_{max} (without any calibration) to those reported by Xu and Baldocchi [147].

The observed seasonal variation in V_{cmax} and J_{max} is well reproduced with the optimal down-regulated path from the maximum value of assimilation. The peak values of V_{cmax} and J_{max} during

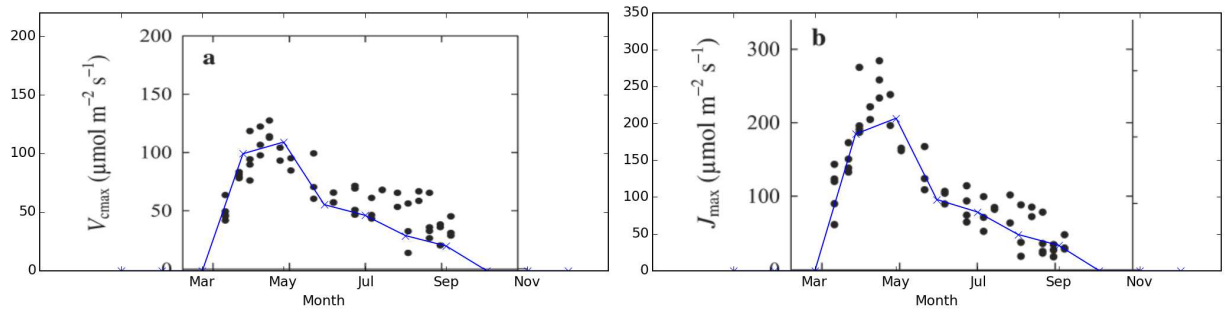

Figure 3.5: Comparison of Seasonal Co-Limited Down Regulation to Observed Data. Blue line is a trace of the V_{cmax} and J_{max} values at a state of co-limitation using only observed maximum assimilation rate data. Data obtained from a study by Xu and Baldocchi, 2003 [147]. Note: these results are uncalibrated.

leaf flushing (initial growth of leaves during the spring) is not fully captured, most likely from increased leaf respiration not included in the model during this period. Regardless, as assimilation and stomatal conductance become limited during the summer due to soil moisture stress, the down-regulation of the photosynthetic system is replicated. This result further supports the idea of optimal allocation, and demonstrates how the optimal approach can allow for a dynamic seasonal response of photosynthetic capacity.

3.4 Summary and Concluding Remarks

We have introduced a new optimality based approach for considering leaf level partitioning of nitrogen in various environments. Although many simplifications were made, the optimal allocation of organic nitrogen between components of the photosynthetic systems results in photosynthetic system capacities as well as relationships between those capacities and levels of organic nitrogen and irradiance that replicate those observed in nature as reported in the literature.

This includes relationships between N_{org} and V_{cmax}, light environment and ω, and the response of photosynthetic system capacity during periods of down-regulation. This approach provides a new mechanism to incorporate dynamic responses of V_{cmax} and J_{max} for C3 photosynthesis in TBMs.

Accurate parameterization of the photosynthetic system is paramount in coupled TBMs and global circulation models with respect to carbon and water cycling processes, and critical to these processes are the maximum rates of electron transport and carboxylation capacity. Assuming constant values for these capacities, as is currently done (e.g., at $J_{max_{25}}$ and $V_{cmax_{25}}$), may introduce

significant accumulated errors in the carbon and water balances over multi-decadal model projections [116]. Utilizing this optimal allocation approach addresses these variations with environment.

The optimal allocation approach allows a unique perspective into seasonal and climatic variation of photosynthetic capacity with a finite supply of resources, and opens many avenues of research allowing an improved understanding of vegetation dynamics in our changing climate.

Chapter 4

An Empirical Harmonic Approach for Climatic Leaf Area Index Phenology

Every blade in the field - Every leaf in the forest - lays down its life in its season as beautifully as it was taken up.

– **Henry David Thoreau**

4.1 Introduction

Changes in climate are resulting in significant variations of the biota and flora across the planet [141], including changes of leaf *phenology* [18, 112], the seasonal timing of leaf budding, growth and senescence [23]. Changing phenology and peak *leaf area index* (LAI), the approximate one-sided area of canopy leaves per unit ground area, is troublesome for estimation of canopy level transpiration, precipitation interception, and gross primary productivity [50] over projected multi-decadal periods in macro-scale terrerstrial biosphere models (TBMs). These variations in annual LAI phenology are critical for understanding the long-term influence on the hydrologic cycle, gross primary production, and carbon cycling.

Physically based approaches for predicting vegetation, sometimes referred to as mechanistic methods, may be used to evaluate the response of vegetation cover in a changing climate. These classes of models are called *Dynamic Global Vegetation Models* (DGVMs) [49, 74, 118, 122], and require assumptions for: carbon allocation within an individual species [83], growth limitations and

mortality, water use strategies, nutrient supplies, stress responses, and potentially accounting for competition amongst individuals [22, 119]. Besides being highly parameterized, it is common to assume that parameterization under past climates will remain valid in novel climates [119]. Further, generalized land cover classes may be used in DGVMs, but either the associated phenology is static for each class, or the relationships determining the phenology are static (e.g. specified value of degree-days for bud burst).

An alternative approach to DGVMs is to utilize a regression approach linking vegetation to climatic covariates. One of the earlier studies using this approach was completed by Box in 1981 [12], which concluded that, '*general macroclimatic conditions are more important than any other factors... in determining general ecologic structure on most sites*'. This model used eight climate variables for prediction of land cover plant growth forms, and also included limits for acceptable ranges of growth forms.

A biome regression model was also developed by Prentice et.al. [115], where climatic covariates included the mean coldest month temperature, annual accumulated temperature over 5°C, and a drought index to consider seasonality of soil moisture availability. This model was able to predict natural vegetation with a high degree of fitness across the globe, with the intended application of using the model to understand changes in land cover and carbon balance in a changing climate.

More recently, a regression model for phenologic response (in the form of a greenness index) was developed by Jolly, et.al. 2005, [64] using variables of photoperiod, vapor pressure deficit, and minimum temperatures. This model was able to accurately replicate seasonal timing of NDVI observations, with proposed applications for projecting future climatic vegetation responses.

Clearly, a direct link between climate and vegetation cover exists that can be used for reanalysis and prediction of vegetation responses. As resource availability changes, so does the response of the terrestrial vegetation with respect to phenology and supportable biomass; it is theorized that vegetation will optimally use available resources to maximize biomass but minimize the chance of mortality. A regression of phenology (essentially a seasonal measure of biomass production) is a regression of this optimal state of resource utilization.

The unique aspect of this chapter compared to previous studies is the linking of climate directly to the Leaf Area Index values as a temporal (harmonic) series, allowing prediction of annual LAI phenology - this has greater direct utility in applications for macro-scale hydrologic modeling,

compared to estimates of NDVI or categorical regression for biomes, for example. We are specifically interested in the change in the magnitude and timing of LAI, based solely on descriptions of the local climate.

The growth and maintenance of vegetation biomass, which requires leaf area, involves many complicated and interacting processes as noted, and is critical to understand in the development of hydrologic projection models in novel climates. Although a regression approach moves away from physical explanation of certain processes, it does allow for a more dynamic response of vegetation accounting for latent processes currently unexplainable even through the most advanced and highly parameterized physically based modeling systems.

A *space-for-time* substitution requires regression solely on *climatic* variables, excluding space dependent covariates such as: soil type, elevation, latitude, etc. For the purposes of fitting parameters in this analysis, climate is assumed to represent the mean values of covariates over a 30-year period. Therefore, the locations evaluated through space are considered to be responding to the same process, but within a different climate, which allows us to evaluate new climates over time and the potential vegetation response in the form of annual LAI phenology.

4.2 Approach

4.2.1 Harmonic Regression and Phenology

Leaf phenology is highly temporally correlated over a season creating a relatively smooth harmonic function from leaf growth to senescence. Any temporally varying continuous process can be fully defined by a Fourier Series.

The first order of a Fourier Series is the *primary harmonic*, and all sequential series are multiples at higher frequencies of the primary harmonic. We consider a stationary series using only the primary harmonic to estimate the seasonal phenology - this can be defined in real-dimensional space as,

$$L_t = \beta_0 + \beta_1 \times cos(2\pi t/T) + \beta_2 \times sin(2\pi t/T) \tag{4.1}$$

where, t is the time (month and fraction, [0,12] [1]), L_t is the LAI at t, T is the primary period (12

[1] This approximates each month as the same duration.

months), and the β terms are scalar coefficients. This form of Eq. 4.1 meets the definition of a linear model that can be used in a first-order linear regression - even though the response function is a non-linear harmonic, the coefficients are linear. Further, it's noted that the entire continuous seasonal phenology is defined solely by the three β parameters, rather than requiring specification of LAI by month (12 parameters), or parameterizing a mechanistic model to develop phenology (>>12 parameters), for example.

The three β parameters, which wholly define the annual phenology, are functions of climate. Therefore, our goal is to develop regressed relationships between climate and the set of β's that are used to describe the temporal sequence of annual phenology - as the climate changes, so does the resulting annual phenology. In order to develop regressed relationships between βs and climate, we first need to develop a set of β values using the harmonic regression model Eq.(4.1), where the observed sequence of LAI is the response variable L_t . In other words, we need to use observations of LAI to fit β values defining the harmonics across a wide geographic region, and then regress those β values on the local climate at each location.

Extensive spatial and temporal data is required to develop relationships between seasonal phenologic responses (described by the harmonic parameters) and the associated description of climate at each location. We only consider locations with natural vegetation to develop relationships between phenology and climate - managed landscapes, urban areas, agricultural lands and highly disturbed lands are not representative of natural landscape level vegetation responses to climate.

In order to only assess natural vegetation, the National Land Cover Dataset (NLCD2011) [60] was used to filter out non-natural vegetation regions by only including large contiguous areas of NLCD classifications of: Deciduous Forest, Evergreen Forest, Mixed Forest, Shrub/Scrub, Grassland/Herbaceous, and Woody Wetlands. The spatial resolution of NLCD2011 data is 30 meters, creating regions of highly variable natural and non-natural vegetation. To eliminate these regions, the natural land cover was up-scaled using a majority filter (ESRI, 2011) resulting in regions of what is more likely to include natural vegetation. Finally, these large regions were converted into a regular point-grid, resulting in 2883 points across the contiguous United States (CONUS), as shown in Figure 4.1. These points were further filtered for outliers resulting in a dataset of 2414 points covering the CONUS.

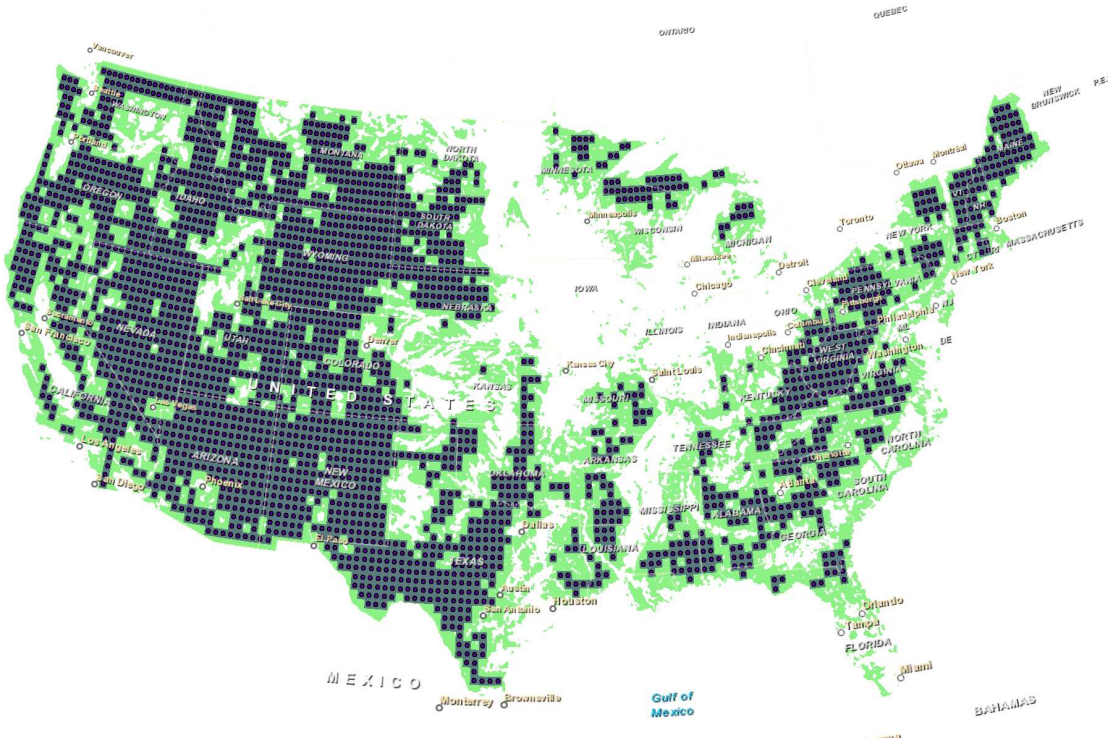

Figure 4.1: Natural vegetation point locations used for LAI sampling and regression

Bi-Weekly Leaf Area Index Phenology

The Boston University Department of Earth and Environment developed a 1/12 degree resolution reanalysis of bi-weekly (two per month) LAI values for 30+ years (1980-2010)[2] [151], referred to as LAI3g. A temporal series of 30-year bi-weekly LAI values was extracted for each natural vegetation point shown in Figure 4.1. In this case, the phenology represents a lumped average estimate of LAI from remotely sensed data of the 1/12 degree region during a given two-week period, and not a specific species or single PFT.

For each extracted LAI3g dataset, an ordinary least squares (OLS) regression was used to estimate the three harmonic β coefficients of the leaf phenology using Eq.(4.1). This analysis was performed using R[3]. As a result, spatially varying coefficients (βs) fitted to the LAI3g dataset across the CONUS were developed. These coefficients, shown in Figure 4.2 for just the Colorado River Basin, describe the spatially varying phenologic process, which is then regressed against climate covariates at each location.

[2] http://sites.bu.edu/cliveg/datacodes/

[3] `https://cran.r-project.org/`

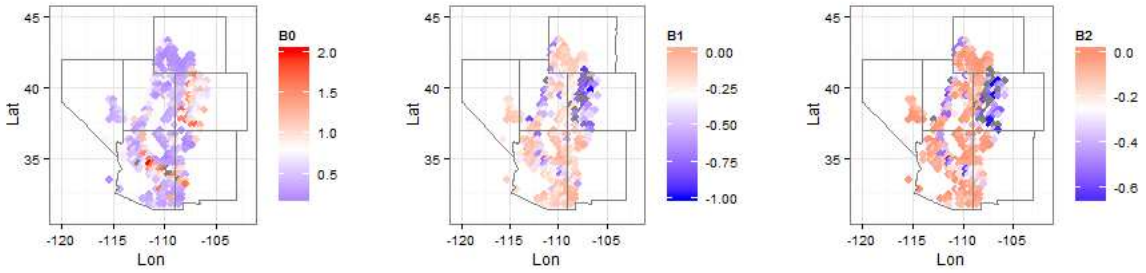

Figure 4.2: Fitted Harmonic Coefficients across the Colorado River Basin

As part of exploratory data analysis, a non-parametric Mann-Kendall trend test was performed on the extracted LAI3g data. For each location, the bi-weekly values of LAI were averaged to a single monthly value over the period of record (for use in monthly LAI phenology regression and easier description of monthly responses). The Mann-Kendall test results in a p-value for significance of trend, and a τ value in set [-1,1] indicating the strength and direction of the trend. Locations with p-values ≤ 0.05 were extracted and then displayed spatially by month, and color-shaded by the τ value, as shown in Figure 4.3. The result is a figure showing locations and directions of LAI trends by month across the CONUS.

As can be observed, Figure 4.3 shows significant trends in both positive and negative directions for monthly average LAI values across the country, with significant aggregated regional trends. Of significance, the extensive greening of the east coast in late-season months is quite apparent, indicating a wide-spread extension of the growing season, with a similar (but less extensive) pattern at the beginning of the growing season. Additionally, note the persistent year-round loss of vegetation cover as measured by LAI in the southwest CONUS. And finally, there appears to be a winter decrease of LAI and a fall growing season extension of LAI in Idaho and Montana; this is significant, as it may indicate shifts from conifer evergreen species to deciduous species, as has been observed by others [18].

This brief data exploration of trends in seasonal phenologic magnitudes also highlights the motivation for a dynamic parameterization - across the CONUS, statistically significant shifts in vegetation LAI are observed, and the magnitude and direction of trends also varies by time within an annual season. For long-term hydrologic projection modeling, utilization of stationary LAI values, or even fixed patterns of phenology, may lead to gross errors in the water balance and certainly in the carbon balance. Utilization of methods associating expected phenology with climate allow the

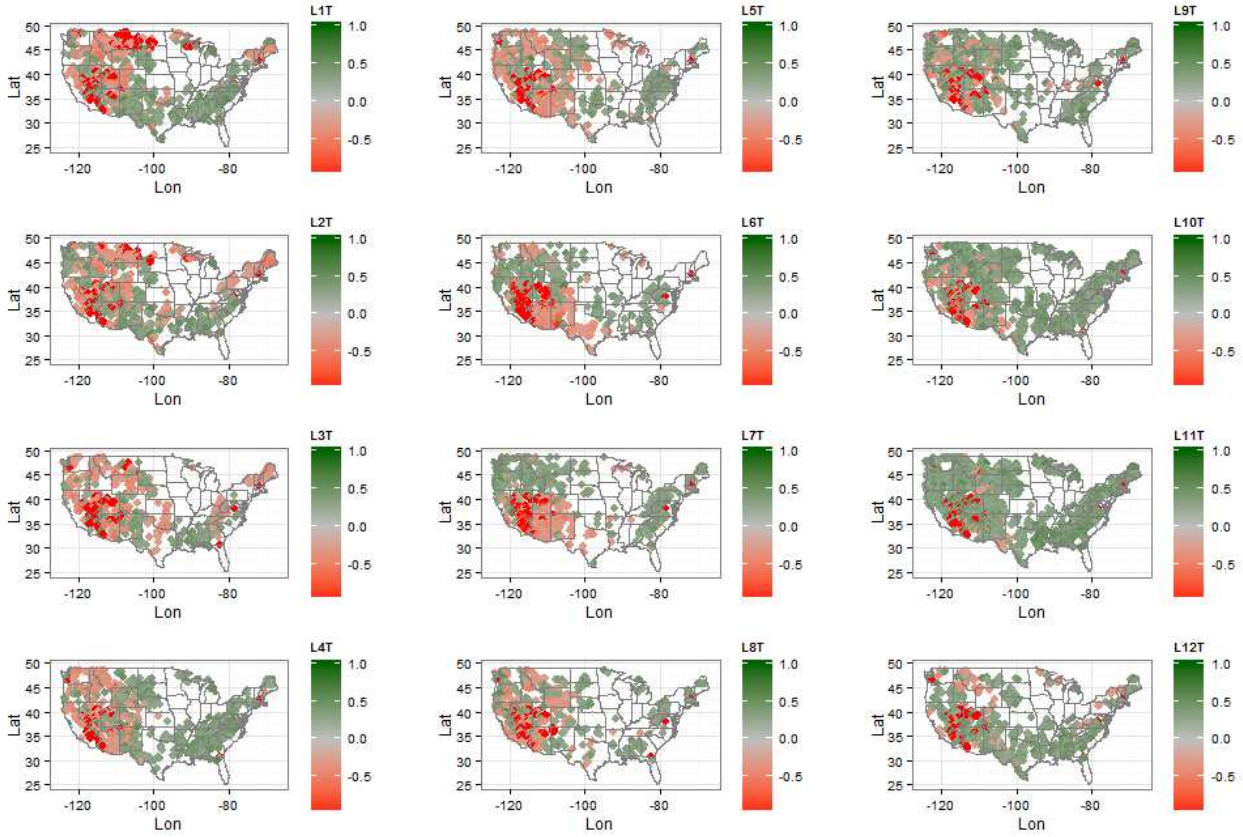

Figure 4.3: Significant Trend Locations of Average LAI by Month - Points indicate the Mann-Kendall τ value, and Months are indexed as shown in the colorbar legend.

vegetation to adapt dynamically over long periods of time, following the assumption that vegetation processes will maintain an assumed optimal balance of seasonal LAI with the prevailing climate.

4.2.2 Climate Data

Climate data is required for each location where harmonic covariates were developed, which was assembled from two different data sources: PRISM[4] and Daymet[5].

PRISM data is distributed at a 1-km spatial resolution across the CONUS on a monthly timescale, but also includes published values for the 30-year average of each parameter. From this latter long-term mean dataset, values were extracted for: annual precipitation total (*ppt*), mean annual max daily temperature (*tmax*), mean annual min daily temperature (*tmin*), mean annual daily minimum vapor pressure deficit (*vpdmin*), and mean annual daily maximum vapor pressure deficit (*vpdmax*). Additional monthly specific parameters were assembled including the average January minimum daily temperature (*tmin*01), average July maximum temperature (*tmax*07), total January precipitation (*ppt*01), and total July precipitation (*ppt*07). These covariates were selected partly from an understanding of known important factors for vegetation growth and maintenance, in addition to factors that explained significant variance during model development and testing phases.

The second source of climate data was from **Daymet**, which was used to obtain long-term mean annual snow water equivalent (*swe*), and annual mean day-light period solar irradiance (*srad*).

As a summary, each natural vegetation point has a temporal series of LAI phenology that was used to regress three β parameters defining the observed phenologic process (β_0, β_1 and β_2), in addition to a set of climate covariates describing the long-term mean climate. Now, the phenologic coefficients can be regressed against climate.

4.2.3 Transformations

Plots of histograms of the climate covariates indicate several that require transformation to reduce excess skew. These include the snow water equivalent values, and the annual precipitation totals. Secondly, the mean of each covariate was subtracted to reduce effects of multicollinearity.

[4]http://www.prism.oregonstate.edu/
[5]http://daymet.ornl.gov/

Table 4.1: Regression Model Parameters, Descriptions and Units

Parameter	Description	Units
ppt	Total annual precipitation	$mm/year$
tmin	Annual mean of daily min temperature	$°C$
tmax	Annual mean of daily max temperature	$°C$
vpdmin	Annual mean of minimum daily VPD	hPa
vpdmax	Annual mean of maximum daily VPD	hPa
ppt01	Total January precipitation	$mm/month$
ppt07	Total July precipitation	$mm/month$
tmax07	Mean July max daily temperature	$°C$
tmin01	Mean January min daily temperature	$°C$
srad	Annual mean shortwave radiation	W/m^2
swe	Annual SWE (Sum of SWE on first of each month)	mm
lswe1	Log of non-zero SWE	mm
lppt	Log of annual total precipitation	mm

Transformations were also applied to the response variables (i.e. the β values) to reduce skew. For β_0, all values were positive and therefore were simply scaled by a power of 0.25. For β_1 and β_2, a small number of values were positive - upon further review, many of these positive values were located in potentially non-natural vegetation locations. Therefore, positive values were removed allowing a 0.25 power of the negative values of β_1 and β_2 (i.e. powers of positive values). Additional transformations were considered along *Tukey's Ladder of Transformations* [126], including the log, square root and the inverse root, but the quarter root resulted in the best model residual diagnostics (Q-Q Plot).

4.2.4 Regress Harmonic Coefficients on Climate

Three separate and independent regressions of the β parameters on climate were completed using a simple linear regression expressed as,

$$\beta_k = \sum_{i=0}^{N} \alpha_{k,i} \times Parameter_{k,i} \tag{4.2}$$

where k is the *beta* parameter in integer set [0,1,2], $Parameter$ is the independent climate covariate, $Parameter_{k,0} \forall k = 1$ represents the intercept parameter, α is the regressed coefficient, and N is the number of covariates in the regression model. The list of full model covariates is shown in Table 4.1.

To create the most parsimonious yet explanatory model, a stepped Akaike Information Criterion (AIC) approach was used to evaluate reduced models from the full model. This process considers both forward and backward removal/addition of covariates and the resulting AIC value, which is used to select a reduced model. Output for for stepped AIC model selection for the intercept β_0 term (referred to in the R code as $INTq$) is demonstrated in the output included below.

The output shows both the *Initial Model* and the *Final Model* covariates; note the reduced set in the Final Model, where covariates such as *srad* and *tmin01* have been removed, for example. The output then shows each step used to arrive at the reduced Final Model, where line '1' is the Full Model. Line '2' shows the model without *ppt*, resulting in an increase to residual degrees of freedom from 317 to 318, and a concurrent reduction in AIC (the goal is the minimum AIC value). Line '3' removes another covariate, *tmin01*, and again the AIC is checked. This process is repeated until further removal of covariates does not result in further decrease of the AIC - this represents a balanced model between explanation and parsimony.

```
Stepwise Model Path
Analysis of Deviance Table

Initial Model:
INTq ~ ppt + tmin + tmax + vpdmin + vpdmax + ppt01 + ppt07 +
    tmax07 + tmin01 + srad + swe + lswe1 + lppt

Final Model:
INTq ~ tmin + tmax + vpdmin + vpdmax + ppt01 + ppt07 + swe +
    lswe1 + lppt


      Step Df      Deviance Resid. Df Resid. Dev       AIC
1                                 317   2.224349 -1627.878
2    - ppt  1 0.0007261522        318   2.225075 -1629.770
3 - tmin01  1 0.0019229559        319   2.226998 -1631.485
```

```
4    - srad   1 0.0040702392          320    2.231068 -1632.880
5 - tmax07   1 0.0087938320          321    2.239862 -1633.578
```

Note the reduction in covariates between the *Initial Model* and the *Final Model*, only retaining those terms resulting in the lowest AIC value (a balance between variance explained and the number of covariate terms).

The full model only considers simple model covariates, and does not include higher powers of covariates or interactions. A significant concern in regression, especially here for use in projection in novel climates, is *hidden extrapolation*, or the consideration of data outside the *regressor variable hull* (RVH). Hidden extrapolation can potentially lead to erroneous results when covariates are outside of the available RVH support, where the extrapolation is potentially exaggerated when including interactions and higher order terms. Refer to Section 4.3.3 for detailed review and analysis of models and results.

With each model of regressed β parameters on climate, the expected parameters were used to re-evaluate the expected phenology. This predicted phenology was then compared to the original fitted LAI phenology to indicate degree of fitness. Three measures of fitness were used to assess the predictive power of the climate-based relationships. These include a Nash-Sutcliffe (NS) measure of efficiency [100], comparison of residuals of peak LAI, and residuals of mean LAI.

The Nash-Sutcliffe measure of efficiency, NS, is described by,

$$NS = 1 - \sum_{i=1}^{N} \frac{(Mod_i - Obs_i)^2}{(Obs_i - \overline{Obs})^2} \tag{4.3}$$

where N is the number of observations, Mod is the set of model predicted values, Obs is the set of observations, and $\overline{Obs}$ is the mean of the observation set. The NS measure of efficiency can take values in set $[-\infty, 1]$, where 1 represents a perfect correlation between the model and the observations.

Finally, temporal LAI sequences were developed and compared against observations over a 20-year period from 1980 to 2000. Additionally, the model was then used to predict changes in phenology to year 2100 with Global Circulation Model (GCM) projection data as an example application of the space-for-time substitution approach.

4.3 Results

Results of this effort include the harmonic regression models, in addition to tests of fitness and reanalysis.

4.3.1 Regression of Phenology Harmonics on Climate

With the collection of β terms and climate covariates for each point, a regression model for each β term was completed. The following reduced models were determined, with coefficients shown in Table 4.2.

$$\begin{aligned}\beta_0 = \alpha_0 \quad + \quad & \alpha_1 \times tmin + \alpha_2 \times tmax + \alpha_3 \times vpdmin + \alpha_4 \times vpdmax + \\ & \alpha_5 \times ppt01 + \alpha_6 \times ppt07 + \alpha_7 \times swe + \alpha_8 \times lswe1 + \alpha_9 \times lppt \end{aligned} \tag{4.4a}$$

$$\begin{aligned}\beta_1 = \alpha_0 \quad + \quad & \alpha_1 \times ppt + \alpha_2 \times tmin + \alpha_3 \times vpdmax + \alpha_4 \times ppt01 + \\ & \alpha_5 \times tmin01 + \alpha_6 \times swe + \alpha_7 \times lppt \end{aligned} \tag{4.4b}$$

$$\begin{aligned}\beta_2 = \alpha_0 \quad + \quad & \alpha_1 \times ppt + \alpha_2 \times tmin + \alpha_3 \times tmax + \alpha_4 \times vpdmin + \\ & \alpha_5 \times ppt07 + \alpha_6 \times tmax07 + \alpha_7 \times tmin01 + \alpha_8 \times swe + \alpha_9 \times lppt \end{aligned} \tag{4.4c}$$

Diagnostics A series of diagnostic tests were performed on each of the three regression models, including checks for outliers (residual and studentized residual plots), checks for normality of residuals (Q-Q plots), and checks for excessive influence on the regression (Cook's Distance, DFFITS, and DFBETAS). Figures of diagnostics for each β regression model are included in Appendix C.1. Review of the diagnostics show acceptable model performances with good residuals, normality, influence and outliers.

Table 4.2: Summary of Regressed Model Coefficients

Coefficient	β_0	β_1	β_2
α_0	8.599e-1	6.938e-1	5.835e-1
α_1	-2.091e-2	-5.472e-4	-3.946e-4
α_2	4.074e-2	4.163e-2	3.964e-2
α_3	3.171e-2	-6.290e-3	3.034e-2
α_4	-2.147e-2	1.493e-3	-3.122e-2
α_5	1.206e-3	-4.278e-2	-1.658e-3
α_6	1.022e-3	-7.498e-7	-3.007e-2
α_7	-1.018e-6	5.157e-1	-4.461e-2
α_8	1.536e-2	-	-5.637e-7
α_9	1.836e-1	-	6.540e-1

Model Performance Using just climate variables and the fitted β regressions, the expected phenology was determined and compared to the phenology described by the fitted phenologic series of randomly selected points through the modeled domain, as shown in Figure 4.4. Included on each sample comparison is the Nash-Sutcliffe measure of efficiency. This random sample demonstrates that over a range of LAI phenologies and climates, an acceptable phenologic response can be achieved based solely on long-term mean climate parameters.

This figure also shows points where the phenology was over- and under-predicted, although in the mean process, the bias of the predicted phenologic harmonics is zero. Also note locations where the LAI decreases to zero, whereas other locations may maintain positive values of LAI year-round. In this case, phenologic differences between conifers and deciduous species may be captured. Clearly for any location, a mix of conifer and deciduous species may actually be present, in addition to overstory gaps, and errors in the original development of the LAI3g dataset, but the focus here is on the mean phenologic process of lumped canopy LAI based on climate. For these purposes, the responses appear to be well captured, and can be summarized quantitatively with measures of fitness over space.

For each point evaluated, three measures of fitness were determined and are shown in Figure 4.5. The first figure of this set (a) shows the Nash-Sutcliffe values over the model domain. Very high values (where 1 is a perfect response), are shown in regions with high annual maximum LAIs, and poorer efficiencies are shown in lower LAI regions. Although Nash-Sutcliffe can be a reasonable

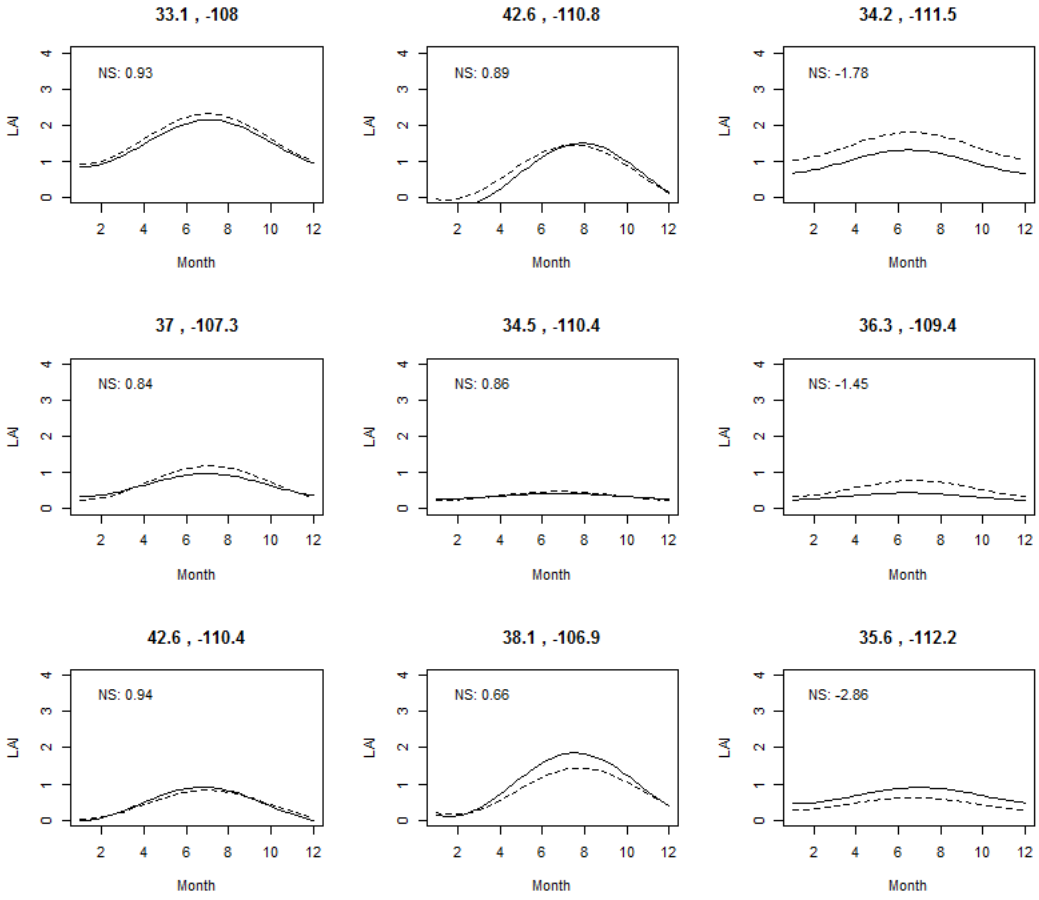

Figure 4.4: Sample Phenology of Random Location Sample

indicator of model fitness, in regions of low variation of annual LAI, small errors produce very poor model efficiencies, thus not providing a good indicator of fitness alone, and additional measures of fitness should be considered.

The second figure of this set, Figure 4.5(b) is the difference of maximum LAI (Model-Original). Here, we see a spectacular fit in regions with low LAI (where NS was showing poor values), clearly indicating appropriate reanalysis of biomass in arid regions. Regions with higher LAI include locations of bias for under-estimating maximum seasonal LAI values, in addition to regions that show an over-estimation of LAI.

The third metric is the difference in mean annual LAI (Figure 4.5(c)), which is near zero across most of the domain indicating good fitness of the mean LAI process.

4.3.2 Projected Climate Phenology

Regressed relationships of annual phenology harmonics can also be applied to projected climate data to estimate future phenologic conditions. Data from the Canadian GCM (CAN) and concentration emission profile RCP85 was assembled for several locations in CORB. The GCM data does not include all the required covariates for regression of annual phenology, therefore portions of the data were obtained as direct output from model runs (VIC Model). Using this climate data and the fit regressions, plots of the projected average phenology by month was determined. As an example, a sample location east of the Town of Bondurant, Wyoming (Lat=43.1875, Lon=-110.1875) was selected for detailed review.

The climate data shows a clear and steady increase in average daily minimum, maximum and July maximum temperatures, in addition to an expected increase in annual precipitation. During this period, the location also shows a clear steady decrease in the annual expected SWE. Using this climate data (and other data not shown), the expected annual phenology sequence was prepared, shown in Figure 4.8. This figure shows a clear increase in the expected peak LAI, but it is difficult to distinguish more specific changes in the temporal sequence, whereas separating out the trend for each month is more informative, as shown in Figure 4.9.

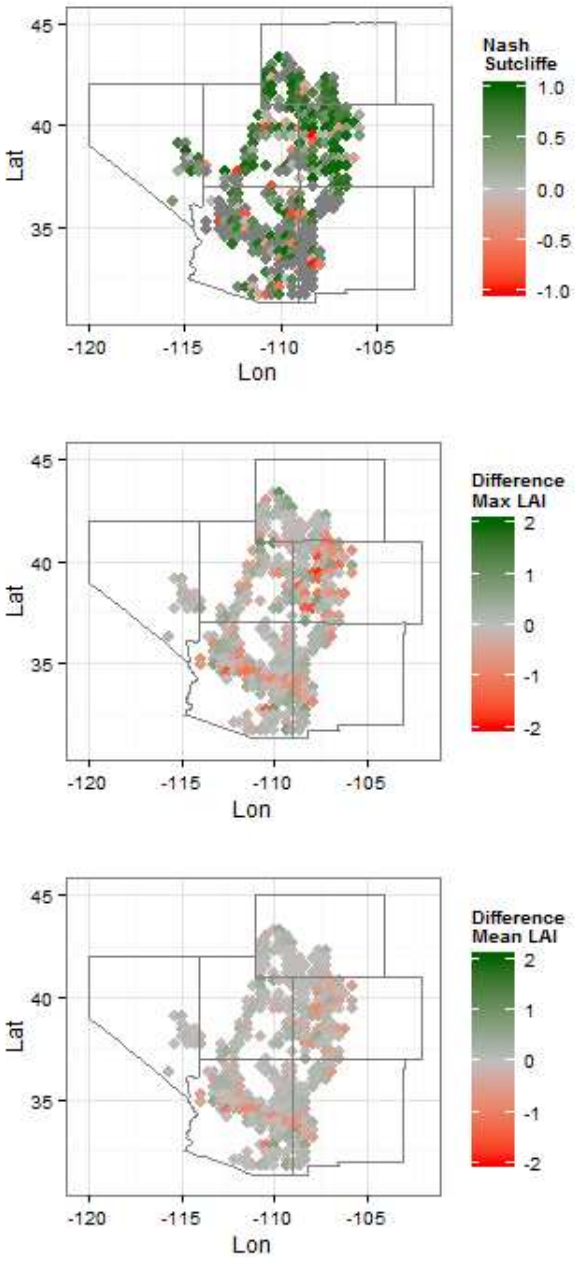

Figure 4.5: Model Fitness Metrics

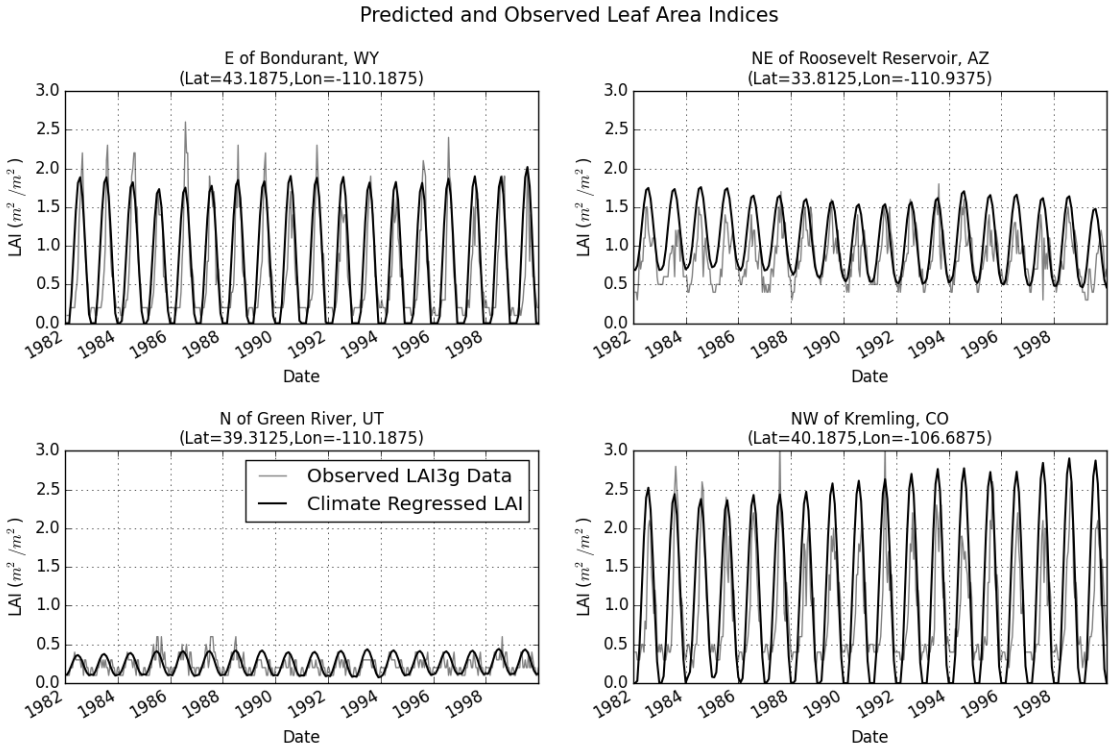

Figure 4.6: Re-Analysis of Predicted LAI Phenology Compared to Observations

The phenologic response for this location in the Wyoming headwaters of the CORB, for the CAN:RCP85 projection, is an increase in LAI across the growing season. This indicates both an increase for Gross Primary Productivity (GPP), but also an extension of the growing season as conditions are increasingly favorable for longer periods of time.

Conversely, for the same GCM and RCP, at an alternate location in the mountains northeast of Roosevelt Reservoir, Arizona (Lat=33.8125, Lon=-110.9375), indicates an opposite phenologic response. Annual climate data is shown in Figure 4.10, and the projected monthly phenology is shown in Figure 4.11. Here, increased temperatures and vapor pressure deficits may be inhibiting vegetation growth in spite of minimal changes in precipitation. It is also worth observing the projection of annual SWE at this location reaching approximately zero by year 2100.

4.3.3 Multi-Colinearity and Hidden Extrapolation

In developing and fitting regression models, care should be given to both mutli-colinearity and hidden extrapolation.

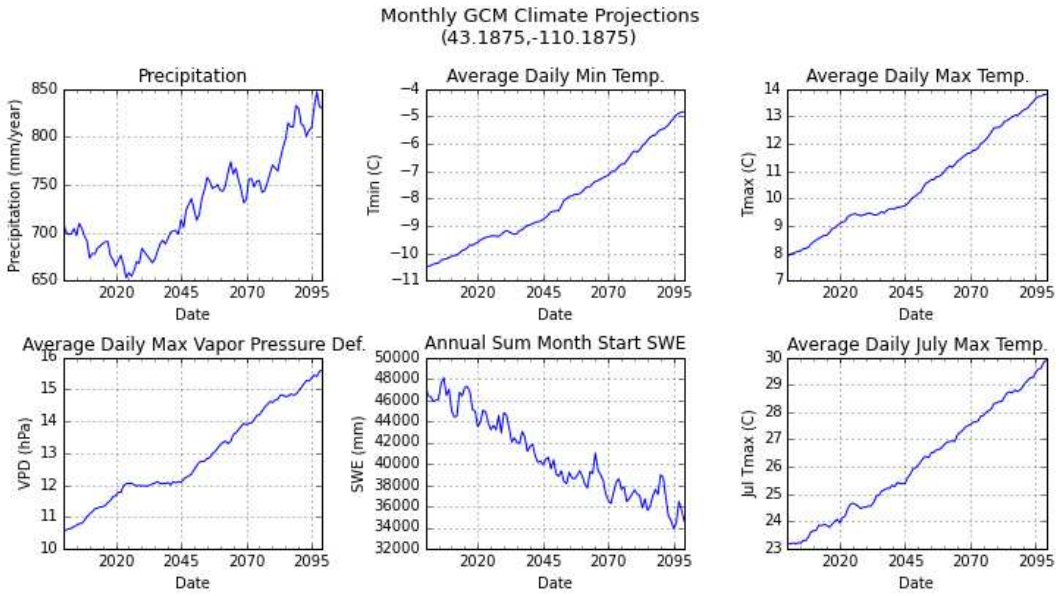

Figure 4.7: Mean 20-Year Projected Climate Data near Bondurant, WY (CAN,RCP85)

Multi-colinearity is a dependence between the covariates (independent variables) that can lead to expected coefficients with high standard errors (e.g. extremely sensitive coefficients). Coefficient sensitivity and high standard error is primarily of concern for covariate explanation, but is less of concern for prediction, which is our primary goal here. When predicting values with models developed using partially dependent covariates, it's important to check the location of the point to be predicted with respect to the regressor variable hull (RVH), or the non-Euclidean space envelope of the covariates. Projected points beyond the RVH are considered a *hidden extrapolation*. Covariates outside of the RVH can potentially lead to erroneous predictions.

For low-dimensional space (e.g. 2 or 3-dimensions), location of covariates with respect to the RVH can be evaluated graphically, but for higher dimensional space, this is infeasible. Instead, the *hat-values* of the covariate set (h_0), a measure of the distance from the mean of the covariate set, also referred to as leverage, may be checked against the maximum hat value of the regression (h_{max}). If $h_0 > h_{max}$, then the point is extreme and may be considered an extrapolated regression outside of the RVH. Large hat-values beyond the RVH are questionable and should be evaluated carefully [75].

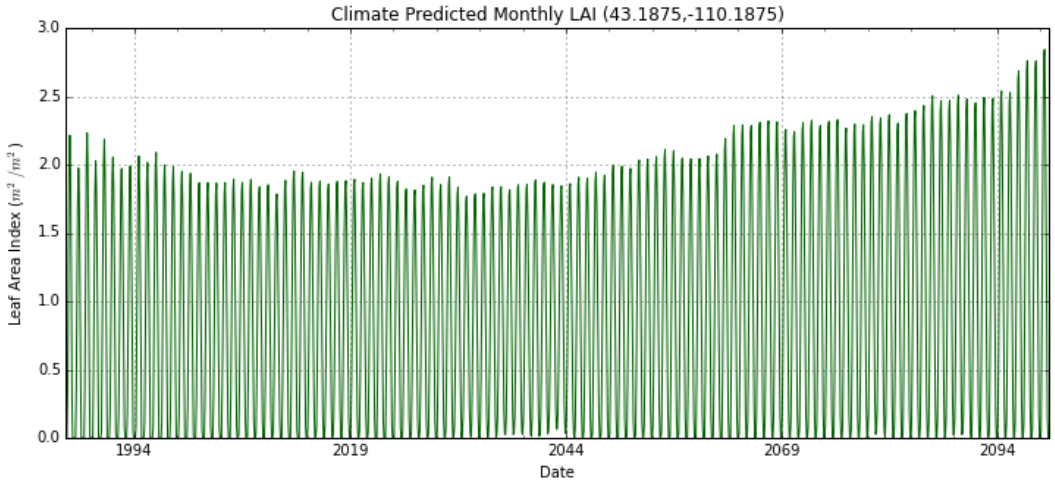

Figure 4.8: Leaf Area Index Projections near Bondurant, WY (CAN,RCP85)

Hat-values are the diagonal values of hat-matrix, which is,

$$H = X(X'X)^{-1}X' \tag{4.5}$$

where X is the covariate matrix (and X' is the transpose of X). For the given set of support, each point has a unique hat-value. The maximum hat-value is then defined as h_{max}.

An individual hat-value (h_0) for a given set of covariates (X_0), is,

$$h_0 = X_0'(X'X)^{-1}X_0 \tag{4.6}$$

Therefore, for any extreme or potentially unique covariates, we can consider the location of the point and estimate if it is a hidden extrapolation. Unfortunately, considering we are moving into novel climates, it is virtually impossible to avoid hidden extrapolation - observations of the vegetation response to future climates are not available. Instead, to consider the magnitude and frequency for potential hidden extrapolation through the study domain, we determined the hat-values (h_0) for each year for 2000 randomly selected points in the domain - for 114 modeled years (the first year is not included), this results in 228,000 hat-values for each of the three regressions.

Histograms for each of the regressions are shown in Figure 4.12, and summaries of the results are in Table 4.3.

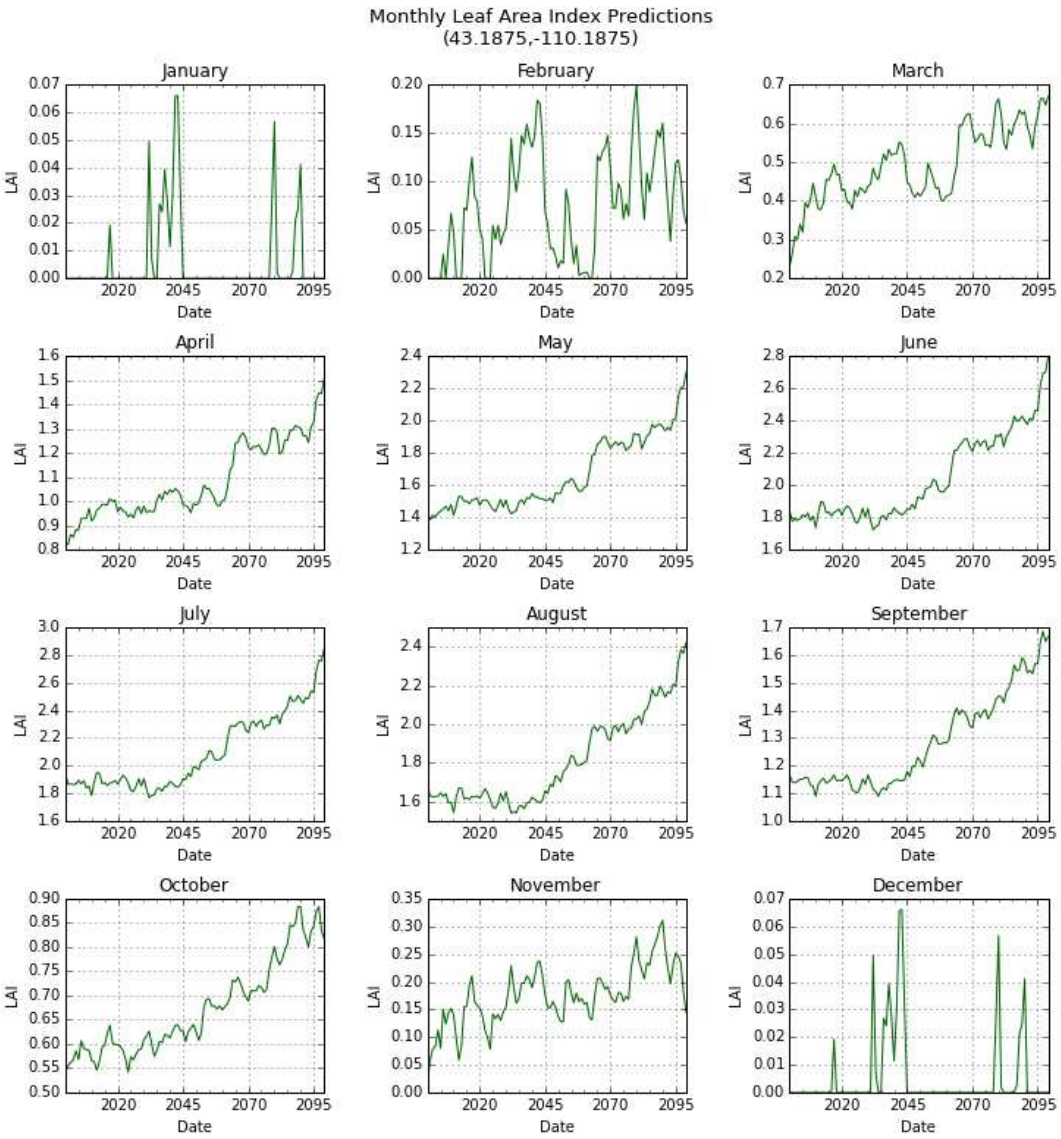

Figure 4.9: Predicted Leaf Area Indices by Month near Bondurant, WY (CAN,RCP85)

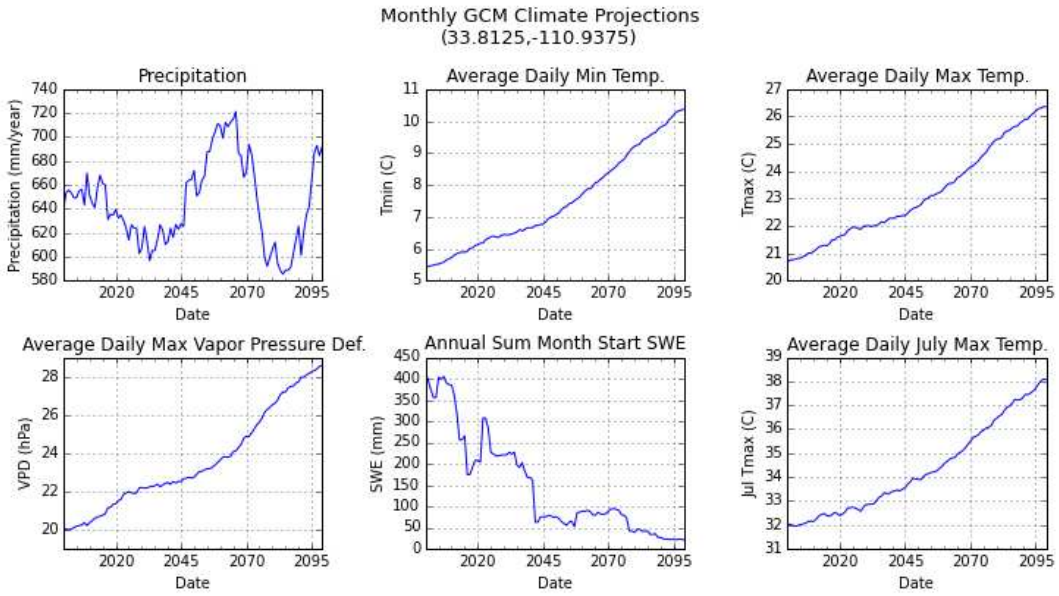

Figure 4.10: Mean 20-Year Projected Climate Data near Roosevelt Reservoir, AZ (CAN,RCP85)

Table 4.3: Summary of Hat-Values

Model	h_{max}	$\% > h_{max}$
β_0	0.228	19.8
β_1	0.206	9.2
β_2	0.226	10.0

The CAN:RCP85 model was selected, as it represents a model with extreme set of predicted covariates to year 2100, and thus may be considered near the upper end of potential expected hidden extrapolation. The percent of hidden extrapolation trials varies between each of the models, as they use different subsets of selected covariates. The regression for β_0 has over 80% of the projected climate covariates within the RVH, whereas β_1 and β_2 are within the RVH for more than 90% of the projected covariates. Preventing hidden extrapolations is impossible without reducing the explanatory power of the model by reducing the number of covariates. Instead, results were carefully reviewed to determine if any hidden extrapolations resulted in extreme or abnormal behavior. Further, utilization of a linear model, without interactions and higher order terms, helps to prevent extreme results at extrapolated points.

This method is not exhaustive in checking for hidden extrapolation and extreme responses, but certainly increases confidence that that regression models are appropriate for applications in novel conditions, even when evaluating potential values beyond the support. Through model checking of

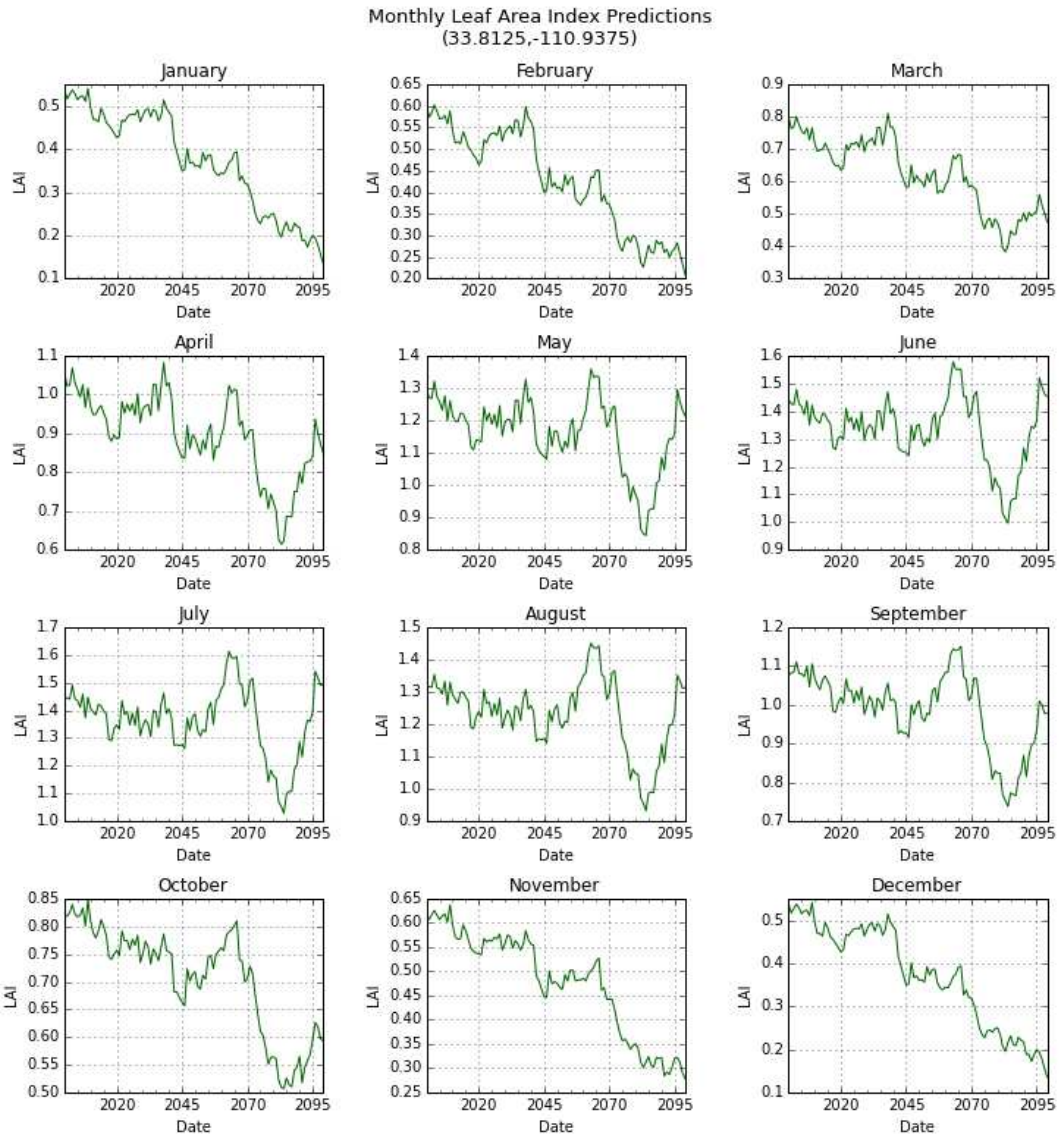

Figure 4.11: Predicted Leaf Area Indices by Month near Roosevelt Reservoir, AZ (CAN,RCP85)

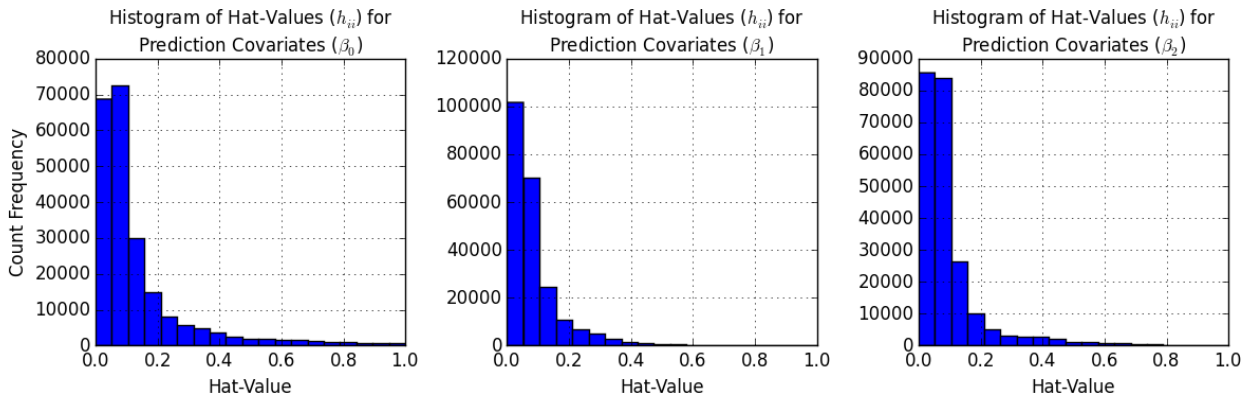

Figure 4.12: Histogram of Hat-Values in Projected Climate to Year 2100

predicted parameters and review of the magnitude of extrapolation (i.e. h_0), the model is considered acceptable for applications of phenologic prediction.

4.4 Discussion and Conclusions

Observational data in many different forms are indicating rapid changes in vegetation with respect to species composition and diversity, density, health, and the seasonal phenology of leaf flushing, magnitudes of LAI, and senescence [51]. Vegetation cover has a direct effect on the water and energy balance of the land surface, and thus accurate estimates of how vegetation cover changes in our changing climate are essential.

Mechanistic DGVMs may be used to estimate vegetation cover, which can perform well, but are highly parameterized and may not fully capture the complicated processes over time in new climates, especially with fixed physiologic process definitions. Further, incorporation of DGVMs in macro-scale hydrologic models over large spatial domains covering many different climates is subject to great uncertainty in model parameterization. An alternative approach is to consider regression of natural vegetation responses, in the form of a temporal sequence of annual LAI values based solely on climate, assuming these responses are following an optimal but latent process. Our approach performs a space-for-time substitution such that vegetation parameterization is dynamic, accounting for these latent processes difficult to capture using mechanistic models, which can then be used for projection modeling.

Here, we describe the temporal pattern of seasonal LAI using a primary harmonic parameterized by three coefficients that are based on estimates of the local climate. A harmonic model is linear in the coefficients, and thus a simple linear regression was used to estimate phenologic coefficients across the Colorado River Basin using a set of bi-weekly LAI estimates over a 30-year period. These harmonic coefficients were then regressed against the local climate to create climate dependent relationships. As these relationships were developed solely using climate data, they may be used in a space-for-time substitution to estimate future responses of vegetation phenologic patterns in a changing climate.

A reanalysis of observed LAI data (LAI3g) was completed by comparing the predicted phenologic parameters to the observed response over a 20-year period in four different climates. This reanalysis showed a high degree of skill for replicating the magnitude and timing of phenologic sequences using only local climate as the independent data.

Reanalysis shows some regions of over and under-estimation of peak annual LAI, but the mean process was well captured. The models also present high values of Nash-Sutcliffe efficiency (NS) for regions of moderate to high LAI, but regions with low annual LAI variability indicated poor values of NS. This does not necessarily indicate poor performance, but is rather a statement of appropriateness of NS for use with small LAI magnitudes and minimal temporal variation. In this case, comparison of the difference of maximum annual and mean annual LAI are more indicative of model fitness. It was determined that the model was able to sufficiently replicate LAI phenology using climate-based relationships.

For novel climates to year 2100, it was determined the regression relationships had acceptable hat-values (i.e. within the RVH) for at least 80% of the projected annual climate series. Through testing of various locations, it was also observed that even extreme hat-values did not result in an erratic regressed response.

Description of the seasonal phenology using three parameters in a Fourier Series primary harmonic is a reasonable approximation for reduction of parameter space, and allows easy regression against climate. Significant improvements in the model fitness are possible by including spatial covariates, such as soils, aspect, latitude, elevation, etc., but this would violate the approach needed when applying these relationships in a space-for-time substitution model. Regardless, additional or alternative covariates to those used in this study could be used to improve model fitness.

As an example, better descriptions of the solar environment, possibly describing growing and dormant season conditions rather than a single annual value, may be helpful. Similarly, seasonal patterns of vapor pressure deficits rather than annual min and max values, or additional means of accounting for seasonal precipitation distribution, could explain further variance in the phenologic response.

This regression model was also developed specifically for the Colorado River Basin, and should not be applied to regions beyond this domain. However, comparison of regressed relationships between different regions could be quite interesting showing similar (or diverging) patterns in predicted harmonic coefficients.

Until mechanistic processes are sufficiently developed to efficiently describe vegetation responses to climate for applications in macro-scale modeling, a regression based approach is ideal to allow dynamic vegetation phenology in macro-scale modeling applications.

Chapter 5

Vegetation Dynamics in Macro-Scale Hydrologic Modeling Applications

Look at a plant in the midst of its range, why does it not double or quadruple its numbers? We know that it can perfectly well withstand a little more heat or cold, dampness or dryness, for elsewhere it ranges into slightly hotter or colder, damper or drier districts. In this case we can clearly see that if we wished in imagination to give the plant the power of increasing in number, we should have to give it some advantage over its competitors, or over the animals which preyed on it. On the confines of its geographical range, a change of constitution with respect to climate would clearly be an advantage to our plant; but we have reason to believe that only a few plants or animals range so far, that they are destroyed by the rigour of the climate alone.

– **Charles Darwin, On the Origin of Species**

5.1 Introduction

Terrestrial Biosphere Models (TBMs) are used to study the interaction and response of the land surface energy and water balance to climatic and meteorologic forcings, including the interaction and feedbacks from vegetation. Global Circulation Models (GCMs) model the land surface responses, including reflection of solar energy, atmospheric carbon assimilation and release of water vapor into the atmosphere, to predict climatic changes. Conversely, the land surface vegetation cover responds to the climate, creating a dynamic system of feedbacks and responses. Here, we are focused on evaluating the latter of these processes, considering how vegetation is changing with climate, and how these changes may affect land surface hydrologic responses [13].

Earth's climate is rapidly changing with respect to temperatures, atmospheric CO_2 concentrations, and patterns of precipitation. These changes are resulting in actively observed responses of vegetation cover, properties and mortality rates [1, 14, 22, 134, 137, 139, 140, 150], although methods to efficiently include vegetation dynamics in macro-scale TBMs are still evolving. Many methods are either excessively simple and ignore certain dynamics, or excessively parameterized limiting their interpretability and utility. Regardless, inclusion of dynamic vegetation responses in TBMs is critical when using climate projection models for estimating future hydrologic responses.

Here, we discuss the implementation of several optimality theories within a TBM, including a) an optimal stomatal control model, b) an optimal photosynthetic resource allocation model, and c) a climate-based leaf-area phenologic harmonic regression model. Inclusion of these theories and approaches within a TBM requires many assumptions to make the modeling system viable for application in a continuous simulation model.

With a developed model, we then consider the model performance at a range of temporal and spatial scales. We start by considering model performance for transpiration (as part of modeled evapotranspiration) against observations, while concurrently comparing against another modeling system. Secondly, we look at model responses using future GCM projection data, and compare the dynamic response to a static vegetation parameterization by evaluating separate components of the hydrologic system. For example, we evaluate canopy transpiration, evaporation, soil moisture, runoff and baseflow separately, rather than as an aggregated response. This highlights the potential significant differences in each component of the hydrologic cycle in response to vegetation differences. Finally, we consider the Colorado River Basin, and evaluate spatial and temporal differences in subcatchment-scale mean decadal yields between a static and dynamic vegetation model. Again, this highlights the potential error in macro-scale models if vegetation dynamics are not included in climate projection modeling.

Implementation of these systems was completed by modifying source code based on VIC 4.1.2M [80] [6], resulting in a new multi-layered dynamic vegetation system referred to as *VIC-VEO*, where *VEO* refers to the **VE**getal **O**ptimality theories employed. It is worth noting that since the original inception of this model, researchers have released VIC-4.2[7], which includes a multi-layered

[6] `http://www.hydro.washington.edu/Lettenmaier/Models/VIC/index-old.shtml`

[7] `https://vic.readthedocs.org/en/vic.4.2.c/`

canopy model and an explicit assimilation model. This latter release model is used for the basis of comparisons with VIC-VEO, rather than comparing to the original base-model of VIC 4.1.2M.

5.2 Optimal Stomatal Control

Key to understanding canopy level transpiration is proper estimation of leaf-level stomatal conductance, or the aperture that allows CO_2 to enter the leaf, and concurrently results in H_2O vapor leaving the leaf. The aperture adjusts in response to light, temperature, vapor pressure deficit and other exogenous and endogenous variables. TBMs require a method to determine an appropriate stomatal conductance in response to these environmental conditions.

There are several existing models for estimating stomatal function in TBMs; one of the earliest and still widely applied models is the *Jarvis model* [62], which included five empirical adjustment functions to a specified minimum stomatal resistance (resistance is the inverse of conductance). Alternatively, another popular empirical approach is the *Ball-Woodrow-Berry model* [5] or it's variants such as the *Leuning model* [78], to determine stomatal conductance. Parameterization of these models is generally based on either fitted data to observations, or estimates based on generalized classes from collections of observations. Although, as noted recently by Belinda Medlyn,

> "...because these stomatal conductance models are empirical, their parameters have no meaning attached. Consequently, there is little understanding of how the parameters vary with species or acclimate to changes in climate, and many models simply assume the parameters are constant for all C3 species... A successful theoretical model of stomatal behaviors is a priority for vegetation modelers because it would provide a synthetic framework for research into acclimation adaptation of carbon-water coupling in terrestrial ecosystems." [97]

Alternative to empirical models is an optimal stomatal conductance approach that can be employed to reduce the required parameterization with more meaningful and explainable parameters.

5.2.1 Optimal Stomatal Conductance and Assimilation Model

Optimal stomatal control assumes that stomata operate to maximize (or minimize) some objective function over time, although the objective function and timescale vary between different theories [2, 3, 26–28, 32, 52, 56, 90, 94]. Ideas of optimal stomatal control (and optimal vegetation responses, in general) have been studied for well over 50-years. An optimal control approach has the advantage of allowing certain parameters to become emergent outcomes, rather than an unknown fitted or empirical parameter [93].

Cowan and Farquhar [28] pioneered early ideas of optimal stomatal control still employed today by utilizing the calculus of variations to solve a constrained maximization problem. This is generally cast as[8],

$$\frac{\partial A_n}{\partial g_s} - \lambda \frac{\partial E_t}{\partial g_s} = 0 \tag{5.1}$$

where A_n is the net rate of leaf-level assimilation, g_s is the leaf stomatal conductance, and E_t is the leaf-level transpiration rate. The coefficient λ is referred to as the *marginal water use efficiency*, and is a Lagrange multiplier. This approach maximizes the integrated assimilation (the benefit) for a given amount of transpired volume (the constraint or cost) over the period of integration. Refer to Chapter 2 for a detailed discussion and derivation of this optimal condition.

The rate of carbon assimilation (A_n) in Eq. (5.1) can be determined using the Farquhar, von Caemmerer and Berry biochemical model of photosynthesis [40], referred to as the FvCB model. Additionally, a simple Fickian diffusive approach can be used to estimate the rate of transpiration (E_t). Solution of this partial differential equation, using a linearized form of the assimilation function (refer to Appendix A) [89], leads to a closed form solution for optimal stomatal conductance (g_s), given as,

$$g_s = \sqrt{\frac{k(kC_a - k\Gamma^* - R_d)}{\lambda a D}} - k \tag{5.2}$$

where k is the carboxylation efficiency, C_a is the atmospheric CO_2 concentration, D is the vapor pressure deficit, and R_d is the rate of mitochondrial respiration. This equation represents a lin-

[8] This is a modification of the original formulation that was stated as a minimization problem, $\partial E_t - \lambda \partial A_n = 0$.

earized assimilation model resulting in an optimal stomatal conductance (g_s), for a given set of environmental and physiological conditions, and a given marginal water use efficiency, λ.

Following the FvCB model, the *carboxylation efficiency* k is determined from the most limiting photosynthetic process - photosynthesis is either limited by the rate of *carboxylation*, or the rate of *electron transport*[9]. Carboxylation is the rate of CO_2 binding to RuBP with the enzyme *RuBisCO* as part of the Calvin-Benson cycle, resulting in glucose as stored energy. For the second potentially limiting system, electron transport is the rate of photon supply and processing available for various photosystem processes, including the regeneration of RuBP, which is essential for continued operation of the Calvin-Benson cycle. The carboxylation efficiency (k) in the linearized model can be defined using general notation as,

$$k = a_1/(rC_a + a_2) \tag{5.3}$$

where a_1 is equal to either V_{cmax} or $J/4$, and a_2 is equal to either K_m or $2\Gamma^*$, for carboxylation or electron transport limited systems, respectively. Here, V_{cmax} is the maximum rate of carboxylation, J is the electron transport rate (a function of J_{max}, the irradiance at the leaf surface and Photosystem-II absorptance capacity of the leaf), K_m is the Michaelis-Menten half rate capacity, Γ^* is the CO_2 compensation point in the absence of mitochondrial respiration, r is a near-constant ratio of internal leaf (C_i) to ambient atmospheric (C_a) CO_2 concentrations [148]. Refer to Appendix A for further details of the Γ^*, R_d, D, K_m, and r parameters.

Two remaining key parameters of this model are V_{cmax} and J_{max}, the maximum rate of carboxylation ($\mu moles\ CO_2\ m^{-2}s^{-1}$) and maximum rate of electron transport ($\mu moles\ e^-\ m^{-2}s^{-1}$). These rates determine the level of assimilation under a given set of environmental conditions, which are key to determine the stomatal conductance and rate of transpiration.

Typically V_{cmax} and J_{max} are fixed values for a given plant functional type or biome region [116], and are defined by selecting a value from published literature [146] or fitted to gas exchange measurements [120]. Unfortunately, the values of V_{cmax} and J_{max} vary significantly between species,

[9]This does not include a third potential limitation, triose-phosphate utilization (TPU), which generally only occurs during extreme conditions.

within species, with age, within a season, from water stress, and even within a single canopy at any time, making reliable parameterization difficult. Later, we discuss how these parameters can be estimated using an optimal allocation approach.

Leaf kinetics are also highly temperature dependent - therefore, temperature response functions are needed to adjust parameters from some given value at a reference temperature.

5.2.2 Temperature Response Functions

Typically, estimates of kinetic parameters are made at a reference temperature of $25°C$, referred to as $V_{cmax_{25}}$ or $K_{c_{25}}$, for example, which are then adjusted from this reference temperature based on the current leaf temperature. The photosynthetic capacities of each system are highly sensitive to leaf temperature, thus the capacity of each system needs to be adjusted accordingly.

Here we utilize two separate temperature response functions: the Arrhenius and the Peaked Arrhenius function [63]. The former utilizes a monotonically increasing relationship between some parameter and temperature, whereas the latter assumes a peaked function at some temperature, with decreasing capacity with further temperature increase.

The Arrhenius and Peaked Arrhenius models are described by Medlyn and Bernacchi [10, 96]. In the former, increases in temperature increase the kinetic constants monotonically, whereas in the latter form, eventually a sufficiently high temperature results in a decrease of the kinetic value, possibly from protein denaturing, for example [105].

The simple monotonically increasing Arrhenius form is described as,

$$f(T_k) = k_{25} exp\left[\frac{(T_k - 298)E_a}{298RT_k}\right] \tag{5.4}$$

where k_{25} is the parameter of interest at a reference temperature of $25°C$, T_k is the temperature in Kelvin, and R is the universal gas constant ($8.314 J\ mol^{-1}K^{-1}$).

Alternatively, the peaked Arrhenius model is given as,

$$f(T_k) = k_{opt} \frac{H_d exp(\frac{H_a(T_k - T_{opt})}{T_k R T_{opt}})}{H_d - H_a(1 - exp(\frac{H_d(T_k - T_{opt}}{T_k R T_{opt}}))} \tag{5.5}$$

where,

$$T_{opt} = \frac{H_d}{\Delta S - R ln[\frac{H_a}{H_d - Ha}]} \tag{5.6}$$

Parameterization of the Peaked Arrhenius model includes the activation energy (H_a), the deactivation energy (H_d), the entropy (S), in addition to simply providing an estimate of the leaf temperature [131]. Although this process is well defined and can be fit to observed data, implementation within a broader general TBM over a range of climates is extremely difficult. The kinetic properties for temperature response vary between species, but also acclimate within species dependent on growth conditions [68] making estimation and parameterization of these terms for general applications challenging. Further, the system includes a series of feedbacks between leaf temperature and kinetics - growth conditions affect the kinetic temperature response function, which in-turn affects stomatal conductance and transpiration, and transpiration affects leaf temperature through transfer of latent heat. Separating these effects for application in a generalized PFT based big-leaf macro-scale TBM is likely impossible.

To solve this problem, we assume a) a generalized set of static kinetic properties, and b) leaf temperatures equivalent to air temperatures ignoring latent cooling or increased temperatures from absorbed solar energy. Kinetic constants follow those utilized by Medlyn et. al. [96], and Bernacchi et.al. [10].

5.2.3 Marginal Water Use Efficiency

The optimal stomatal control model requires an estimate of the marginal water use efficiency (λ). Although typically thought of as an empirical parameter, it instead is directly related to the total depth of transpiration for a given set of environmental conditions over the period of integration (Chapter 2). Manzoni et.al. [89] proposed an exponential decay of λ from some maximum well-watered value, referred to as λ_0. This reduction in stomatal conductance is similar to the originally postulated approach by Jarvis [62], a more recent approach using a logistic function [127], and even

an exponential abscisic acid response [55]. In all cases, an estimated decrease in stomatal function due to water stressed conditions is required; here, we utilize Manzoni et.al.'s approach described as,

$$\lambda = \lambda_0 exp(-\beta \Psi_L) \tag{5.7}$$

where β is a coefficient of the leaf water potential, Ψ_L (MPa).

Without explicit knowledge of the leaf water potential (which varies with canopy height, stomatal conductance, transpiration rate, and root-leaf conductance), we can approximate the leaf water potential Ψ_L from the soil water potential, Ψ_S [55]. Although we know that $\Psi_L < \Psi_S$, even under low transpiration rates, this assumption can provide a reasonable estimation of leaf water potential adjusted for variable soil moisture status.

The soil water potential Ψ_s (MPa) is determined as a function of the pore size distribution index (m) and the degree of saturation (s_0) [35].

$$\Psi_S = -\Psi_1 s_0^{-1/m} \tag{5.8}$$

5.2.4 Light Environment

Light in the canopy is attenuated based on a simple reduction of the above-canopy irradiance following Beer's extinction law for a homogeneous media [130], given as,

$$Irr = Irr_0 exp(-K_L \times L_c) \tag{5.9}$$

where Irr_0 is the irradiance at the top of the canopy, K_L is a light attenuation factor dependent on leaf angle, shape and density, L_c is the cumulative leaf area index *above* a given layer of leaf (e.g. the top leaf layer of a canopy has $L_c = 0$), and Irr is the reduced irradiance[10].

The value of irradiance (Irr) is required to determine the rate of electron transport J.

[10] A simple estimate of $K_L = 0.8$ has been utilized for all classes, which approximates slightly non-horizontal leaves and/or clumping [65], although the VIC-VEO vegetation library allows adjustment of this parameter by PFT

5.3 Optimal Monthly Resource Allocation

Stomata adjust rapidly to changing environmental conditions, whereas the photosynthetic system capacity adjusts at much slower timescales [108]. An increase or reduction of photosynthetic capacity is expressed by the maximum rate of carboxylation (V_{cmax}) and electron transport (J_{max}) when using the FvCB model, due to water stress [135, 147], light environment [8, 36, 57, 58, 142], or nutrient supplies [27, 38]. A common practice in current TBM modeling is to utilize a fixed photosynthetic capacity parameterization by biome or PFT class [116], but this static parameterization doesn't allow for variation of a single PFT within different climates, or for a PFT to adjust parameterization as environmental conditions change. Here, we implement the optimal allocation approach for estimation of photosynthetic system capacities in response to environmental conditions.

The optimal allocation approach considers a fixed amount of available nitrogen, and determines how the nitrogen should be allocated between V_{cmax}, J_{max} and Chl (the latter resulting in a certain absorptance efficiency, α) such that the expected assimilation rate is maximized. For modeling applications in TBMs, an appropriate timescale is one month; kinetics are constantly adapting, but a month allows sufficient time for protein development and re-generation (if needed), or nutrient translocation [88, 123, 136].

Further, the determination of optimal allocation is performed for all leaf layers such that capacity of the photosynthetic system changes with depth in the canopy [30, 104, 144]. Here, we consider integer levels of leaf area, with any fractions of LAI evaluated as a ratio of the full rounded up integer LAI level. Not only is this process repeated through the canopy depth, but also for each vegetation class at the start any month.

5.3.1 Maximize Expected Assimilation Rate

The optimal allocation model has been developed to find the constrained values that maximize the expected assimilation rate using the optimal assimilation model previously discussed. Derivation of the maximum expected assimilation rate is not included here (refer to Chapter 3), but rather discussion is focused on how it has been implemented within the TBM modeling framework. When each leaf layer is allocated optimally, we then also know that the total canopy expected assimilation rate is optimal. The expected assimilation rate is based on mean conditions from the previous

month, thus allowing changes in light environment, vapor pressure deficits, temperatures, etc. to affect how resources for photosynthesis are allocated.

Mean air temperature and vapor pressure deficit are simply estimated as the mean from the previous 30-day period. The maximum value of irradiance (Irr_{max}) is found as the maximum value of the previous 30-day period, and is used in the scaled irradiance distribution function (refer to Appendix B.1.1).

Although the maximum leaf-level nitrogen concentration is specified by PFT, these concentrations are not reached at lower canopy levels shaded by upper leaf layers. To account for this variation in nitrogen with depth in the canopy, we implement a limitation following the marginal nitrogen use efficiency, discussed next.

5.3.2 Marginal Nitrogen Use Efficiency

Each vegetation class is given a typical expected maximum organic nitrogen concentration ($gN\ m^{-2}$) based on available literature [67, 109, 145]. This is an expected upper limit of the concentration, but it is well known that concentrations decay exponentially with canopy depth [33, 104]. Therefore, rather than incorrectly assuming a constant nitrogen concentration by unit leaf area through the canopy, the marginal nitrogen use efficiency is determined [41]. A simple finite difference can be used to estimate the marginal nitrogen use efficiency,

$$\eta = \frac{\partial A_n}{\partial N} \approx \frac{A_{n_i} - A_{n_{i-1}}}{N_i - N_{i-1}} \tag{5.10}$$

where A_{n_i} is the assimilation rate at an upper canopy layer i, and $A_{n_{i-1}}$ is the assimilation rate one layer lower in the canopy. Similarly, N_i and N_{i-1} are the leaf-level nitrogen concentrations per unit area at the respective layers. In an optimal canopy, the value of η will be constant with canopy depth as determined using a calculus of variations approach [17].

We utilize this approach to determine the decrease in nitrogen with canopy depth as the light environment changes (refer to Chapter 3). Through incremental increases in nitrogen concentration, and determining the optimal expected assimilation rate for that level of nitrogen, Eq. 5.10 can be used to estimate the marginal nitrogen use efficiency. As nitrogen levels increase, the efficiency continues to decrease, until it reaches or falls below the specified threshold of η.

With a means of finding the assimilation rate given a set of expected environmental conditions and light distributions, the allocation that maximizes the expected assimilation for each leaf-layer can be determined using a numerical solution procedure.

5.3.3 Particle Swarm Optimization

Solving the optimal resource allocation problem resulting in the maximum expected assimilation is found by integrating over the irradiance distribution, but a closed form analytical solution to this problem does not exist, therefore, a numerical solution procedure is required. *Particle Swarm Optimization* (PSO) is a heuristic approach utilizing a population of individuals searching the decision space for an optimal solution, where the 'flock' can 'communicate' and direct optimal search directions [72]. For this application, the decision space is the set of constrained resource allocations resulting in photosynthetic capacities described by V_{cmax} and J_{max} (refer to Chapter 3). Fortunately, this decision space is a simple convex surface, thus convergence near the global optimum is certain.

For this study, a population of ten particles was used to search the decision space. Each of the particles is moved according to the PSO algorithm limited by a maximum step length [24] until one of two stopping criteria is met: either the number of iterations exceeds seven (a limit found acceptable during testing phases), or the average of the sum-squared-errors from the average value is than 0.05 (i.e. the population is clustered around the same point). The number of points, the maximum step length (also referred to as a 'velocity'), and the stopping criteria, were all tested iteratively to find an acceptable response for a variety of decision space surfaces.

For each iteration in the PSO process, for each of the particles, for every leaf layer, and each plant functional type, the expected assimilation value is determined. Although computationally expensive, the process has been streamlined in the VIC-VEO code, and only occurs at the start of any month, helping to limit computational burden. Completion of these processes continuously, rather than on a monthly basis, would be exceptionally limiting computationally. Further details are discussed in Chapter 3 and in Appendix B.2.

In addition to varying photosynthetic capacities by month, the leaf area index follows a monthly step-function using a harmonic phenologic regression, which is completed at the start of every new calendar year.

5.4 Annual Leaf Area Index Phenology

Leaf area plays a significant role in TBMs greatly affecting the energy and water balance through interception, boundary layer roughness and the transpiration of soil moisture, among other processes [11]. Even at macro-hydrologic scales, appropriate description of the leaf canopy area is critical for description and prediction of long-term energy and water balances. Additionally, leaf area and the associated carbon assimilation is of paramount importance for estimating the global carbon balance between sources and sinks [94].

Climatic regression considers a description of the climate (e.g. temperatures, precipitation amounts, seasonal patterns, solar environment, etc., over multiple decades), which is used to estimate the vegetation cover. Categorical approaches use climatic covariates to describe the type of expected land cover, such as deciduous forest, grassland, conifer evergreen, etc., but this does not make any statement regarding the LAI magnitude and phenology [12]. Categorical approaches could be used to describe the type of land cover, but utilize inappropriate fixed relationships for LAI phenology within each category. For this study, we utilize an approach that fits a harmonic model based on climate (Chapter 4), which allows a dynamic response in leaf area magnitudes and phenology as climate changes. A regression approach accounts for many unaccounted and latent processes in LAI responses not captured in more complex DGVMs.

The annual leaf area phenology is determined here using a regression approach, which assumes a big-leaf multi-layered canopy scheme. Clearly canopies have widely variable leaf area densities, but for macro-scale applications, it can be generalized as a simpler multi-layer big-leaf process [30]. The annual phenology is determined at the start of any model year, and specifies a monthly variation using a step-wise function; each month has a uniform total big-leaf area that adjusts as a step at the start of the proceeding month.

The phenologic regression model employed here uses climate parameters which are described using a 20-year pulled rolling average. Monthly parameters (e.g. mean July daily maximum temperature) considers only data from July months over this past 20-year period, for example. Natural disturbances such as wind-throw or forest fires are not included in this model; it only considers mean expected vegetation leaf area phenology.

5.5 Model Implementation

Implementation of these various processes into a macro-scale eco-hydrologic model requires the development of an algorithm which includes many interrelated and dependent steps. To best outline this process, the major components of this system are outlined in a process line diagram in Figure 5.1, which shows the relationship of each step in the solution procedure. Major components can be summarized as,

Annual Phenology Climate defined by a 20-year rolling mean period is used to estimate the leaf area index phenology of the general vegetation cover using a regression approach, as discussed in detail in Chapter 4. This process is called at the start of any new calendar year, and determines monthly phenology for the coming year, based on the previous climate period.

Monthly Photosynthetic Capacity At the start of each month, the previous month conditions including light, water availability, and temperatures, are used to determine an optimal allocation of available nitrogen. This was discussed in detail in Chapter 3, and is completed for each discrete canopy layer.

Particle Swarm For a single layer in the the canopy, a given set of environmental conditions and a specified maximum nitrogen concentration, the optimal solution is determined through a numerical Particle Swarm solution procedure. Details of this process are discussed in Appendix B.2.

Expected Assimilation This process is repeated using a distribution of irradiance which is used to determine the expected assimilation rate, where the optimal allocation maximizes this expected assimilation rather than any given individual rate. Photosynthetic assimilation includes many steps, which have been discussed in detail in Chapter 3 and Appendix A.

Temperature Normalization Optimal allocation is temperature sensitive; once optimal parameters have been found, they are normalized to a common industry standard temperature of $25°C$.

The phenology for the year is updated at the start of each new modeling calendar year using the pulled moving average conditions of the previous 20-years. This determines the leaf area index,

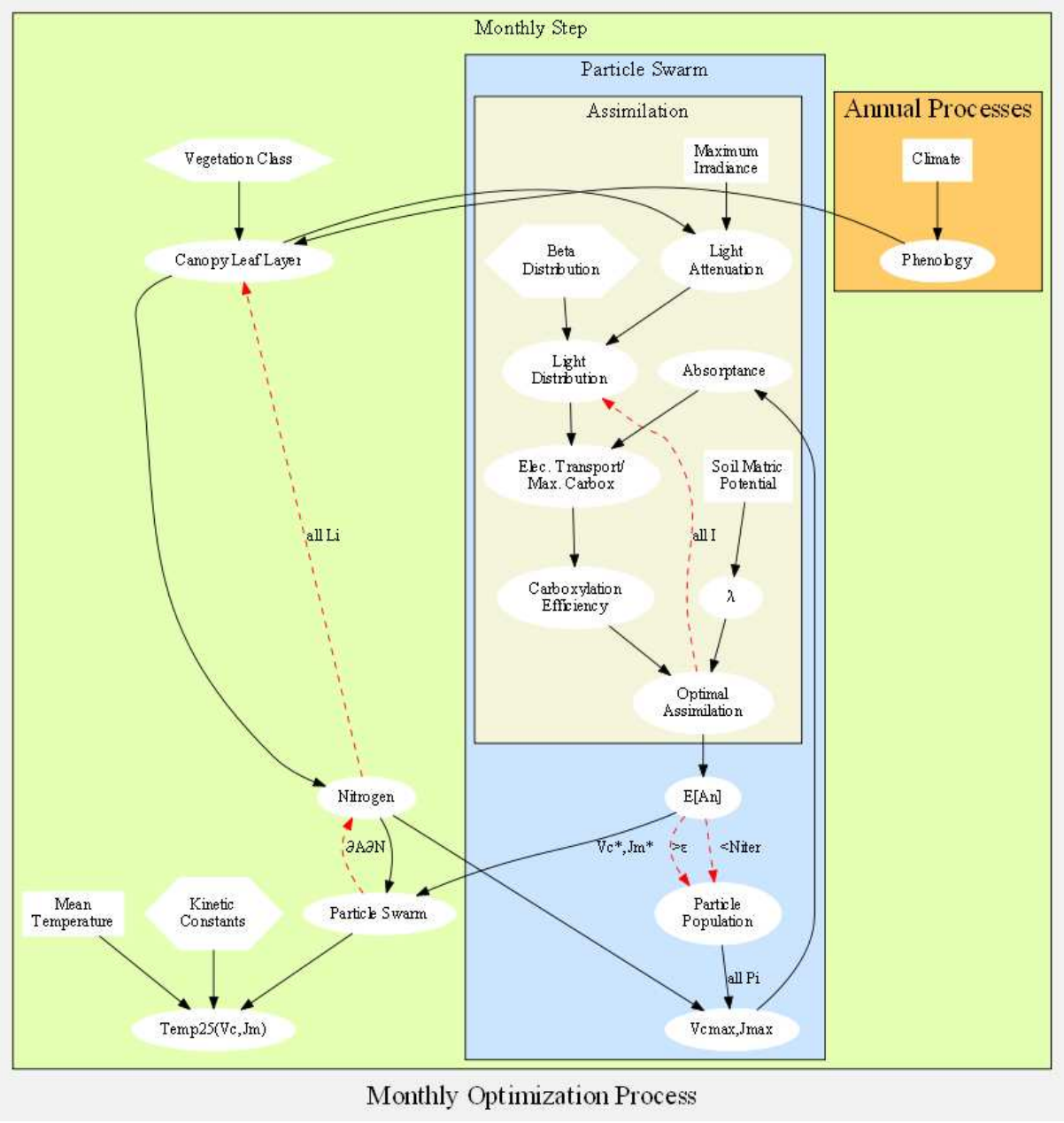

Figure 5.1: VIC-VEO Process Line Diagram

rounded up to the next whole integer, where the optimal allocation of resources to photosynthetic systems is determined. Again, capacity is limited through canopy depth using the marginal nitrogen use efficiency approach. Determination of optimal allocation for each layer is completed by iteratively searching the decision space using Particle Swarm Optimization. For each test of resource allocation, the expected value of assimilation is found by iterating over discrete levels of the irradiance density distribution, where assimilation is found at each increment using the FvCB model of photosynthesis and the optimal stomatal control model. Parameters are adjusted based on soil moisture status, light environment and temperature. Once the optimal allocation is found for each layer, it is held constant for the reference temperature for the month, and the process is repeated at the start of the next month, allowing a dynamic response of the photosynthetic system.

5.6 Evapotranspiration Model Verification

Several different tests were completed to evaluate the performance of the VIC-VEO optimal stomatal responses by comparing modeled evapotranspiration (ET) fluxes to a) ET observations and b) calculated ET from the most recent VIC release.

Transpiration is the process of water vapor moving from leaf internal mesophyll pore spaces into the atmosphere, primarily through stomatal pores. Long-term large-scale measurements of transpiration at the leaf or canopy level are not available for assessment of model fitness. Although, as a surrogate, aggregated long-term canopy level measurements of ET are available from Fluxnet towers[11]. Evapotranspiration includes processes of evaporation from soil and vegetation surfaces, in addition to transpiration, creating a source identifiability issue.

Therefore, as a measure of model performance, we compare hourly observations from Fluxnet data to total hourly ET calculated from VIC-VEO. As a secondary evaluation, the results are also compared to the hourly integrated ET from the most recent release of VIC-4.2. The latter also includes a multi-layered canopy model, but uses the ubiquitous Jarvis model of stomatal resistance. Identical sets of forcing variables are used for the VIC-VEO and the VIC-4.2 models,

[11] `http://fluxnet.ornl.gov/`

thereby processes of snow accumulation, melt, precipitation interception, surface evaporation, soil evaporation, etc. are nearly identical, and any differences of modeled ET can be attributed wholly to stomatal function and the estimated rate of transpiration.

Note, for these performance tests, a fixed monthly phenology of leaf area index and resource allocation was used to create an equal comparison for evaluation of the influence of stomatal model differences on ET.

5.6.1 Study Sites

Six Fluxnet locations from diverse biomes across the United States were selected to compare calculated ET to observed data. Available data was downloaded, although available years and durations differered between sites. Original Fluxnet data is available in 30-minute increments; this information was aggregated to create hourly averaged datasets, matching the output timestep from the VIC models.

The six study sites included:

Tablelands, NM - A Pinyon-Juniper arid scrubland

Willow, WI - A northern Wisconsin deciduous site

Mary's River, OR - A closed canopy evergreen fir site

Sandhills, NE - Open grasslands with excessively drained soils

Duke, NC - Mixed evergreen and deciduous canopy

Howland, ME - An evergreen dominated location in central Maine

Fluxnet towers report the latent heat flux in $W\ m^{-2}$, which can approximate the ET rate in $mm\ hr^{-1}$ using,

$$Flux(mm\ hr^{-1}) = Flux(W\ m^{-2}) \times 0.00147 \tag{5.11}$$

This allows direct comparison of the Ameriflux ET rates to the VIC-VEO (or VIC4.2) output for calculation of various fitness functions.

Environmental forcing data for each site was created using Daymet data, which provided daily precipitation, and daily minimum and maximum temperatures. Wind was assumed a constant for

each site due to limited data availability. The model duration evaluated for each site varied based on local site data availability, but included a minimum three contiguous years of model time.

The Nash-Sutcliffe (NS) measure of efficiency was used to describe the model fitness for total evapotranspiration [100] using hourly data. Evapotranspiration follows a diurnal pattern as stomata open and close with variable irradiance and vapor pressure deficits. In order to further evaluate the fitness with NS, the data was divided into monthly blocks (rather than a single NS value for an entire year or multiple years) to assess degrees of fitness between seasons under variable phenology and environmental conditions. Nash-Sutcliffe values are constrained in the range of $[-\infty, 1]$, where an NS=1 indicates an identical match to observations.

As a second measure of fitness, the variance of the hourly residual was determined, where again the data were divided into monthly blocks to ascertain seasonal differences in model variance. Clearly, lower variance would represent a more fit response with tighter clustering of the residuals around the observed values.

5.6.2 Evapotranspiration Results

Models were run for both the VIC-VEO and the VIC-4.2 producing ET estimates at each of the six sites. A sample comparison of the VIC-VEO and VIC-4.2 model ET outputs against observations at Willow, Wisconsin, for the month of June in 2005, is shown in Figure 5.2. This figure shows periods of significant deviations from observations, most likely due to environmental conditions that vary from those used in driving the models, such as wind, vapor pressure or irradiance. Although with significant variation, this period still mimics the diurnal patterns measured by the Fluxnet towers. This figure also demonstrates a period where there is continuous bias of over-estimating ET flux from VIC-4.2, whereas VIC-VEO appears to be producing lower residuals and bias.

Clearly, results for any modeling framework can be adjusted through a calibration procedure to increase/decrease residuals against observations, but the goal here was simply to demonstrate the feasibility of reproducing observed ET fluxes using an alternative stomatal model in a macro-scale modeling framework; no 'calibration' or adjustment of parameters used in either model was performed, but rather it was based on best estimates of parameters, as is typically done in large-scale modeling efforts.

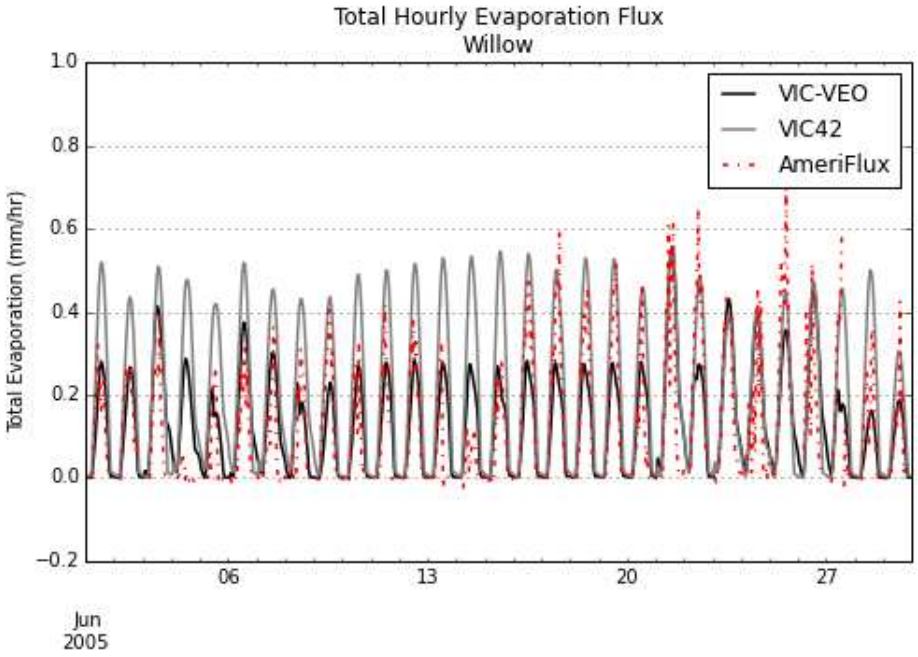

Figure 5.2: Hourly Evapotranspiration Fluxes

When considering the metric of residuals and bias, the VIC-VEO consistently shows improved performance of reduced mean monthly residual and lower degrees of bias compared to VIC-4.2 across all study sites (Figure 5.3). Further, the VIC-VEO optimal model generally maintains lower standard errors from observations across all sites. Figure 5.3 shows the mean difference between Fluxnet total canopy evaporation and model computed values for the six study sites.

The VIC-VEO optimal model also shows higher values of the Nash-Sutcliffe coefficient of efficiency for most months at the six study sites. Figure 5.4 shows these results for each of the sites.

This demonstration shows sufficient skill for application of an optimal stomatal model within a macro-scale modeling framework, requiring minimal parameterization. Magitudes of residuals, timing of ET, and stomatal response to environmental conditions are well-captured within the optimal stomatal model paradigm.

5.7 Macro-Scale Hydrologic Response with Climate Projections

Although similar to the previous section of testing the VIC-VEO model, in this section we are specifically interested in a) extension to climate projection data and b) review of impacts on

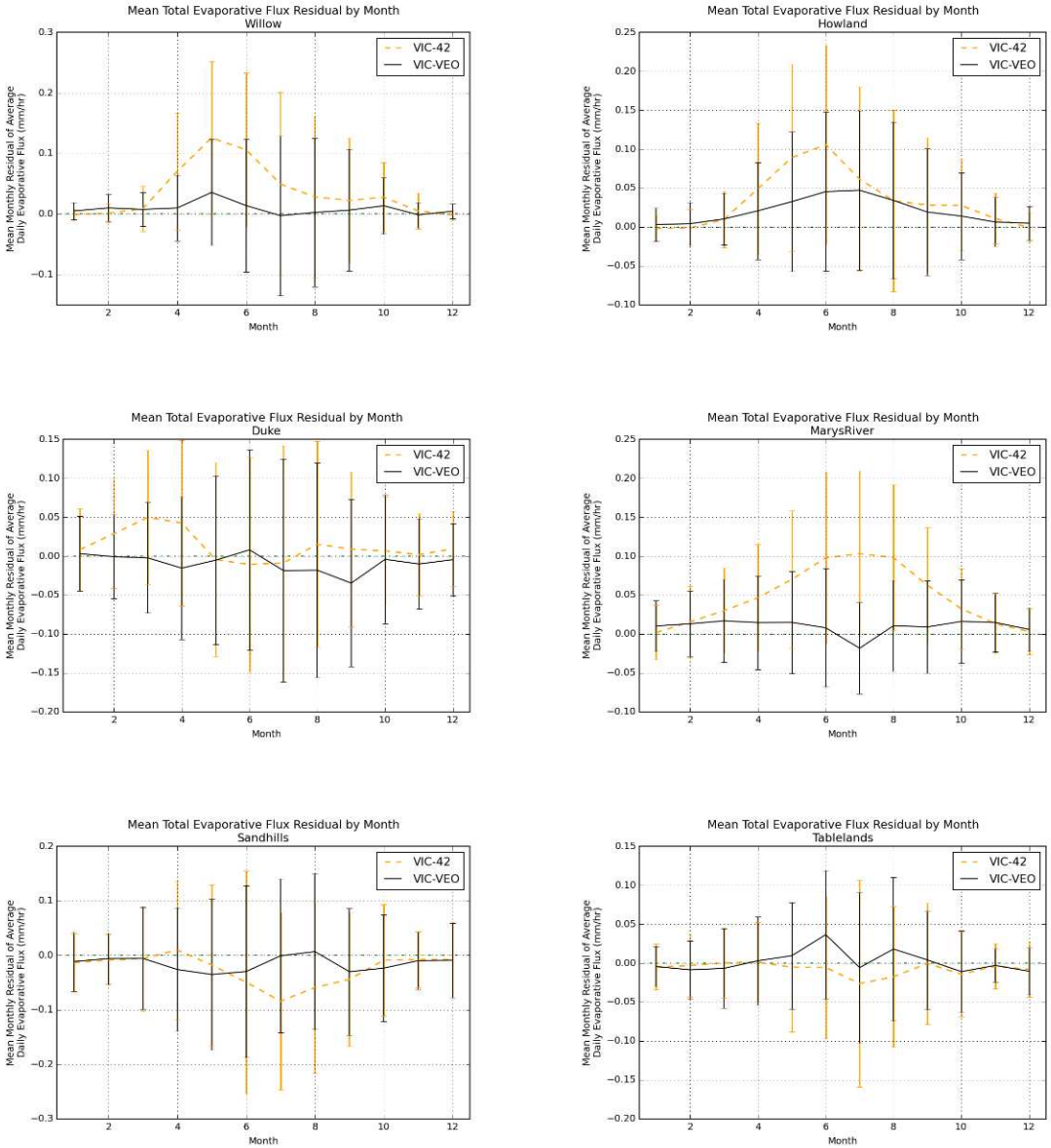

Figure 5.3: Mean Monthly Residual. Comparison of VIC-VEO and VIC-4.2 total canopy evaporation and mean residual by month. Error bars indicate 5% and 95% errors.

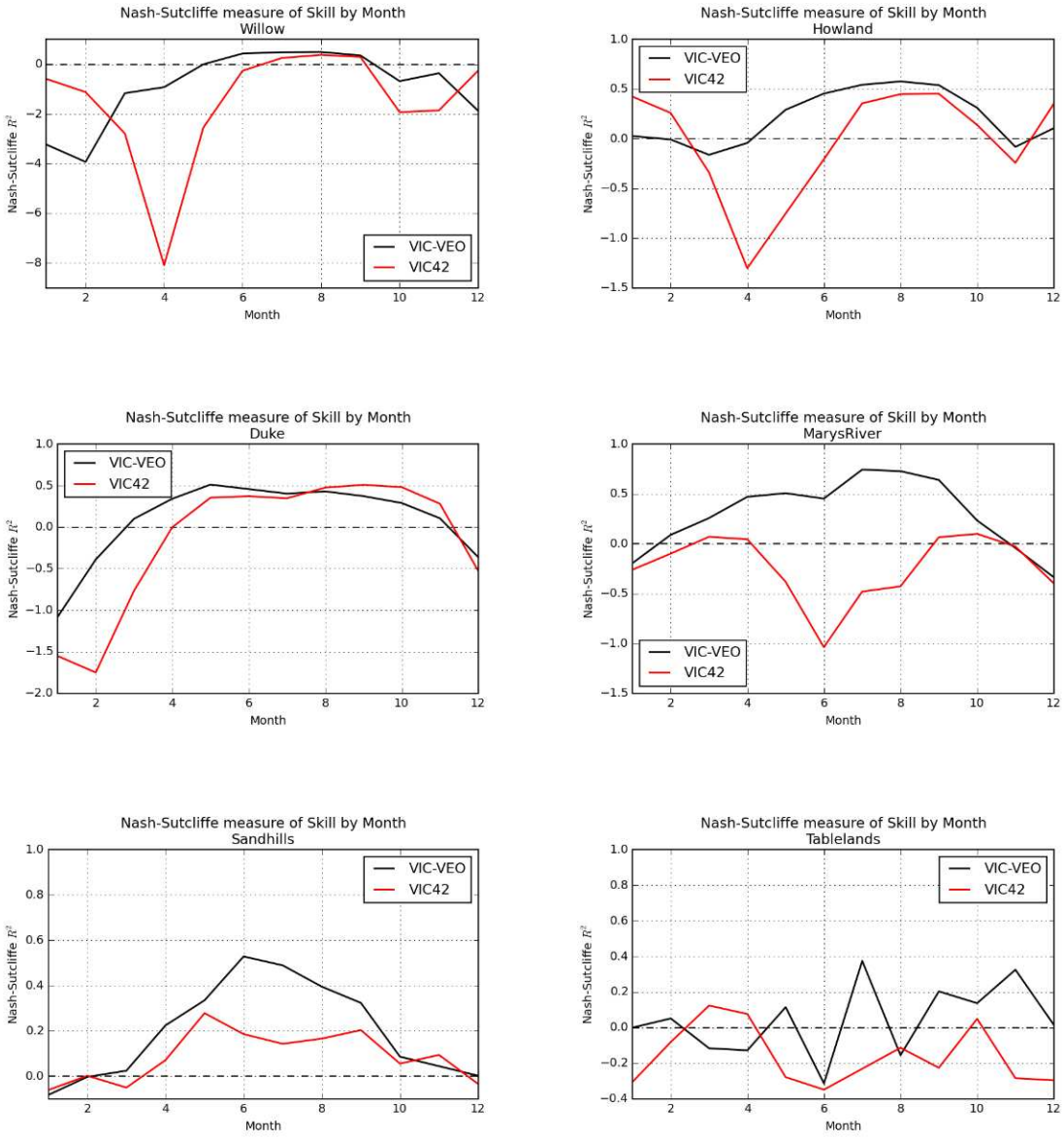

Figure 5.4: Nash-Sutcliffe Measures of Efficiency. Comparison of VIC-VEO and VIC-4.2 total canopy evaporation and mean residual by month. Error bars indicate 5% and 95% errors.

hydrologic yield differences when including full dynamic vegetation responses. These tests are conducted by now including the models for variable LAI phenology, optimal stomatal control, and optimal photosynthetic resource allocation approaches (i.e. the 'full' VIC-VEO model).

Although comparison of model hydrologic responses from future GCM projections to observations is obviously not possible [73], comparison between models with and without vegetation dynamics is informative for macro-scale hydrologic model sensitivity to the impact of dynamic vegetation on the hydrologic response.

5.7.1 Approach

We consider two separate scales of comparison: a single 'point' in the macro-scale hydrologic model that includes detailed information regarding evaporation, runoff, baseflow, soil moisture, etc., and secondly an aggregated watershed level hydrologic response, which is the sum of runoff and baseflow from multiple points over a large region. The former is informative to understand how individual components of the hydrologic cycle are affected, whereas the latter provides estimates of changes in macro-scale potential yield if vegetation is responding dynamically. Each of these scenarios are run using a *dynamic* and a *static* version of the VIC-VEO model.

The static model essentially means the dynamic components are 'turned-off', compared to running an alternate model like VIC-4.2, ensuring an equal comparison between models. The components that are turned off include a) the dynamic phenology and b) the optimal resource allocation routines - the optimal stomatal model is still retained, but parameterization of that routine does not change over time in the static model.

All models are forced using the same datasets, over the same modeled time domain, with identical soils information.

The comparison is accomplished by running identical dynamic models from year 1985 to mid-summer of 1999 (14.5 years). Then the 'static' model stops updating photosynthetic capacities and leaf area indices, maintaining values set during the last update. In this manner, we ensure equivalent starting positions of the model, allowing evaluation of the divergence in hydrologic responses.

The reason updating of the static model was stopped during the mid-summer period was to maintain expected summer period photosynthetic parameterization. This is common practice in TBMs, where a single value for V_{cmax} and J_{max} at a reference temperature (usually $25°C$) is used

for all seasons for a given vegetation or PFT. Here, we are mimicking that response in the static model runs. This does not preclude the capacity of the model to adjust the value due to standard temperature responses, but rather simply maintains a constant reference value throughout the year.

5.7.2 Climate and Model Data

Projected climate data from the most recent CMIP5[12] ensemble collection was utilized. Specifically, this section utilizes the Beijing Climate Center (BCC) model[13], with the representative concentration pathway (RCP) 8.5, the most 'aggressive' emission scenario with the largest predicted greenhouse gas emissions and climatic temperature increases. The focus of this section is to discuss specific model vegetation responses in a changing climate, rather than focusing on comparing a range of GCM and RCP scenarios; these models are discussed in Chapter 6. Forcing data was supplied to the models on a 24-hr timestep and included daily minimum temperature, daily maximum temperature, total daily precipitation, and daily average wind speed[14].

The VIC-VEO model was run from a period of January of 1985, through December of 2099, using a three-hour timestep. Results were retained at an aggregated daily timestep, and include: Runoff, Baseflow, Evaporation (Canopy, Surface, Soil), Transpiration, Soil Moisture (three layers), Sublimation (Surface, Canopy, Blowing), Potential Evapotranspiration (Open Water and Natural Vegetation), and Snow Water Equivalent (SWE).

5.7.3 Results - Difference in Projected Point Hydrologic Response

We compare the partitioned hydrologic responses between the dynamic and the static models up to year 2100 using the GCM projections. The partitioned response is important to see how and where changes in hydrologic response may be occurring if vegetation is allowed to change with climate. The lumped hydrologic response may show no changes in yield, for example, but is this due to increased transpiration counteracted with decreased canopy interception with a thinner canopy? By comparing the individual components of the hydrologic response, we can start to understand the complex and interacting components of the hydrologic cycle and the potential response.

[12] https://cmip-pcmdi.llnl.gov/cmip5/
[13] http://cmdp.ncc.cma.gov.cn/pred/en_cs.php
[14] http://gdo-dcp.ucllnl.org/

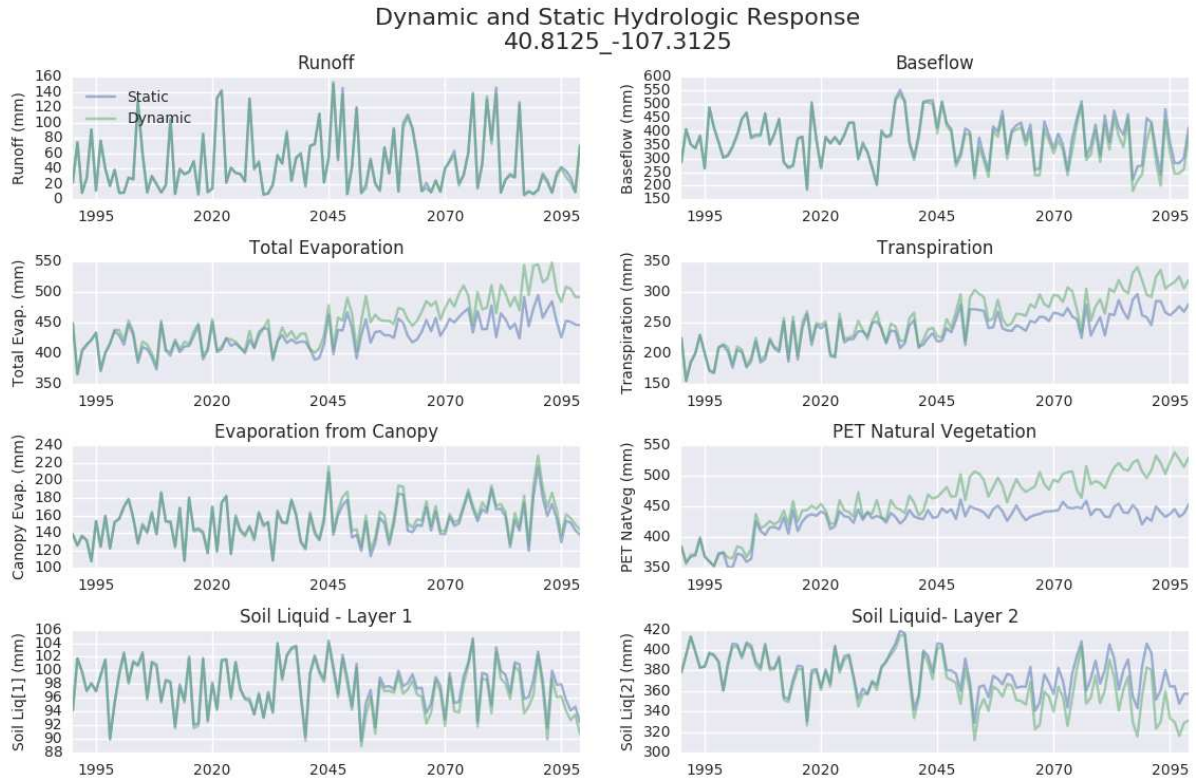

Figure 5.5: Annual Aggregated Hydrologic Responses of Dynamic and Static Vegetation Model

Using the BCC GCM model for the RCP 8.5 concentration profile, the hydrologic response from several different locations from the VIC-VEO model were compared. Figure 5.5 shows partitions of hydrologic responses for both the static and the dynamic model runs at one location (40.8125N,107.3125W) within the Colorado River Basin. As can be seen, the responses are nearly identical until mid-sumer 1999[15], and then start to diverge in their hydrologic response.

Most apparent is the difference in the *Potential Transpiration* from the natural vegetation; we see a clear and steady increase in the PET from the dynamic model, whereas we observe a stagnant response from the static model. Not only is there a change in the potential transpiration, but the actual transpiration is increasing with the dynamic model. As a result, there are lower soil moistures, lower baseflow rates, and slightly lower runoff.

Although some differences are obvious when reviewing the absolute values in Figure 5.5, we can instead review Figure 5.6 which shows the percent change between models for each variable. Here,

[15]The model uses heuristic optimization techniques, so some small differences may be observed

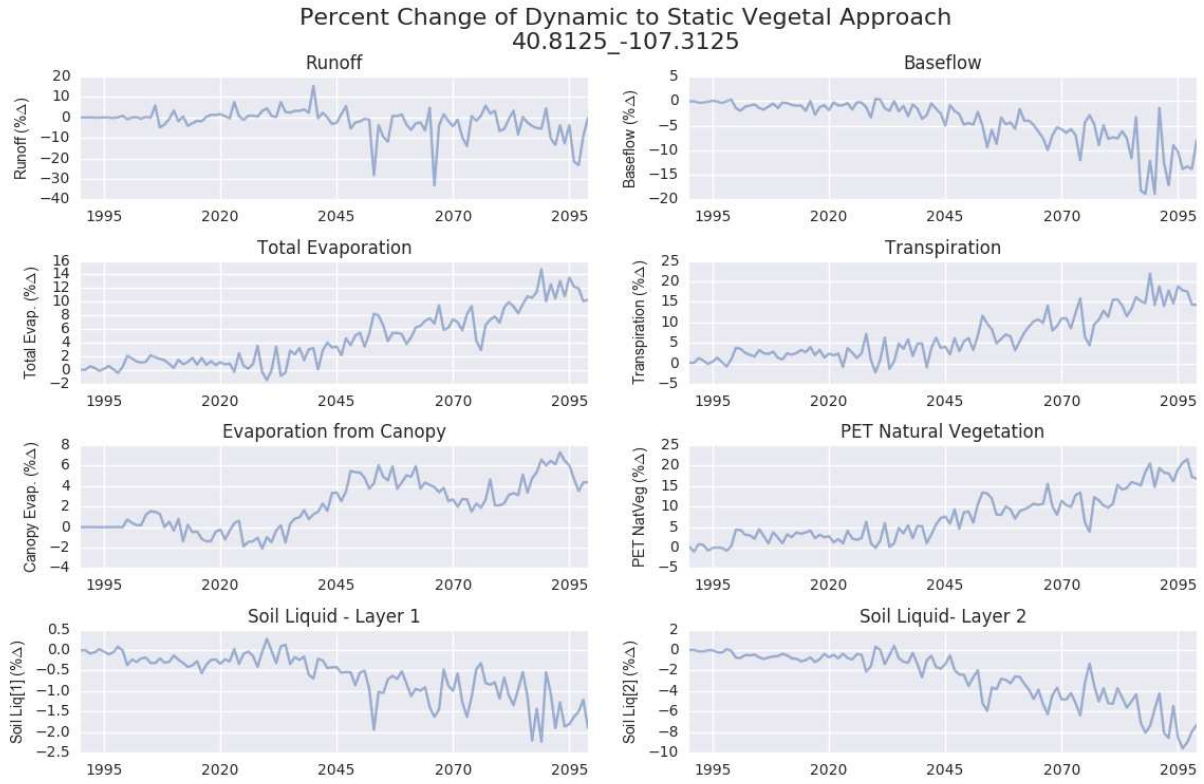

Figure 5.6: Percent Change in Annual Hydrologic Responses of Dynamic and Static Vegetation Model (Location-1)

trends and changes are much more apparent. We again note the steady increase in PET from the canopy, the increase in the modeled transpiration, and the decreases in soil moisture. Although now, the changes in baseflow and runoff are more apparent in the percent difference figure, clearly showing changes between the static and dynamic models towards the end of the century on the order of a 10% reduction in flow. Note, this is not stating a 10% reduction in yield due to climate change, but is rather stating that accounting for a dynamic vegetation response will result in 10% lower flow than would be expected assuming a static representation of vegetation at this location.

This response is from a single point for a single GCM and RCP, and is certainly not indicative of the expected response from other locations in the modeling domain. As an example of an opposite response, we can evaluate the percent differences as shown in Figure 5.7, which is a location further south and west of the first study site in the Colorado River Basin. Here, we can see a slight increase in baseflow, but a significant change in runoff and canopy evaporation. Although not shown explicitly here, this is due to a decrease in the leaf area index - less leaf area is available for

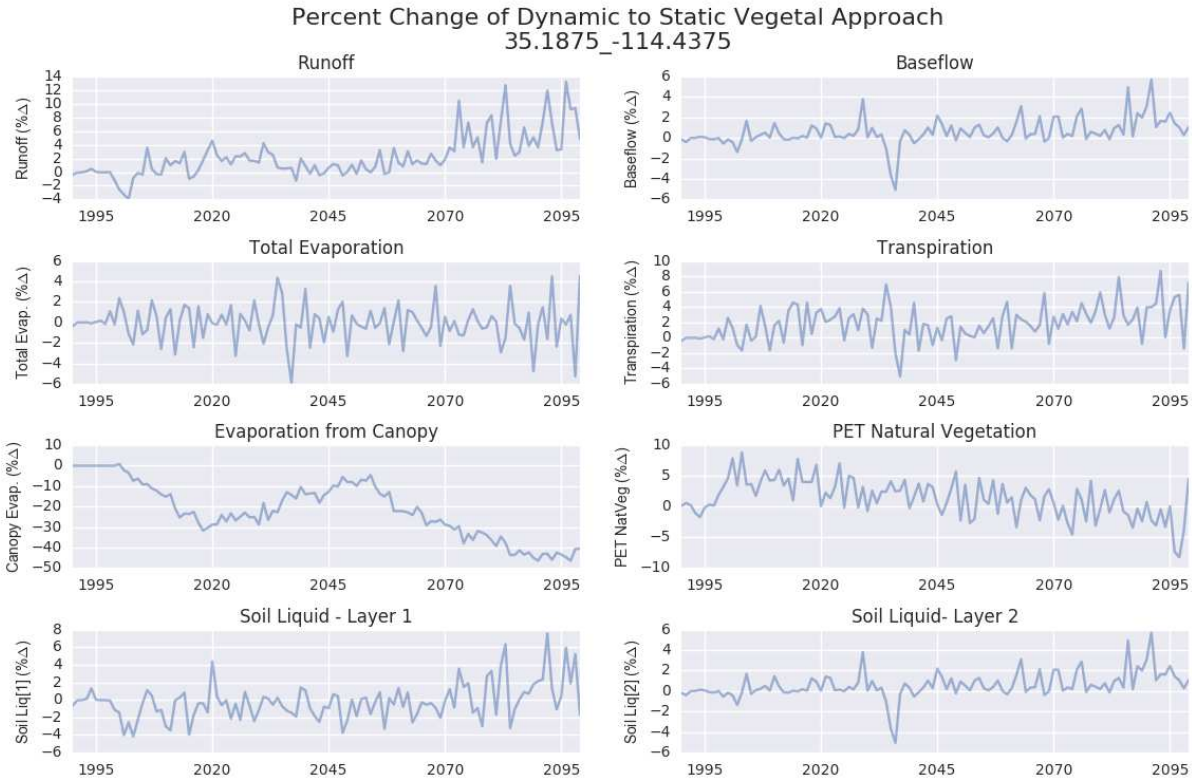

Figure 5.7: Percent Change in Annual Hydrologic Responses of Dynamic and Static Vegetation Model (Location-2)

intercepting precipitation that can be evaporated, which is also resulting in a greater surface runoff response from excess precipitation. Finally, percent differences in soil moisture, transpiration and total evaporation are only a few percent between the static and the dynamic models. Increases in transpiration are potentially from greater vapor pressure deficits offsetting any decrease in leaf area or change in stomatal function.

5.7.4 Results - Difference in Watershed Scale Yield

Rather than considering a single point response, we now scale up to an aggregated watershed level response and consider the changes in total expected yield should dynamic vegetation be included in TBMs compared to a static vegetation response.Continuing with the utilization of

the BCC GCM and RCP 8.5, the baseflow and runoff for all contributing distributed cells are routed through a subcatchment using a linear time invariant model based on the de St. Venant equations [85], resulting in outflow hydrographs at various locations for both the static and dynamic model scenarios.

Throughout the Colorado River Basin, 41 different subcatchments have been defined - flows for each of the subcatchments have been routed for both the static and dynamic models. This allows comparison of the hydrologic yields for each subcatchment across a large and diverse region for considering the hydrologic response difference from dynamic vegetation. Again, this assumes approximately 15-years of nearly identical modeled conditions, followed by the static model not updating photosynthetic capacities or leaf phenology.

For each subcatchment in both model scenarios, flows were aggregated into a total annual yield. These values were then grouped by decade (e.g. 1990-1999, 2000-2009, etc.) and the mean for each decadal block was determined. Finally, the percent change for each subcatchment by decadal block was found by simply finding $(Qd_{d,i} - Qs_{d,i})/Qs_{d,i} \times 100 \; \forall \; d, i$, where Qs is the yield from the static model, Qd is the yield from the dynamic model, d is the decade block, and i is the subcatchment.

Figure 5.8 shows the percent change between the dynamic and static vegetation models by decadal block for all of the subcatchments. It needs to be emphasized that this is the percent difference in mean decadal yield between a static and dynamic vegetation response. This figure obviously shows no difference in the first decadal block starting in 1990, while some slight differences are noted in the subsequent decadal period, mostly as an increase in yield with a dynamic model through the northern portions of the Upper Colorado River watershed. Quickly, yield increases significantly ($> 20\%$) with a dynamic model compared to the static model in several locations (e.g. west of Lake Powell, western edges of lower Green River), with smaller differences throughout the entire basin. Towards the end of the century, the increases in yield begin to subside, with many locations showing a reduction in yield when using a dynamic vegetation model.

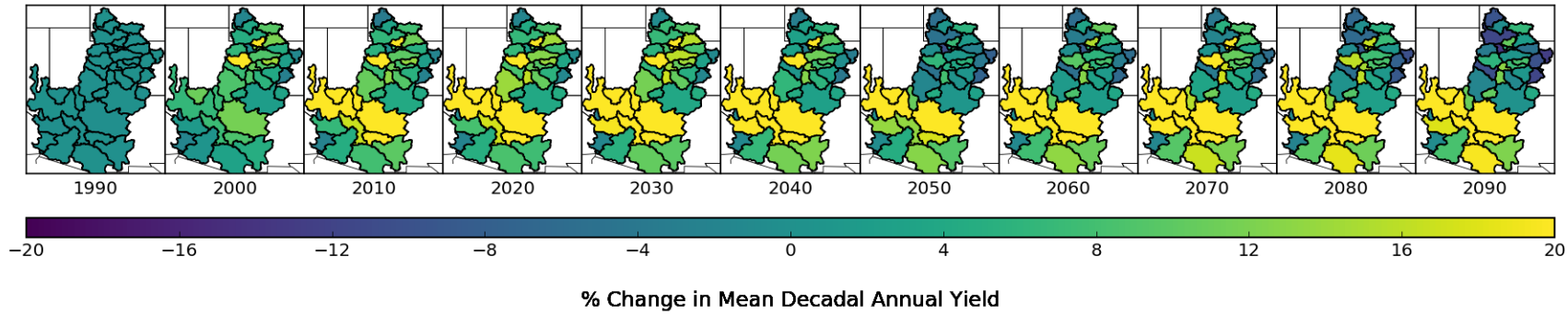

Figure 5.8: Percent Change in Distrbuted Subcatchment Yield by Decade - Difference is from Static to Dynamic model, where positive values indicate an increase in annual mean decadal yield when accounting for dynamic vegetation responses, whereas negative values indicate dynamic vegetation will reduce the expected yield. Note, positive or negatives values are not a statement of total increases or decreases in yield, but solely the difference when accounting for a dynamic vegetation response.

The critical nature of the influence of vegetation on hydrologic response should be apparent, with differences in annual yield $> 40\%$ in some locations. As the LAI density decreases due to changing climatic conditions (i.e. vegetation is responding to climate), the amount of precipitation intercepted and transformed as canopy evaporation will decrease allowing a greater potential depth of either infiltration or runoff. Conversely, the canopy may maintain similar LAI densities, but become more favorable to photosynthetic assimilation thus allowing an increase in stomatal conductance and transpiration rates.

Rather than comparing the percent differences between model responses, we can also look at the total difference in aggregated yield for the entire watershed by decadal block. Simply subtracting the static from the dynamic yield would show the changes in modeled yield when accounting for dynamic vegetation.

Figure 5.9 shows the aggregated difference in response for the entire Colorado River Basin in mean MAF/year by decade with the inclusion of a dynamic vegetation model. We see a clear increase in yield for the first half of the century, followed by a decreasing trend in the latter half with a small increase around 2075 in response to the variable climate. For the entire Colorado River Basin, a 2 MAF/year increase is approximately a 15% difference in total yield; this is certainly a significant change in yield for such a water scarce basin. It's worth noting the absolute magnitude of yield for both the static and the dynamic models show a decreasing trend through the century, only that the dynamic vegetation model shows a smaller trend (i.e. 15% less) in yield loss.

Finally, these differences are for a single GCM and RCP scenario, but the influence of changing vegetation on the hydrologic cycle should be apparent, regardless of which GCM or RCP is selected to be tested in this comparison. GCM and RCP scenarios resulting in greater climatic changes will have greater potential differences in hydrologic yield between a static and dynamic vegetation parameterization approach.

5.8 Discussion

Inclusion of an optimal and dynamic vegetation response in a macro-scale hydrologic modeling framework involves several complicated and interacting components at a range of spatial and temporal scales. Stomata respond nearly instantaneously to rapidly changing environment conditions,

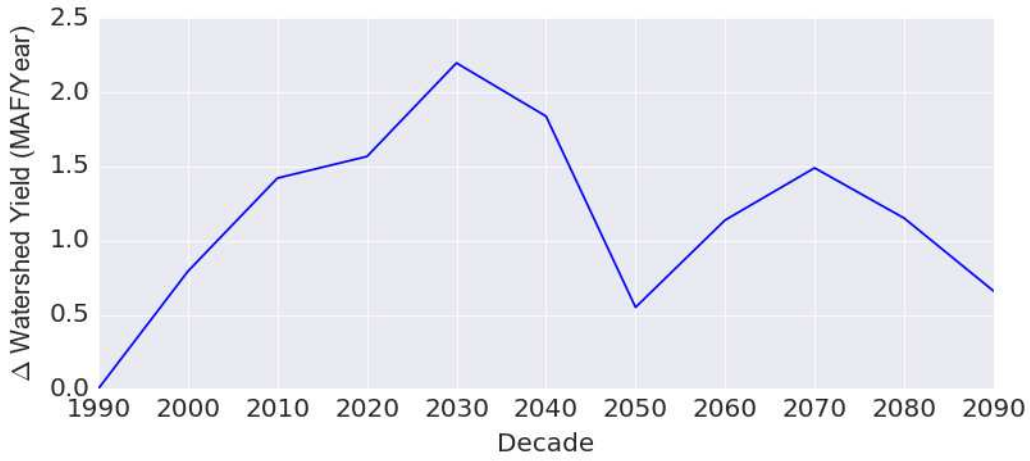

Figure 5.9: Accumulated Mean Decadal Difference in Yield - Total accumulated difference in MAF averaged by decade for all subcatchments.

such as light, temperature, vapor pressure deficit, etc. The rate of assimilation and the most limiting photosynthetic system depend on the capacities of two separate yet interacting photosynthetic systems. The capacities are described by the terms V_{cmax} and J_{max}, which depend on available resource supplies and environmental conditions, which also change seasonally. We postulated an optimal allocation approach which adjusts these parameters to maximize the expected assimilation rates for the given environmental conditions and set of limited resources. Finally, we considered variable leaf area phenologic responses based on long-term mean climatic conditions using a regression approach. This allows the parameters defining periodic LAI phenology to change, where LAI amplitude, frequency and phase can shift as a function of climate. It is assumed the relationship between climate and phenology over multiple decades is optimal, which is used to parameterize the regression approach, therefore the regression is mimicking an observed optimal response of natural vegetation.

Bringing these components together into a macro-scale modeling framework for large-scale long-term modeling requires a series of assumptions and numerical approximations. Although several simplifying assumptions are required, they are not considered to significantly affect the macro-scale response. For example, we are utilizing a multi-layered big-leaf model; although multi-layered models provide an improved response over a single big-leaf approach, the canopy is still assumed to be integrated into discrete big-leaf layers, a simplifying assumption. Similarly, for this macro-

scale approach, we assume a well-coupled system between the vegetation and the atmosphere - this implies that the leaf temperature is approximated by the ambient air temperature, and the vapor pressure deficit above the leaf boundary layer is assumed identical to the ambient atmospheric vapor pressure. These assumptions, amongst others utilized, are not novel, but are required to create a numerically solvable solution procedure.

Testing of the optimal stomatal model utilized Fluxnet data, which includes combined evaporation and transpiration responses from an integrated canopy, rather than solely transpiration responses at the leaf level. Transpiration measurements are typically available in certain studies at short temporal periods, but macro-scale modeling requires larger spatial and temporal scales only comparable to available Fluxnet data. To help understand the performance of the VIC-VEO model against observations, a second model was run (VIC 4.2) using identical soil and forcing data, with a static canopy and resource allocation. The VIC-VEO model with an optimal stomatal model consistently showed improved performance with reduced residuals, bias, and variance. This was further supported with improved values of the Nash-Sutcliffe measure of efficiency.

Testing of the long-term dynamic response, including dynamic resource allocation and climatic regressed phenology, was done as a comparison between the dynamic and static models. Longer term phenologic testing against LAI observations was completed in Chapter 4, whereas here we were specifically interested in the long-term partitioned and aggregated hydrologic response. Partitioning of the long-term response showed how water is re-allocated between different processes as vegetation adjusts to a changing climate - it was noted that solely focusing on yield may neglect how it is partitioned between baseflow and runoff, or focusing on total ET may not be informative for changes in transpiration versus canopy evaporation, for example. In some applications, it may be critical to understand partitioning within the various components of the hydrologic cycle.

Finally, for the long-term simulations with both the static and dynamic vegetation models, we considered an aggregated hydrologic response for 41 subcatchments across the Colorado River Basin. In this analysis, we evaluated the mean annual yield in decadal blocks, and then determined the percent difference between static and dynamic responses for each subcatchment and decadal block. This shows the differences in yield between both approaches, and helps illustrate the significant effect vegetation plays on the hydrologic cycle, along with the non-uniform spatial response. When

hydrologic yield was aggregated across the entire Colorado River Basin, the magnitude of the difference between an assumed static and dynamic model becomes apparent.

Inclusion of dynamic vegetation parameterization is not unique for macro-scale hydrologic TBMs; what is unique here is an application using optimal stomatal control, optimal resource allocation scheme for depth varying photosynthetic parameterization, and a climatic based leaf area phenologic regression approach. Each of these models employed in VIC-VEO were determined to be both fit in performance, and show a significant effect on the hydrologic cycle. Inclusion of dynamic vegetation responses is critical in long-term hydrologic modeling in our rapidly changing climate.

Chapter 6

Water Supply Vulnerability Analysis

The Colorado's modern notoriety, however, stems not from its wild rapids and plunging canyons, but from the fact that it is the most legislated, most debated, and most litigated river in the entire world. It also has more people, more industry, and a more significant economy dependent on it than any comparable river in the world.

– **Marc Reisner, Cadillac Desert**

6.1 Introduction

A critical future economic and societal risk is the possibility of insufficient water supply to meet the various demands and consumptive uses, and very few regions in the world face a greater risk than the Colorado River Basin [19]. This watershed covers an area of approximately 243,000 sq.miles and drops 14,000 feet of elevation to the sea. More than 33 million people depend directly (wholly or in part) on the Colorado River for their water supply[16], where water supply includes water for irrigation for food security, stream flow for recreation and habitat, and hydropower generation.

The demands for consumptive water use have continued to increase over the past century, whereas the actual supply of water available to meet those demands has not grown in recent years, and is uncertain in the future, especially in light of our rapidly changing climate [138].

Many studies have been completed to assess changes in potential future hydrologic yield [106] and seasonal runoff timing [25, 31], whereas others have included detailed evaluations of variable demand in a changing climate using such projections [6,16,46–48]. Significant uncertainty surrounds

[16] `http://www.coloradoriverbasin.org/about-the-colorado-river-basin`

the Global Circulation Model (GCM) projections [82], the downscaling [44], and the consequent hydrologic response [91]. Despite those uncertainties, GCM projections still remain the best source of data for understanding the potential future hydrologic yield for use in demand and vulnerability analyses.

Hydrologic responses are determined using Terrestrial Biosphere Models (TBMs), which model the interaction of short-term meteorology within the earth's soil, plant, and atmospheric boundary region. Within this domain, vegetation plays a significant role in the mediation of the earth's energy and water balance, although vegetation is extremely dynamic. Vegetation responses can be short-term on the order of minutes (e.g. stomatal movement), medium-term responses on the order of months (e.g. nutrient translocation, leaf senescence, growth, mortality), and long-term responses on the order of years (e.g. canopy level biomass, seasonal phenology). Assuming a static response, such as a single stomatal conductance value, a fixed photosynthetic capacity within and between years, or a fixed leaf area phenology, is not appropriate in such a dynamic system and can lead to significant errors in the energy and water balance for long-term large-scale TBM simulations.

Here, we apply a new spatially-distributed dynamic vegetation parameterization model, VIC-VEO, to the Colorado River Basin to study the vulnerability of water supply to meet projected spatially varying demands at the fourth Hydrologic Unit Code (HUC4) level. Previous analysis using VIC-VEO showed significant variation in the projected yield when accounting for dynamic vegetation responses compared to a static dynamic response (Chapter 5); here, we now include demand, storage, and routing components for assessment of long-term supply and vulnerability to delivery shortages throughout the Colorado River Basin.

Vulnerability is defined here as the probability that supply will not be sufficient to meet the required demand [6,46–48], or $P[Supply \leq Demand]$. This assumes that demands are not adapting to shortages - in this case, demand estimates showing vulnerability provide an indication of where adaptation will likely be required.

Similar to previous studies [106], the Gila River Basin was not included in the detailed demand analysis, although diversions into this basin were still included in the modeling efforts. The Gila River basin does not include a sufficient record of naturalized yield for model calibration, and thus analysis of the supply vulnerability is unreliable. The lower reaches of the Gila River are generally

completely dry, thus any potential supply to downstream reaches to help meet required deliveries to Mexico are negligible and completely ignored in this analysis.

6.2 Approach

The VIC-VEO is a spatially distributed hydrologic model that includes a dynamic parameterization model based on optimality theories and space-for-time climatic regression models. It accounts for many detailed processes of the hydrologic cycle including both energy and water fluxes. For the purposes of this analysis, we are interested in the spatially distributed yield in the form of direct runoff and baseflow. Refer to Appendix D.3 for additional details of VIC-VEO development and model specification details.

Spatially distributed hydrologic modeling was completed on a 1/8th decimal degree scale (cell length of approximately 11km), where each cell allows sub-grid heterogeneity of vegetation classes and elevation bands. Calculations were performed at a three-hour timestep, with output at an aggregated daily level. The VIC-VEO models were run from January 1985 through December 2099.

Total yield output (mm) was then routed through each subcatchment cell and aggregated for each of 41 different subcatchments, resulting in a set of daily discharge hydrographs. Subcatchments were specified at the level of HUC4 or finer, possibly including subcatchment breaks at significant reservoirs or gaging stations, as appropriate. As a spatially distributed model, contribution from each cell was fractioned by the drainage area located in the given subcatchment, which is critical along watershed boundaries. This implies that each subcatchment has a unique flow direction grid, as grid cells that share a fraction of area are required to drain in separate directions. All processing was completed using ESRI ArcMap and Python/ArcPy scripting.

Once hydrographs for each subcatchment were calculated for each GCM-RCP scenario (fourteen scenarios in total), the data were aggregated into a monthly series of yield volumes, which were imported into the WEAP model for routing. The WEAP model routes flows through the stream network and accounts for consumptive demand withdrawals, trans-basin diversions, and reservoir storage and allocation. It also uses a priority scheme to determine how flows (and possibly deficits) should be allocated between competing demands. Filling of reservoir storage is lowest on the

priority list, compared to meeting required demands. In addition to demand requirements, the WEAP model includes minimum in-stream flow requirements (highest priority) which were set as 10% of the annual streamflow uniformly distributed through the year [6, 46–48].

Model results include monthly reservoir storage volumes, unmet demand volumes, unmet in-stream flow requirements, unmet trans-basin diversions, and monthly streamflow volumes, for each of the GCM-RCP scenarios. These model results were then used to determine the vulnerability by calculating the probability that demand is greater than supply.

6.2.1 WEAP Model Development

A watershed operations model was used to characterize the interaction of supply and demand, dependent on reservoir operations and trans-basin diversions, to estimate potential shortages throughout the Colorado River Basin. The routing model utilized for this study was the *Water Evaluation and Planning System* (WEAP)[17]. This system allows the specification of temporally changing demands, reservoir-storage operations and allocations, and prioritization of water allocations and rights. Further, it allows easy assessment of different climate scenarios for each GCM and RCP.

A schematic of the WEAP model layout for the Colorado River Basin is shown in Figure 6.1, which shows the major HUC4 delineations (red lines), finer resolution subdivisions of HUC4 basins creating 41 subcatchments (gray lines), river segments (blue lines), demand sites (red circles), and trans-basin diversions (green and orange lines).

For the climate projection scenarios, the WEAP model was run at a monthly timestep from 1985 through 2099, matching the available period of demand data. This was repeated for seven GCMs, each with two RCPs, resulting in 14 different model scenarios. The WEAP geometry was specified as 'current' conditions with respect to reservoirs and trans-basin diversions; new reservoirs or diversion projects, changing priorities, or removal of existing projects was not analyzed over the modeled period.

As a result of the WEAP model, each scenario produced monthly deficits for demand at each HUC4, in addition to the projected reservoir volumes over time.

[17] `www.weap21.org`

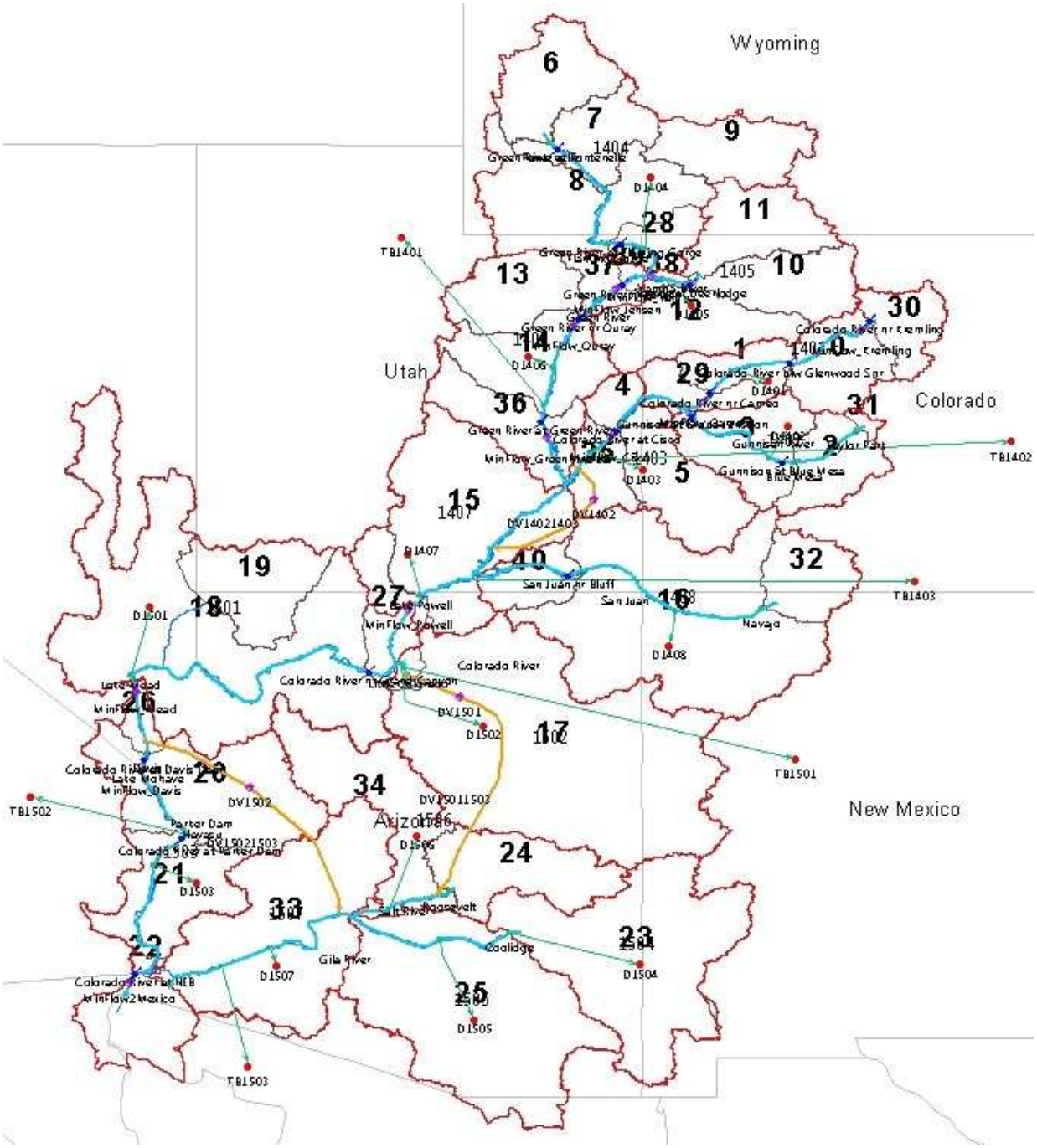

Figure 6.1: Schematic of WEAP Model Layout - Red basins are HUC4 delineations labeled with 4-digit codes, gray lines are divisions of HUC4 into subcatchments (41 in total) labled with bold face up to 2-digits [0-40]. Blue lines are major connecting rivers, green lines are trans-basin diversion connections, yellow lines are intra-basin diversions, red dots are HUC4 consumptive demand sites. Outlines of the State boundaries are included for clarity.

6.2.2 Climate Projections

The vulnerability study was completed by assessing hydrologic response to future projections of climate from down-scaled CMIP5 model projections [18]. This dataset was downscaled to the 1/8th degree scale spatially, and as daily data temporally [19]. Downscaled data provided daily values of minimum and maximum temperature, along with daily total precipitation amounts. A fourth climate parameter, daily wind, was developed separately from downscaled estimates of monthly GCM wind values.

Seven different GCM models were evaluated for this study,

BCC Beijing Climate Center

CAN Canadian Centre for Climate Modelling and Analysis

CSIRO Commonwealth Scientific and Industrial Research Organisation, Australia

GFDL Geophysical Fluid Dynamics Laboratory

IPSL Institut Pierre-Simon Laplace

MIROC Atmosphere and Ocean Research Institute (The University of Tokyo), National Institute for Environmental Studies, and Japan Agency for Marine-Earth Science and Technology

MPI Max Planck Institute for Meteorology

For each of the GCMs, two emission profiles were considered (RCP 4.5 and RCP 8.5), resulting in fourteen unique projection scenarios. Data for each scenario was extracted from the NetCDF file system into individual 1/8th degree text files, which are read by VIC-VEO at runtime.

6.2.3 Demand Analysis

The *demand* is the required consumptive (non-return) flow for all uses distributed throughout the Colorado River Basin. These uses include: domestic and public, industrial and commercial, thermoelectric, agricultural irrigation, and livestock and aquaculture [16, 46, 47]. For the Colorado

[18] `http://gdo-dcp.ucllnl.org/downscaled_cmip_projections/dcpInterface.html`
[19] `http://gdo-dcp.ucllnl.org/downscaled_cmip_projections/dcpInterface.html`

River Basin, two different types of Demands are considered - this includes the HUC level within-basin consumptive use, in addition to trans-basin diversions out of the basin.

Consumptive Demands Demands were generously provided by Thomas C. Brown of the U.S. Forest Service using historic 5-year consumptive use data in conjunction with climate projection data to determine projected monthly demand to year 2100 [unpublished] following previously established methodologies [16]. This monthly demand data is used 'as-is' within the WEAP modeling framework.

Monthly data was provided from January 1985 to December 2099, on the HUC4 spatial scale, for a range of CMIP5 GCM projections. For this analysis, we utilized the Representative Concentration Profile (RCP) 4.5 and 8.5, for seven GCM models (BCC, CAN, CSIRO, GFDL, IPSL, MPI, MIROC), resulting in fourteen unique supply-demand scenarios.

As an example, Figure 6.2 shows the projected annual demand by HUC4 in the Colorado River basin as a stacked plot. Simply looking at the annual total clearly indicates a steady trend in overall total demand increases through the century, where some basins are accounting for most of the increased demand, compared to others with minimal projected change. A similar trend of increased projected demand can be seen in all of the other projected demand scenarios.

The total annual demand volumes for each HUC4 are changing over time, but a static fraction of the annual total is used to downscale this demand to a monthly scale. Figure 6.3 shows the repeating pattern of fractional allocations by month. This pattern is fixed for all years, and is identical for each of the GCM-RCP scenarios.

Trans-Basin Diversions In addition to within-basin consumptive demands, various agreements have been made to divert water outside of the Colorado River basin, referred to as *trans-basin diversions*. Although the demand beyond the basin may change, we assumed the agreements remain constant over the coming century and the specified fixed volume of water is diverted annually to meet these agreements. Further, it is assumed that trans-basin diversions have priority over internal basin consumptive demands.

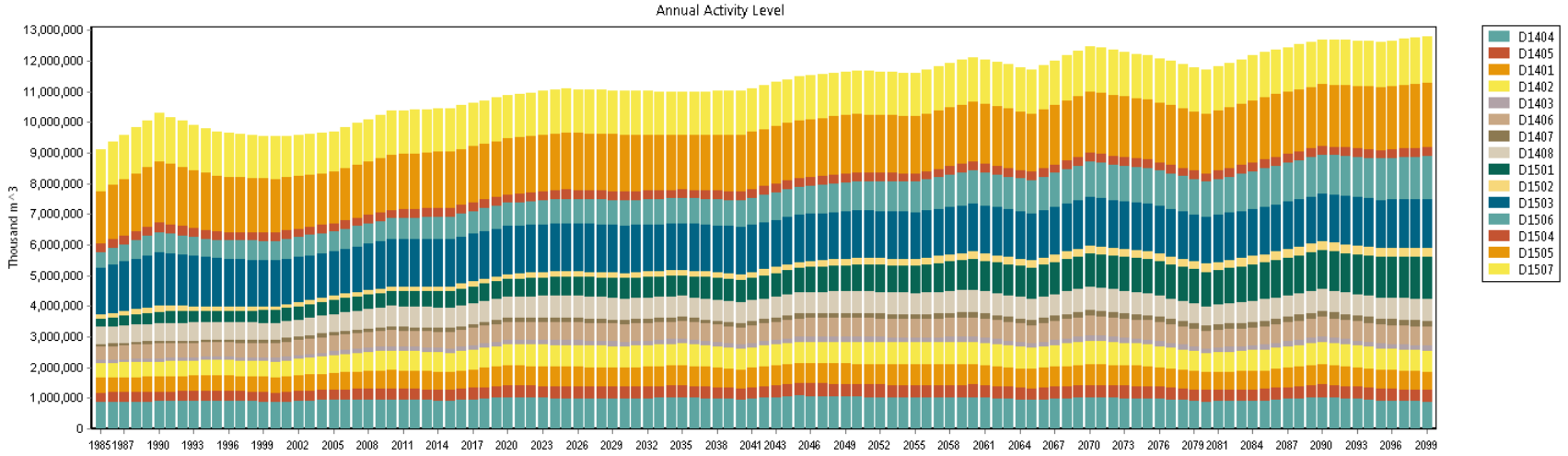

Figure 6.2: Annual Demand Volumes by HUC (BCC45) - Consumptive In-Basin demands; Trans-Basin demands included separately.

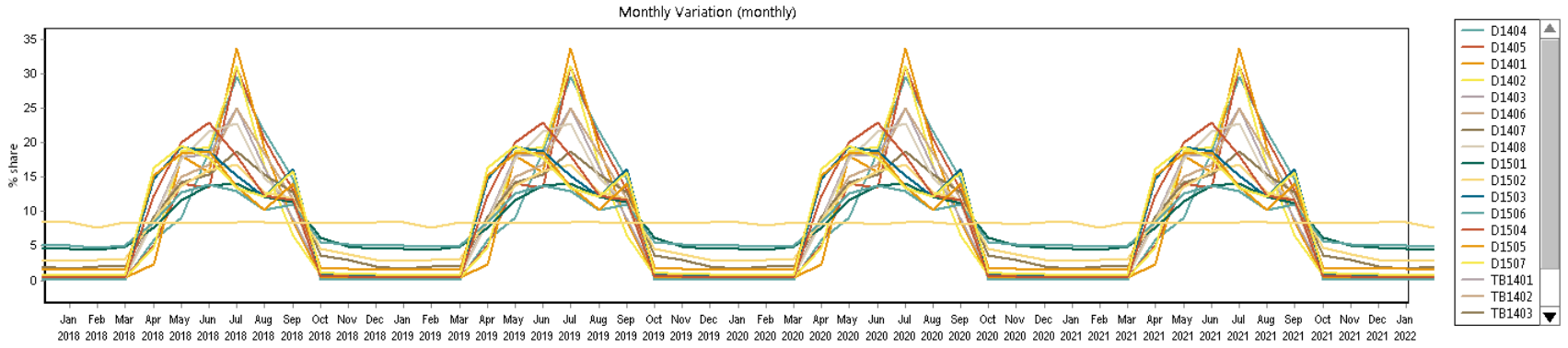

Figure 6.3: Monthly Fractional Allocation of Annual Demand

Diversions outside of the continental Colorado River basin are shown in Table 6.1. These are annual volumes which are then divided into a monthly temporal demand based on a fixed monthly fraction pattern.

Table 6.1: Annual Trans-Basin Diversions - Assessment Sub-Region (ASR) from original demand study, whereas HUC is a smaller scale downstream basin within the ASR where demand is withdrawn.

ASR	HUC	Diversion (m^3 10^{-3})
1401	1406	108,395
1402	1403	619,268
1403	1407	115,301
1502	1503	7,328,310
1503	1507	154,091

In addition to consumptive diversions beyond the Colorado River basin watershed, internal diversions are included between HUC4s (Table 6.2).

Table 6.2: Annual Intra-Basin Diversions - Required annual supply between HUC4s that remains within the Colorado River Basin.

From HUC	To HUC	Diversion (m^3 10^{-3})
1502	1506	10,928
1503	1507	2,352,152

6.2.4 VIC-VEO Model Development and Calibration

The VIC-VEO model was setup to run 41 subcatchments defining the Colorado River Basin. Subbasins and the stream network topology are used to develop hydrographs at a number of locations through the watershed. A simplified stream routing network was used with zero-lag; the temporal scale of interest for the vulnerability and demand analysis is one-month, thus detailed routing methods were deemed not necessary.

Spatially distributed meteorologic forcing data (precipitation, daily minimum and daily maximum temperatures) for model calibration were obtained from a reanalysis dataset[20] of Maurer [34]. Daily forcing data is at the 1/8th degree spatial scale, and extends from January 1949 to July of 2000. It is the best representation of the historic spatially distributed daily meteorology across the Colorado River Basin.

[20] `http://www.hydro.washington.edu/Lettenmaier/Data/gridded/index_maurer.html`

Calibration of the hydrologic model also requires observations of historic yield, which is used to guide adjustment of model parameters. However, the Colorado River Basin is a highly regulated region including multiple trans-basin diversions, storages, irrigation and diversion projects, and other consumptive uses. As such, unless all of these processes are correctly accounted for, utilization of observed streamflow from USGS gages will result in an incorrect calibration of the hydrologic process. Instead, the USBR has prepared *naturalized flows*, or a reanalysis of flows that would have occurred without excessive within-basin regulation.

Naturalized flow data[21] of monthly flow volumes at various locations are available throughout the Colorado River Basin. For calibration and verification of the VIC-VEO hydrologic model, this dataset removes the need to account for reservoir operations, transbasin diversions, or other consumptive uses when evaluating hydrographs of yield. Records of naturalized flow are henceforth referred to as 'observations'.

The VIC-VEO model was run on a 1/8th decimal degree spatially distributed grid across the Colorado River basin. Hydrographs of yield represent an aggregation of the yield (as runoff and baseflow) from the accumulating cells upstream. For 41 different subcatchments, watershed boundaries cross these 1/8th degree grids resulting in fractional yields by area. Therefore, each of the subcatchments was routed separately with a unique grid defining the fraction of contributing area, in addition to a unique flow direction raster. With those components, the VIC *rout* model was then used, which is a kinematic wave routing model, resulting in individual subcatchment hydrographs. These hydrographs were then further routed through the river network model (WEAP) allowing development of aggregated hydrographs throughout the Colorado River Basin. Hydrographs were then compared to the observed record during the calibration process.

The model was calibrated in an 'upstream-to-downstream' manner, thus reducing compensatory calibration in lower mainstem reaches. Figure 6.4 shows the monthly values of calculated and observed yield at sixteen locations throughout the Colorado River Basin. These locations represent a range of locations, including headwater basins, lower Colorado River reaches, and arid subcatchments, such as the Little Colorado River.

[21] `http://www.usbr.gov/lc/region/g4000/NaturalFlow/`

In general, the model represents the seasonal patterns well with magnitudes of peak streamflow and inter-annual variation of wet and dry years. As a vulnerability analysis, we are interested particularly in the volumes of yield, especially at the annual scale.

Figure 6.5 shows the aggregated annual yield volume compared to observations for each of the sixteen observation locations. Here, it is easier to discern model fitness, replicating the inter-annual variation in yield fairly well over the historic record of naturalized flows.

The Nash-Sutcliffe measure of efficiency quantifies model fitness, and is summarized at both the monthly and annual hydrograph level in Table 6.3. In general, the model performs quite well in representing both temporal scales.

The exception is the Little Colorado River, a highly ephemeral river along the lower reaches, which is difficult to replicate with the given spatially distributed model and routing approach. Although Nash-Sutcliffe values are near zero for the Little Colorado River, this does not represent a completely random process, but still indicates some degree of model fitness (Nash-Sutcliffe values $<< 0$ are possible). Considering the limited contributing volumes from the Little Colorado River subcatchment, the low Nash-Sutcliffe values for that specific gage are not concerning.

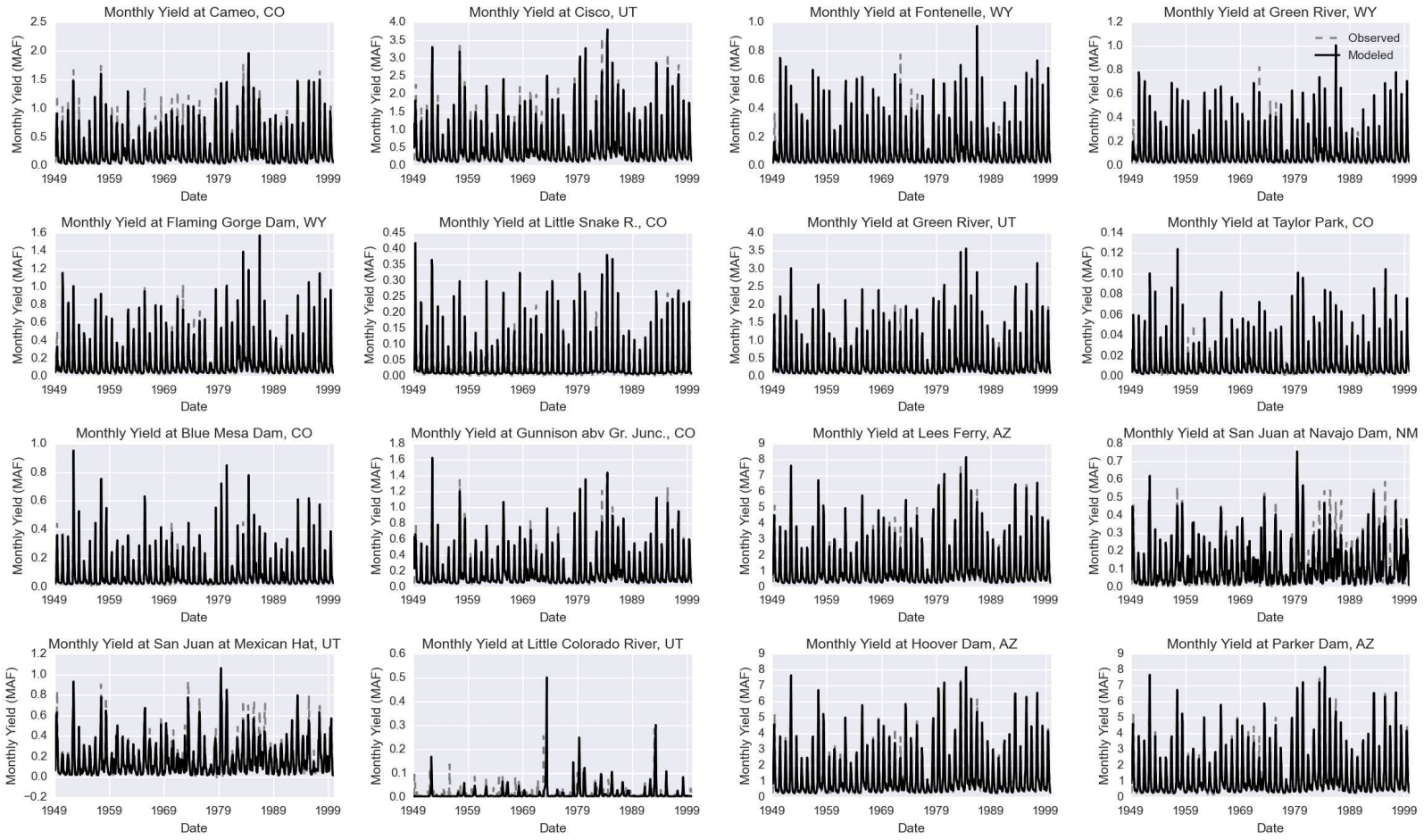

Figure 6.4: Comparison of Calibrated and Observed Monthly Yield

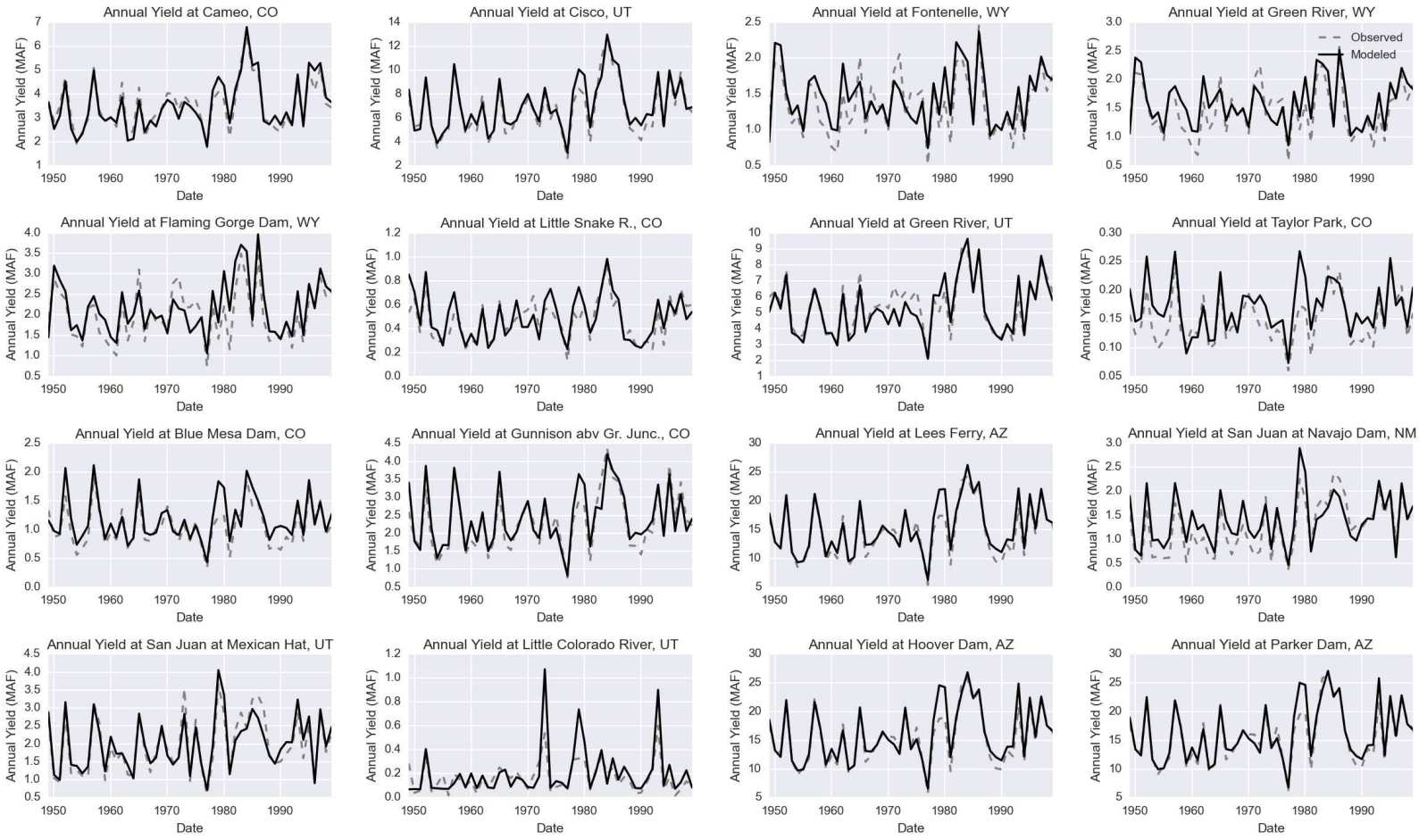

Figure 6.5: Comparison of Calibrated and Observed Annual Yield

Table 6.3: Monthly and Annual Nash-Sutcliffe Measures of Efficiency - All Nash-Sutcliffe efficiencies based on natural flows, even if the location is listed as below a dam; this is merely for reference of locations. No storage routing or diversion models were used in calculating natural yield.

Site	Monthly NS	Annual NS
Fontenelle Dam, WY	0.771571	0.648332
Green River, WY	0.767528	0.654389
Flaming Gorge Dam, WY	0.706326	0.620407
Colo.Riv. at Cameo, CO	0.756447	0.882783
Colo.Riv. at Cisco, UT	0.880417	0.903717
Green River, UT	0.835144	0.843421
Lees Ferry, AZ	0.909699	0.889583
Hoover Dam, AZ	0.89752	0.884937
Parker Dam, AZ	0.898596	0.899146
Taylor Park Dam, CO	0.541275	0.456001
Blue Mesa Dam, CO	0.70341	0.637858
Little Snake Riv., CO	0.563994	0.626993
San Juan Riv. at Navajo	0.771209	0.672496
San Juan Riv. at Mexican Hat	0.826078	0.873046
Gunnison Riv. at Grand Junction, CO	0.856683	0.828705
Little Colorado River	-0.0316123	0.0157677

6.3 Vulnerability Analysis Results

The vulnerability analysis is used to provide insight into the probability of insufficient supply to meet demand, but additional useful diagnostics of the system health and response are available. We start this section by looking at several different datasets developed during the process of assessing vulnerability.

Forcing data are used with the TBM (VIC-VEO) to estimate the hydrologic yield by subcatchment. Here, we review temporal (using bi-decadal blocks and four seasonal periods per year) and spatial variation (HUC4 level) of the hydrologic response using histograms of the yield. This process allows insight into where yield is changing the greatest, and how it may be shifting with seasons over the next century.

Various reservoirs are included as part of the routing model (WEAP) to allow for storage and allocation of flows used to meet demand. We look at several major reservoirs in the Colorado River Basin, and find the probability of complete storage loss due to excessive demand and insufficient supply.

Finally, the routing model provides an indication of the number and location of shortages throughout the Colorado River Basin. These results allow an estimate of the probability of shortage, otherwise referred to as the vulnerability. Again, this vulnerability is further evaluated in time using 20-year temporal blocks, and spatially at the HUC4 level, for each of the GCM and RCP scenarios.

6.3.1 Estimate PDFs of Climate Forcing

Each of the GCM and RCP scenarios has a unique set of downscaled meteorologic forcings including daily precipitation, minimum daily temperature, maximum daily temperature, and daily average wind speed. Of interest is how these meteorologic forcings change between GCMs, RCPs, and also over time.

To help visualize this data, histograms of daily precipitation, minimum, and maximum temperature were prepared for each RCP and GCM. Further, the data were divided into 3-month blocks to indicate seasonal meteorologic properties, in addition to 20-year temporal blocks to indicate how these probability distributions are changing over climatic scales. Finally, meteorology and climate vary spatially, thus data was area-weighted for each of the 41 subcatchments through the Colorado River Basin. As a result, over 1100 plots of this climatic forcing PDFs have been prepared (41 subcatchments * 4 seasons * 7 GCMs = 1148 figures).

A sample figure is shown in Figure 6.6 for the IPSL GCM, Subcathment 00 (near Glenwood Springs, CO), and the second seasonal block (Jul-Sep). The probability density function of precipitation is shown with a log-scale to help illustrate differences between bi-decadal blocks. Although the precipitation data exhibit some differences between bi-decadal periods, there do not appear to be any significant differences except for a slight increase in extreme precipitation towards the end of the century. Note, this statement only applies to the IPSL scenario shown here, and is not a global statement for all GCMs; review of each subcatchment and GCM would be required to develop more generalized conclusions. The temperature densities show a more consistent response between GCMs.

Most apparent is a clear and consistent shift of the histogram from lower to warmer temperatures through the rest of the century. This conclusion applies to both the RCP 4.5 and RCP 8.5 emission scenarios, and also applies globally to varying degrees for all other evaluated GCMs and seasonal blocks.

Comparison of different histograms is possible (e.g. same models and differenty seasons, or same season but different models), but it is difficult to quickly visualize differences and the spatio-temporal variation of climatic forcings. Rather than evaluating the entire set of available histograms, we can summarize the difference in means for monthly values between the periods of 2000-2020 and 2080-2100 for each GCM, RCP and subcatchment. For example, the mean daily minimum October temperature difference between the first and last bi-decadal blocks can be found for each subbasin, GCM, and RCP, and then plotted spatially.

This summarizing process was completed for mean monthly daily maximum and daily minimum temperatures, and mean monthly daily precipitation, for both RCP 4.5 and RCP 8.5 as seen in Figures 6.7 - 6.12.

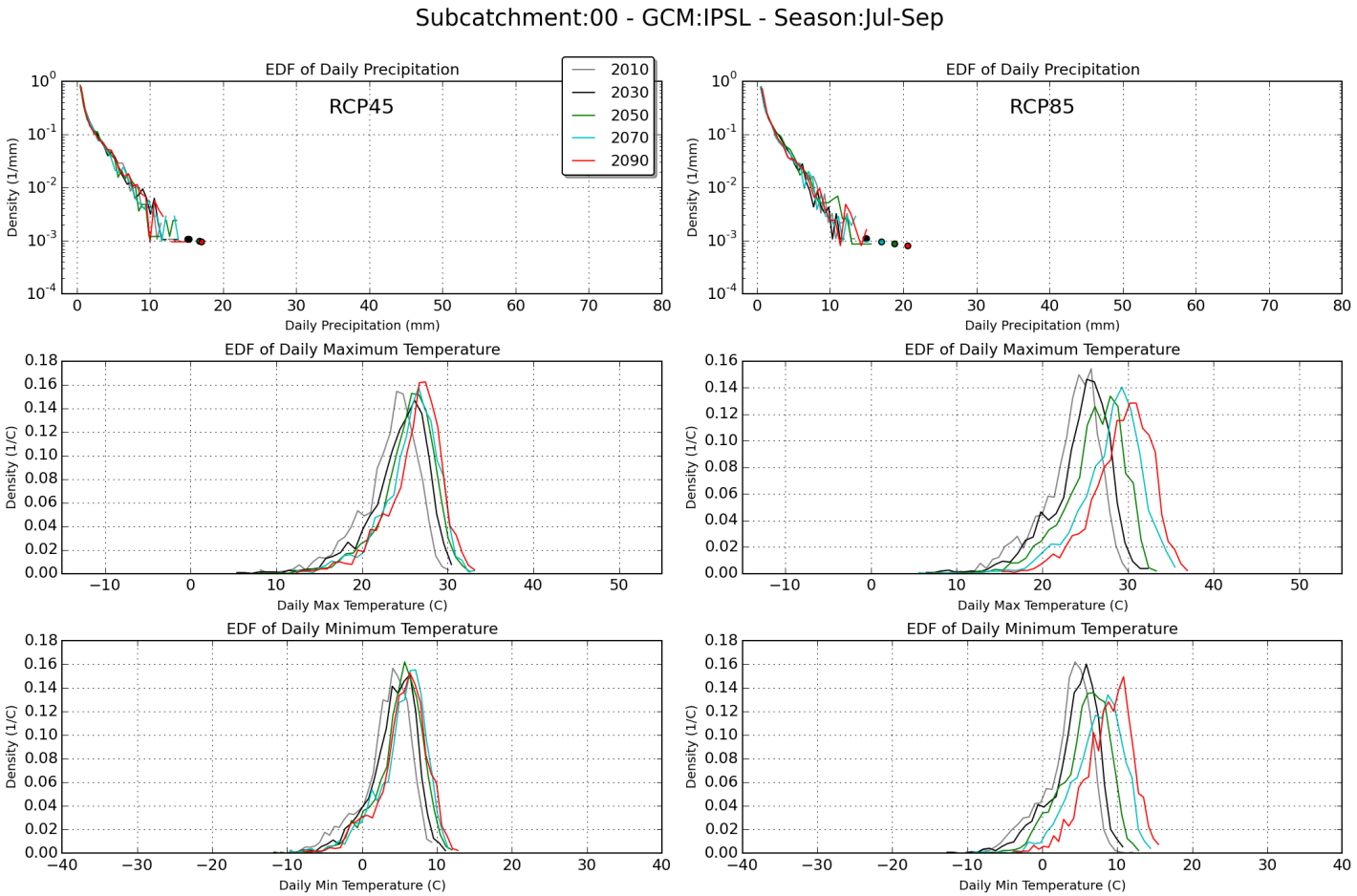

Figure 6.6: Sample PDF of Climatic Forcings - Forcings include Daily Precipitation Total (mm), Daily Maximum Temperature (C), and Daily Minimum Temperature (C). Data series for each forcing are divided into 20-year bins from 2000-2099, with the *center* year shown in the legend. RCP45 in left column, RCP85 in right column.

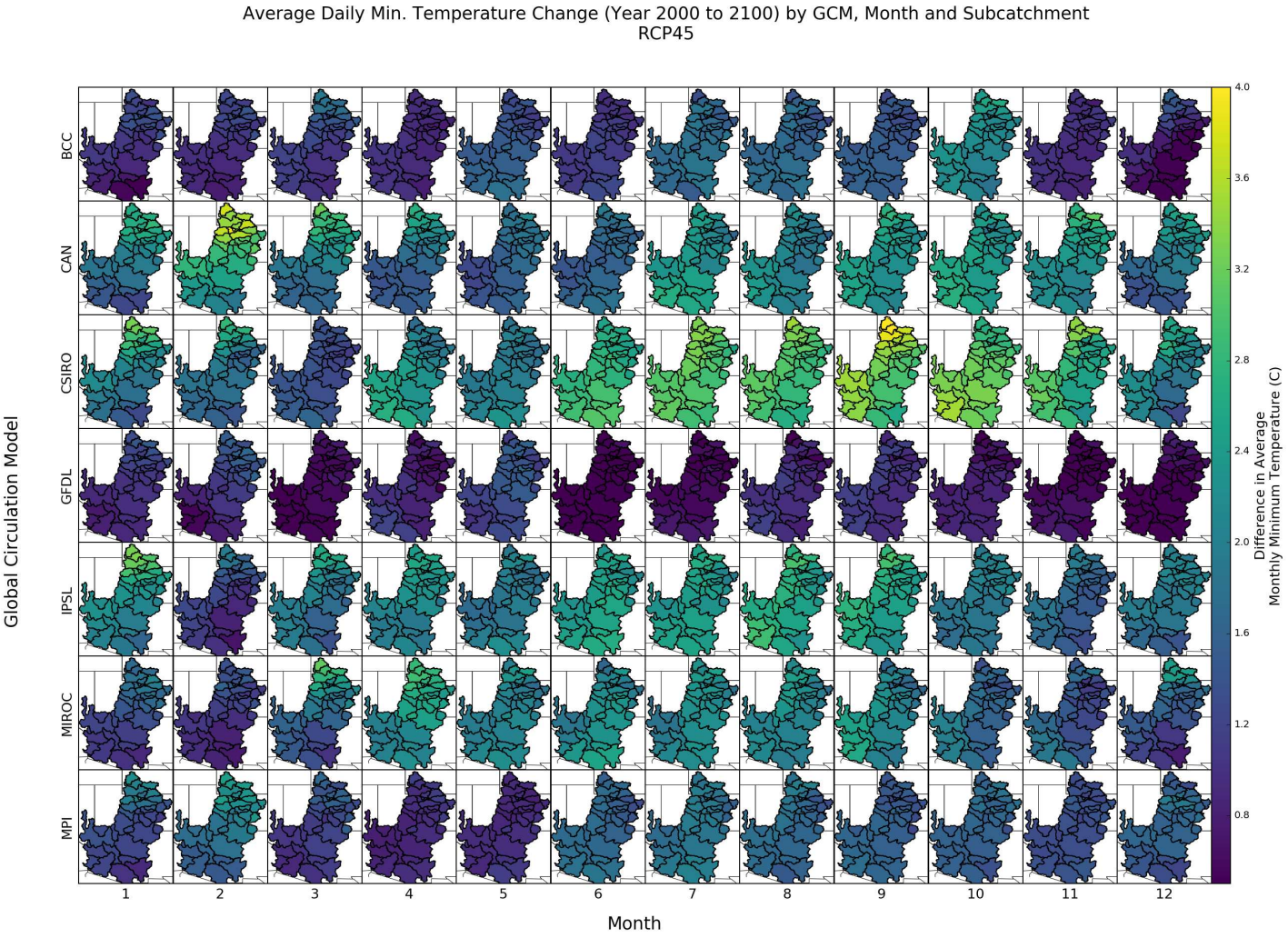

Figure 6.7: Bi-Decadal Difference in Mean Daily Minimum Temperature by Month (RCP 4.5)

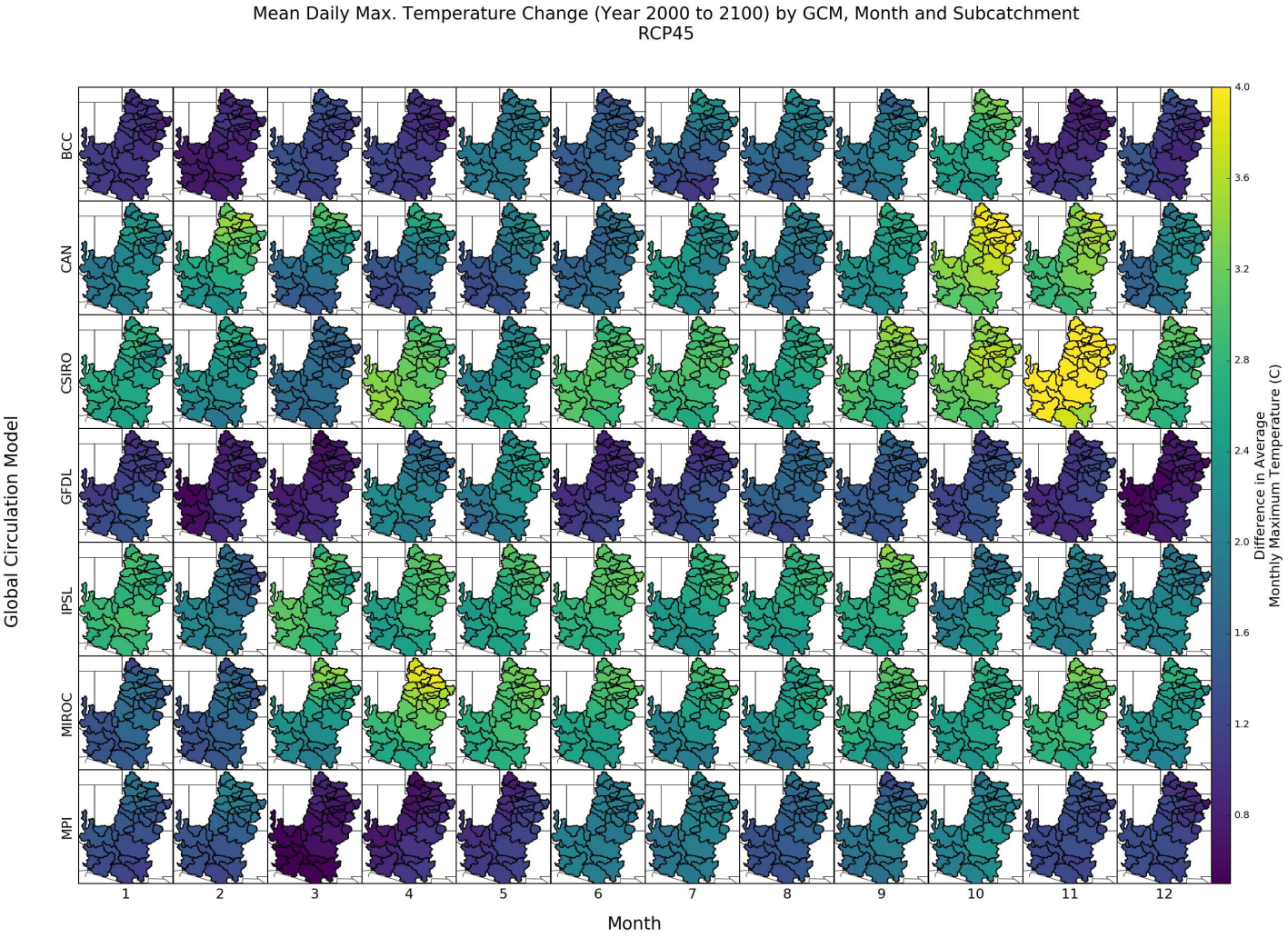

Figure 6.8: Bi-Decadal Difference in Mean Daily Maximum Temperature by Month (RCP 4.5)

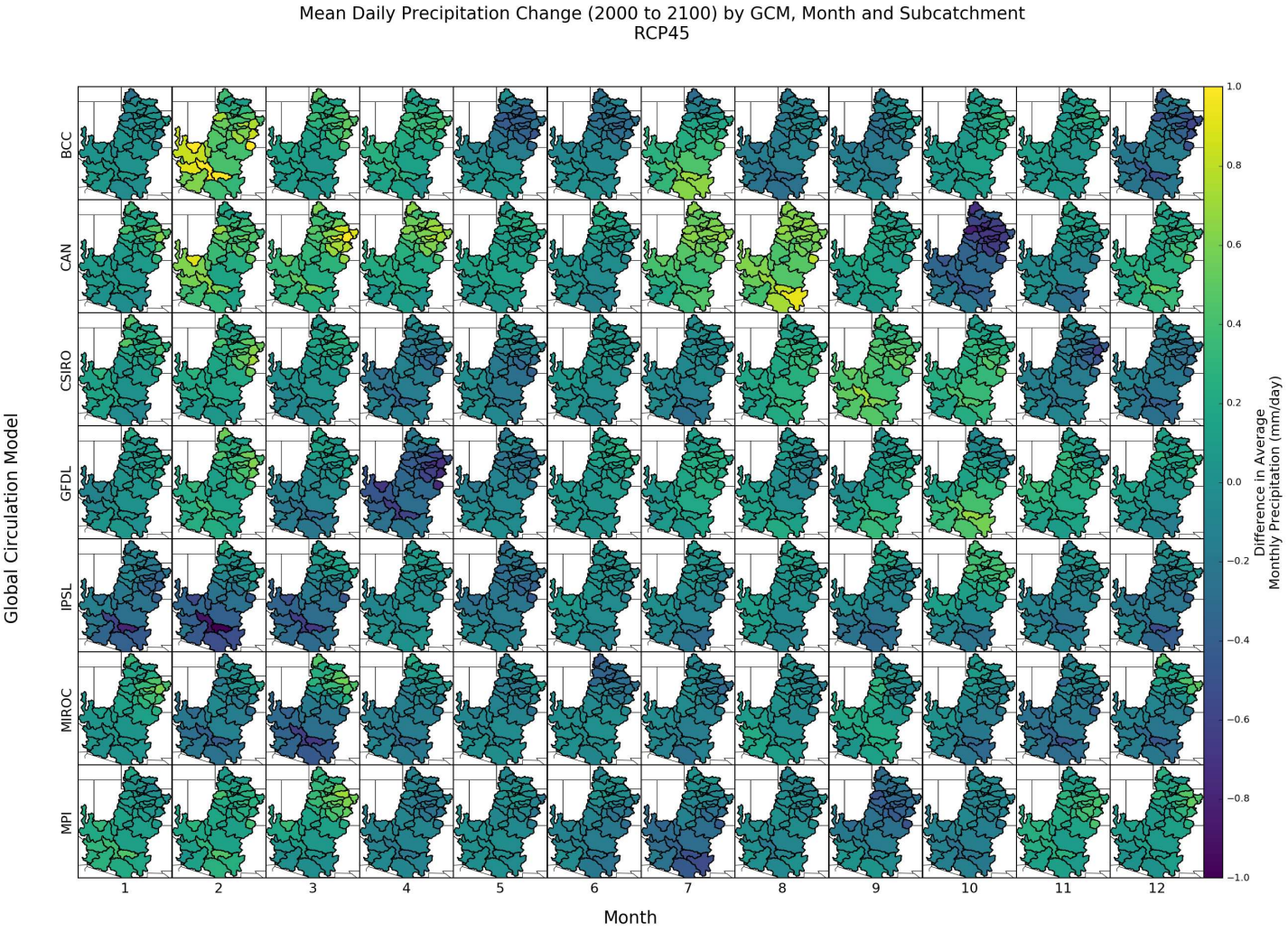

Figure 6.9: Bi-Decadal Difference in Mean Daily Precipitation by Month (RCP 4.5)

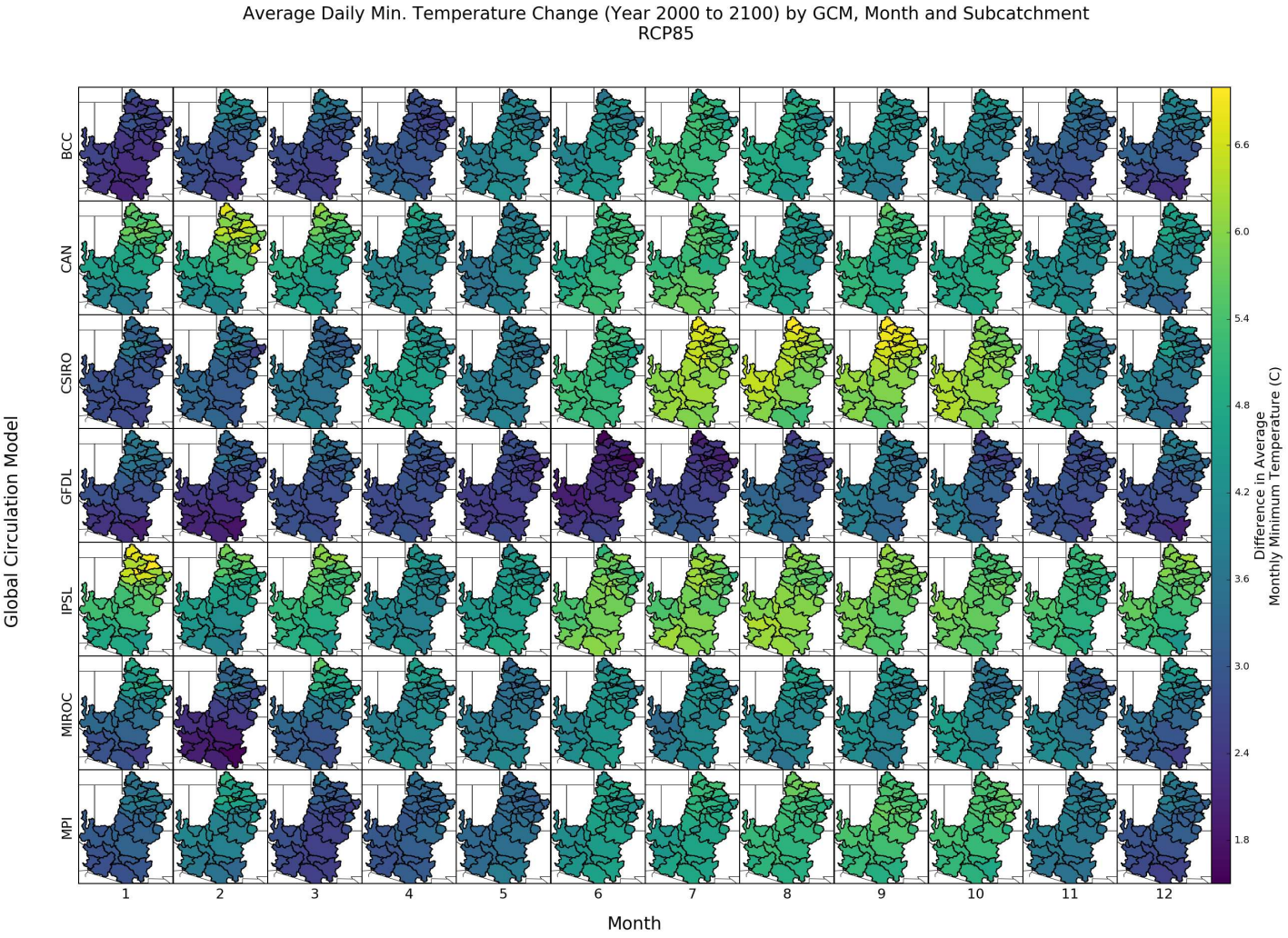

Figure 6.10: Bi-Decadal Difference in Mean Daily Minimum Temperature by Month (RCP 8.5)

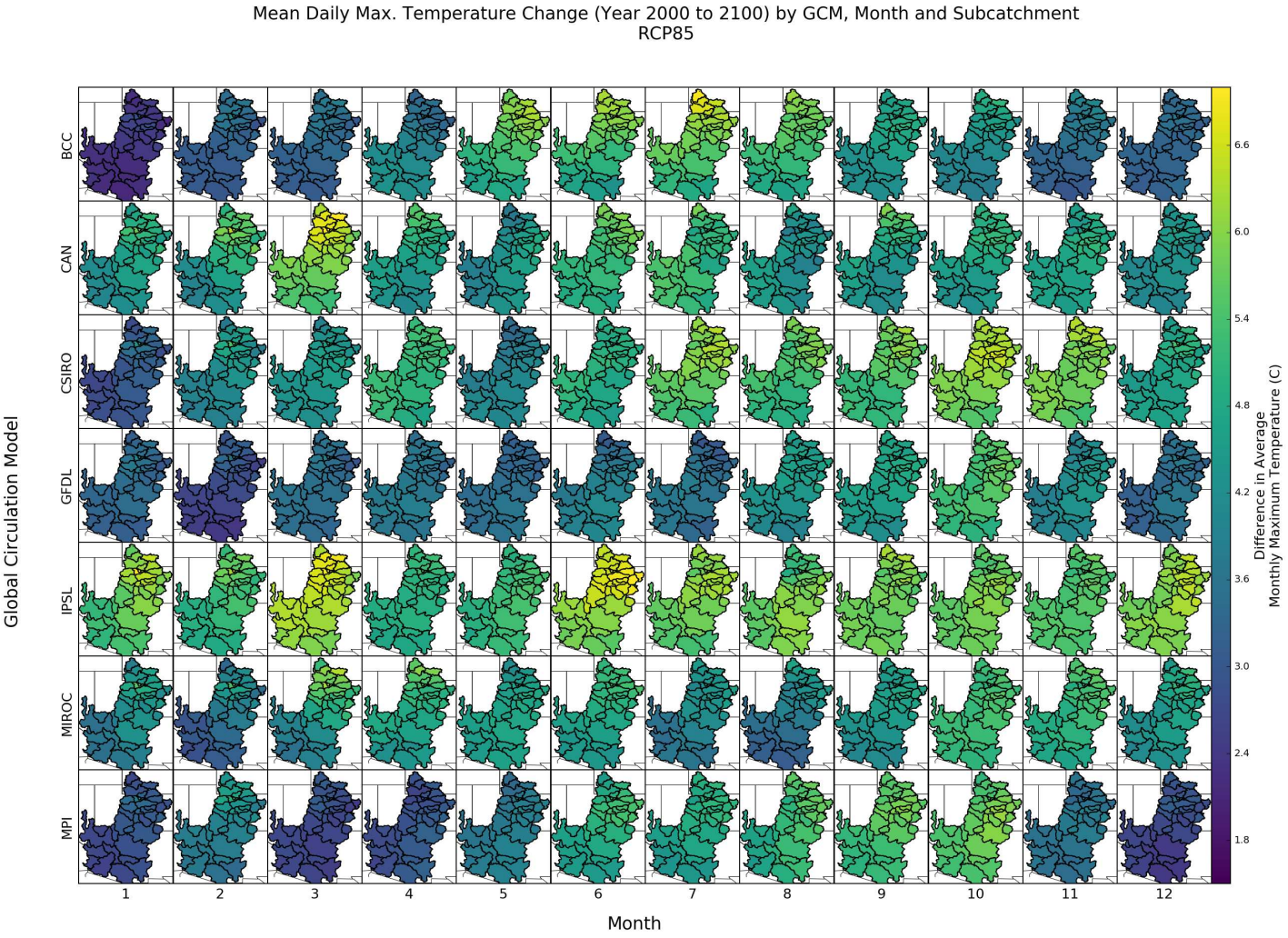

Figure 6.11: Bi-Decadal Difference in Mean Daily Maximum Temperature by Month (RCP 8.5)

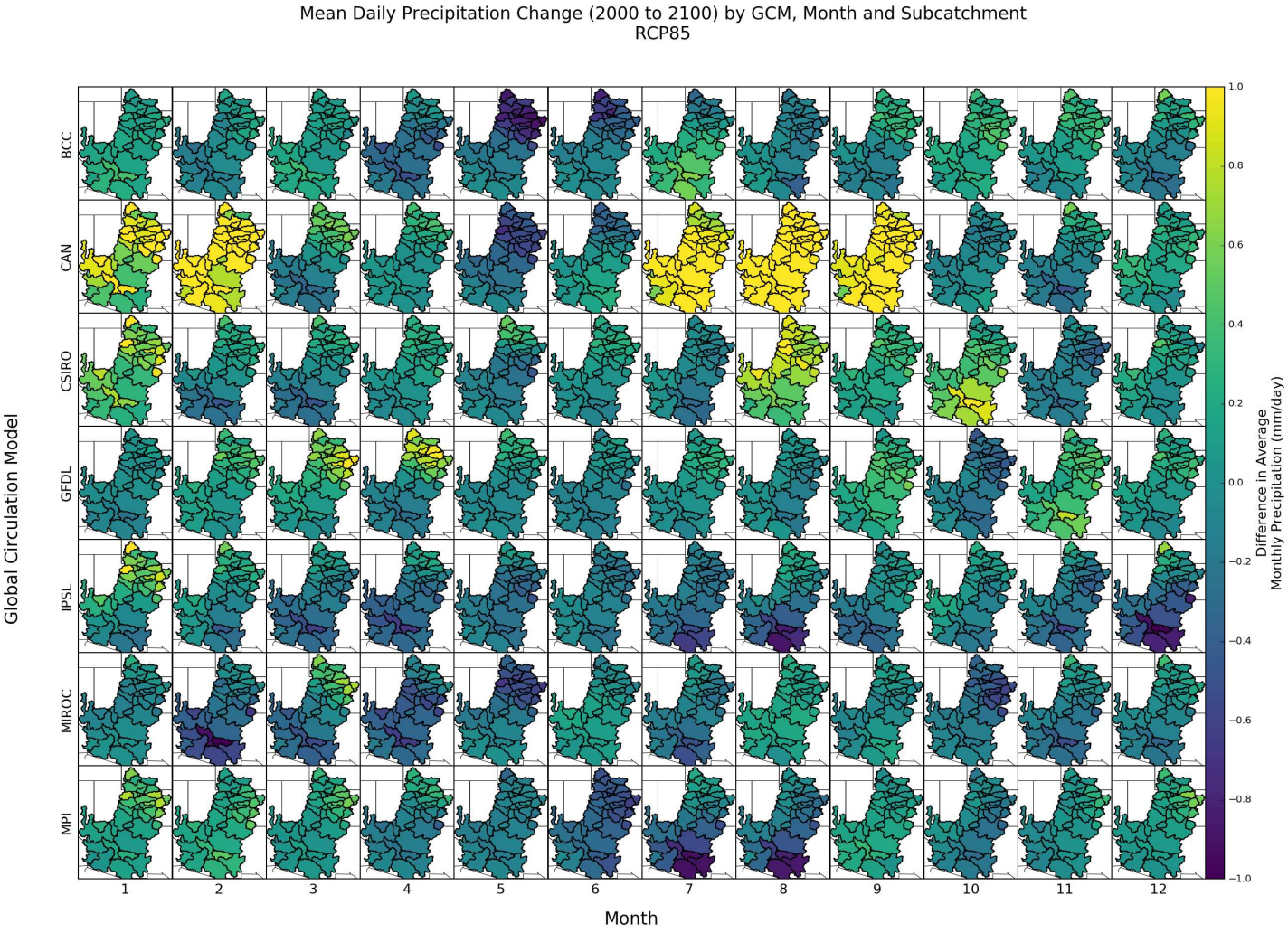

Figure 6.12: Bi-Decadal Difference in Mean Daily Precipitation by Month (RCP 8.5)

Note, the scales obviously vary between parameters, but less obviously, scales vary between RCP emission scenarios. For example, temperature increases for RCP 8.5 are significantly greater than RCP 4.5, and thus the range of the scales were adjusted for clarity.

These spatio-temporal figures show interesting variations in the seasonal and spatial responses between GCMs. For example, considering Figure 6.7 for mean monthly difference in daily minimum temperature, all models show some degree of warming over the century, but CSIRO shows significant warming from June to October, whereas GFDL shows a more uniform warming for all months. The magnitude of warming is also apparently quite different between CSIRO and GFDL, with CSIRO showing maximum daily temperature increases nearly $3°C$ greater than GFDL.

Spatially, a few of the models show greater increases in seasonal temperatures in the northern subcatchments of the watershed, compared to the southern subcatchments. This is significant - a majority of the water supplied in the Colorado River is sourced from the upper mountainous subcatchments. Simply considering aggregated watershed level changes will under represent the changes predicted in water supply source regions.

Figure 6.8 shows similar patterns for daily maximum temperatures under RCP 4.5, although some seasonal differences are more apparent between GCMs, such as the significant temperature increases occurring during the growing season shoulders in the CAN model. Increases in northern subcatchments compared to southern ones are also quite apparent for the daily maximum temperature differences over the coming century.

The differences in mean daily precipitation for RCP 4.5 shown in Figure 6.9 again displays unique differences in the spatial and temporal variation of monthly precipitation. The CAN model shows clear April increases in precipitation in the northern subbasins, whereas the GFDL and CSIRO models show decreases in precipitation. Although individual comparisons can be made, there is no clear pattern in precipitation changes between each of the GCMs, by months, or spatially.

As we move into the RCP 8.5 figures, the differences over the coming century become more extreme than those observed in the RCP 4.5 emission scenario, although the expected patterns of response for a given GCM are similar between emission scenarios. For temperature increases, it is apparent that the GFDL model shows a lower increase in temperature compared to the IPSL model. Similarly, spatial patterns of greater northern subcatchment increases in temperature compared to the southern reaches are apparent for all/most GCMs.

Figure 6.12 shows precipitation differences for the RCP 8.5 scenario - in this figure, the CAN model shows extreme increases in precipitation compared to other GCMs for January-February and July-September periods.

These figures help to illustrate the spatial and temporal variations across GCM projections and emission scenarios. It also helps to highlight the risks in looking at large- temporal or spatial scale averages. Only considering annual or decadal differences will eliminate significant seasonal differences in climate projections. Similarly, an average of temperatures over the Colorado River basin will obscure significant spatial variations in changes between northern and southern, or between mountainous and flatter regions.

For this review, we considered climatic differences between the first and last bi-decadal block of the century, rather than difference between each incremental decadal block. Although this is a reasonable approach for RCP 8.5, in some cases, RCP 4.5 has increased differences in mean climate response toward the middle of the century. In this case, differences between the first and last bi-decadal block may under-estimate the maximum expected difference in climate over the coming century.

6.3.2 Predict PDFs of Hydrologic Yield

Projected meteorologic forcings from the GCM and RCP models are used with VIC-VEO to determine the expected spatially distributed yield. These values are aggregated and routed to develop runoff hydrographs to year 2100 for each subcatchment. To help understand how differences in meteorological forcings between GCMs translate to hydrologic yield, density functions of bi-decadal yield for each HUC4 basin divided into four 3-month seasonal blocks have been prepared.

By considering the HUC level, we can begin to understand differences between headwater basins rather than aggregated watershed level responses. This scale also matches the availability of demand data. Seasonal blocks help to differentiate changes in temporal response. In total, this represents 44 figures (11 HUC4s * 4 seasons) - two of those figures are included below for discussion.

Figure 6.13 shows the response histograms for HUC1402 (Gunnison River headwaters) for a seasonal block of April to June, for both RCP scenarios (two columns) and seven GCMs (seven rows). For any given RCP, differences in densities between GCMs are apparent.For example, the

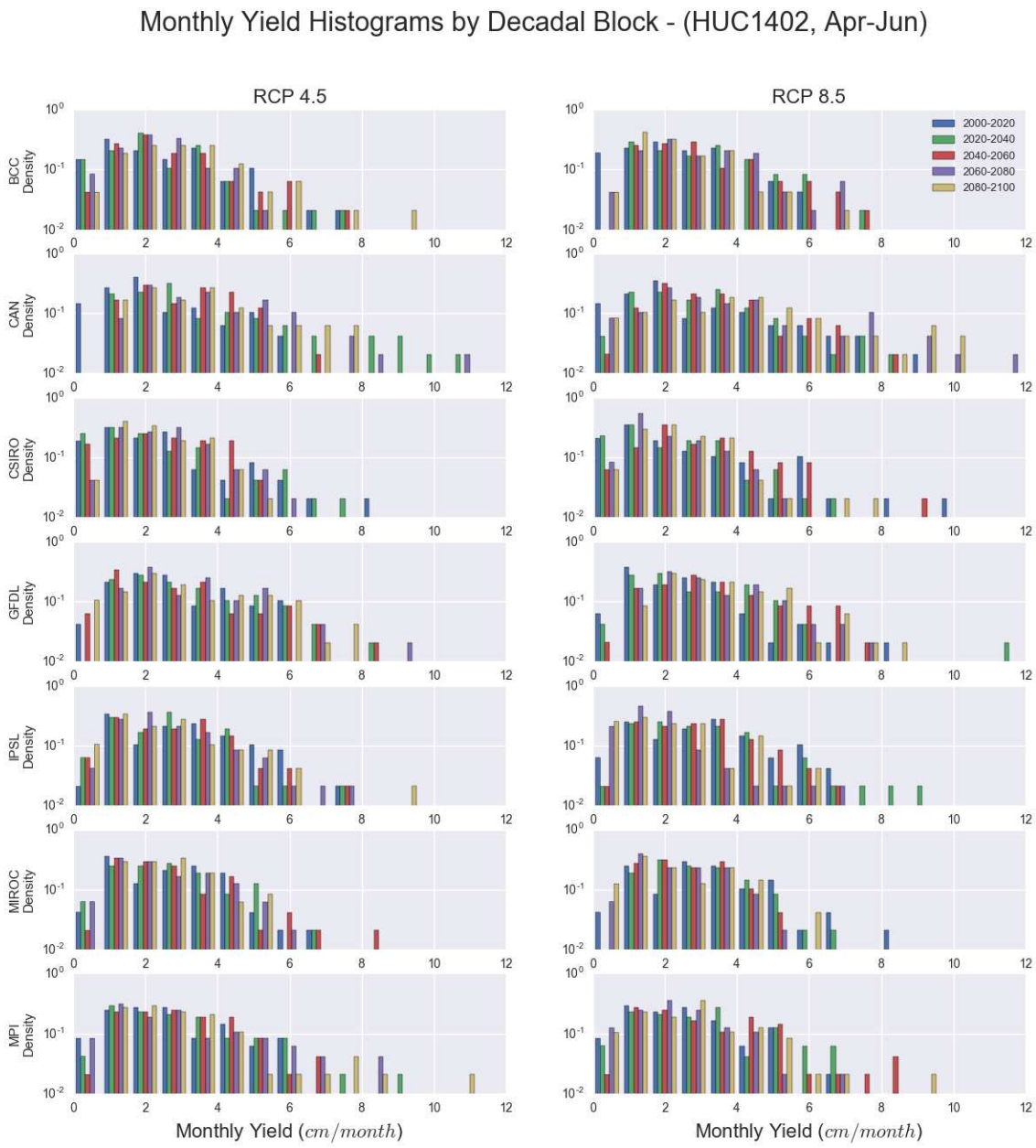

Figure 6.13: Histogram of Monthly Yield by Season (Apr-Jun)

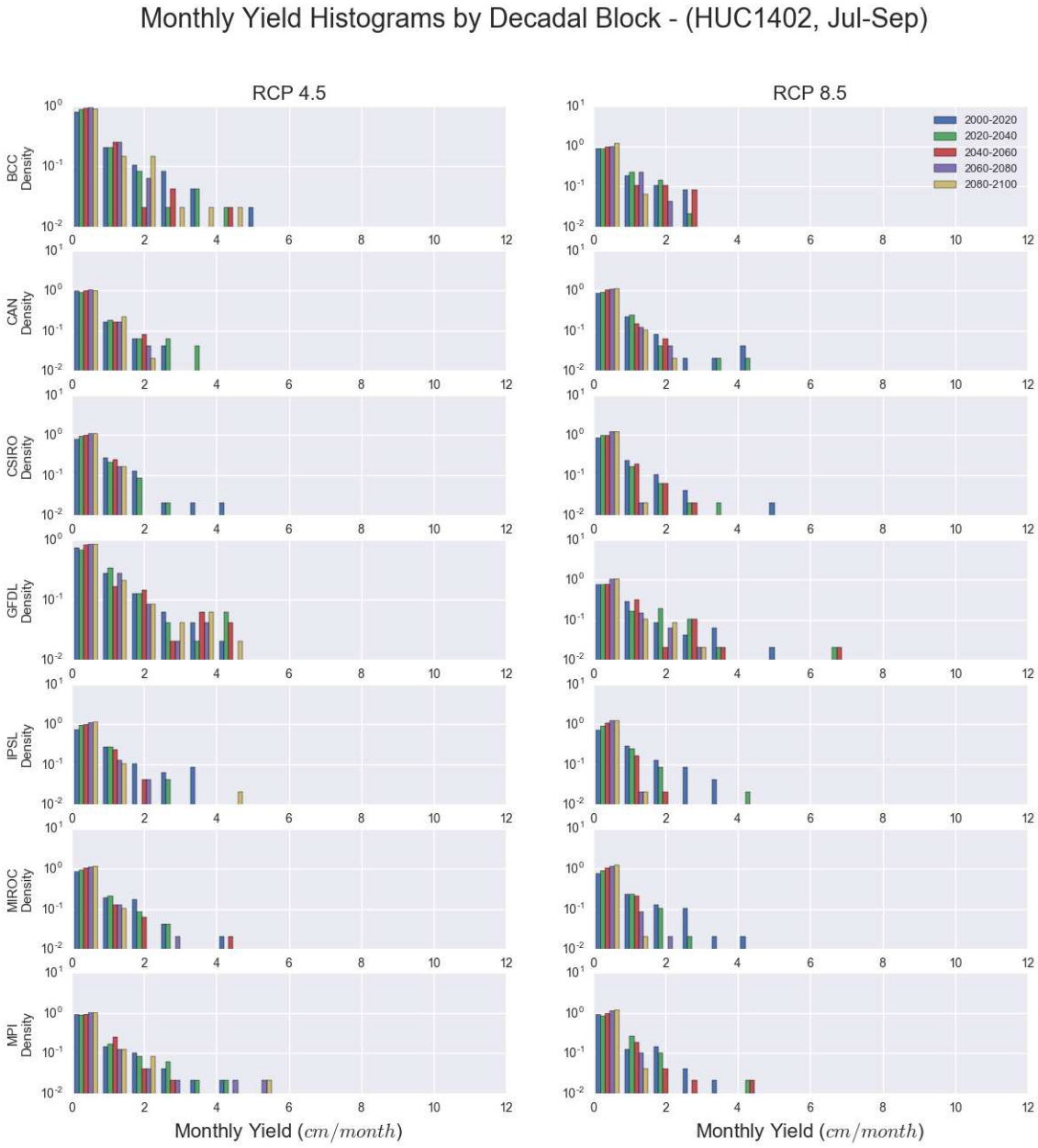

Figure 6.14: Histogram of Monthly Yield by Season (Jul-Sep)

CAN model shows more frequent high monthly yields than other models for both RCP scenarios, whereas the MIROC has fewer extreme runoff events.

Each histogram includes colored bars representing five different bi-decadal periods from 2000-2100, which illustrates how the frequency of a given yield changes over the century. Figure 6.13 shows a fairly consistent increase in higher spring flows, and either marginal change or decrease in the frequency of lower flows. This likely represents increases in spring runoff and loss of snowpack in this headwater basin; warmer temperatures are more likely to produce rainfall compared to snow accumulation, resulting in greater melt and earlier runoff. Evaluation of the next seasonal block helps to support this assertion.

Figure 6.14 shows the following mid- to late-summer seasonal block, July to September, which illustrates a clear and consistent increase in the frequency of low-flow events, and a reduction of higher flow events - the opposite from the previous seasonal period. Towards the end of the century, warmer temperatures are depleting the snow pack earlier in the season, reducing the mid to late-summer yields. Again, this shift is apparent for all GCMs, and even for both RCPs.

6.3.3 Reservoir Storages

Yield for each of the subbasins is used as input for the WEAP water allocation model. The model manages reservoir storage and routing, resulting in a temporal sequence of monthly reservoir storage volumes. Major reservoirs included in this study are Fontenelle, Flaming Gorge, Blue Mesa, Taylor Park, Navajo, Powell and Mead. The WEAP model uses HUC4 level demand data, thus some HUC4 basins include aggregated reservoir volumes (e.g. Fontenelle and Flaming Gorge, or Blue Mesa and Taylor Park).

Plots of the monthly storage volumes for each HUC region are shown in Figure 6.15, where a line represents a trace of a unique GCM and RCP for that HUC. This figure shows significantly varying projections of reservoir volumes, where some GCMs show sufficient supply to meet demand thus avoid emptying the reservoir, whereas others show complete draining of the reservoirs' active storage to meet the required demand. Although individual GCM models perform similarly between RCP scenarios, projections of storage levels between GCMs show little consistency.

For each GCM and RCP, we can tabulate the probability of utilizing all of the active storage by decade (i.e. completely emptying the storage), or

$P[Active\ Storage = 0] \approx (\#\ Months\ Empty)/(Total\#\ Months)$ for each bi-decadal period. These estimates are tabulated for RCP 4.5 and RCP 8.5 in Tables 6.4 and 6.5, respectively.

For the MPI GCM, moving from RCP 4.5 to 8.5 shows a significant increase in the probability of complete storage loss, whereas for other GCMs, such as CSIRO, RCP 4.5 actually shows a higher level of risk over the century for complete storage utilization. Only the CAN GCM shows a chance of utilizing all active storage during the first bi-decadal period (although interestingly it shows sufficient supply for the remainder of the century), and GFDL is the only model showing no risk of complete storage loss for any reservoir.

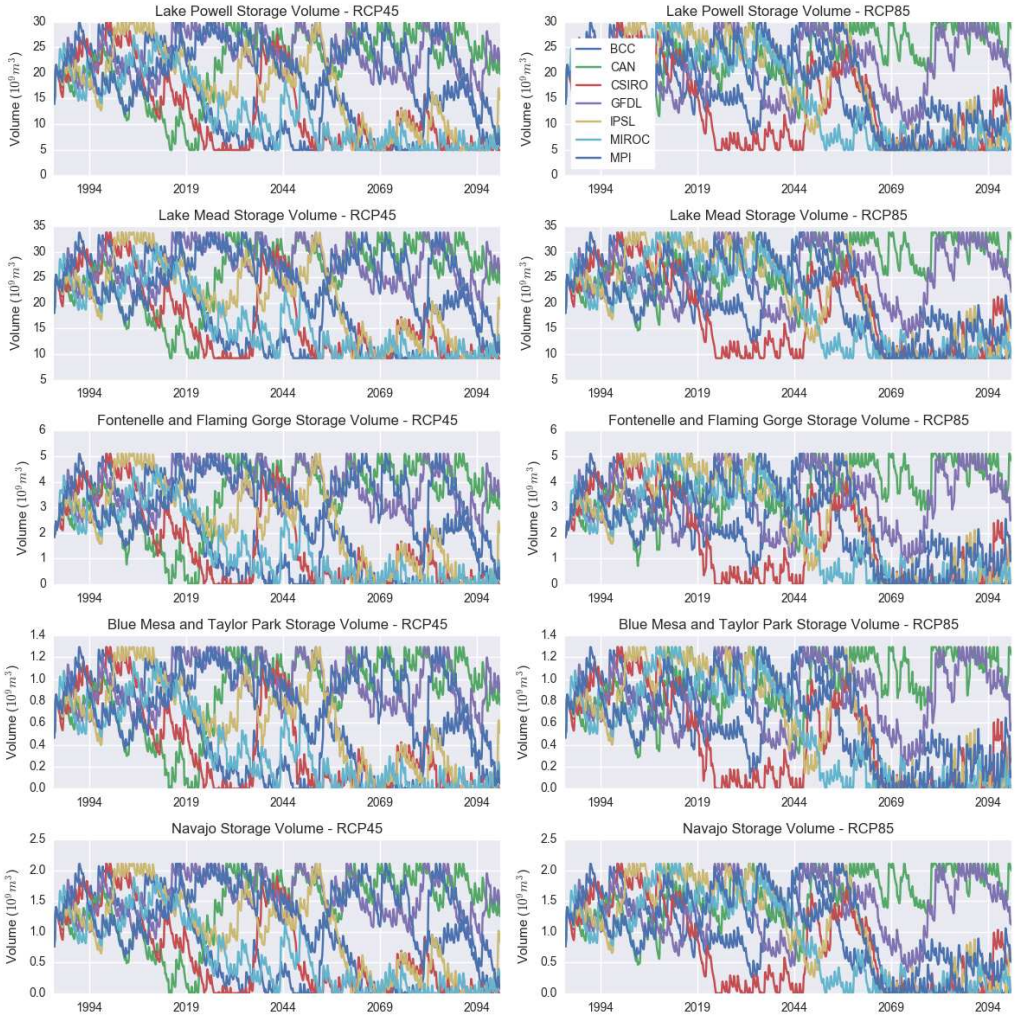

Figure 6.15: Reservoir Storage Volumes for each GCM

Table 6.4: Percent Probability of Fully Utilizing Active Reservoir Storage (RCP 4.5)

HUC	Bi-Decade	BCC	CAN	CSIRO	GFDL	IPSL	MIROC	MPI
1402	2000-2020	0	4.17	0	0	0	0	0
	2020-2040	4.17	5	38.33	0	0	0	0
	2040-2060	25.83	0	10.83	0	0	11.67	0
	2060-2080	39.58	0	17.5	0	16.25	34.17	0
	2080-2100	0	0	40	0	35.83	43.33	0
1404	2000-2020	0	4.17	0	0	0	0	0
	2020-2040	5.83	6.25	39.58	0	0	0	0
	2040-2060	27.08	0	12.08	0	0	13.75	0
	2060-2080	41.67	0	17.5	0	16.25	35	0
	2080-2100	0	0	41.25	0	34.17	46.25	0
1407	2000-2020	0	2.92	0	0	0	0	0
	2020-2040	4.17	5	37.08	0	0	0	0
	2040-2060	25.42	0	10.42	0	0	10.83	0
	2060-2080	36.67	0	15.83	0	14.17	32.92	0
	2080-2100	0	0	36.25	0	32.08	39.17	0
1408	2000-2020	0	3.33	0	0	0	0	0
	2020-2040	4.17	5	37.08	0	0	0	0
	2040-2060	25.42	0	10.42	0	0	10.83	0
	2060-2080	37.5	0	16.25	0	15.83	33.33	0
	2080-2100	0	0	36.67	0	34.17	42.08	0
1501	2000-2020	0	2.5	0	0	0	0	0
	2020-2040	4.17	5	36.67	0	0	0	0
	2040-2060	24.58	0	11.25	0	0	10.83	0
	2060-2080	35.83	0	15	0	14.17	33.33	0
	2080-2100	0	0	35.42	0	31.25	39.58	0

Table 6.5: Percent Probability of Fully Utilizing Active Reservoir Storage (RCP 8.5)

HUC	Bi-Decade	BCC	CAN	CSIRO	GFDL	IPSL	MIROC	MPI
1402	2000-2020	0	0	0	0	0	0	0
	2020-2040	0	0	24.17	0	0	0	0
	2040-2060	0	0	7.92	0	0	7.92	0
	2060-2080	14.58	0	39.17	0	50.42	39.58	25.83
	2080-2100	32.5	0	32.5	0	32.5	42.92	20.83
1404	2000-2020	0	0	0	0	0	0	0
	2020-2040	0	0	24.17	0	0	0	0
	2040-2060	0	0	9.17	0	0	8.75	0
	2060-2080	14.58	0	39.58	0	49.17	39.58	27.5
	2080-2100	32.08	0	29.17	0	28.33	43.33	18.33
1407	2000-2020	0	0	0	0	0	0	0
	2020-2040	0	0	22.92	0	0	0	0
	2040-2060	0	0	7.92	0	0	7.08	0
	2060-2080	10.83	0	34.58	0	45.83	35.83	22.08
	2080-2100	27.5	0	22.5	0	25.42	37.08	15
1408	2000-2020	0	0	0	0	0	0	0
	2020-2040	0	0	23.33	0	0	0	0
	2040-2060	0	0	7.92	0	0	7.08	0
	2060-2080	12.5	0	36.25	0	47.92	35.83	23.75
	2080-2100	29.58	0	25.42	0	28.33	40.42	16.67
1501	2000-2020	0	0	0	0	0	0	0
	2020-2040	0	0	21.67	0	0	0	0
	2040-2060	0	0	7.5	0	0	7.08	0
	2060-2080	10.83	0	32.92	0	43.75	35.42	21.67
	2080-2100	27.08	0	22.08	0	24.17	37.08	15

6.3.4 Vulnerability Analysis - Annualized

Vulnerability is simply defined here as the probability that supply is less than demand, resulting in a delivery shortage. Similar to estimating the probability of draining the reservoir, we can estimate the vulnerability by counting the number of months there is a shortage (not considering magnitude, but simply that there was some degree of shortage), and divide by the months of record. Demand data was available on the HUC4 level; therefore, the vulnerability is also reported on this same spatial scale.

We start by considering changes in yield for each HUC, and then evaluate the vulnerability in bi-decadal blocks for each GCM and RCP grouping all months together.

Determination of vulnerability utilizes output from the WEAP model when it is forced by the yield, which is equal to the sum of runoff and baseflow from each subcatchment. We start by considering the spatial distribution of changes in yield for each GCM and RCP scenario. This is completed by finding the mean *annual* yield for each bi-decadal block, and then determining the difference from the 2000-2020 decadal period, resulting in four figures of bi-decadal block differences.

As an example, Figure 6.16 shows the changes in mean annual yield for the MIROC GCM and RCP 8.5. This example shows continual decreases in expected annual yield, mostly focused around headwater basins, especially on the east side of the basin. Further, no basins show any significant increases in expected yield for any of the bi-decadal periods. Figures of all GCMs and RCPs for changes in hydrologic yield are included in Appendix D.1.1.

Using the yield, demands, instream flows requirements, reservoirs, and the stream network, the WEAP model was used to find the delivery shortages for each HUC4 basin. Dividing the data again into bi-decadal blocks, the probability of a shortage is plotted for each GCM and RCP.

As an example, Figure 6.17 shows the vulnerability for the MIROC GCM and RCP 8.5 (same figure for yield changes shown above). The increase in vulnerability over time matches the expected response with decreased yield throughout the century as previously observed, eventually reaching nearly a 50% chance of not meeting demand (e.g. nearly half the months, most HUCs will have insufficient supply to meet demand). This also shows the extremely vulnerable state of the Lower Colorado River basin with excessive shortages. A very similar pattern is seen for all GCMs (all figures included in Appendix D.1.2) under the RCP 8.5 scenario, except for the GFDL GCM.

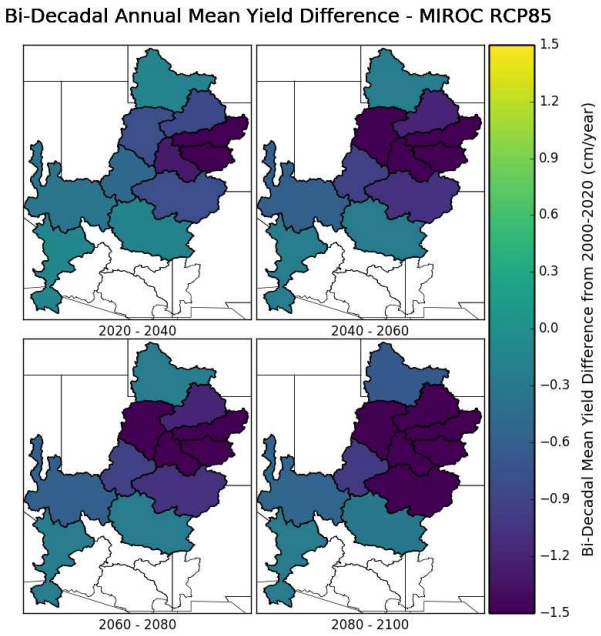

Figure 6.16: Change in Mean Bi-Decadal Yield from 2000-2020 Period (MIROC-RCP 8.5)

Of interest, when comparing changes in yield to the changes vulnerability, is the difference in spatial distributions. The yield reductions are focused mainly in the mountainous headwater basins, whereas the vulnerability increase is shared across all HUCs in the Colorado System.

The lower emissions scenario RCP 4.5 shows mixed ranges of vulnerabilities, some with marginal changes such as CAN and GFDL, whereas IPSL, MIROC and BCC show increased vulnerabilities through the 21st century.

Summary tables of the vulnerability as a percent of months experiencing a delivery shortage are included here for each GCM. Here, we can see the change between RCP scenarios, in addition to the change in vulnerability over time between bi-decadal blocks.

6.3.5 Vulnerability Analysis - Monthly

In a similar manner to the annual analysis, we can also extract the vulnerabilities by month to understand the range of seasonal differences between models and bi-decadal blocks. A single

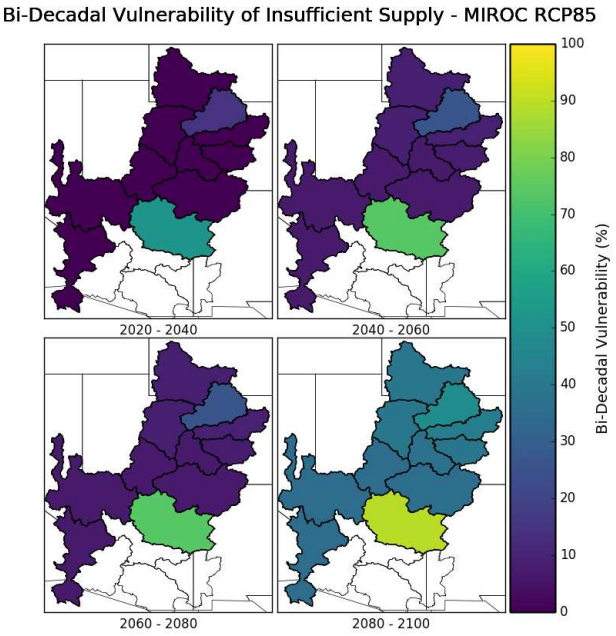

Figure 6.17: Vulnerability to Insufficient Supply (MIROC-RCP8.5)

Table 6.6: Summary of Bi-Decadal Vulnerability (%) by HUC4 (BCC)

GCM	RCP	HUC	2000-2020	2020-2040	2040-2060	2060-2080	2080-2100
BCC	RCP45	1401	0	6.25	27.08	40	5
		1402	0	6.25	27.08	40.42	1.67
		1403	0	5.83	26.67	39.17	1.67
		1404	0	7.92	28.33	42.5	1.67
		1405	8.75	23.33	40.42	48.75	17.5
		1406	0	7.92	28.33	42.5	1.67
		1407	0	5.83	26.67	37.5	1.67
		1408	0	5.83	26.67	38.33	1.67
		1501	0	5.83	26.67	37.5	1.67
		1502	0	5.42	21.67	31.67	1.67
		1503	0	5.83	26.67	37.5	1.67
	RCP85	1401	0	0	4.17	18.33	38.33
		1402	0	0	0	14.58	32.92
		1403	0	0	0	14.17	31.25
		1404	0	0	0	15	32.5
		1405	9.17	13.75	15	27.08	42.92
		1406	0	0	0	15	32.5
		1407	0	0	0	10.83	27.5
		1408	0	0	0	12.5	29.58
		1501	0	0	0	10.83	27.5
		1502	44.58	47.5	61.25	75	82.08
		1503	0	0	0	10.83	27.5

Table 6.7: Summary of Bi-Decadal Vulnerability (%) by HUC4 (CAN)

GCM	RCP	HUC	2000-2020	2020-2040	2040-2060	2060-2080	2080-2100
CAN	RCP45	1401	4.58	6.25	0.83	3.33	5.42
		1402	4.17	5	0	0	0
		1403	3.75	5	0	0	0
		1404	4.17	6.25	0	0	0
		1405	19.58	16.67	15	12.08	13.75
		1406	4.17	6.25	0	0	0
		1407	2.92	5	0	0	0
		1408	3.33	5	0	0	0
		1501	2.92	5	0	0	0
		1502	47.08	43.33	59.17	58.75	78.75
		1503	2.92	5	0	0	0
	RCP85	1401	0	0	2.5	5.83	10
		1402	0	0	0	0	0
		1403	0	0	0	0	0
		1404	0	0	0	0	0
		1405	12.5	15.83	13.75	14.58	12.92
		1406	0	0	0	0	0
		1407	0	0	0	0	0
		1408	0	0	0	0	0
		1501	0	0	0	0	0
		1502	41.67	47.5	58.75	60.42	56.67
		1503	0	0	0	0	0

Table 6.8: Summary of Bi-Decadal Vulnerability (%) by HUC4 (CSIRO)

GCM	RCP	HUC	2000-2020	2020-2040	2040-2060	2060-2080	2080-2100
CSIRO	RCP45	1401	0	37.92	15.83	20.83	43.75
		1402	0	38.33	11.25	17.5	41.25
		1403	0	37.5	10.83	16.67	38.75
		1404	0	39.58	12.08	17.5	41.25
		1405	11.67	46.67	26.67	29.17	50.42
		1406	0	39.58	12.08	17.5	41.25
		1407	0	37.08	10.42	15.83	35.83
		1408	0	37.08	10.42	15.83	36.67
		1501	0	37.08	10.42	15.83	35.83
		1502	42.5	72.5	69.17	69.58	86.25
		1503	0	37.08	10.42	15.83	35.83
	RCP85	1401	1.25	25.83	13.75	45.42	40
		1402	0	24.17	7.92	39.58	32.5
		1403	0	22.92	7.92	37.5	26.67
		1404	0	24.58	9.17	40	29.58
		1405	12.92	36.25	25	52.08	42.08
		1406	0	24.58	9.17	40	29.58
		1407	0	22.92	7.92	34.58	22.08
		1408	0	23.33	7.92	36.25	25.42
		1501	0	22.92	7.92	34.58	22.08
		1502	40.83	63.75	62.08	83.33	77.5
		1503	0	22.92	7.92	34.58	22.08

Table 6.9: Summary of Bi-Decadal Vulnerability (%) by HUC4 (GFDL)

GCM	RCP	HUC	2000-2020	2020-2040	2040-2060	2060-2080	2080-2100
GFDL	RCP45	1401	0	0	0	0	1.67
		1402	0	0	0	0	0
		1403	0	0	0	0	0
		1404	0	0	0	0	0
		1405	7.08	7.92	13.33	13.75	12.08
		1406	0	0	0	0	0
		1407	0	0	0	0	0
		1408	0	0	0	0	0
		1501	0	0	0	0	0
		1502	37.5	44.58	58.33	62.08	70.42
		1503	0	0	0	0	0
	RCP85	1401	0	0	0.42	1.67	6.25
		1402	0	0	0	0	0
		1403	0	0	0	0	0
		1404	0	0	0	0	0
		1405	12.08	10.42	11.67	17.5	17.08
		1406	0	0	0	0	0
		1407	0	0	0	0	0
		1408	0	0	0	0	0
		1501	0	0	0	0	0
		1502	37.92	48.33	52.92	71.67	72.08
		1503	0	0	0	0	0

Table 6.10: Summary of Bi-Decadal Vulnerability (%) by HUC4 (IPSL)

GCM	RCP	HUC	2000-2020	2020-2040	2040-2060	2060-2080	2080-2100
IPSL	RCP45	1401	0	0.83	6.25	23.33	38.33
		1402	0	0	0	16.67	36.25
		1403	0	0	0	16.25	33.75
		1404	0	0	0	16.67	34.17
		1405	8.33	17.5	17.92	31.67	45
		1406	0	0	0	16.67	34.17
		1407	0	0	0	14.17	32.08
		1408	0	0	0	15.83	34.17
		1501	0	0	0	14.17	32.08
		1502	38.33	49.17	60.42	70	87.92
		1503	0	0	0	14.17	32.08
	RCP85	1401	0	0.83	8.75	54.58	40.83
		1402	0	0	0	50.83	33.33
		1403	0	0	0	48.33	28.75
		1404	0	0	0	49.58	29.58
		1405	9.58	17.08	19.58	57.92	42.92
		1406	0	0	0	49.58	29.58
		1407	0	0	0	45.83	25.42
		1408	0	0	0	47.92	28.33
		1501	0	0	0	45.83	25.42
		1502	37.08	47.92	55.83	91.67	82.5
		1503	0	0	0	45.83	25.42

Table 6.11: Summary of Bi-Decadal Vulnerability (%) by HUC4 (MIROC)

GCM	RCP	HUC	2000-2020	2020-2040	2040-2060	2060-2080	2080-2100
MIROC	RCP45	1401	0	0	14.17	36.67	45.42
		1402	0	0	12.08	34.17	44.17
		1403	0	0	11.25	32.92	41.25
		1404	0	0	13.75	35	46.25
		1405	12.08	18.33	28.33	46.25	55.83
		1406	0	0	13.75	35	46.25
		1407	0	0	10.83	32.92	39.17
		1408	0	0	10.83	33.33	42.08
		1501	0	0	10.83	32.92	39.17
		1502	42.5	53.33	75	89.17	91.67
		1503	0	0	10.83	32.92	39.17
	RCP85	1401	0	0	9.17	42.5	48.33
		1402	0	0	7.92	39.58	44.58
		1403	0	0	7.08	37.5	41.67
		1404	0	0	8.75	40	44.17
		1405	8.33	15	26.25	48.75	52.5
		1406	0	0	8.75	40	44.17
		1407	0	0	7.08	35.42	37.08
		1408	0	0	7.08	35.83	40.42
		1501	0	0	7.08	35.42	37.08
		1502	38.75	52.08	74.17	89.58	88.75
		1503	0	0	7.08	35.42	37.08

Table 6.12: Summary of Bi-Decadal Vulnerability (%) by HUC4 (MPI)

GCM	RCP	HUC	2000-2020	2020-2040	2040-2060	2060-2080	2080-2100
MPI	RCP45	1401	0.42	1.67	1.25	7.92	7.5
		1402	0	0	0	0	0
		1403	0	0	0	0	0
		1404	0	0	0	0	0
		1405	7.92	12.08	14.17	17.08	14.58
		1406	0	0	0	0	0
		1407	0	0	0	0	0
		1408	0	0	0	0	0
		1501	0	0	0	0	0
		1502	40	49.58	56.25	65.83	76.67
		1503	0	0	0	0	0
	RCP85	1401	0	0.83	4.17	33.75	30
		1402	0	0	0	27.5	20.83
		1403	0	0	0	25.83	18.33
		1404	0	0	0	27.5	18.75
		1405	7.92	11.67	17.5	40.83	34.17
		1406	0	0	0	27.5	18.75
		1407	0	0	0	22.08	15
		1408	0	0	0	23.75	16.67
		1501	0	0	0	22.08	15
		1502	42.5	50.42	60.42	80	79.17
		1503	0	0	0	22.08	15

table for the MIROC GCM with RCP 8.5 emissions scenario is shown in Table 6.13, which indicates interesting seasonal patterns not identified through the annual lumping analysis. The full collection of monthly summary tables for each GCM and RCP have been included in Appendix D.2.

For MIROC, RCP 8.5, the 2020-2040 period shows limited vulnerability, except for HUC 1502, where vulnerability is already severe. This HUC is the Little Colorado River, which includes transbasin diversions out of the Colorado River Basin, in addition to diversions into the Gila River Basin. Again, the Gila was not explicitly included in the hydrologic yield, but the required basin diversions were still retained in the WEAP operations model.

The next bi-decadal period, 2040-2060, shows an increase in vulnerability with a quite interesting pattern during an unexpected period - winter months. Demand data for each HUC was supplied as an annual volume, which was then disaggregated by month for the vulnerability analysis. The other set of demand data was for transbasin diversions, which were supplied as an annual volume equally distributed throughout the year. The total demand is appropriate, but the temporal pattern of actual trans-basin diversions may not match a uniform distribution. Therefore, periods of low natural yield, combined with low reservoir storage volumes, may lead to high cool-season vulnerabilities.

Determining whether this temporal demand pattern for transbasin diversions is realistic, leading to cool-season vulnerabilities, would require further investigation of temporal diversion disaggregation. Regardless, the storage volume supplied is appropriately determined in the WEAP model, and the annualized vulnerabilities are represented appropriately.

The final two bi-decadal periods show continued increases in vulnerabilities across all months, although at lower levels during spring-melt periods. Similar to the annual results, this specific GCM and RCP scenario shows gross increases in vulnerability in the coming decades.

Review of other GCM and RCP scenarios show similar patterns of cool-season vulnerabilities (Appendix D.2), although the magnitude of vulnerabilities between various models changes similarly to the annualized data. For example, the CAN and GFDL GCMs show limited vulnerability for all bi-decadal periods, although do show late-summer vulnerabilities when they occur (August and September). Conversely, the CSIRO model shows gross shortages for most months and bi-decadal periods. Even in the CSIRO model, the vulnerability decreases substantially during April, May and June, as would be expected with months of increased spring yield.

Table 6.13: Summary of Bi-Decadal Vulnerability (%) by HUC4 and Month (MIROC, RCP85)

Decadal Block	Month	1401	1402	1403	1404	1405	1406	1407	1408	1501	1502	1503
2020-2040	1	0	0	0	0	0	0	0	0	0	0	0
	2	0	0	0	0	0	0	0	0	0	0	0
	3	0	0	0	0	0	0	0	0	0	0	0
	4	0	0	0	0	0	0	0	0	0	35	0
	5	0	0	0	0	0	0	0	0	0	75	0
	6	0	0	0	0	0	0	0	0	0	100	0
	7	0	0	0	0	20	0	0	0	0	100	0
	8	0	0	0	0	85	0	0	0	0	100	0
	9	0	0	0	0	75	0	0	0	0	100	0
	10	0	0	0	0	0	0	0	0	0	75	0
	11	0	0	0	0	0	0	0	0	0	40	0
	12	0	0	0	0	0	0	0	0	0	0	0
2040-2060	1	20	20	20	20	20	20	20	20	20	30	20
	2	20	20	20	20	20	20	20	20	20	55	20
	3	10	10	10	10	10	10	10	10	10	20	10
	4	0	0	0	0	0	0	0	0	0	50	0
	5	0	0	0	0	0	0	0	0	0	90	0
	6	0	0	0	0	0	0	0	0	0	100	0
	7	0	0	0	0	60	0	0	0	0	100	0
	8	20	10	0	5	100	5	0	0	0	100	0
	9	5	0	0	15	70	15	0	0	0	100	0
	10	5	5	5	5	5	5	5	5	5	100	5
	11	15	15	15	15	15	15	15	15	15	90	15
	12	15	15	15	15	15	15	15	15	15	55	15
2060-2080	1	50	50	50	50	50	50	50	50	50	75	50
	2	60	60	60	60	60	60	60	60	60	85	60
	3	35	35	35	35	35	35	35	35	35	55	35
	4	5	5	5	5	5	5	5	5	5	70	5
	5	0	0	0	0	0	0	0	0	0	95	0
	6	20	20	20	20	20	20	20	20	20	100	20
	7	55	45	45	40	75	40	35	35	35	100	35
	8	70	60	40	55	100	55	35	40	35	100	35
	9	70	55	50	70	95	70	40	40	40	100	40
	10	40	40	40	40	40	40	40	40	40	100	40
	11	50	50	50	50	50	50	50	50	50	100	50
	12	55	55	55	55	55	55	55	55	55	95	55
2080-2100	1	55	55	55	55	55	55	55	55	55	85	55
	2	55	55	55	55	55	55	55	55	55	70	55
	3	35	35	35	35	35	35	35	35	35	50	35
	4	5	5	5	5	5	5	5	5	5	65	5
	5	5	5	5	5	5	5	5	5	5	95	5
	6	15	15	15	15	15	15	15	15	15	100	15
	7	60	55	45	50	95	50	25	40	25	100	25
	8	95	70	55	65	100	65	35	50	35	100	35
	9	85	70	60	75	95	75	45	55	45	100	45
	10	45	45	45	45	45	45	45	45	45	100	45
	11	60	60	60	60	60	60	60	60	60	100	60
	12	65	65	65	65	65	65	65	65	65	100	65

Although the WEAP model does produce monthly vulnerabilities, without improved temporal disaggregation information for transbasin diversions, the actual magnitudes and frequencies of vulnerabilities should be interpreted with caution. Regardless, the annualized model is appropriately considering demands, storages and shortages, and may be a more reliable estimate of projected future vulnerabilities.

6.4 Discussion and Conclusions

Significant uncertainty surrounds the future water supply for users of the Colorado River Basin waters, but many climate models, TBMs, and demand models show similar patterns of increased strain on the watershed's limited resources. This pattern matches recent trends in observations, with continued increases in consumptive demand, and decreases in yield and major reservoir storage levels. Even with great uncertainty in projected yield through the 21st century, the outlook for sustainable and sufficient supply to meet demand is bleak.

For this assessment, we used the best available consumptive demand data in conjunction with a dynamic vegetation response model in order to estimate spatially distributed vulnerability. The dynamic vegetation model accounts for changing short-term stomatal response as vapor pressure and soil moisture states change, allows for a dynamic allocation of photosynthetic resources, and also varies the leaf area phenology following long-term mean climate properties. It was demonstrated that accounting for changes in vegetal processes can lead to upwards of 15% difference in expected hydrologic yield (Chapter/Section 5.7.4), highlighting the significance of these changes for long-term water yield projection modeling.

A storage and allocation model, WEAP, provided a means of estimating the location and frequency of shortages for seven different climate models and two emission scenarios using one-month temporal periods at the HUC4 level. Summarizing this volume of data is challenging, therefore data was aggregated to represent a mean bi-decadal response, where appropriate.

A majority of the annual yield is provided from the upper headwater reaches of the basin, which coincides with the region of greatest potential decreases in expected hydrologic yield (Table 6.14). But, the Colorado River Basin is a large network with distributed consumptive uses. Because lower subcatchments may be dominated by irrigation utilizing water not sourced locally, spatially

distributed shortages display a more uniform vulnerability compared to decreases in yield. This can be visualized in vulnerability figures, which show fairly uniform changes in vulnerability with time (e.g. shared shortages).

The risk of excessive loss of reservoir storage through the century is high, with four of the seven models showing a high risk of complete utilization of active storage. The calculated frequency is likely over-estimated, as the WEAP model assumes the specified demands are completely satisfied if possible prior to supply curtailment. In reality, water conservation practices and mandatory supply limitations would help reduce the storage loss prior to complete loss of active storage. Regardless, these projections highlight potential future risks in meeting demand and maintaining sufficient storage levels.

Most of the models show a significant increase in supply vulnerability in the coming decade, with some of the models showing extreme vulnerability. Even under cases of limited change to yield over the coming century, the ability to meet the continued increases in demand with population growth, increased consumption from energy and food production, and increased evapotranspiration, will remain a significant challenge for this already stressed watershed.

Table 6.14: Summary of Expected Annual Yield (MAF) in Bi-Decadal Blocks for Upper and Lower Colorado River Regions

GCM	RCP	Region	2000-2020	2020-2040	2040-2060	2060-2080	2080-2100
BCC	RCP45	Upper	14.64	13.54	14.2	12.56	15.33
		Lower	1.01	1.07	1.46	0.94	1.56
	RCP85	Upper	14.26	15.77	15.44	14.83	12.68
		Lower	0.96	1.29	1.29	1.3	1.12
CAN	RCP45	Upper	13.34	17.71	16.24	17.76	16.8
		Lower	1.02	1.92	1.56	2	1.72
	RCP85	Upper	15.64	15.85	17.65	19.7	22.57
		Lower	1.3	1.58	1.95	3.22	5.53
CSIRO	RCP45	Upper	13.58	12.93	13.02	14.05	12.21
		Lower	1.02	1.36	1.12	1.54	1.19
	RCP85	Upper	13.57	12.81	15.44	11.19	13.5
		Lower	1.19	1.09	1.81	1.21	1.98
GFDL	RCP45	Upper	15.95	18.39	16.32	16.28	16.9
		Lower	1.19	1.9	1.56	1.21	1.43
	RCP85	Upper	14.56	16.89	17.91	15.62	17.4
		Lower	1.06	1.41	1.73	1	1.51
IPSL	RCP45	Upper	16.59	14.9	14.96	13.7	13.79
		Lower	1.87	1.29	1.46	1.33	1.19
	RCP85	Upper	16.94	15.69	15.69	10.13	13.85
		Lower	1.74	1.78	1.83	0.87	1.48
MIROC	RCP45	Upper	14.88	14.17	14.13	12.75	12.71
		Lower	1.28	1.18	1.26	0.9	0.87
	RCP85	Upper	17.19	15.05	13.82	12.16	12.47
		Lower	1.56	1.2	0.93	0.94	0.97
MPI	RCP45	Upper	15.69	15.85	15.51	15.3	15.78
		Lower	1.12	1.45	1.25	1.49	1.46
	RCP85	Upper	14.97	16.38	15.93	12.3	14.84
		Lower	1.16	1.33	1.49	1.01	1.34

Bibliography

[1] Craig D Allen, Alison K Macalady, Haroun Chenchouni, Dominique Bachelet, Nate Mcdowell, Michel Vennetier, Thomas Kitzberger, Andreas Rigling, David Breshears, Patrick Gonzalez, Rod Fensham, Zhen Zhang, Jorge Castro, Natalia Demidova, Jong hwan Lim, Gillian Allard, Steven W Running, Akkin Semerci, and Neil Cobb. A global overview of drought and heat-induced tree mortality reveals emerging climate change risks for forests. *Forest Ecology and Management*, Vol. 259:660–684, 2010.

[2] Niels P. R. Anten. Optimal photosynthetic characteristics of individual plants in vegetation stands and implications for species coexistence. *Annals of Botany*, 95(3):495–506, 2005.

[3] NielsP.R. Anten and HeinjoJ. During. Is analysing the nitrogen use at the plant canopy level a matter of choosing the right optimization criterion? *Oecologia*, 167(2):293–303, 2011.

[4] N.P.R. Anten, F. Schieving, E. Medina, M.J.A. Werger, and P. Schuffelen. Optimal leaf area indices in c3 and c4 mono- and dicotyledonous species at low and high nitrogen availability. *Physiologia Plantarum*, 95(4):541–550, 1995.

[5] J. Timothy Ball, Ian E. Woodrow, and Joseph A Berry. A model predicting stomatal conductance and its contribution to the control of photosynthesis under different environmental conditions. *Progress in Photosynthesis Research*, Vol. 4:221–224, 1987.

[6] Chenchayya T. Bathala, editor. *Integrated Hydrological/Ecological/Economic Modeling for Examining the Vulnerability of Water Resources to Climate Change*, number 978-0-7844-0166-8 in Proceedings, North American Water and Environment Congress 1996 - ASCE, pp. 2157-2162. ASCE, 1996.

[7] William L. Bauerle, Joseph D. Bowden, and G. Geoff Wang. The influence of temperature on within-canopy acclimation and variation in leaf photosynthesis: spatial acclimation to microclimate gradients among climatically divergent acer rubrum l. genotypes. *Journal of Experimental Botany*, 58(12):3285–3298, 2007.

[8] William L. Bauerle, Ram Oren, Danielle A. Way, Song S. Qian, Paul C. Stoy, Peter E. Thornton, Joseph D. Bowden, Forrest M. Hoffman, and Robert F. Reynolds. Photoperiodic regulation of the seasonal pattern of photosynthetic capacity and the implications for carbon cycling. *Proceedings of the National Academy of Sciences*, 109(22):8612–8617, 2012.

[9] Richard Bellman. *Dynamic Programming*. Princeton University Press, Princeton, NJ, USA, 1 edition, 1957.

[10] C. J. Bernacchi, E. L. Singsaas, C. Pimentel, A. R. Portis Jr, and S. P. Long. Improved temperature response functions for models of rubisco-limited photosynthesis. *Plant, Cell & Environment*, 24(2):253–259, 2001.

[11] G. B. Bonan, M.Williams, R. A. Fisher, and K. W. Oleson. Modeling stomatal conductance in the earth system: linking leaf water-use efficiency and water transport along the soil-plant-atmosphere continuum. *Geoscientific Model Development*, 7:21932222, 2014.

[12] Elgene O. Box. Predicting physiognomic vegetation types with climate variables. *Vegetatio*, 45(2):127–139, 1981.

[13] Steven Brantley, Chelcy R. Ford, and James M. Vose. Future species composition will affect forest water use after loss of eastern hemlock from southern appalachian forests. *Ecological Applications*, 23(4):777–790, June 2013.

[14] David D Breshears, Neil S Cobb, Paul M Rich, Kevin P Price, Craig D Allen, Y G Balice, William H Romme, Jude H Kastens, M Lisa Floyd, Jayne Belnap, Jesse J Anderson, Orrin B Myers, and Clifton W Meyer. Regional vegetation die-off in response to global-change-type drought. *Proceedings of the National Academy of Sciences*, Vol. 102:15144–15148, 2005.

[15] L.S. Broeckx, R. Fichot, M.S. Verlinden, and R. Ceulemans. Seasonal variations in photosynthesis, intrinsic water-use efficiency and stable isotope composition of poplar leaves in a short-rotation plantation. *Tree Physiology*, 34(7):701–715, 2014.

[16] Thomas C. Brown, Romano Foti, and Jorge A. Ramirez. Projected freshwater withdrawals in the united states under a changing climate. *Water Resources Research*, 49:1259–1276, 2013.

[17] Thomas N. Buckley, Graham D. Farquhar, and Jeffrey M. Miller. The mathematics of linked optimisation for water and nitrogen use in a canopy. *Silva Fennica*, 36(3):639–669, 2002.

[18] Robert Buitenwerf, Laura Rose, and Steven I. Higgins. Three decades of multi-dimensional change in global leaf phenology. *nature climate change*, 5:364–368, April 2015.

[19] Stephanie L. Castle, Brian F. Thomas, John T. Reager, Matthew Rodell, Sean C. Swenson, and James S. Famiglietti. Groundwater depletion during drought threatens future water security of the colorado river basin. *Geophysical Research Letters*, 41:5904–5911, 2014.

[20] Haishan Chen, Robert E. Dickinson, Yongjiu Dai, and Liming Zhou. Sensitivity of simulated terrestrial carbon assimilation and canopy transpiration to different stomatal conductance and carbon assimilation schemes. *Climate Dynamics*, 36(5-6):1037–1054, 2011.

[21] Jia-Lin Chen, James F. Reynolds, Peter C. Harley, and John D. Tenhunen. Coordination theory of leaf nitrogen distribution in a canopy. *Oecologia*, 93(1):pp. 63–69, 1993.

[22] James S. Clark, David M. Bell, Matthew C. Kwit, and Kai Zhu. Competition-interaction landscapes for the joint response of forests to climate change. *Global Change Biology*, pages n/a–n/a, 2014.

[23] James S. Clark, Jerry Melillo, Jacqueline Mohan, and Carl Salk. The seasonal timing of warming that controls onset of the growing season. *Global Change Biology*, 20(4):1136–1145, 2014.

[24] M. Clerc and J. Kennedy. The particle swarm - explosion, stability, and convergence in a multidimensional complex space. *Evolutionary Computation, IEEE Transactions on*, 6(1):58–73, Feb 2002.

[25] David W. Clow. Changes in the timing of snowmelt and streamflow in colorado: A response to recent warming. *Journal of Climate*, Vol. 23:2293–2306, 2010.

[26] I.R. Cowan. *Regulation of Water Use in Relation to Carbon Gain in Higher Plants*, volume Vol. 12B of *Encyclopedia of Plant Physiology, Physiological Plant Ecology*, chapter Ch. 17, pages 589–613. Springer-Verlag, Berlin, Germany, 1982.

[27] I.R. Cowan. *On the economy of plant form and function*, chapter Economics of carbon fixation in higher plants, pages 133–170. Cambridge University Press, 1986.

[28] I.R. Cowan and G.D. Farquhar. Stomatal function in relation to leaf metabolism and environment. *Experimental Biology Symposium*, pages 471–505, 1977.

[29] Edoardo Daly, Amilcare Porporato, and Ignacio Rodrguez-Iturbe. Coupled dynamics of photosynthesis, transpiration, and soil water balance. part i: Upscaling from hourly to daily level. *Journal of Hydrometeorology*, 5:546–558, 2004.

[30] D. G. G. De Pury and G. D. Farquhar. Simple scaling of photosynthesis from leaves to canopies without the errors of big-leaf models. *Plant, Cell & Environment*, 20(5):537–557, 1997.

[31] Michael D. Dettinger and Daniel R. Cayan. Trends in snowfall versus rainfall in the western united states. *Journal of Climate*, Vol. 19:4545, 2006.

[32] Roderick C. Dewar, Oskar Franklin, Annikki Mkel, Ross E.Mcmurtrie, and Harry T. Valentine. Optimal function explains forest responses to global change. *Bioscience*, 59(2):127–139, 2009.

[33] Roderick C. Dewar, Lasse Tarvainen, Kathryn Parker, Gran Wallin, and Ross E. McMurtrie. Why does leaf nitrogen decline within tree canopies less rapidly than light? an explanation from optimization subject to a lower bound on leaf mass per area. *Tree Physiology*, 32(5):520–534, 2012.

[34] J. C. Adam E. P. Maurer, A. W. Wood, D. P. Lettenmaier, and B. Nijssen. A long-term hydrologically based dataset of land surface fluxes and states for the conterminous united states. *American Meteorological Society*, Vol. 15:3237–3251, 2002.

[35] Peter S. Eagleson. Climate, soil and vegetation 3 - a simplified model of soil moisture movement in the liquid phase. *Water Resources Research*, Vol. 14, 1978.

[36] J. R. Evans and H. Poorter. Photosynthetic acclimation of plants to growth irradiance: the relative importance of specific leaf area and nitrogen partitioning in maximizing carbon gain. *Plant, Cell & Environment*, 24(8):755–767, 2001.

[37] John R. Evans. Partitioning of nitrogen between and within leaves grown under different irradiances. *Australian Journal of Plant Physiology*, 16:533–548, 1989.

[38] John R. Evans. Photosynthetic acclimation and nitrogen partitioning within a lucerne canopy. i. canopy characteristics. *Australian Journal of Plant Physiology*, 20(1):55–67, 1993.

[39] John Richard Evans. *Developmental Constraints on Photosynthesis: Effects of Light and Nutrition*, volume 5 of *Advances in Photosynthesis and Respiration*, pages 281–304. Springer Netherlands, 1996.

[40] G.D. Farquhar, S. von Caemmerer, and J.A. Berry. A biochemical model of photosynthetic co2 assimilation in leaves of c3 species. *Planta*, Vol. 149:78–90, 1980.

[41] Graham D. Farquhar, Thomas N. Buckley, and Jeffrey M. Miller. Optimal stomatal control in relation to leaf area and nitrogen content. *Silva Fennica*, Vol. 36:625–637, 2002.

[42] Caroline E. Farrior, Ignacio Rodriguez-Iturbe, Ray Dybzinski, Simon A. Levin, and Stephen W. Pacala. Decreased water limitation under elevated co2 amplifies potential for forest carbon sinks. *Proceedings of the National Academy of Sciences*, 2015.

[43] J. Flexas and H. Medrano. Drought-inhibition of photosynthesis in c3 plants- stomatal and non-stomatal limitations revisited. *Annals of Botany*, Vol. 89:183–189, 2002.

[44] Lorraine E Flint and Alan L Flint. Downscaling future climate scenarios to fine scales for hydrologic and ecological modeling and analysis. *Ecological Processes*, 1(1), February 2012.

[45] Chelcy R. Ford, Robert M. Hubbard, Brian D. Kloeppel, and James M. Vose. A comparison of sap flux-based evapotranspiration estimates with catchment-scale water balance. *Agricultural and Forest Meteorology*, 145:176–185, 2007.

[46] Romano Foti, Jorge A. Ramirez, and Thomas C. Brown. Vulnerability to u.s. water supply to shortage. Technical Report RMRS-GTR-295, U.S. Department of Agriculture, Forest Service, 2012.

[47] Romano Foti, Jorge A. Ramirez, and Thomas C. Brown. A probabilistic framework for assessing vulnerability to climate variability and change: The case of the us water supply system. *Climate Change*, 125:413427, 2014.

[48] Romano Foti, Jorge A. Ramirez, and Thomas C. Brown. Response surfaces of vulnerability to climate change: the colorado river basin, the high plains, and california. *Climatic Change*, 125(3):429–444, 2014.

[49] A.D. Friend, A.K. Stevens, R.G. Knox, and M.G.R. Cannell. A process-based, terrestrial biosphere model of ecosystem dynamics (hybrid v3.0). *Ecological Modelling*, 95(23):249 – 287, 1997.

[50] Andrew D. Friend. Terrestrial plant production and climate change. *Journal of Experimental Botany*, 61(5):1293–1309, 2010.

[51] Yongshuo S. H. Fu, Matteo Campioli, Yann Vitasse, Hans J. De Boeck, Joke Van den Berge, Hamada AbdElgawad, Han Asard, Shilong Piao, Gaby Deckmyn, and Ivan A. Janssens. Variation in leaf flushing date influences autumnal senescence and next years flushing date in two temperate tree species. *PNAS*, 111(20):7355–7360, 2014.

[52] Thomas J. Givnish. *On the economy of plant form and function*, chapter Optimal stomatal conductance, allocation of energy between leaves and roots, and the marginal cost of transpiration, pages 171–213. Cambridge University Press, 1986.

[53] Thomas J. Givnish and Geerat J. Vermeij. Sizes and shapes of liane leaves. *The American Naturalist*, 110(975), 1976.

[54] M. Groenendijk, A. J. Dolman, C. Ammann, A. Arneth, A. Cescatti, D. Dragoni, J. H. C. Gash, D. Gianelle, B. Gioli, G. Kiely, A. Knohl, B. E. Law, M. Lund, B. Marcolla, M. K. van der Molen, L. Montagnani, E. Moors, A. D. Richardson, O. Roupsard, H. Verbeeck, and G. Wohlfahrt. Seasonal variation of photosynthetic model parameters and leaf area index from global fluxnet eddy covariance data. *Journal of Geophysical Research: Biogeosciences*, 116(G4):n/a–n/a, 2011.

[55] V. P. Gutschick and T. Simonneau. Modelling stomatal conductance of field-grown sunflower under varying soil water content and leaf environment: comparison of three models of stomatal response to leaf environment and coupling with an abscisic acid-based model of stomatal response to soil drying. *Plant Cell & Environment*, 25:1423–1434, 2002.

[56] Pertti Hari, Annikki Makela, Eeva Korpilahti, and Maria Holmberg. Optimal control of gas exchange. *Tree Physiology*, 2(1-2-3):169–175, 1986.

[57] K. Hikosaka, Y. T. Hanba, T. Hirose, and I. Terashima. Photosynthetic nitrogen-use efficiency in leaves of woody and herbaceous species. *Functional Ecology*, 12(6):896–905, 1998.

[58] K. Hikosaka and I. Terashima. A model of the acclimation of photosynthesis in the leaves of c3 plants to sun and shade with respect to nitrogen use. *Plant, Cell & Environment*, 18(6):605–618, 1995.

[59] Kouki Hikosaka and Tadaki Hirose. Leaf angle as a strategy for light competition: optimal and evolutionarily stable light-extinction coefficient within a leaf canopy. *Ecoscience*, 4(4):501–507, 1997.

[60] C.G. Homer, J.A. Dewitz, Jin S. Yang, L., P. Danielson, G. Xian, J. Coulston, N.D. Herold, J.D. Wickham, and K. Megown. Completion of the 2011 national land cover database for the conterminous united states-representing a decade of land cover change information. *Photogrammetric Engineering and Remote Sensing*, 81(5):345–354, 2015.

[61] Mevin B. Hooten and Christopher K. Wikle. Statistical agent-based models for discrete spatio-temporal systems. *Journal of American Statistical Association*, 105(489):236–248, 2010.

[62] P.G. Jarvis. The interpretation of the variations in leaf water potential and stomatal conductance found in canopies in the field. *Philosophical Transactions of the Royal Society of London. Series B, Biological Sciences*, Vol. 273:593–610, 1976.

[63] Frank H. Johnson, Henry Eyring, and R. W. Williams. The nature of enzyme inhibitions in bacterial luminescence: Sulfanilamide, urethane, temperature and pressure. *Journal of Cellular and Comparative Physiology*, 20(3):247–268, 1942.

[64] William M. Jolly, Ramakrishna Nemani, and Steven W. Running. A generalized, bioclimatic index to predict foliar phenology in response to climate. *Global Change Biology*, 11(4):619–632, 2005.

[65] Hamlyn G. Jones. *Plants and Microclimate - A Quantitative Approach to Environmental Plant Physiology*. Cambridge University Press, 3rd edition, 2014.

[66] H.G. Jones and R.A. Sutherland. Stomatal control of xylem embolism. *Plant , Cell and Environment*, Vol. 14:607–612, 1991.

[67] J. Kattge, S. Daz, S. Lavorel, I. C. Prentice, P. Leadley, G. Bnisch, E. Garnier, M. Westoby, P. B. Reich, I. J. Wright, J. H. C. Cornelissen, C. Violle, S. P. Harrison, P. M. Van Bodegom, M. Reichstein, B. J. Enquist, N. A. Soudzilovskaia, D. D. Ackerly, M. Anand, O. Atkin, M. Bahn, T. R. Baker, D. Baldocchi, R. Bekker, C. C. Blanco, B. Blonder, W. J. Bond, R. Bradstock, D. E. Bunker, F. Casanoves, J. Cavender-bares, J. Q. Chambers, F. S. Chapin Iii, J. Chave, D. Coomes, W. K. Cornwell, J. M. Craine, B. H. Dobrin, L. Duarte, W. Durka, J. Elser, G. Esser, M. Estiarte, W. F. Fagan, J. Fang, F. Fernndez-mndez, A. Fidelis, B. Finegan, O. Flores, H. Ford, D. Frank, G. T. Freschet, N. M. Fyllas, R. V. Gallagher, W. A. Green, A. G. Gutierrez, T. Hickler, S. I. Higgins, J. G. Hodgson, A. Jalili, S. Jansen, C. A. Joly, A. J. Kerkhoff, D. Kirkup, K. Kitajima, M. Kleyer, S. Klotz, J. M. H. Knops, K. Kramer, I. Khn, H. Kurokawa, D. Laughlin, T. D. Lee, M. Leishman, F. Lens, T. Lenz, S. L. Lewis, J. Lloyd, J. Llusi, F. Louault, S. Ma, M. D. Mahecha, P. Manning, T. Massad, B. E. Medlyn, J. Messier, A. T. Moles, S. C. Mller, K. Nadrowski, S. Naeem, . Niinemets, S. Nllert, A. Nske, R. Ogaya, J. Oleksyn, V. G. Onipchenko, Y. Onoda, J. Ordoez, G. Overbeck, W. A. Ozinga, S. Patio, S. Paula, J. G. Pausas, J. Peuelas, O. L. Phillips, V. Pillar, H. Poorter, L. Poorter, P. Poschlod, A. Prinzing, R. Proulx, A. Rammig, S. Reinsch, B. Reu, L. Sack, B. Salgado-negret, J. Sardans, S. Shiodera, B. Shipley, A. Siefert, E. Sosinski, J.-f. Soussana, E. Swaine, N. Swenson, K. Thompson, P. Thornton, M. Waldram, E. Weiher, M. White, S. White, S. J. Wright, B. Yguel, S. Zaehle, A. E. Zanne, and C. Wirth. Try a global database of plant traits. *Global Change Biology*, 17(9):2905–2935, 2011.

[68] J. Kattge and W. Knorr. Temperature acclimation in a biochemical model of photosynthesis: a reanalysis of data from 36 species. *Plant , Cell and Environment*, 30(9):1176–1190, 2007.

[69] Jens Kattge, Wolfgang Knorr, Thomas Raddatz, and Christian Wirth. Quantifying photosynthetic capacity and its relationship to leaf nitrogen content for global-scale terrestrial biosphere models. *Global Change Biology*, 15(4):976–991, 2009.

[70] G. Katul, S. Manzoni, S. Palmroth, and R. Oren. A stomatal optimization theory to describe the effects of atmospheric co2 on leaf photosynthesis and transpiration. *Annals of Botany*, Vol. 105(No. 3):431–442, 2010.

[71] Gabriel G. Katul, Sari Palmroth, and Ram Oren. Leaf stomatal responses to vapour pressure deficit under current and co2-enriched atmosphere explained by the economics of gas exchange. *Plant , Cell and Environment*, Vol. 32:968–979, 2009.

[72] J. Kennedy and R. Eberhart. Particle swarm optimization. In *Neural Networks, 1995. Proceedings., IEEE International Conference on*, volume 4, pages 1942–1948 vol.4, 1995.

[73] Thomas R. Knutson and Robert E. Tuleya. Reply. *Journal of Climate*, 18:5183–5187, 2005.

[74] Christopher J. Kucharik, Jonathan A. Foley, Christine Delire, Veronica A. Fisher, Michael T. Coe, John D. Lenters, Christine Young-Molling, Navin Ramankutty, John M. Norman, and Stith T. Gower. Testing the performance of a dynamic global ecosystem model: Water balance, carbon balance, and vegetation structure. *Global Biogeochemical Cycles*, 14(3):795–825, 2000.

[75] Michael H. Kutner, Christopher J. Nachtsheim, John Neter, and William Li. *Applied Linear Statistical Models*. MxGraw-Hill, 5th edition, 2005.

[76] O.L. Lange, R. Lsch, E.-D. Schulze, and L. Kappen. Responses of stomata to changes in humidity. *Planta*, 100(1):76–86, 1971.

[77] Michael J. Lauer and John S. Boyer. Internal co2 measured directly in leaves - abscisic acid and low leaf water potential cause opposing effects. *Plant Physiology*, 98(4):1310–1316, 1992.

[78] R. Leuning. A critical appraisal of a combined stomatal-photosynthesis model for c3 plants. *Plant, Cell and Environment*, Vol. 18:339–355, 1995.

[79] R. Leuning. Scaling to a common temperature improves the correlation between the photosynthesis parameters jmax and vcmax. *Journal of Experimental Biology*, 48(2):345–347, 1997.

[80] Lettenmaier Liang, Wood. Surface soil moisture parameterization of the vic-2l model: Evaluation and modification. *Global and Planetary Change*, Vol. 13:195–206, 1996.

[81] Yan-Shih et.al. Lin. Optimal stomatal behaviour around the world. *Nature Climate Change*, 5:459–464, 2015.

[82] Jeremy S. Littell, Marketa McGuire Elsner, Guillaume Mauger, Eric Lutz, Alan F. Hamlet, and Eric Salath. Regional climate and hydrologic change in the northern us rockies and pacific northwest: Internally consistent projections of future climate for resource management. Technical report, Climate Impacts Group University of Washington College of the Environment, 2011.

[83] Creighton M. Litton, James W. Raich, and Michael G. Ryan. Carbon allocation in forest ecosystems. *Global Change Biology*, 13(10):2089–2109, 2007.

[84] Jon Lloyd. Modelling stomatal responses to environment in macadamia integrifolia. *Australian Journal of Plant Physiology*, 18(6):649–660, 1991.

[85] Raschke Lohmann, Nolte-Holube. A large scale horizontal routing model to be coupled to land surface parameterization schemes. 1996.

[86] Rosana Lpez, Unai Lpez de Heredia, Carmen Collada, Francisco Javier Cano, Brent C. Emerson, Herv Cochard, and Luis Gil. Vulnerability to cavitation, hydraulic efficiency, growth and survival in an insular pine (pinus canariensis). *Annals of Botany*, 111(6):1167–1179, 2013.

[87] David R. Maidment, editor. *Handbook of Hydrology*. McGraw Hill, 1992.

[88] Vincent Maire, Pierre Martre, Jens Kattge, Franois Gastal, and Gerd Esser. The coordination of leaf photosynthesis links c and n fluxes in c3 plant species. *PLoS ONE*, 7(6), 2012.

[89] Stefano Manzoni, Giulia Vico, Gabriel Katul, Philip A. Fay, Wayne Polley, Sari Palmroth, and Amilcare Porporato. Optimizing stomatal conductance for maximum carbon gain under water stress: a meta-analysis across plant functional types and climates. *Functional Ecology*, Vol. 25:456–467, 2011.

[90] Stefano Manzoni, Giulia Vico, Gabriel Katul, Sari Palmroth, and Amilcare Porporato. Optimal plant water-use strategies under stochastic rainfall. *Water Resources Research*, 50:5379–5394, 2014.

[91] Edwin P Maurer and Philip B. Duffy. Uncertainty in projections of streamflow changes due to climate change in california. *Geophysical Research Letters*, 32(L03704), 2005.

[92] EdwinP. Maurer. Uncertainty in hydrologic impacts of climate change in the sierra nevada, california, under two emissions scenarios. *Climatic Change*, 82(3-4):309–325, 2007.

[93] RE McMurtrie, RJ Norby, RC Medlyn, BE amd Dewar, DA Pepper, PB Reich, and CVM Barton. Why is plant-growth response to elevated co2 amplified when water is limiting, but reduced when nitrogen is limiting? a growth-optimisation hypothesis. *Functional Plant Biology*, 35(6):521–534, 2008.

[94] Ross E. McMurtrie and Roderick C. Dewar. Leaf-trait variation explained by the hypothesis that plants maximize their canopy carbon export over the lifespan of leaves. *Tree Physiology*, 31(9):1007–1023, 2011.

[95] B. E. Medlyn, F. W. Badeck, D. G. G. De Pury, C. V. M. Barton, M. Broadmeadow, R. Ceulemans, P. De Angelis, M. Forstreuter, M. E. Jach, S. Kellomki, E. Laitat, M. Marek, S. Philippot, A. Rey, J. Strassemeyer, K. Laitinen, R. Liozon, B. Portier, P. Roberntz, K. Wang, and P. G. Jstbid. Effects of elevated [co2] on photosynthesis in european forest species: a meta-analysis of model parameters. *Plant, Cell & Environment*, 22(12):1475–1495, 1999.

[96] B. E. Medlyn, E. Dreyer, D. Ellsworth, M. Forstreuter, P. C. Harley, M. U. F. Kirschbaum, X. Le Roux, P. Montpied, J. Strassemeyer, A. Walcroft, K. Wang, and D. Loustau. Temperature response of parameters of a biochemically based model of photosynthesis. ii. a review fo experimental data. *Plant, Cell & Environment*, 25(9):1167–1179, 2002.

[97] Belinda E. Medlyn, Remko A. Duursma, Derek Eamus, David S. Ellsworth, I. Colin Prentice, Craig V. M. Barton, Kristine Y. Crous, Paolo De Angelis, Michael Freeman, and Lisa Wingate. Reconciling the optimal and empirical approaches to modelling stomatal conductance. *Global Change Biology*, 17(6):2134–2144, 2011.

[98] Laurent Misson, Kevin P. Tu, Ralph A. Boniella, and Allen H. Goldstein. Seasonality of photosynthetic parameters in a multi-specific and vertically complex forest ecosystem in the sierra nevada of california. *Tree Physiology*, 26:729–741, 2006.

[99] Russel K. Monson, Michael R. Sackschewsky, and George J. Williams III. Field measurements of photosynthesis, water-use efficiency, and growth in agropyron smithii (c3) and bouteloua gracilis (c4) in the colorado shortgrass steppe. *Oecologia*, Vol. 68:400–409, 1986.

[100] J.E. Nash and J.V. Sutcliffe. River flow forecasting through conceptual models part i a discussion of principles. *Journal of Hydrology*, 10(3):282 – 290, 1970.

[101] . Niinemets and J. D. Tenhunen. A model separating leaf structural and physiological effects on carbon gain along light gradients for the shade-tolerant species acer saccharum. *Plant, Cell & Environment*, 20(7):845–866, 1997.

[102] lo Niinemets. Optimization of foliage photosynthetic capacity in tree canopies: towards identifying missing constraints. *Tree Physiology*, 32(5):505–509, 2012.

[103] lo Niinemets, Olevi Kull, and John D. Tenhunen. An analysis of light effects on foliar morphology, physiology, and light interception in temperate deciduous woody species of contrasting shade tolerance. *Tree Physiology*, 18(10):681–696, 1998.

[104] Ulo Niinemets, Olevi Kull, and J.D. Tenhunen. Within-canopy variation in the rate of development of photosynthetic capacity is proportional to integrated quantum flux density in temperate deciduous trees. *Plant , Cell and Environment*, 27:293–313, 2004.

[105] Park S. Nobel. *Physicochemical and Environmental Plant Physiology*. Elsevier, 4th edition, 2009.

[106] United States Bureau of Reclamation. West-wide climate risk assessments: Bias-corrected and spatially downscaled surface water projections. (Technical Memorandum No. 86-68210-2011-01), 2011.

[107] E Ogren and J.R. Evans. Photosynthetic light-response curves- i. the influence of co2 partial pressure and leaf inversion. *Planta*, 189(2):182–190, 1993.

[108] Yusuke Onoda, Kouki Hikosaka, and Tadaki Hirose. Seasonal change in the balance between capacities of rubp carboxylation and rubp regeneration affects co2 response of photosynthesis in polygonum cuspidatum. *Journal of Experimental Botany*, 56(412):755–763, 2005.

[109] Jeanne L. D. Osnas, Jeremy W. Lichstein, Peter B. Reich, and Stephen W. Pacala. Global leaf trait relationships: Mass, area, and the leaf economics spectrum. *Science*, 340(6133):741–744, 2013.

[110] Alan Owen and Inman Harvey. Adapting particle swarm optimization for fitness landscapes with neutrality. In *Proceedings of the 2007 IEEE Swarm Intelligence Symposium*, Proceedings of the 2007 IEEE Swarm Intelligence Symposium, pages 258–265. IEEE Press, 2007.

[111] Mikko S. Peltoniemi, Remko A. Duursma, and Belinda E. Medlyn. Co-optimal distribution of leaf nitrogen and hydraulic conductance in plant canopies. *Tree Physiology*, 32(5):510–519, 2012.

[112] Caroline A. Polgar and Richard B. Primack. Leaf-out phenology of temperate woody plants: from trees to ecosystems. *New Phytologist*, 191(4):926–941, 2011.

[113] Hendrik Poorter, Steeve Pepin, Toon Rijkers, Yvonne de Jong, John R. Evans, and Christian Krner. Construction costs, chemical composition and payback time of high- and low-irradiance leaves. *Journal of Experimental Botany*, 57(2):355–371, 2006.

[114] Hendrik Poorter, ClaudiusA.D.M. van de Vijver, RenG.A. Boot, and Hans Lambers. Growth and carbon economy of a fast-growing and a slow-growing grass species as dependent on nitrate supply. *Plant and Soil*, 171(2):217–227, 1995.

[115] I. Colin Prentice, Wolfgang Cramer, Sandy P. Harrison, Rik Leemans, Robert A. Monserud, and Allen M. Solomon. A global biome model based on plant physiology and dominance, soil properties and climate. *Journal of Biogeography*, 19(2):pp. 117–134, 1992.

[116] Alistair Rogers. The use and misuse of vc,max in earth system models. *Photosynthesis Research*, 119:15–29, 2014.

[117] P.J. Sands. Modelling canopy production. i. optimal distribution of photosynthetic resources. *Australian Journal of Plant Physiology*, 22(4):593–601, 1995.

[118] Hisashi Sato, Akihiko Itoh, and Takashi Kohyama. Seibdgvm: A new dynamic global vegetation model using a spatially explicit individual-based approach. *Ecological Modelling*, 200(34):279 – 307, 2007.

[119] Simon Scheiter, Liam Langan, and Steven I. Higgins. Next-generation dynamic global vegetation models: learning from community ecology. *New Phytologist*, 198(3):957–969, 2013.

[120] Thomas D. Sharkey, Carl J. Bernacchi, Graham D. Farquhar, and Eric L. Singsaas. Fitting photosynthetic carbon dioxide response curves for c3 leaves. *Plant, Cell & Environment*, 30(9):1035–1040, 2007.

[121] Yuhui Shi and RussellC. Eberhart. Parameter selection in particle swarm optimization. In V.W. Porto, N. Saravanan, D. Waagen, and A.E. Eiben, editors, *Evolutionary Programming VII*, volume 1447 of *Lecture Notes in Computer Science*, pages 591–600. Springer Berlin Heidelberg, 1998.

[122] Sitch, Smith, Prentice, Arneth, Bondeau, Cramer, Kaplan, Levis, Lucht, Sykes, Thonicke, and Venevsky. Evaluation of ecosystem dynamics, plant geography and terrestrial carbon cycling in the lpj dynamic global vegetation model. *Global Change Biology*, Vol. 9:161–185, 2003.

[123] Y. Suzuki, A. Makino, and T. Mae. Changes in the turnover of rubisco and levels of mrnas of rbcl and rbcs in rice leaves from emergence to senescence. *Plant, Cell & Environment*, 24(12):1353–1360, 2001.

[124] F. Tardieu, T. Lafarge, and Th. Simonneau. Stomatal control by fed or endogenous xylem aba in sunflower: interpretation of correlations between leaf water potential and stomatal conductance in anisohydric species. *Plant, Cell & Environment*, 19(1):75–84, 1996.

[125] J.D. Tenhunen, O.L. Lange, J. Gebel, W. Beyschlag, and J.A. Weber. Changes in photosynthetic capacity, carboxylation efficiency, and co2 compensation point associated with midday stomatal closure and midday depression of net co2 exchange of leaves of quercus suber. *Planta*, 162(3):193–203, 1984.

[126] J.W. Tukey. *Exploratory Data Analysis*. Addison-Wesley, MA, 1977.

[127] A. Tuzet, A. Perrier, and R. Leuning. A coupled model of stomatal conductance, photosynthesis and transpiration. *Plant , Cell and Environment*, Vol. 26:1097–1116, 2003.

[128] M T Tyree and J S Sperry. Vulnerability of xylem to cavitation and embolism. *Annual Review of Plant Physiology and Plant Molecular Biology*, 40(1):19–36, 1989.

[129] L. M. Verheijen, V. Brovkin, R. Aerts, G. Bönisch, J. H. C. Cornelissen, J. Kattge, P. B. Reich, I. J. Wright, and P. M. van Bodegom. Impacts of trait variation through observed traitclimate relationships on performance of an earth system model: a conceptual analysis. *Biogeosciences*, 10(8):5497–5515, 2013.

[130] von Beer. Bestimmung der absorption des rothen lichts in farbigen flussigkeiten. *Annalen der Physik*, 86:78–88, 1852.

[131] S. von Caemmerer. *Biochemical Models of Leaf Photosynthesis*. CSIRO Publishing, 2000.

[132] S. von Caemmerer and Graham D. Farquhar. Some relationships between the biochemistry of photosynthesis and the gas exchange of leaves. *Planta*, 153(4):376–387, 1981.

[133] Susanne von Caemmerer, John R. Evans, Graham S. Hudson, and T. John Andrews. The kinetics of ribulose-1,5-bisphosphate carboxylase/oxygenase in vivo inferred from measurements of photosynthesis in leaves of transgenic tobacco. *Planta*, 195(1):88–97, 1994.

[134] James M. Vose, David L. Peterson, and Toral Patel-Weynand, editors. *Effects of Climatic Variability and Change on Forest Ecosystems: A Comprehensive Science Synthesis for the US Forest Sector*. United States Department of Agriculture, 2012.

[135] Joseph C.V. Vu and George Yelenosky. Water deficit and associated changes in some photosynthetic parameters in leaves of 'valencia' orange (citrus sinensis [l.] osbeck). *Plant Physiology*, 88(2):375–378, 1988.

[136] Anthony P. Walker, Andrew P. Beckerman, Lianhong Gu, Jens Kattge, Lucas A. Cernusak, Tomas F. Domingues, Joanna C. Scales, Georg Wohlfahrt, Stan D. Wullschleger, and F. Ian Woodward. The relationship of leaf photosynthetic traits vcmax and jmax to leaf nitrogen, leaf phosphorus, and specific leaf area: a meta-analysis and modeling study. *Ecology and Evolution*, 4(16):3218–3235, August 2014.

[137] Jeffrey M. Warren, Richard J. Norby, and Stan D. Wullschleger. Elevated co2 enhances leaf senescence during extreme drought in a temperate forest. *Tree Physiology*, 31:117–130, 2011.

[138] Richard A Wildman and Noelani A Forde. Management of water shortage in the colorado river basin - evaluating current policy and the viability of interstate water trading. *Journal of the American Water Resources Association*, Vol. 48:411–422, 2012.

[139] A. Park Williams, Craig D. Allen, Constance I. Millar, Thomas W. Swetnam, Joel Michaelsen, Christopher J. Still, and Steven W. Leavitt. Forest responses to increasing aridity and warmth in the southwestern united states. *PNAS*, Vol. 107:21289–21294, 2010.

[140] Park Williams, Craig D. Allen, Alison K. Macalady, Daniel Griffin, Connie A. Woodhouse, David M. Meko, Thomas W. Swetnam, Sara A. Rauscher, Richard Seager, Henri D. Grissino-Mayer, Jeffrey S. Dean, Edward R. Cook, Chandana Gangodagamage, Michael Cai, and Nate G. McDowell. Temperature as a potent driver of regional forest drought stress and tree mortality. *Nature Climate Change*, 3:292–297, 2013.

[141] Charles G. Willis, Brad Ruhfel, Richard B. Primack, Abraham J. Miller-Rushing, and Charles C. Davis. Phylogenetic patterns of species loss in thoreau's woods are driven by climate change. *Proceedings of the National Academy of Sciences*, 105(44):17029–17033, 2008.

[142] Kell B. Wilson, Dennis D. Baldocchi, and Paul J. Hanson. Spatial and seasonal variability of photosynthetic parameters and their relationship to leaf nitrogen in a deciduous forest. *Tree Physiology*, 20:565–578, 2000.

[143] I E Woodrow and J A Berry. Enzymatic regulation of photosynthetic co2, fixation in c3 plants. *Annual Review of Plant Physiology and Plant Molecular Biology*, 39(1):533–594, 1988.

[144] Ian J. Wright, Michelle R. Leishman, Cassia Read, and Mark Westoby. Gradients of light availability and leaf traits with leaf age and canopy position in 28 australian shrubs and trees. *Functional Plant Biology*, 33:407–419, 2006.

[145] Ian J. Wright, Peter B. Reich, Mark Westoby, David D. Ackerly, Zdravko Baruch, Frans Bongers, Jeannine Cavender-Bares, Terry Chapin, Johannes H. C. Cornelissen, Matthias Diemer, Jaume Flexas, Eric Garnier, Philip K. Groom, Javier Gulias, Kouki Hikosaka, Byron B. Lamont, Tali Lee, William Lee, Christopher Lusk, Jeremy J. Midgley, Marie-Laure Navas, Ulo Niinemets, Jacek Oleksyn, Noriyuki Osada, Hendrik Poorter, Pieter Poot, Lynda Prior, Vladimir I. Pyankov, Catherine Roumet, Sean C. Thomas, Mark G. Tjoelker, Erik J. Veneklaas, and Rafael Villar. The worldwide leaf economics spectrum. *Nature*, 428(6985):821–827, April 2004.

[146] Stan D. Wullschleger. Biochemical limitations to carbon assimilation in c3 plants–a retrospective analysis of the a/ci curves from 109 species. *Journal of Experimental Botany*, Vol. 44:907–920, 1993.

[147] Liukang Xu and Dennis D. Baldocchi. Seasonal trends in photosynthetic parameters and stomatal conductance of blue oak (quercus douglasii) under prolonged summer drought and high temperature. *Tree Physiology*, 23(13):865–877, 2003.

[148] F. Yoshie. Intercellular co2 concentration and water-use efficiency of temperate plants with different life-forms and from different microhabitats. *Oecologia*, 68(3):370–374, 1986.

[149] S. Zaehle and A. D. Friend. Carbon and nitrogen cycle dynamics in the o-cn land surface model: 1. model description, site-scale evaluation, and sensitivity to parameter estimates. *Global Biogeochemical Cycles*, 24(1):n/a–n/a, 2010.

[150] Jian Zhanga, Shongming Huang, and Fangliang He. Half-century evidence from western canada shows forest dynamics are primarily driven by competition followed by climate. *PNAS*, 2015.

[151] Zaichun Zhu, Jian Bi, Yaozhong Pan, Sangram Ganguly, Alessandro Anav, Liang Xu, Arindam Samanta, Shilong Piao, Ramakrishna R. Nemani, and Ranga B. Myneni. Global data sets of vegetation leaf area index (lai)3g and fraction of photosynthetically active radiation (fpar)3g derived from global inventory modeling and mapping studies (gimms) normalized difference vegetation index (ndvi3g) for the period 1981 to 2011. *Remote Sensing*, 5(2):927–948, 2013.

Appendix A

Optimal Stomatal Control

A.1 Farquhar, von Caemmerer and Berry Model of Photosynthesis

Carbon assimilation from photosynthesis is assessed using the ubiquitous Farquhar, von Caemmerer, Berry (FvCB) biochemical model of photosynthesis [40]. Carboxylation rate limited net assimilation for C3 photosynthesis can be defined as,

$$A_c = \frac{V_{cmax}(C_i - \Gamma^*)}{C_i + K_m} - R_d \tag{A.1}$$

where, A_c is the net rate of carboxylation limited assimilation ($\mu mol\ CO_2\ m^{-2}s^{-1}$), V_{cmax} is the maximum rate of carboxylation ($\mu mol\ CO_2\ m^{-2}s^{-1}$), C_i is the leaf internal pore space CO_2 concentration ($\mu mol\ mol^{-1}$), Γ^* is the CO_2 compenation point in the absence of mitochondrial respiration ($\mu mol\ mol^{-1}$), K_m is the Michaelis-Menten half-rate constant ($\mu mol\ mol^{-1}$), and R_d is the rate of mitochondrial respiration ($\mu mol\ CO_2\ m^{-2}s^{-1}$). The Michaelis-Menten constant K_m can be expanded [133, 143],

$$K_m = K_c \times (1 + K_o/O_2) \tag{A.2}$$

where K_c is the rate constant for carboxylation reactions, O_2 is the concentration of oxygen ($\mu mol\ mol^{-1}$), and K_o is the rate constant for oxygenation reactions with RuBisCO. K_m describes the competitively inhibited carboxylation rate due to the presence of oxygen.

The RuBP limited rate of assimilation may also be defined as,

$$A_j = \frac{J(C_i - \Gamma^*)}{4C_i + 8\Gamma^*} - R_d \tag{A.3}$$

where, A_j is the RuBP limited rate of net assimilation, and J is the electron transport rate. The rate J depends on absorbed irradiance for photosynthetic processing, and can be approximated with a non-rectangular hyperbola [107],

$$J = \frac{1}{2\theta}\left[I_2 + J_{max} - \sqrt{(I_2 + J_{max})^2 - 4\theta I_2 J_{max}}\right] \tag{A.4}$$

where θ is a curvature factor within [0 (for a rectangular hyperbola), 1 (for a Blackman-type hyperbola)], J_{max} is the maximum rate of electron transport, and I_2 is the irradiance absorbed by the chlorophyll such that,

$$I_2 = \alpha I(1 - f)/2 \tag{A.5}$$

where I is the photosynthetically active radiation (PAR, wavelengths between 400-700nm [65], $\mu mol\ m^{-2}s^{-1}$), α is the absorptance fraction [36], f adjusts for light quality (typically 0.15), and it is divided by 2 to approximate the split between Photosystems I and II [105].

The relationship between chlorophyll concentration and absorptance can be described as [36],

$$\alpha = \frac{\chi}{\chi + 76} \tag{A.6}$$

The form of Eqs.(A.1) and (A.3) are quite similar. Converting to generalized symbology, each equation can be represented as,

$$A_* = \frac{a_1(C_i - \Gamma^*)}{C_i + a_2} - R_d \tag{A.7}$$

where, a_1 is either V_{cmax} or $J/4$, and a_2 is either K_m or $2\Gamma^*$.

The Farquhar biochemical model of photosynthesis only represents the 'demand' of photosynthesis, and is not constrained from the supply side, such as would occur with stomatal limitations during soil water deficits. The internal C_i can be replaced with a Fickian diffusive process for assimilation, solved for C_i as,

$$C_i = C_a - A/g \tag{A.8}$$

where A is the net rate of assimilation, g is the stomatal conductance to CO_2, and C_a is the ambient atmospheric CO_2 concentration ($\mu mol\ mol^{-1}$). Further, a simplifying assumption resulting in a 'linearized' biochemical model may be made by assuming that the denominator C_i in Eq. (A.7) is

constant [70], and may be approximated as a fraction of the atmospheric CO_2 concentration, $C_i \approx rC_a$, where r is the long-term ratio of C_i/C_a. It is well-known that the internal CO_2 concentration is relatively constant over a range of irradiances and seasons [77,125,148], and thus the approximation is not unreasonable with an appropriate estimate of r.

Re-writing Eq.(A.7) with the substituted denominator, also replacing the C_i in the numerator with Eq.(A.8), and solving for A, results in,

$$A_n = \frac{g_s(kC_a - \Gamma k - R_d)}{k + g_s} \tag{A.9}$$

where k is the carboxylation efficiency, and is defined as $k = a_1/(rC_a + a_2)$.

The net rate of assimilation is then the minimum of the two assimilation rates, $A = min(A_c, A_j)$.

Transpiration can be estimated also using a Fickian diffusive process,

$$E_t = ag_sD \tag{A.10}$$

where, E_t is the transpiration rate, a is the ratio of conductance of H_2O vapor to CO_2 (assumed a constant ($a \approx 1.6$) under normal environmental conditions), and D is the vapor pressure deficit.

The vapor pressure deficit D is the difference from leaf internal pore space vapor pressure and vapor pressure above the leaf boundary layer. Several simplifying assumptions allow closed form solution of this aspect, including assuming the leaf internal pore space is saturated, assuming leaf temperature is equivalent to the ambient air temperature, and also assuming the ambient vapor pressure is equivalent to the vapor pressure above the leaf boundary layer. In coupled micro-climates, these assumptions have minimal affect on the result.

The vapor pressure deficit D is found as,

$$D = VP_{leaf} - VP_{amb} \tag{A.11}$$

where VP_{amb} is the ambient atmospheric vapor pressure, and VP_{leaf} is the leaf internal pore space vapor pressure, which is assumed saturated.

Saturated vapor pressure can be estimated using the Clausius-Clapeyron equation [87],

$$D_{sat} = 611 * exp(-2.5e6/461.5 * (1/T_k - 1/273.15)) \tag{A.12}$$

where T_k is the temperature in Kelvin.

A.2 Optimal Stomatal Control with Euler-Lagrange

Optimal stomatal response is that where over the course of some period of integration, and for some finite supply of resources, the stomata operate in a manner to maximize some objective function, defined here as the net assimilation. The problem is formulated as a calculus of variations problem, which can be solved using the Euler-Lagrange equation (refer to Chapter 2).

Bringing Eqs.(A.9) and (A.10) together as a Lagrange function,

$$\mathcal{L} = \frac{g_s(kC_a - \Gamma k - R_d)}{k + g_s} - \lambda \times a g_s D \tag{A.13}$$

where λ is a Lagrange parameter, also referred to here classically as the *marginal water use efficiency*.

Differentiating both Eq.(A.13) with respect to stomatal conductance (g), setting equal to 0, and solving for stomatal conductance results in,

$$g = \sqrt{\frac{k(kC_a - k\Gamma^* - R_d)}{\lambda a D}} - k \tag{A.14}$$

Therefore, for a given λ, and carboxylation efficiency k (function of irradiance, V_{cmax}, J_{max}, K_m, C_a and r), the optimal stomatal conductance may be found. This may then be substituted into Eq. A.9 to determine the net assimilation rate.

Appendix B

Numerical Solution Procedures

B.1 Optimal Allocation

The optimal resource allocation problem of Eq. 3.2 and Eq.3.3 is not easily solved analytically. However, because the assimilation rate for a given N_{org}, V_{cmax} and J_{max} can be uniquely determined, the optimal resource allocation problem can be solved numerically as follows:

1. Set an estimate of leaf nitrogen concentration N_{org}, and select values of V_{cmax} and J_{max} from a feasible set,

2. Solve 3.8 for the chlorophyl content as,

$$\chi = \frac{1}{0.0331}[N_{org} - 0.079J_{max} - \frac{V_{cmax}}{6.25V_{cr}\xi} - \nu J_{max} - N_O] \tag{B.1}$$

3. Determine the absorptance, α, using Eq. A.6,

4. Adjust K_m for temperature based on mean monthly values [96],

5. For a given discrete level of irradiance, determine the rate of assimilation using the FvCB model and the optimal stomatal conductance of Eqs. A.9 and A.14, respectively,

6. Iterate for each level of irradiance from the density function in Eq. 3.2 and Eq.3.3 and obtain estimates of the expected rate of assimilation,

7. This process is then repeated for new values of V_{cmax} and J_{max} (with N_{org} constant), resulting in a different expected value of assimilation.

Spanning the feasible solution space of V_{cmax} and J_{max}, results in a surface of expected assimilation values for a given concentration of leaf nitrogen and light distribution, referred to as the *decision surface*. The maximum value of expected assimilation, and therefore the corresponding values of V^*_{cmax} and J^*_{max} solving Eq. 3.2 and Eq.3.3, may then be extracted from the decision surface providing an estimate of the optimal solution.

B.1.1 Solar Irradiance Density Distribution

Although it may be possible to estimate daily irradiance using a uniform distribution [39], this may over-estimate the high irradiance density.

More appropriately, a scaled-Beta distribution may be used to estimate the solar irradiance density function. A Beta distribution is defined between the range $[0, 1]$, which easily allows definition of a constrained distribution between 0 (or some minimum value) and a specified maximum value (i.e. scaled).

The Beta Density function can be defined as,

$$Beta(X) = \frac{\Gamma(\alpha + \beta)}{\Gamma(\alpha)\Gamma\beta} \times X^{\alpha-1}(1 - X)^{\beta-1} \tag{B.2}$$

where Γ is the Gamma Function, α and β are shape parameters, and X is some fraction in set $[0 - 1]$. This is scaled by simply multiplying the fraction X by some maximum value of irradiance, I_{max}.

As an example, 20-years of hourly data during May at the Denver International Airport were analyzed [22], where a scaled Beta density was fit to the irradiances (greater than 50 $W\ m^{-2}$ shown), and are shown in Figure B.1. Here, it becomes apparent how a uniform density would over estimate the probability density of high irradiances.

The numerical solution procedure divides the density function into 20 equal intervals, which are then used to find the expected value of daily integration.

[22] `http://rredc.nrel.gov/solar/old_data/nsrdb/1991-2010`

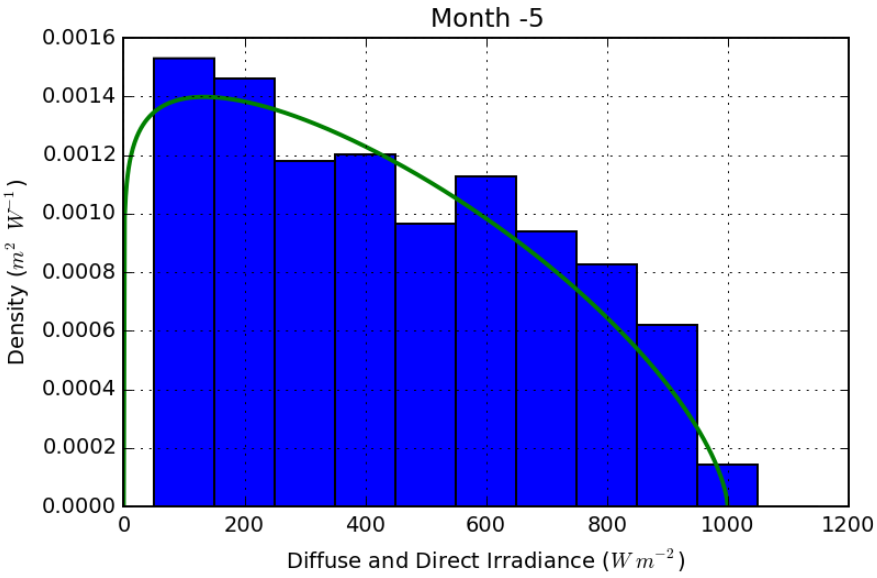

Figure B.1: Fitted Beta Density Distribution of Hourly Irradiance in May - Denver International Airport. Irradiance is the sum of direct and diffuse radiation on a horizontal surface. Includes hourly data from the years 1991-2010, and excludes radiation below 50 $W\ m^{-2}$.

B.2 Particle Swarm Optimization

Particle swarm optimization (PSO) is a heuristic optimization approach that utilizes a population of self and co-aware particles 'flying' through decision space. The numerical process is designed to mimic flocking behavior of a population where information (e.g. the best or most optimal location from all individuals) is shared between individuals, in addition to individual memory of the personal best location. This knowledge is used to then move each point through decision space, converging on the optimal solution. Originally presented by Kennedy and Eberhart in 1995 [72], several modifications and improvements have been proposed to both the parameterization and solution procedure [24, 110, 121]. Here, we present the PSO used for the optimal resource optimization procedure.

Let us define a population of N particles located in D dimensional space. Each individual (N_i) has a position, defined as, $X_{i,d}$, a personal best location of $PD_{i,d}$ associated with the personal best value of PV_i, and a population wide global best location of GD_d with a value of GV, $\forall i \in N$ and $\forall d \in D$. The location of each individual is initialized randomly through D dimension space, and the personal best value PV is then assigned as the value at the starting location X, where

$PD = X$. From the population of personal bests, the global best solution GV and location GD_d are assigned.

For each iteration step t, the velocity[23] and position of each point is then updated by,

$$V_{t+1,i,d} = C_k V_{t,i,d} + C_1 R_1 (P_{i,d} - X_{i,d}) + C_2 R_2 (GD_d - X_{i,d}) \tag{B.3a}$$

$$X_{t+1,i,d} = X_{t,i,d} + V_{t+1,i,d} \; \forall i \in N \text{ and } \forall d \in D \tag{B.3b}$$

where C_k, C_1, C_2 are inertial parameters for the velocity, personal best and global best positions, respectively, and R_1 and R_2 are random uniform values in $[0, 1]$. The velocity inertia C_k is a decaying coefficient defined as,

$$C_k = C_0 exp^{-\zeta k} \tag{B.4}$$

where k is the current iteration, and ζ is a rate of decay parameter, here set equal to 0.1. Further, the resulting velocities V are checked against set simple non-reflecting bounds such that $V_{min} \leq V \leq V_{max}$ for each d in D (i.e. each d has a unique set of velocity bounds).

For each new position X_{t+1} (i and d implied for simpler notation), the value of the function is then evaluated. For each individual, if the current value is better than the personal best value, then both PD and PV are updated. If any personal best is greater than the global personal best, then GV and GD would also be updated.

This process is repeated for either a fixed number of K iterations, or until a minimum error tolerance ϵ is not exceeded.

The following summarize the parameters used in the optimal allocation particle search:

```
DVcmin=5.; //Dimensional minimum Vcmax
DVcmax=160.; //Dimensional maximum Vcmax
Dwmin=1.; //Dimensional minimum omega
Dwmax=2.7; // Dimensional maximum omega
Smax=0.1; //maximum Step velocity (scaled 0 to 1)
Smin=-0.1; //minimum Step (velocity) length
C0=0.7298; // Inertia [Clerc and Kennedy 2002]
C1=2.9922/2.; //
C2=2.9922/2.; //weighting factors for personal and global bests
```

[23] The term *velocity* simply refers to a step distance for each dimension for each iteration.

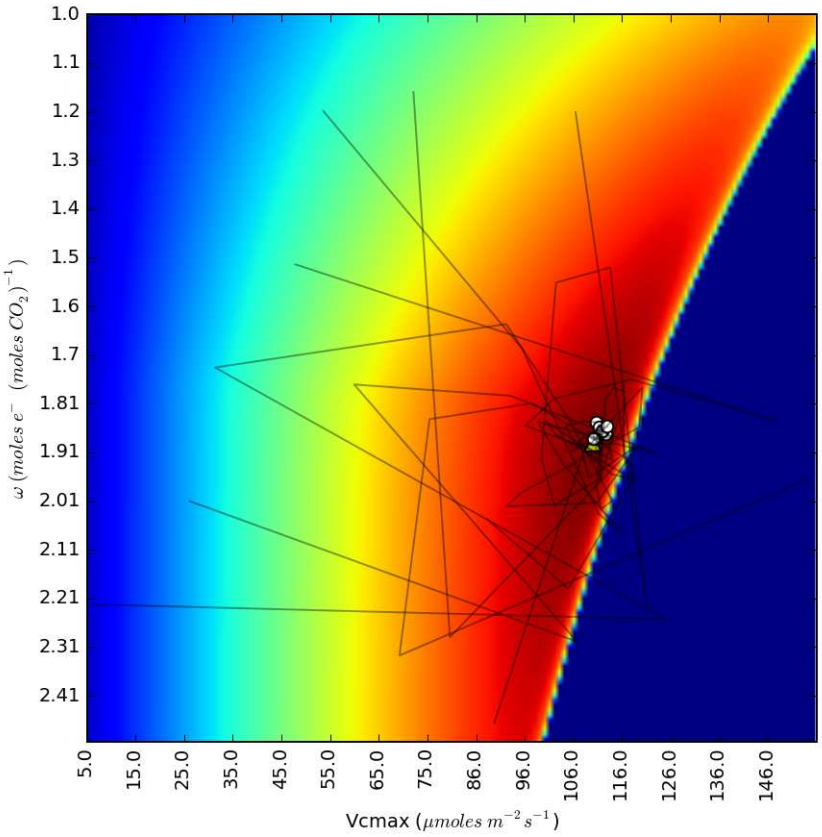

Figure B.2: Sample Particle Swarm Traces - 10 particles converging on the optimal solution in approximately seven steps. White circles show clustering of solutions near optimal, while a small triangle indicates the global best solution. Here, decision space is shown defined as V_{cmax} and ω, where $\omega = J_{max}/V_{cmax}$.

The objective function determined for each point is the expected value of daily integrated assimilation (refer to Chapter 3) in a two-dimensional J_{max} and V_{cmax} decision space.

Since only two-dimensions are being explored, we can easily visualize this process and show traces of particles as they converge on optimal solutions. For $N = 10$, we can see a sample convergence of traces in Figure B.2.

Appendix C

Harmonic Phenologic Regression

C.1 Regression Diagnostics

An important aspect of developing a regression includes evaluation of the model diagnostics. This includes checking for heteroskedasticity, residual bias, residual normality, and data points with extreme leverage adversely affecting the regression.

For each of the β regression models, which are the beta coefficients for the harmonic regression Intercept, Cosine and Sine terms, respectively, a series of four diagnostic plots are included.

Overall, these plots indicate a excellent to acceptable diagnostics. Heteroskedasticity is limited, normality is maintained with a few exceptions for fat-tails at the extremes, and no data points were considered for additional removal due to extreme residual leverage. This information is available in Sections C.1.1 to C.1.3

Additionally, a section of histograms of fitness metrics is included. Each natural vegetation point in the study domain was reanalyzed using the regressed relationships and compared to the fitted values, resulting in: Nash-Sutcliffe measures of efficiency, annual differences of maximum LAI values, and annual differences of mean LAI values. Histograms of each of these three metrics are included in Section C.2

C.1.1 Regression Diagnostic Plots - Intercept (β_0)

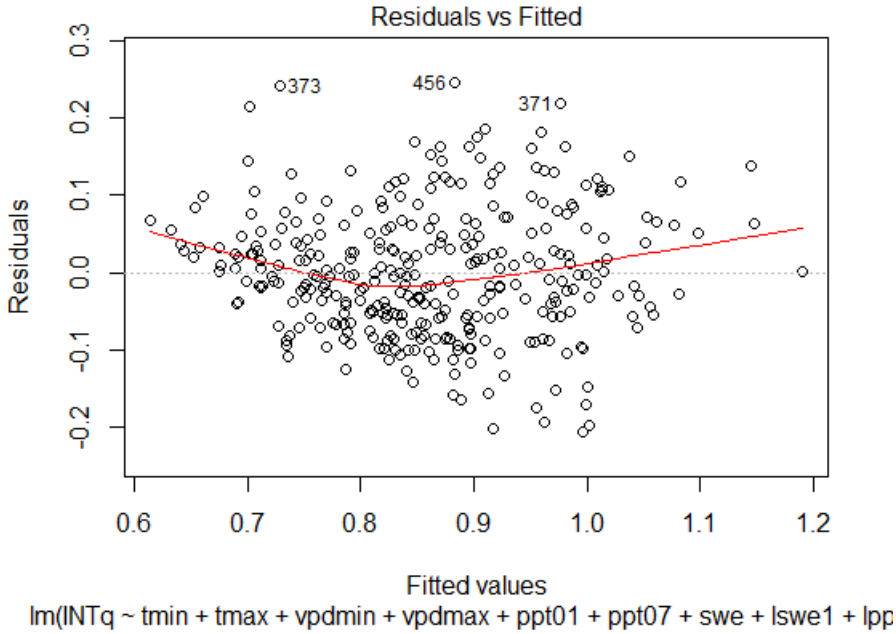

Figure C.1: Intercept (β_0) Regression Diagnostics - Residuals against Fitted

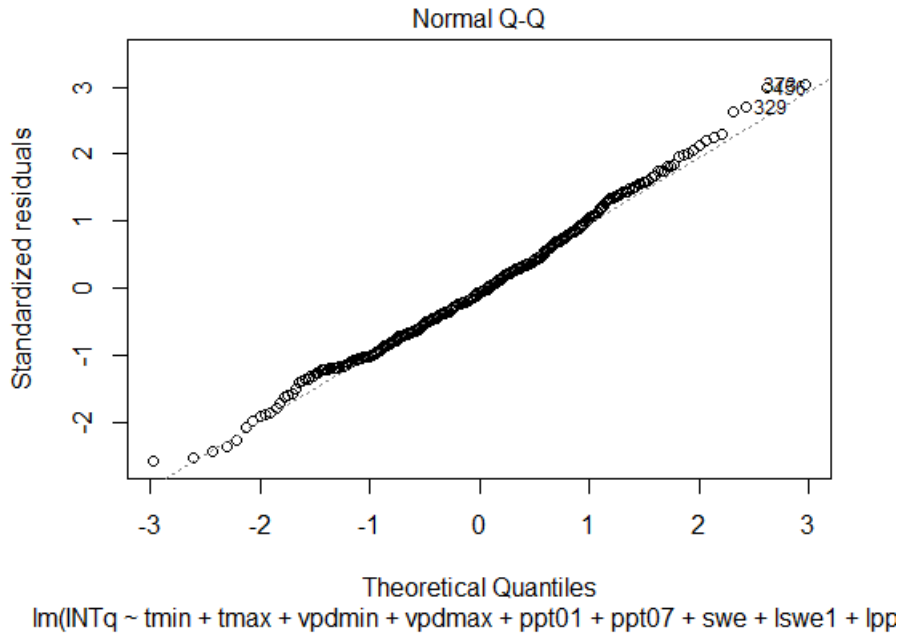

Figure C.2: Intercept (β_0) Regression Diagnostics - Residual QQ Plot

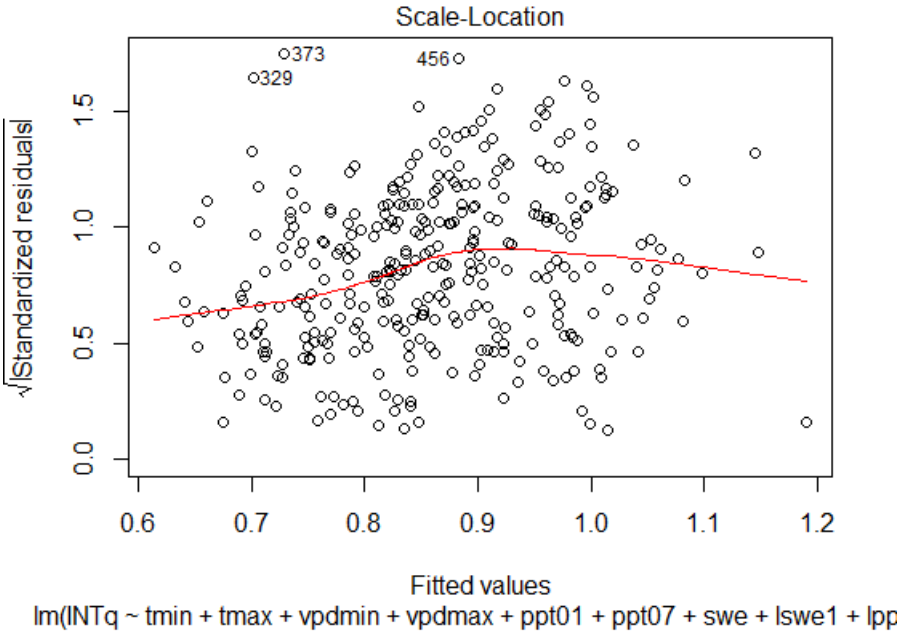

Figure C.3: Intercept (β_0) Regression Diagnostics - Standardized Residuals

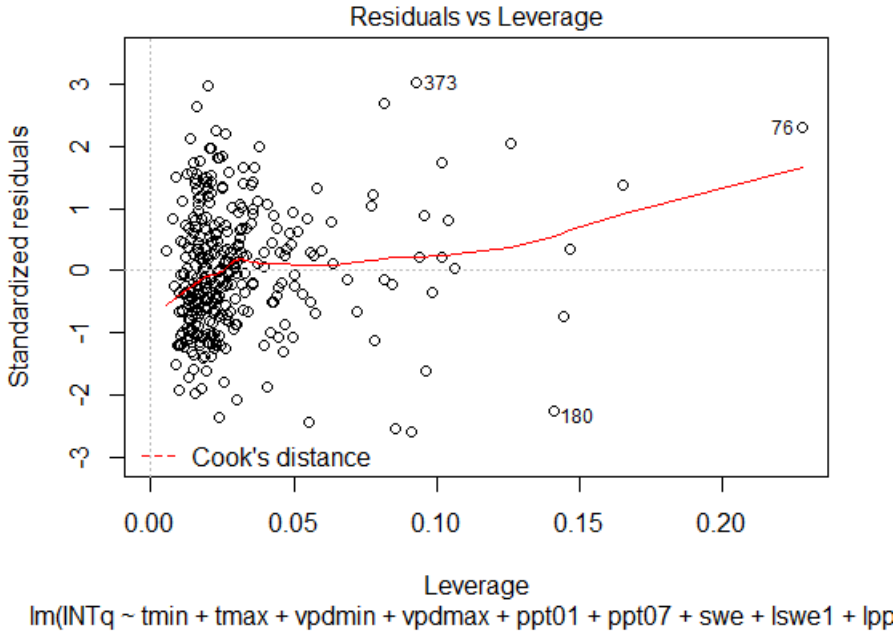

Figure C.4: Intercept (β_0) Regression Diagnostics - Residual Leverage and Cooks Distance

C.1.2 Regression Diagnostic Plots - Cosine Coefficient (β_1)

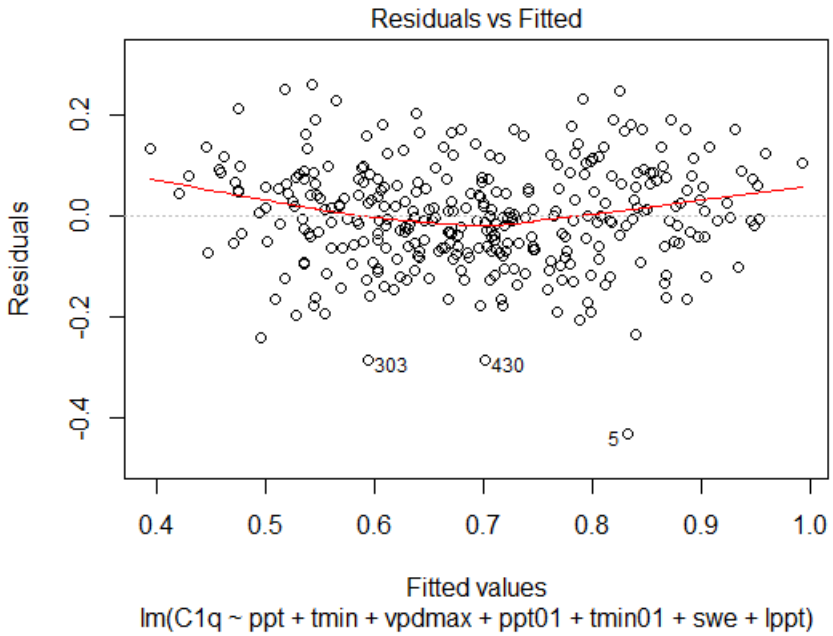

Figure C.5: Cosine Coefficient (β_1) Regression Diagnostics - Residuals against Fitted

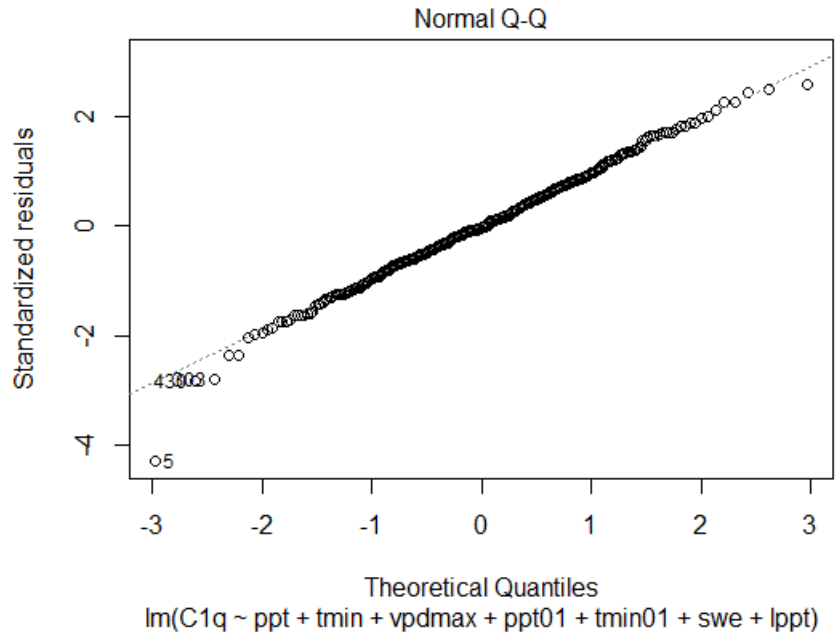

Figure C.6: Cosine Coefficient (β_1) Regression Diagnostics - Residual QQ Plot

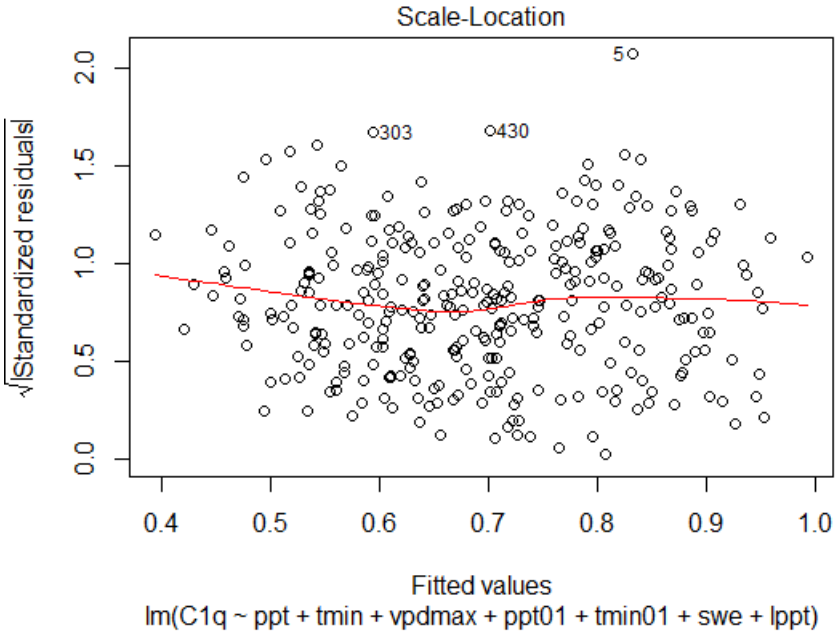

Figure C.7: Cosine Coefficient (β_1) Regression Diagnostics - Standardized Residuals

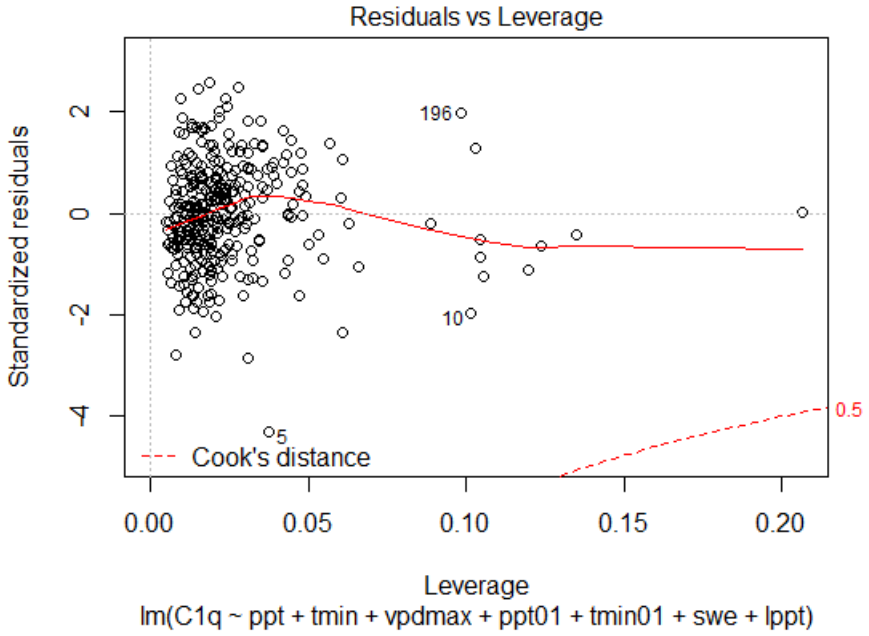

Figure C.8: Cosine Coefficient (β_1) Regression Diagnostics - Residual Leverage and Cooks Distance

C.1.3 Regression Diagnostic Plots - Sine Coefficient (β_2)

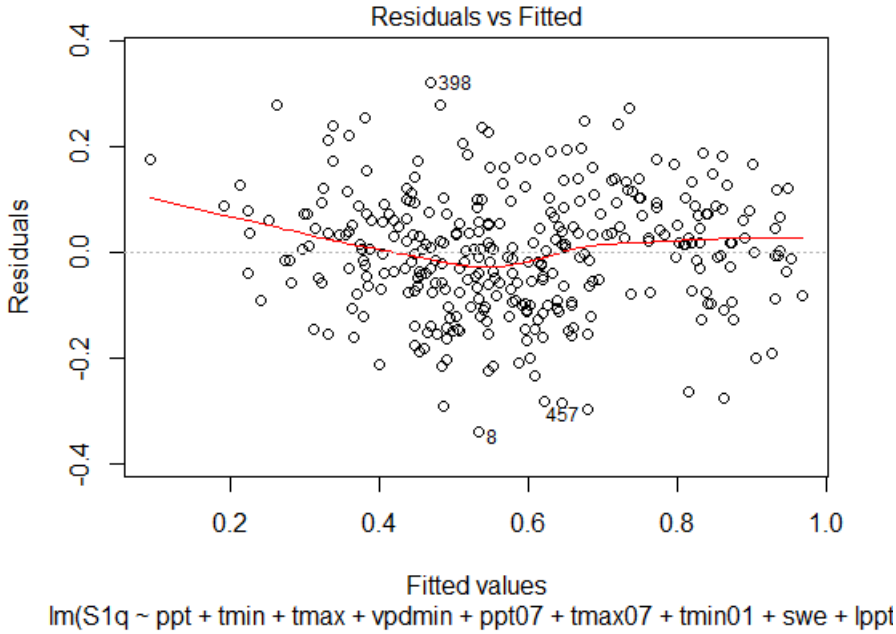

Figure C.9: Sine Coefficient (β_2) Regression Diagnostics - Residuals against Fitted

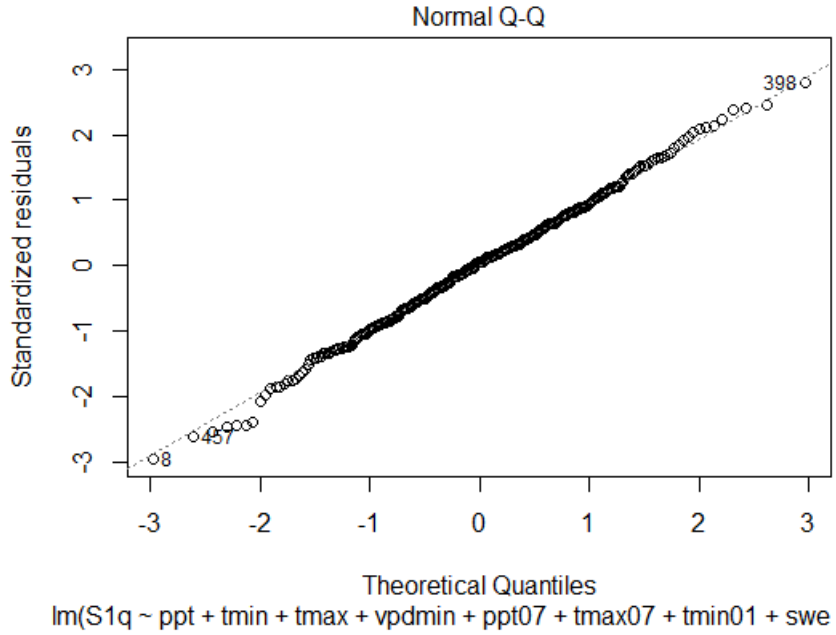

Figure C.10: Sine Coefficient (β_2) Regression Diagnostics - Residual QQ Plot

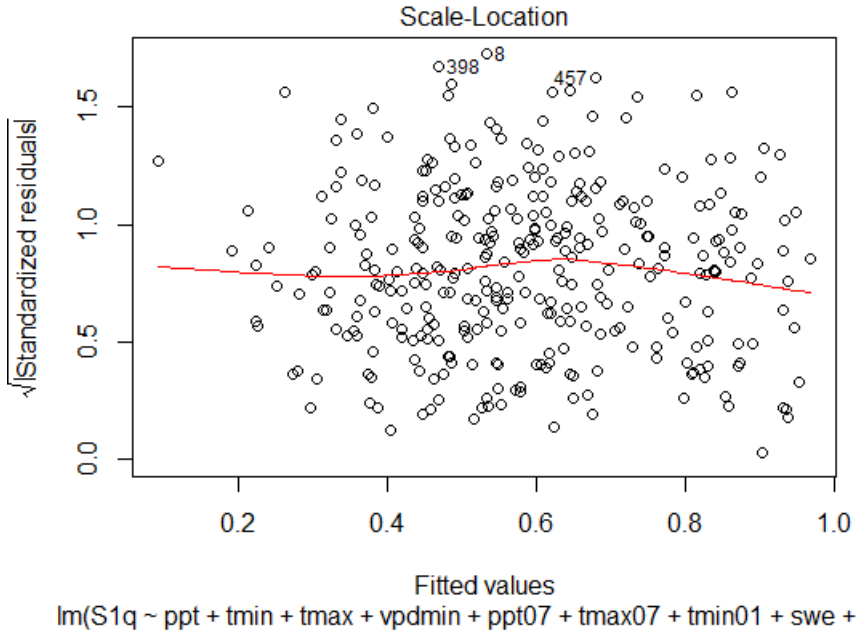

Figure C.11: Sine Coefficient (β_2) Regression Diagnostics - Standardized Residuals

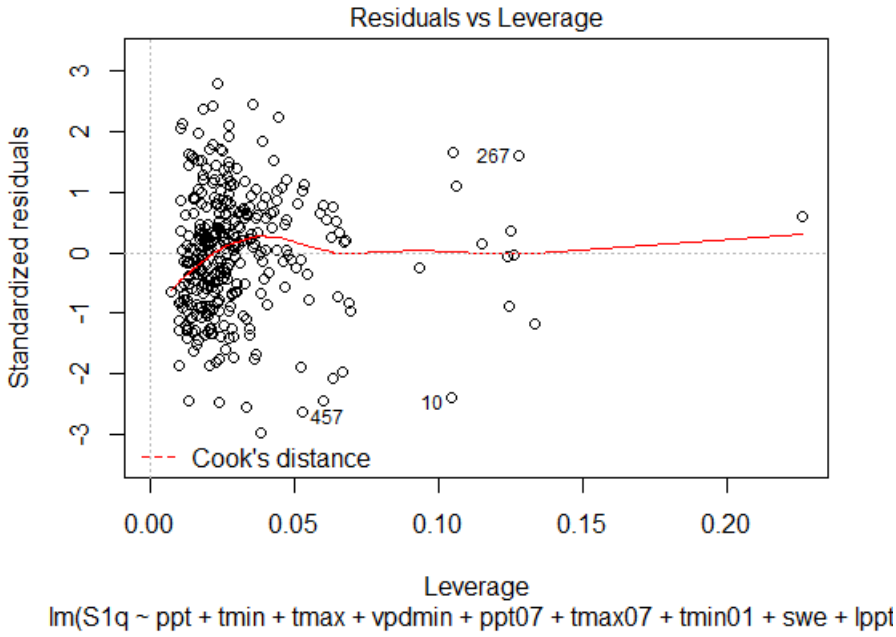

Figure C.12: Sine Coefficient (β_2) Regression Diagnostics - Residual Leverage and Cooks Distance

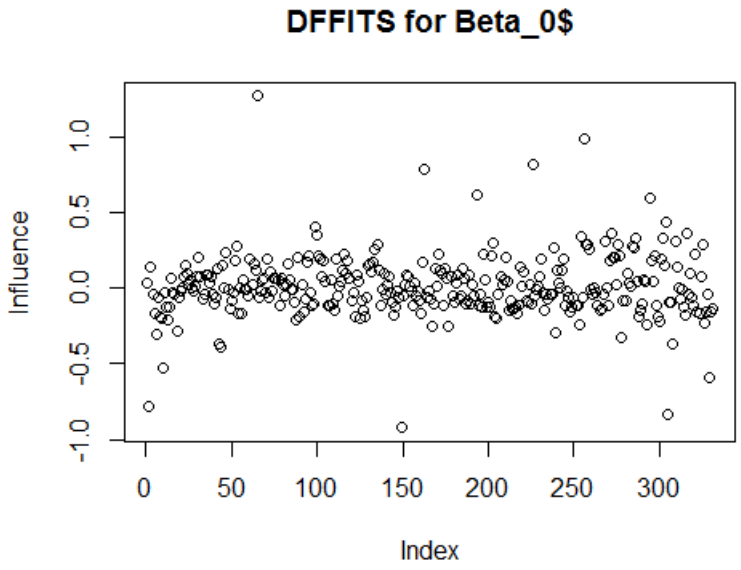

Figure C.13: Measure of Influence on Individual Regressed Observation (DFFITS), β_0

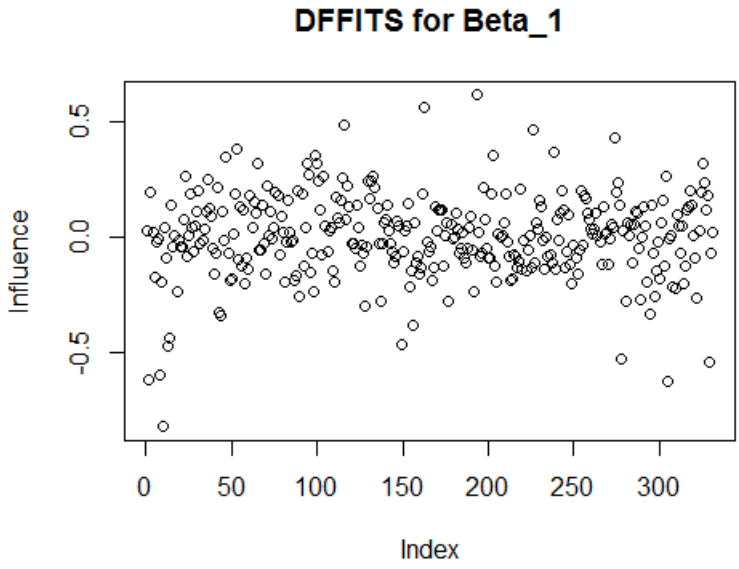

Figure C.14: Measure of Influence on Individual Regressed Observation (DFFITS), β_1

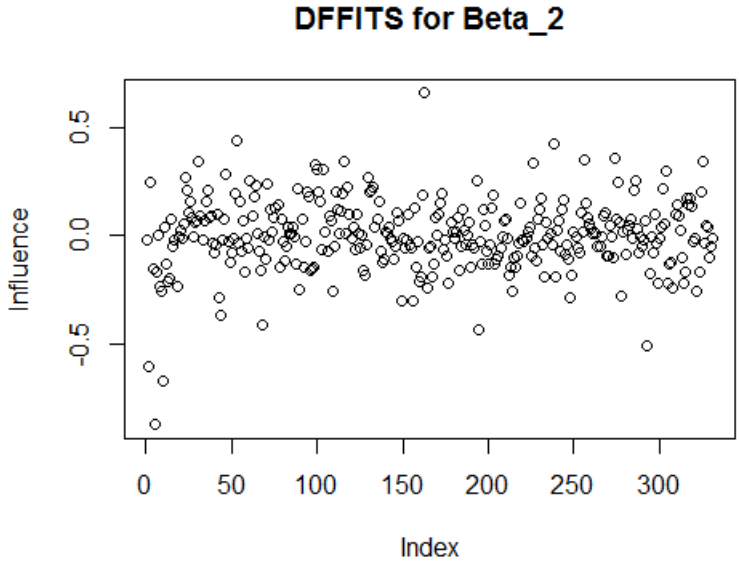

Figure C.15: Measure of Influence on Individual Regressed Observation (DFFITS), β_2

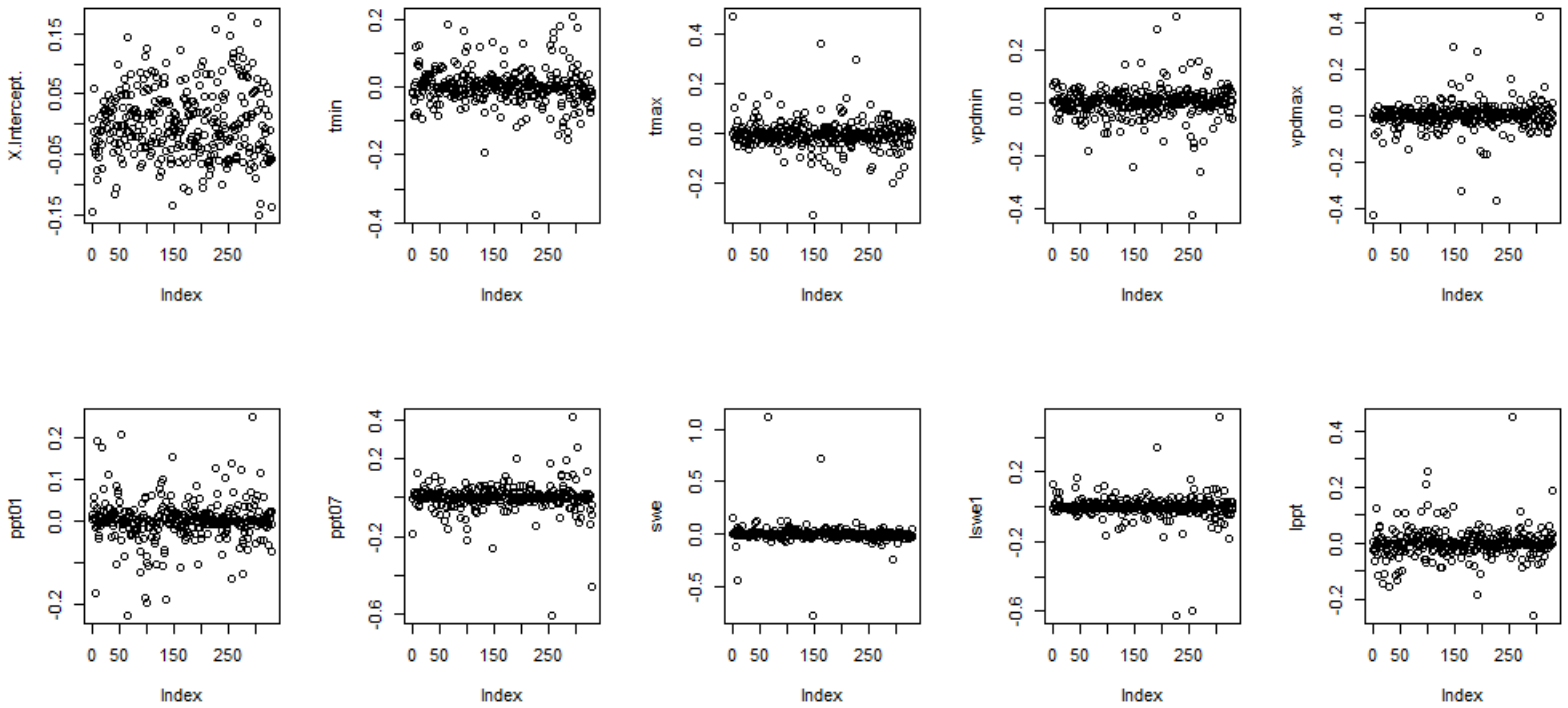

Figure C.16: Measure of Influence on Individual Regressed Coefficient (DFBETA), β_0

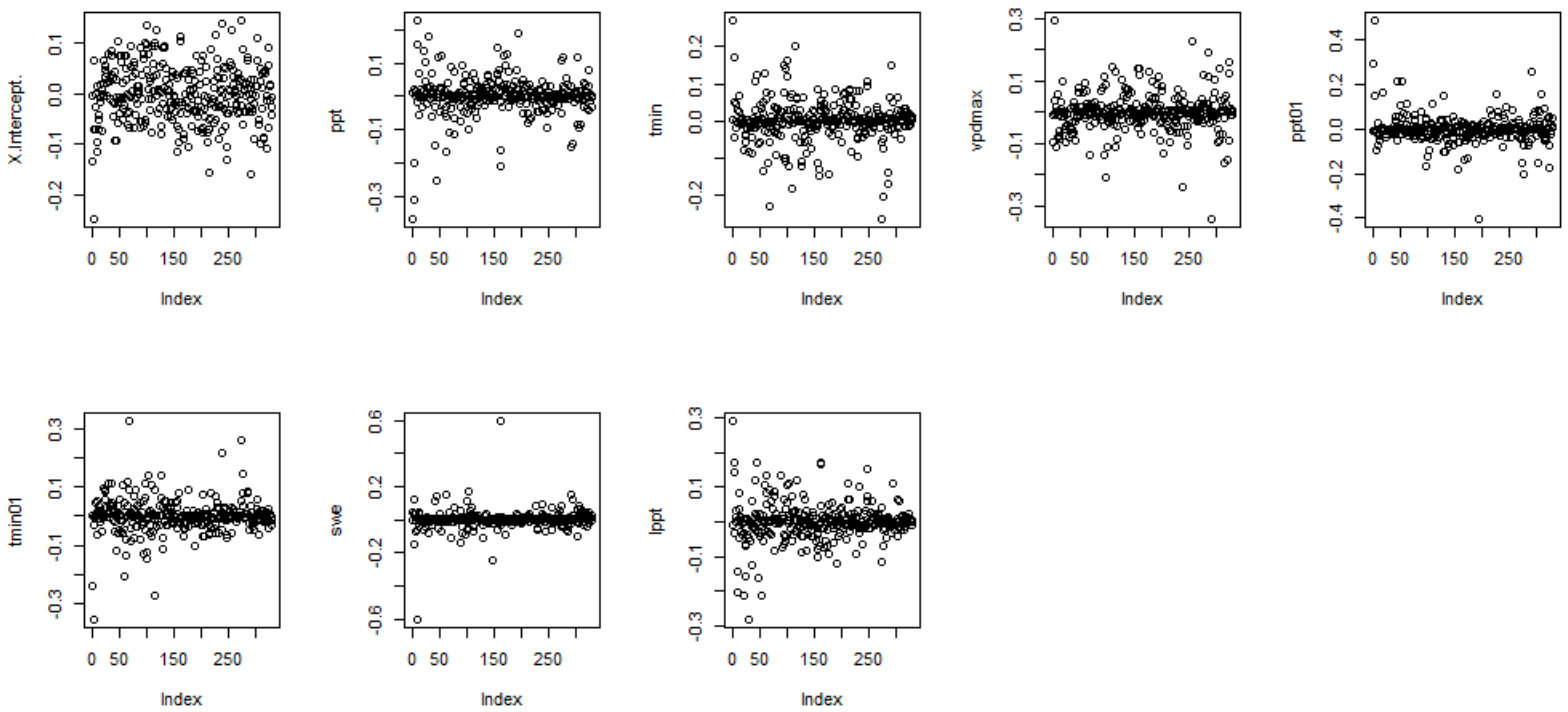

Figure C.17: Measure of Influence on Individual Regressed Coefficient (DFBETA), β_1

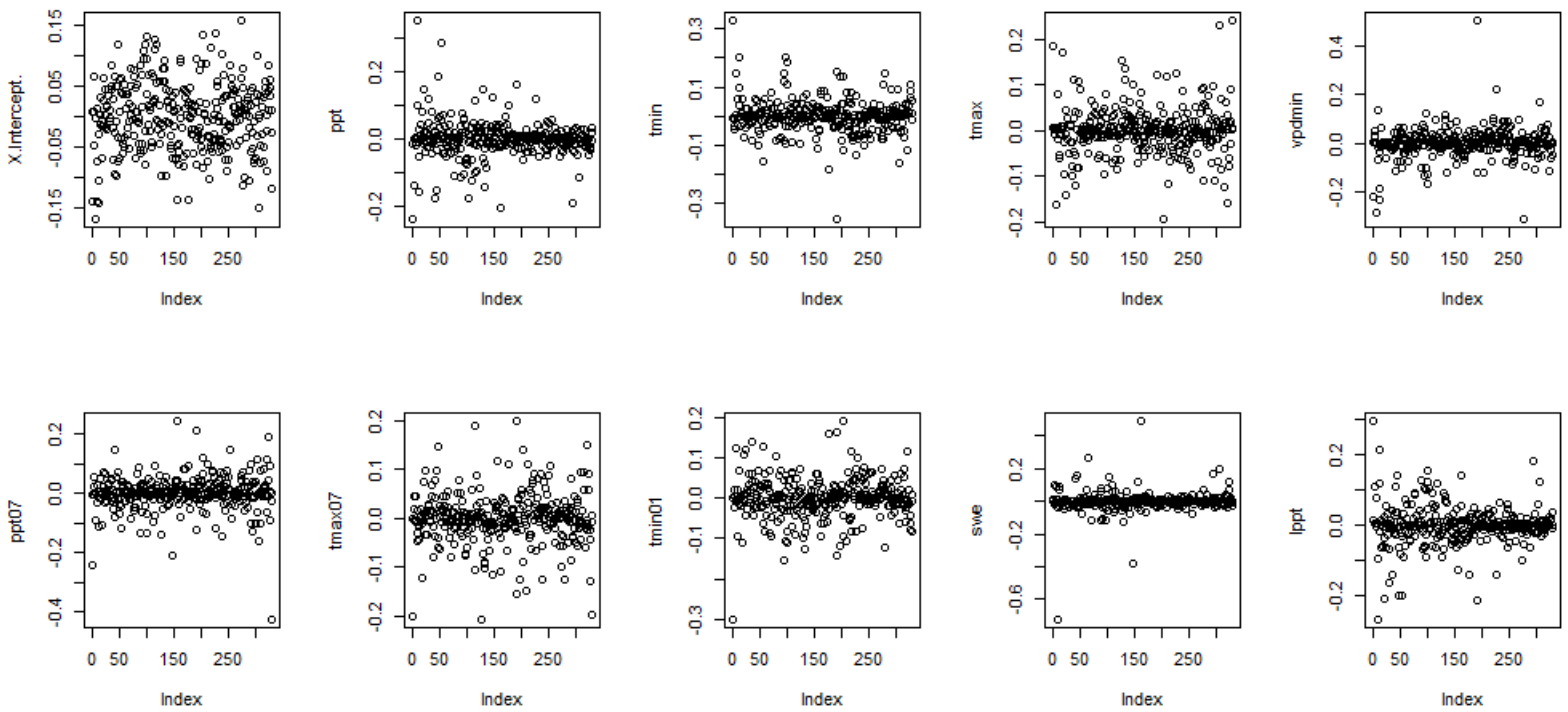

Figure C.18: Measure of Influence on Individual Regressed Coefficient (DFBETA), β_2

C.2 Histograms of Fitness Metrics

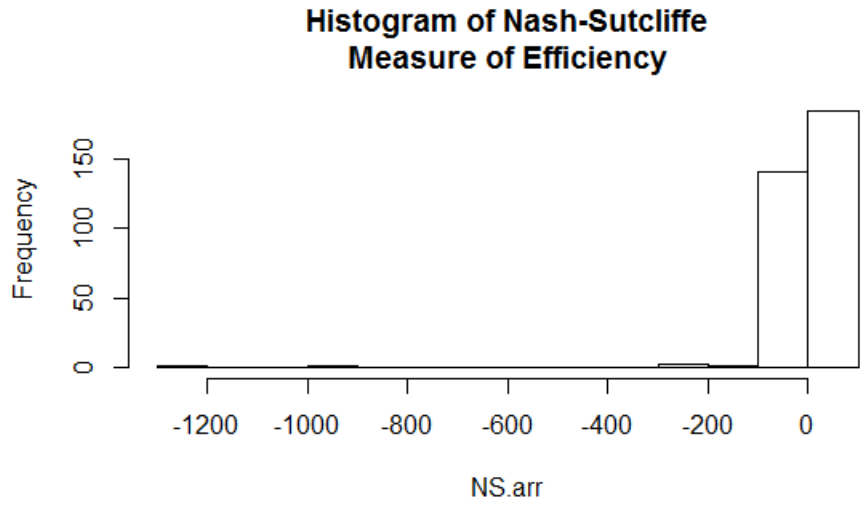

Figure C.19: Histogram of Nash-Sutcliffe Measures of Efficiency

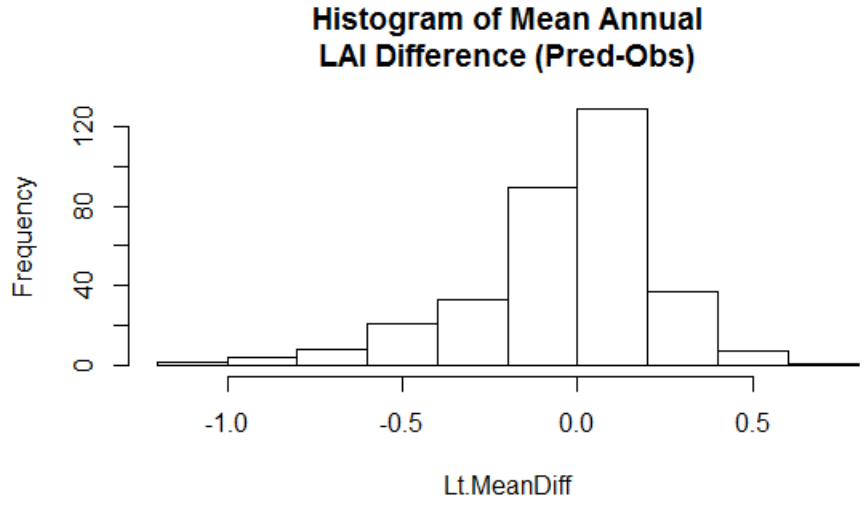

Figure C.20: Histogram of Annual Mean LAI Difference

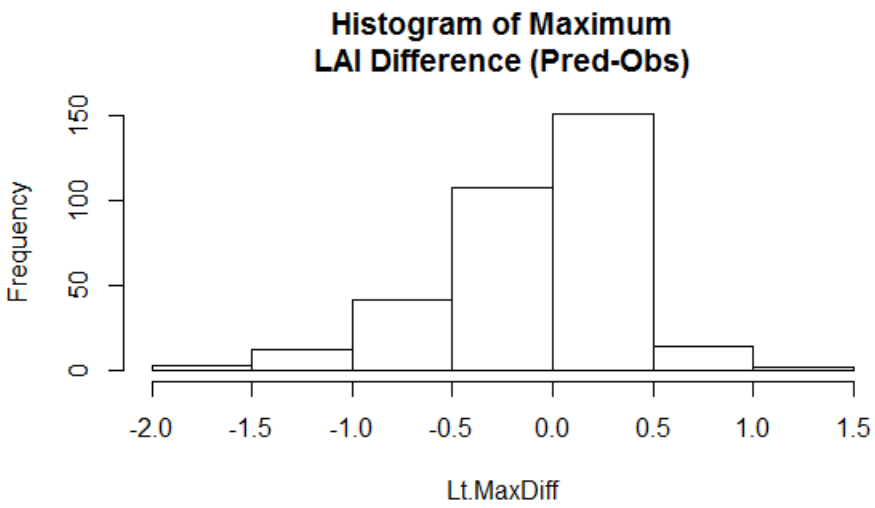

Figure C.21: Histogram of Annual Maximum LAI Difference

Appendix D

Vulnerability Analysis

D.1 Figures

D.1.1 Yield

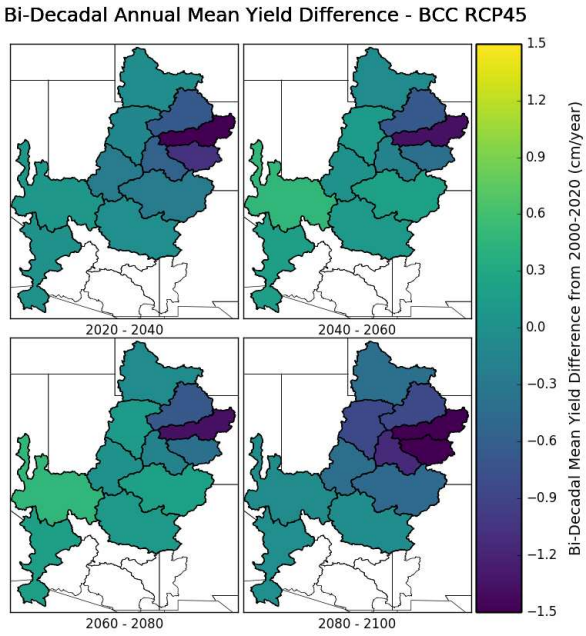

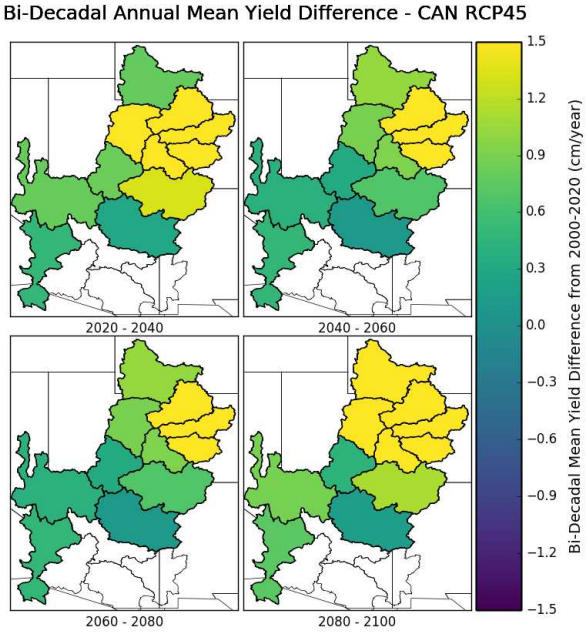
Bi-Decadal Annual Mean Yield Difference - CAN RCP45
2020 - 2040
2040 - 2060
2060 - 2080
2080 - 2100
1.5
1.2
0.9
0.6
0.3
0.0
−0.3
−0.6
−0.9
−1.2
−1.5
Bi-Decadal Mean Yield Difference from 2000-2020 (cm/year)

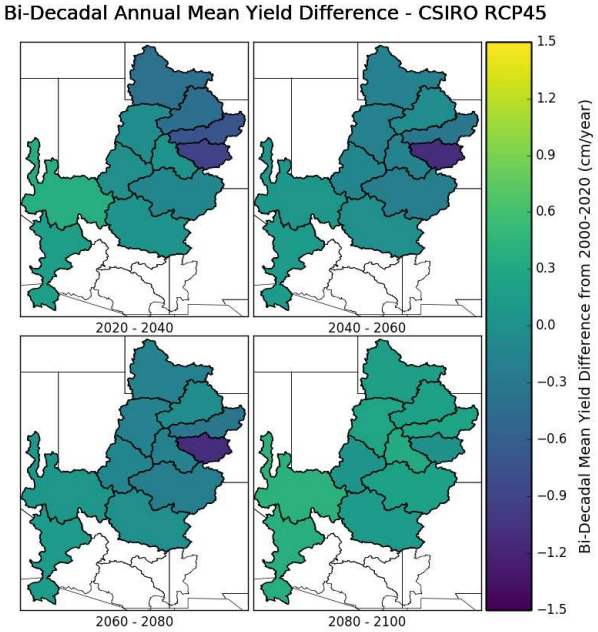
Bi-Decadal Annual Mean Yield Difference - CSIRO RCP45
2020 - 2040
2040 - 2060
2060 - 2080
2080 - 2100
1.5
1.2
0.9
0.6
0.3
0.0
−0.3
−0.6
−0.9
−1.2
−1.5
Bi-Decadal Mean Yield Difference from 2000-2020 (cm/year)

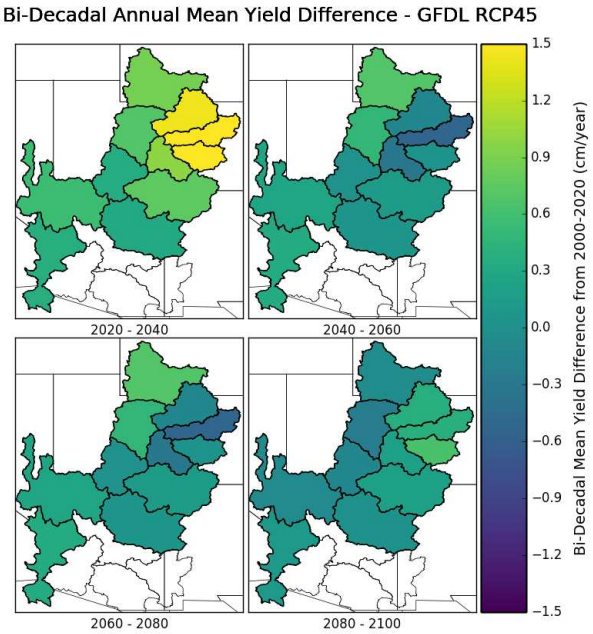
Bi-Decadal Annual Mean Yield Difference - GFDL RCP45
2020 - 2040
2040 - 2060
2060 - 2080
2080 - 2100
1.5
1.2
0.9
0.6
0.3
0.0
−0.3
−0.6
−0.9
−1.2
−1.5
Bi-Decadal Mean Yield Difference from 2000-2020 (cm/year)

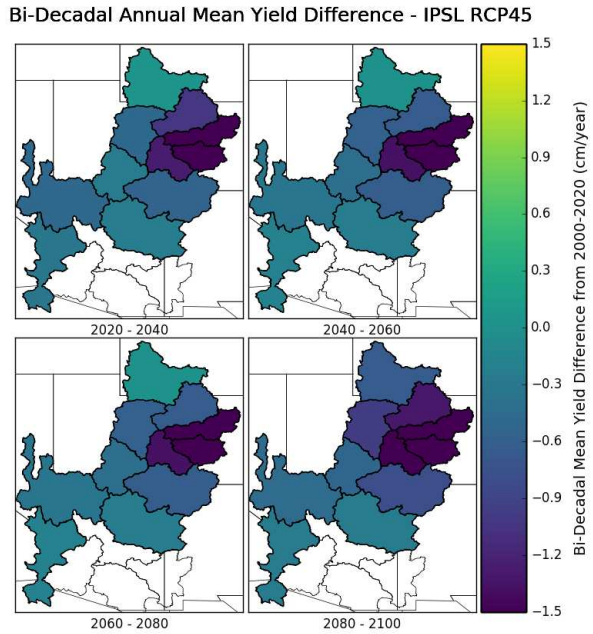
Bi-Decadal Annual Mean Yield Difference - IPSL RCP45
2020 - 2040
2040 - 2060
2060 - 2080
2080 - 2100
1.5
1.2
0.9
0.6
0.3
0.0
−0.3
−0.6
−0.9
−1.2
−1.5
Bi-Decadal Mean Yield Difference from 2000-2020 (cm/year)

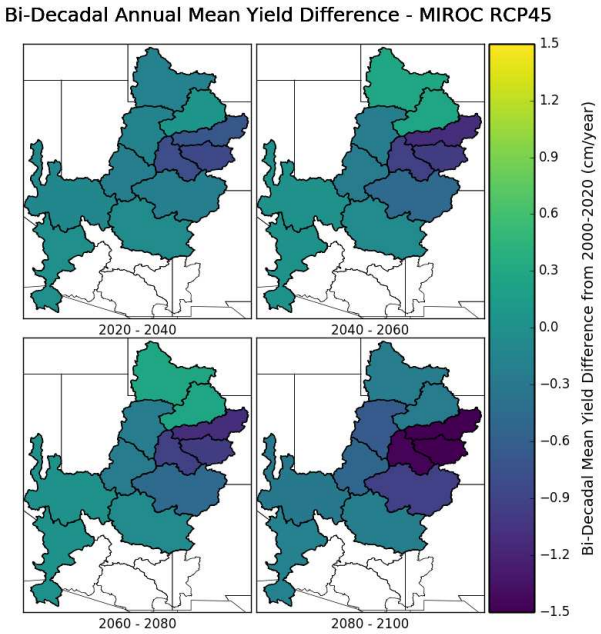
Bi-Decadal Annual Mean Yield Difference - MIROC RCP45
2020 - 2040
2040 - 2060
2060 - 2080
2080 - 2100
1.5
1.2
0.9
0.6
0.3
0.0
−0.3
−0.6
−0.9
−1.2
−1.5
Bi-Decadal Mean Yield Difference from 2000-2020 (cm/year)

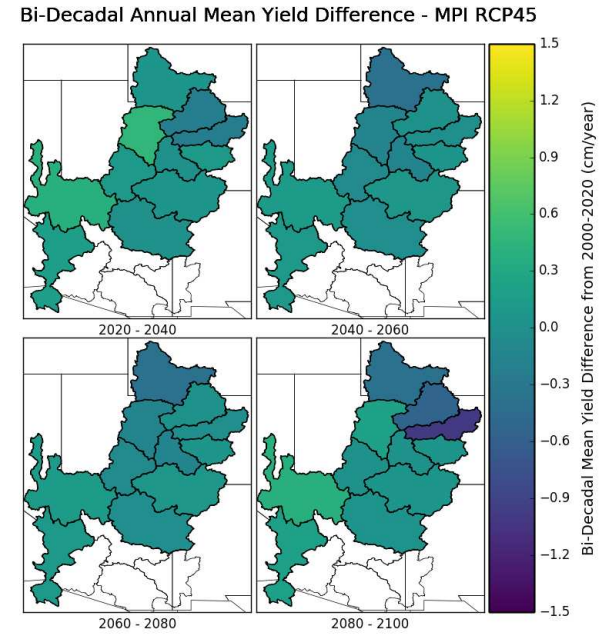
Bi-Decadal Annual Mean Yield Difference - MPI RCP45
2020 - 2040
2040 - 2060
2060 - 2080
2080 - 2100
1.5
1.2
0.9
0.6
0.3
0.0
−0.3
−0.6
−0.9
−1.2
−1.5
Bi-Decadal Mean Yield Difference from 2000-2020 (cm/year)

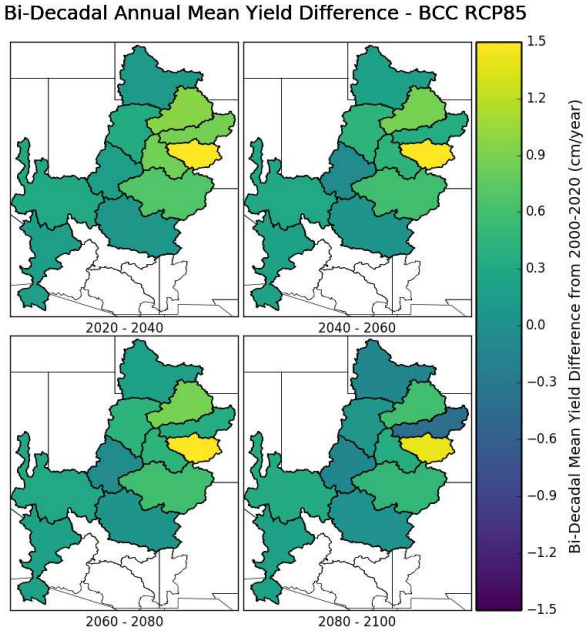
Bi-Decadal Annual Mean Yield Difference - BCC RCP85
2020 - 2040
2040 - 2060
2060 - 2080
2080 - 2100
1.5
1.2
0.9
0.6
0.3
0.0
−0.3
−0.6
−0.9
−1.2
−1.5
Bi-Decadal Mean Yield Difference from 2000-2020 (cm/year)

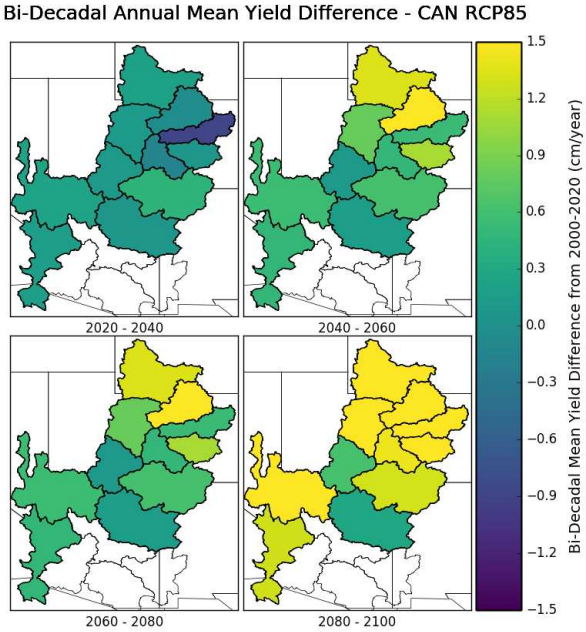
Bi-Decadal Annual Mean Yield Difference - CAN RCP85
2020 - 2040
2040 - 2060
2060 - 2080
2080 - 2100
1.5
1.2
0.9
0.6
0.3
0.0
−0.3
−0.6
−0.9
−1.2
−1.5
Bi-Decadal Mean Yield Difference from 2000-2020 (cm/year)

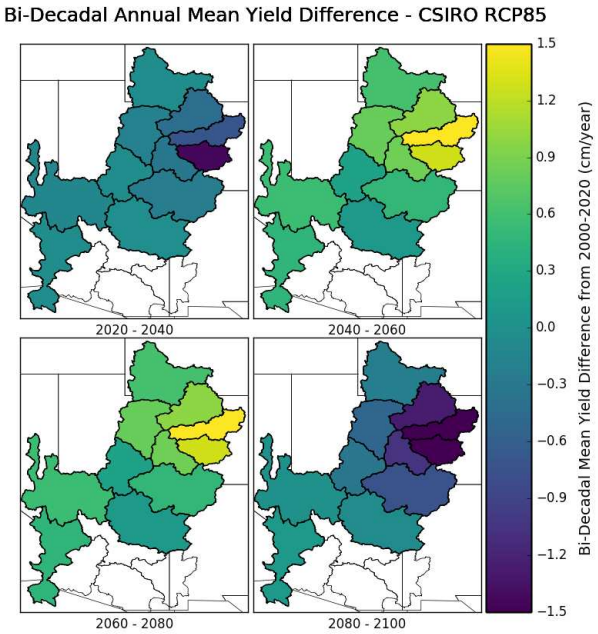
Bi-Decadal Annual Mean Yield Difference - CSIRO RCP85
2020 - 2040
2040 - 2060
2060 - 2080
2080 - 2100
1.5
1.2
0.9
0.6
0.3
0.0
−0.3
−0.6
−0.9
−1.2
−1.5
Bi-Decadal Mean Yield Difference from 2000-2020 (cm/year)

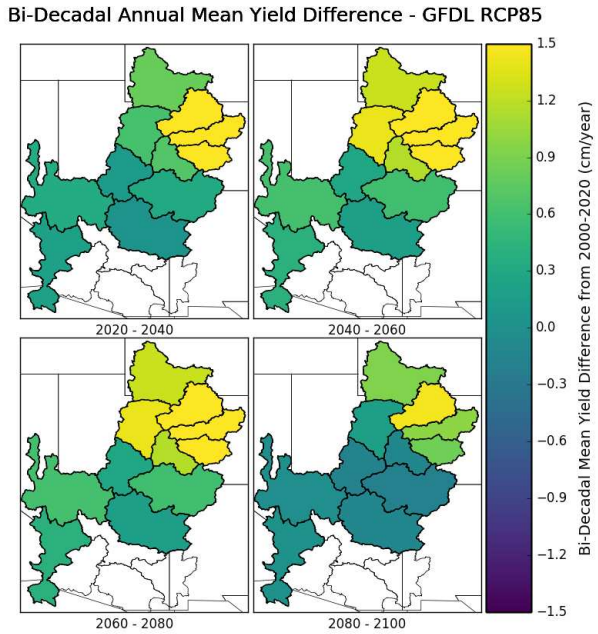
Bi-Decadal Annual Mean Yield Difference - GFDL RCP85
2020 - 2040
2040 - 2060
2060 - 2080
2080 - 2100
1.5
1.2
0.9
0.6
0.3
0.0
−0.3
−0.6
−0.9
−1.2
−1.5
Bi-Decadal Mean Yield Difference from 2000-2020 (cm/year)

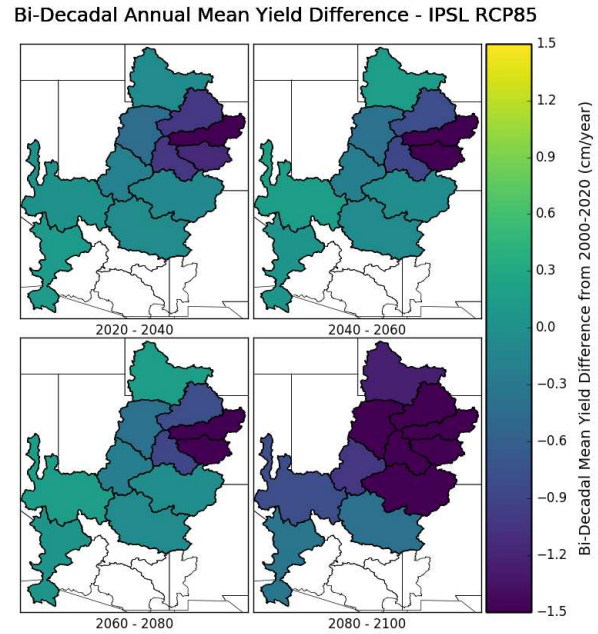
Bi-Decadal Annual Mean Yield Difference - IPSL RCP85
2020 - 2040
2040 - 2060
2060 - 2080
2080 - 2100
1.5
1.2
0.9
0.6
0.3
0.0
−0.3
−0.6
−0.9
−1.2
−1.5
Bi-Decadal Mean Yield Difference from 2000-2020 (cm/year)

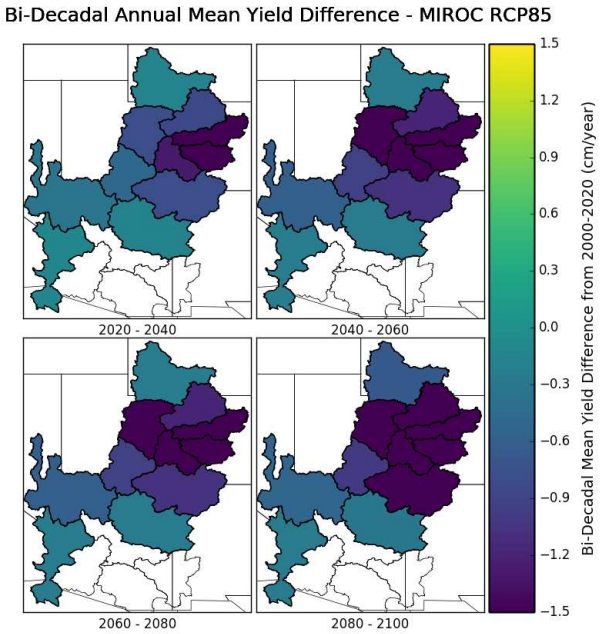
Bi-Decadal Annual Mean Yield Difference - MIROC RCP85
2020 - 2040
2040 - 2060
2060 - 2080
2080 - 2100
1.5
1.2
0.9
0.6
0.3
0.0
−0.3
−0.6
−0.9
−1.2
−1.5
Bi-Decadal Mean Yield Difference from 2000-2020 (cm/year)

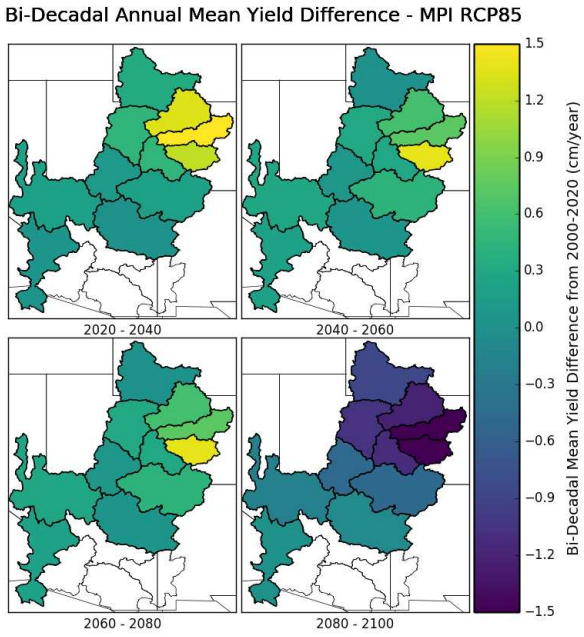
Bi-Decadal Annual Mean Yield Difference - MPI RCP85
2020 - 2040
2040 - 2060
2060 - 2080
2080 - 2100
1.5
1.2
0.9
0.6
0.3
0.0
−0.3
−0.6
−0.9
−1.2
−1.5
Bi-Decadal Mean Yield Difference from 2000-2020 (cm/year)

D.1.2 Vulnerability

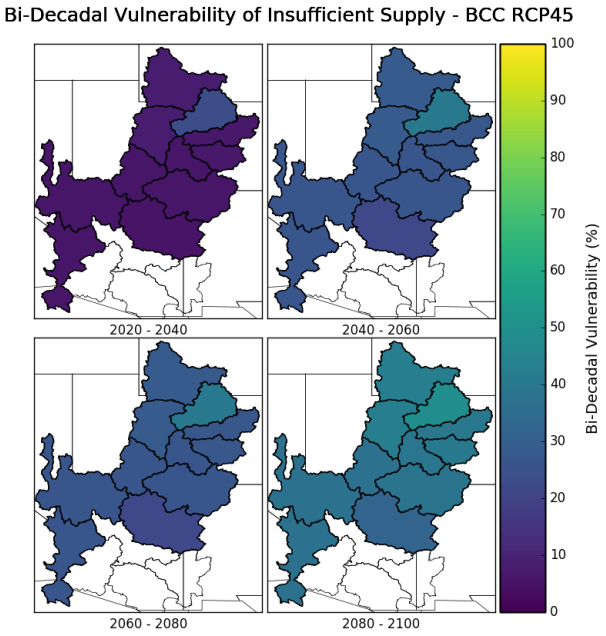

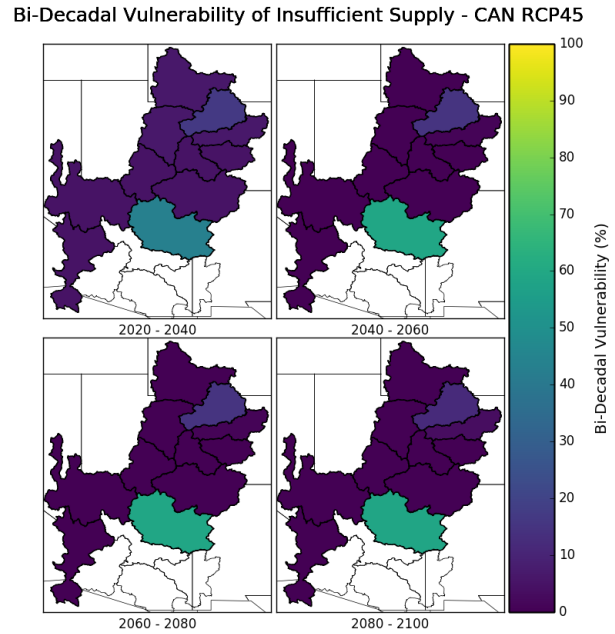
Bi-Decadal Vulnerability of Insufficient Supply - CAN RCP45
2020 - 2040
2040 - 2060
2060 - 2080
2080 - 2100
Bi-Decadal Vulnerability (%)
100
90
80
70
60
50
40
30
20
10
0

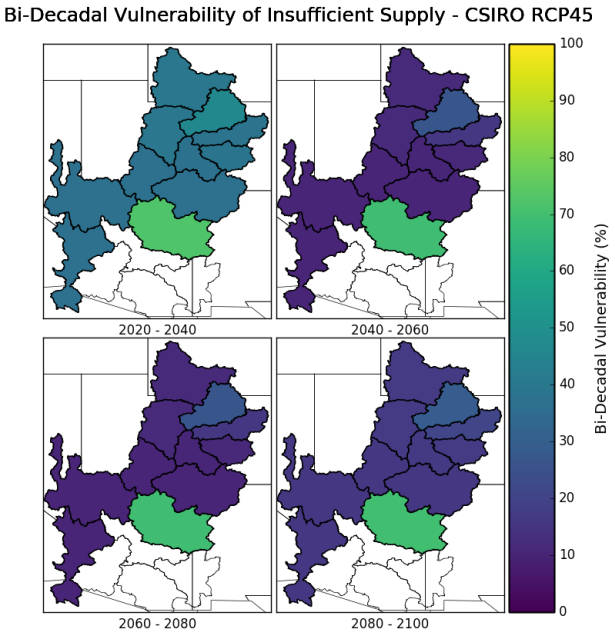
Bi-Decadal Vulnerability of Insufficient Supply - CSIRO RCP45
2020 - 2040
2040 - 2060
2060 - 2080
2080 - 2100
Bi-Decadal Vulnerability (%)
100
90
80
70
60
50
40
30
20
10
0

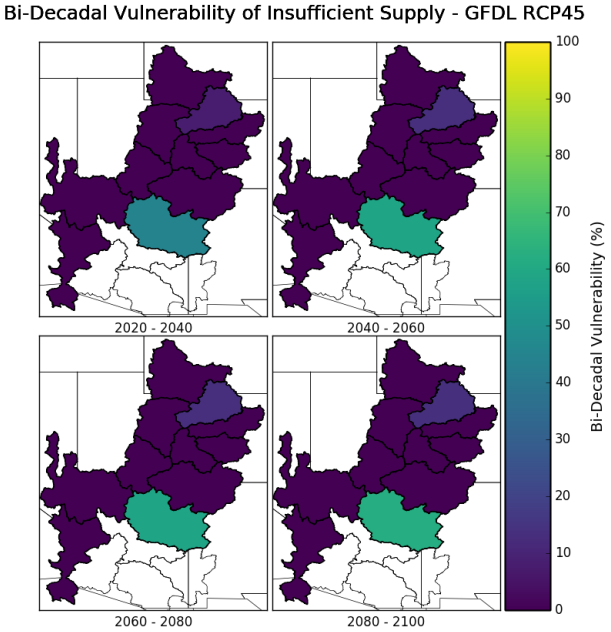
Bi-Decadal Vulnerability of Insufficient Supply - GFDL RCP45
2020 - 2040
2040 - 2060
2060 - 2080
2080 - 2100
Bi-Decadal Vulnerability (%)
100
90
80
70
60
50
40
30
20
10
0

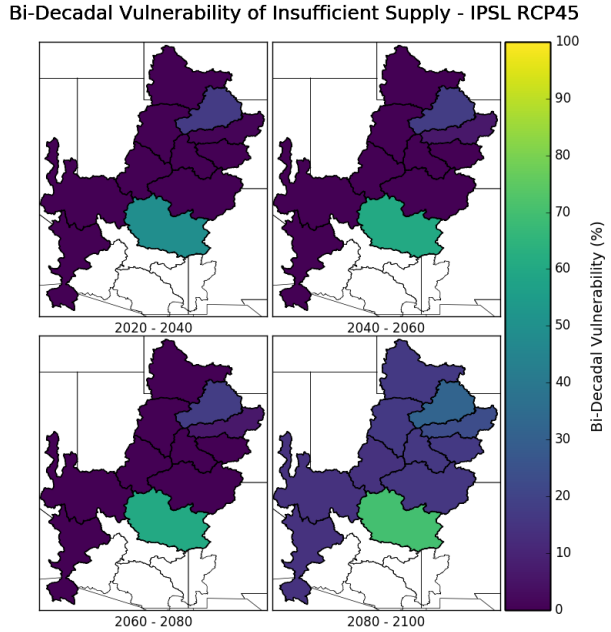
Bi-Decadal Vulnerability of Insufficient Supply - IPSL RCP45
2020 - 2040
2040 - 2060
2060 - 2080
2080 - 2100
Bi-Decadal Vulnerability (%)
100
90
80
70
60
50
40
30
20
10
0

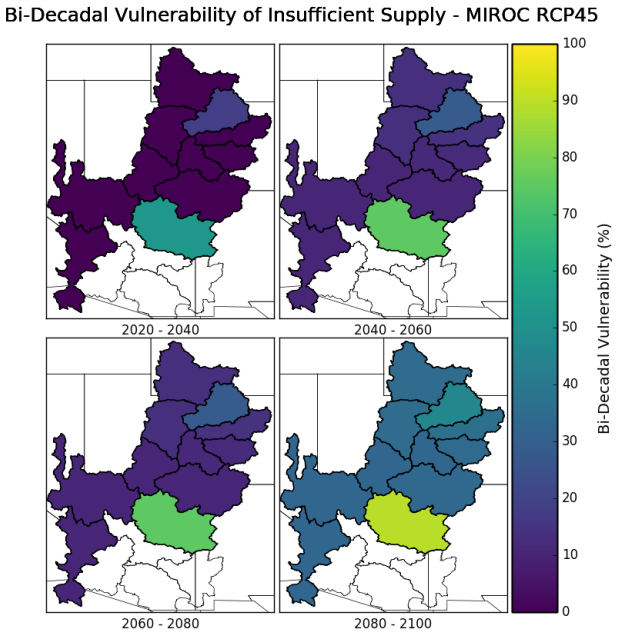
Bi-Decadal Vulnerability of Insufficient Supply - MIROC RCP45
2020 - 2040
2040 - 2060
2060 - 2080
2080 - 2100
Bi-Decadal Vulnerability (%)
100
90
80
70
60
50
40
30
20
10
0

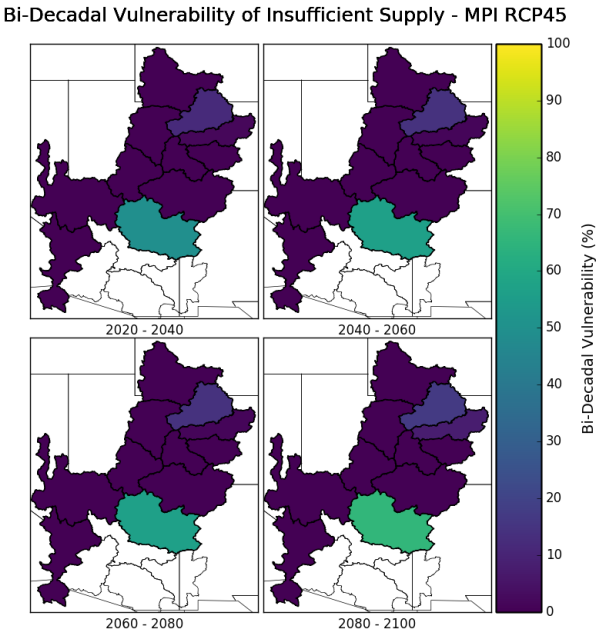
Bi-Decadal Vulnerability of Insufficient Supply - MPI RCP45
2020 - 2040
2040 - 2060
2060 - 2080
2080 - 2100
Bi-Decadal Vulnerability (%)
100
90
80
70
60
50
40
30
20
10
0

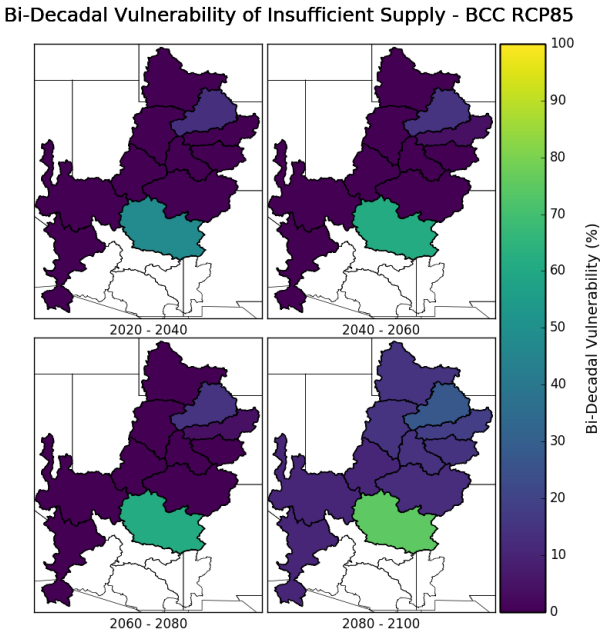
Bi-Decadal Vulnerability of Insufficient Supply - BCC RCP85
2020 - 2040
2040 - 2060
2060 - 2080
2080 - 2100
Bi-Decadal Vulnerability (%)
100
90
80
70
60
50
40
30
20
10
0

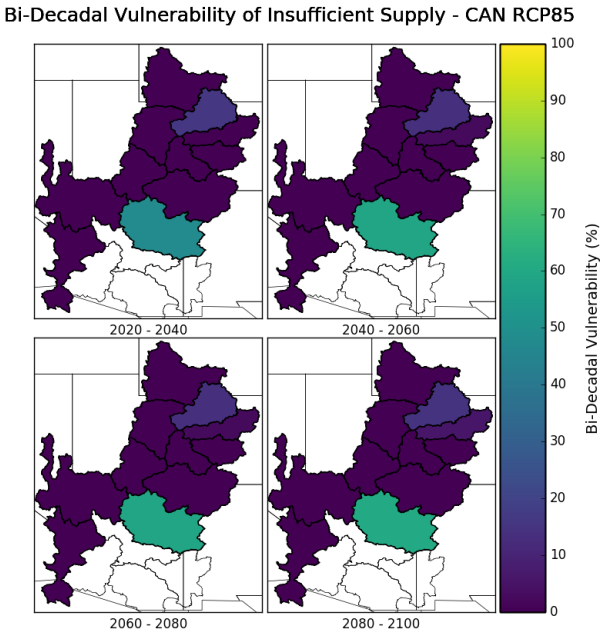
Bi-Decadal Vulnerability of Insufficient Supply - CAN RCP85
2020 - 2040
2040 - 2060
2060 - 2080
2080 - 2100
Bi-Decadal Vulnerability (%)
100
90
80
70
60
50
40
30
20
10
0

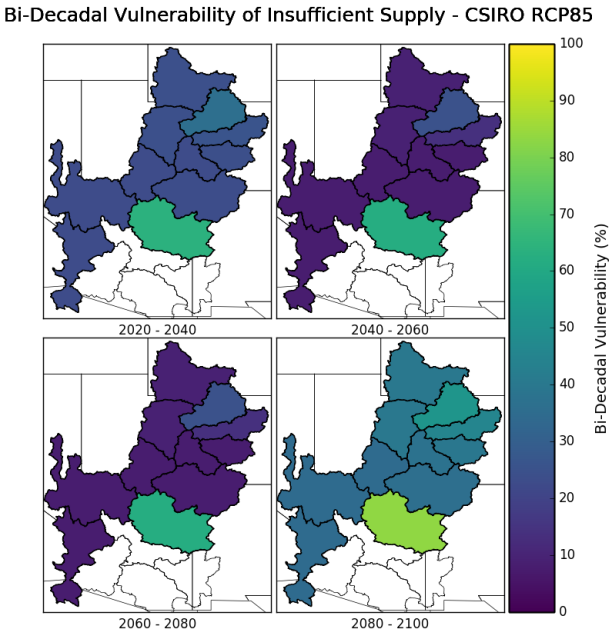
Bi-Decadal Vulnerability of Insufficient Supply - CSIRO RCP85
2020 - 2040
2040 - 2060
2060 - 2080
2080 - 2100
Bi-Decadal Vulnerability (%)
100
90
80
70
60
50
40
30
20
10
0

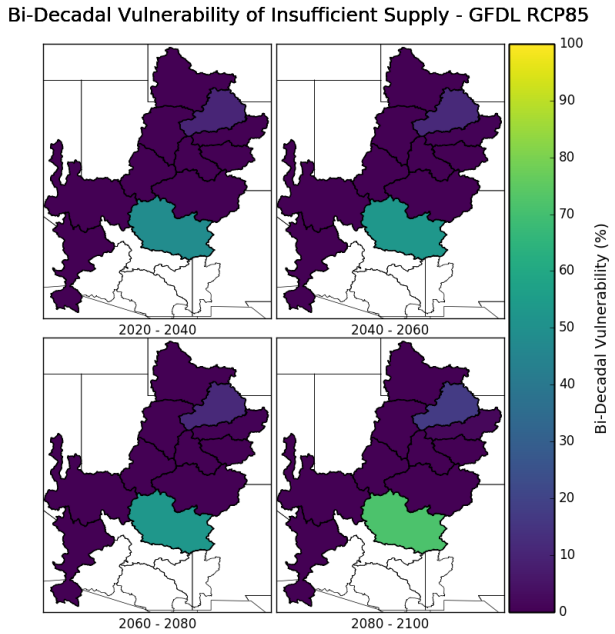
Bi-Decadal Vulnerability of Insufficient Supply - GFDL RCP85
2020 - 2040
2040 - 2060
2060 - 2080
2080 - 2100
Bi-Decadal Vulnerability (%)
100
90
80
70
60
50
40
30
20
10
0

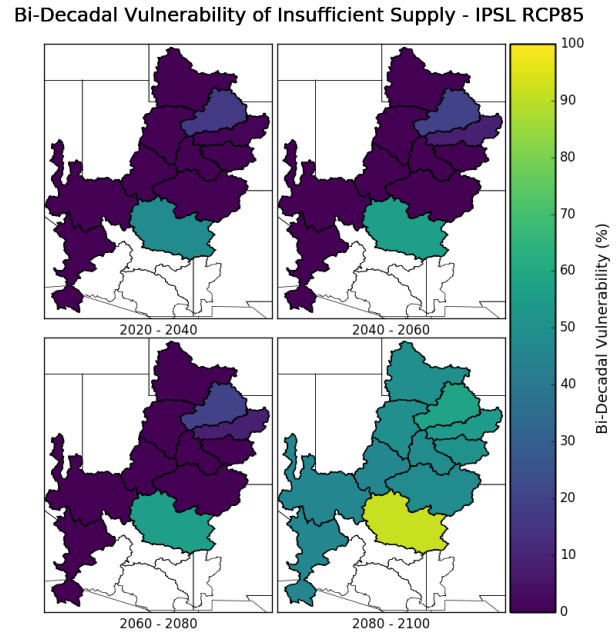
Bi-Decadal Vulnerability of Insufficient Supply - IPSL RCP85
2020 - 2040
2040 - 2060
2060 - 2080
2080 - 2100
Bi-Decadal Vulnerability (%)
100
90
80
70
60
50
40
30
20
10
0

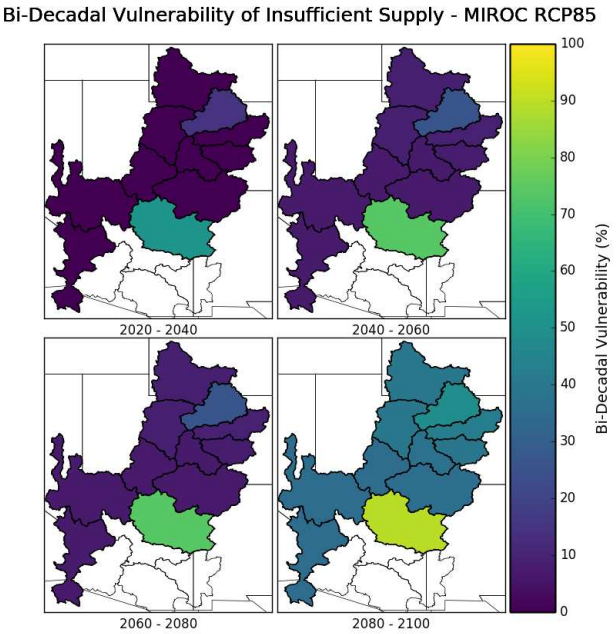
Bi-Decadal Vulnerability of Insufficient Supply - MIROC RCP85
2020 - 2040
2040 - 2060
2060 - 2080
2080 - 2100
Bi-Decadal Vulnerability (%)
100
90
80
70
60
50
40
30
20
10
0

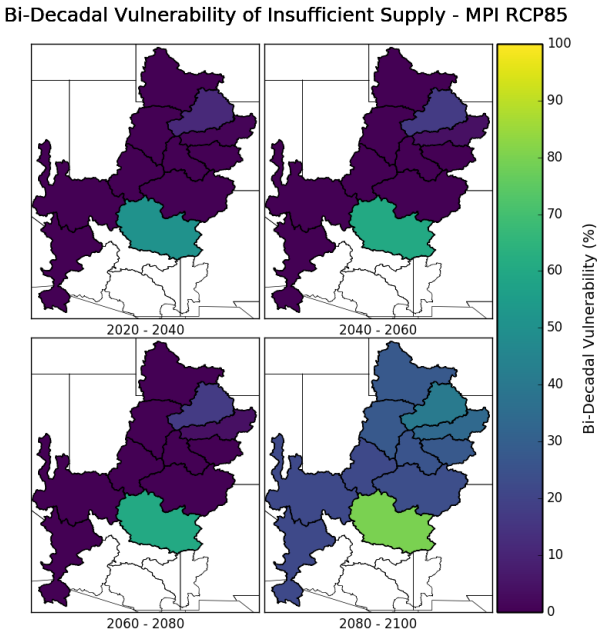
Bi-Decadal Vulnerability of Insufficient Supply - MPI RCP85
2020 - 2040
2040 - 2060
2060 - 2080
2080 - 2100
Bi-Decadal Vulnerability (%)
100
90
80
70
60
50
40
30
20
10
0

D.2 Monthly Vulnerability Summary Tables

Table D.1: Summary of Bi-Decadal Vulnerability (%) by HUC4 and Month (BCC, RCP45)

Decadal Block	Month	1401	1402	1403	1404	1405	1406	1407	1408	1501	1502	1503
2020-2040	1	5	5	5	5	5	5	5	5	5	5	5
	2	10	10	10	10	10	10	10	10	10	10	10
	3	0	0	0	0	0	0	0	0	0	0	0
	4	0	0	0	0	0	0	0	0	0	35	0
	5	0	0	0	0	0	0	0	0	0	80	0
	6	0	0	0	0	0	0	0	0	0	100	0
	7	0	0	0	5	40	5	0	0	0	100	0
	8	5	5	5	10	85	10	5	5	5	100	5
	9	5	5	5	15	95	15	5	5	5	95	5
	10	5	5	5	5	5	5	5	5	5	90	5
	11	10	10	10	10	10	10	10	10	10	40	10
	12	10	10	10	10	10	10	10	10	10	10	10
2040-2060	1	45	45	45	45	45	45	45	45	45	50	45
	2	45	45	45	45	45	45	45	45	45	55	45
	3	30	30	30	30	30	30	30	30	30	40	30
	4	15	15	15	15	15	15	15	15	15	35	15
	5	5	5	5	5	5	5	5	5	5	70	5
	6	5	5	5	5	5	5	5	5	5	95	5
	7	15	20	15	15	45	15	15	15	15	100	15
	8	30	25	25	30	95	30	25	25	25	100	25
	9	25	25	25	40	90	40	25	25	25	100	25
	10	25	25	25	25	25	25	25	25	25	90	25
	11	35	35	35	35	35	35	35	35	35	70	35
	12	35	35	35	35	35	35	35	35	35	50	35

Decadal Block	Month	1401	1402	1403	1404	1405	1406	1407	1408	1501	1502	1503
2060-2080	1	55	55	55	55	55	55	55	55	55	75	55
	2	60	60	60	60	60	60	60	60	60	75	60
	3	50	50	50	50	50	50	50	50	50	55	50
	4	30	30	30	30	30	30	30	30	30	60	30
	5	5	5	5	5	5	5	5	5	5	90	5
	6	0	0	0	0	0	0	0	0	0	100	0
	7	5	20	5	25	40	25	5	10	5	100	5
	8	55	50	50	55	95	55	30	35	30	100	30
	9	50	45	45	60	85	60	45	45	45	100	45
	10	50	50	50	50	50	50	50	50	50	95	50
	11	55	55	55	55	55	55	55	55	55	80	55
	12	55	55	55	55	55	55	55	55	55	80	55
2080-2100	1	0	0	0	0	0	0	0	0	0	60	0
	2	0	0	0	0	0	0	0	0	0	45	0
	3	0	0	0	0	0	0	0	0	0	20	0
	4	0	0	0	0	0	0	0	0	0	35	0
	5	0	0	0	0	0	0	0	0	0	75	0
	6	0	0	0	0	0	0	0	0	0	95	0
	7	0	0	0	0	20	0	0	0	0	100	0
	8	15	0	0	0	95	0	0	0	0	100	0
	9	25	0	0	0	75	0	0	0	0	100	0
	10	0	0	0	0	0	0	0	0	0	95	0
	11	0	0	0	0	0	0	0	0	0	95	0
	12	0	0	0	0	0	0	0	0	0	70	0

Table D.2: Summary of Bi-Decadal Vulnerability (%) by HUC4 and Month (CAN, RCP45)

Decadal Block	Month	1401	1402	1403	1404	1405	1406	1407	1408	1501	1502	1503
2020-2040	1	15	15	15	15	15	15	15	15	15	15	15
	2	15	15	15	15	15	15	15	15	15	15	15
	3	10	10	10	10	10	10	10	10	10	5	10
	4	0	0	0	0	0	0	0	0	0	25	0
	5	0	0	0	0	0	0	0	0	0	50	0
	6	0	0	0	0	0	0	0	0	0	75	0
	7	5	0	0	0	35	0	0	0	0	95	0
	8	5	0	0	10	65	10	0	0	0	90	0
	9	10	5	5	10	45	10	5	5	5	80	5
	10	5	5	5	5	5	5	5	5	5	45	5
	11	5	5	5	5	5	5	5	5	5	20	5
	12	5	5	5	5	5	5	5	5	5	5	5
2040-2060	1	0	0	0	0	0	0	0	0	0	10	0
	2	0	0	0	0	0	0	0	0	0	10	0
	3	0	0	0	0	0	0	0	0	0	0	0
	4	0	0	0	0	0	0	0	0	0	35	0
	5	0	0	0	0	0	0	0	0	0	85	0
	6	0	0	0	0	0	0	0	0	0	100	0
	7	0	0	0	0	45	0	0	0	0	100	0
	8	5	0	0	0	85	0	0	0	0	100	0
	9	5	0	0	0	50	0	0	0	0	95	0
	10	0	0	0	0	0	0	0	0	0	90	0
	11	0	0	0	0	0	0	0	0	0	60	0
	12	0	0	0	0	0	0	0	0	0	25	0
2060-2080	1	0	0	0	0	0	0	0	0	0	25	0
	2	0	0	0	0	0	0	0	0	0	5	0
	3	0	0	0	0	0	0	0	0	0	0	0
	4	0	0	0	0	0	0	0	0	0	30	0
	5	0	0	0	0	0	0	0	0	0	75	0
	6	0	0	0	0	0	0	0	0	0	100	0
	7	0	0	0	0	45	0	0	0	0	100	0
	8	20	0	0	0	70	0	0	0	0	95	0
	9	20	0	0	0	30	0	0	0	0	85	0
	10	0	0	0	0	0	0	0	0	0	70	0
	11	0	0	0	0	0	0	0	0	0	75	0
	12	0	0	0	0	0	0	0	0	0	45	0
2080-2100	1	0	0	0	0	0	0	0	0	0	65	0
	2	0	0	0	0	0	0	0	0	0	45	0
	3	0	0	0	0	0	0	0	0	0	30	0
	4	0	0	0	0	0	0	0	0	0	40	0
	5	0	0	0	0	0	0	0	0	0	85	0
	6	0	0	0	0	0	0	0	0	0	100	0
	7	5	0	0	0	30	0	0	0	0	100	0
	8	20	0	0	0	80	0	0	0	0	100	0
	9	40	0	0	0	55	0	0	0	0	100	0
	10	0	0	0	0	0	0	0	0	0	100	0
	11	0	0	0	0	0	0	0	0	0	95	0
	12	0	0	0	0	0	0	0	0	0	85	0

Table D.3: Summary of Bi-Decadal Vulnerability (%) by HUC4 and Month (CSIRO, RCP45)

Decadal Block	Month	1401	1402	1403	1404	1405	1406	1407	1408	1501	1502	1503
2020-2040	1	45	45	45	45	45	45	45	45	45	45	45
	2	45	45	45	45	45	45	45	45	45	50	45
	3	50	50	50	50	50	50	50	50	50	50	50
	4	50	50	50	50	50	50	50	50	50	65	50
	5	15	15	15	15	15	15	15	15	15	80	15
	6	5	5	5	5	5	5	5	5	5	100	5
	7	20	25	20	30	40	30	20	20	20	100	20
	8	45	45	40	50	95	50	35	35	35	100	35
	9	45	45	45	50	80	50	45	45	45	100	45
	10	45	45	45	45	45	45	45	45	45	80	45
	11	45	45	45	45	45	45	45	45	45	55	45
	12	45	45	45	45	45	45	45	45	45	45	45
2040-2060	1	25	25	25	25	25	25	25	25	25	40	25
	2	25	25	25	25	25	25	25	25	25	50	25
	3	20	20	20	20	20	20	20	20	20	20	20
	4	0	0	0	0	0	0	0	0	0	45	0
	5	0	0	0	0	0	0	0	0	0	85	0
	6	0	0	0	0	0	0	0	0	0	100	0
	7	10	5	0	5	45	5	0	0	0	100	0
	8	40	10	10	10	100	10	5	5	5	100	5
	9	30	10	10	20	65	20	10	10	10	95	10
	10	10	10	10	10	10	10	10	10	10	80	10
	11	10	10	10	10	10	10	10	10	10	75	10
	12	20	20	20	20	20	20	20	20	20	40	20
2060-2080	1	25	25	25	25	25	25	25	25	25	50	25
	2	25	25	25	25	25	25	25	25	25	45	25
	3	20	20	20	20	20	20	20	20	20	30	20
	4	15	15	15	15	15	15	15	15	15	30	15
	5	0	0	0	0	0	0	0	0	0	75	0
	6	0	0	0	0	0	0	0	0	0	100	0
	7	15	20	15	20	50	20	10	10	10	100	10
	8	45	25	25	20	100	20	20	20	20	100	20
	9	50	25	20	30	60	30	20	20	20	95	20
	10	15	15	15	15	15	15	15	15	15	80	15
	11	15	15	15	15	15	15	15	15	15	70	15
	12	25	25	25	25	25	25	25	25	25	60	25
2080-2100	1	55	55	55	55	55	55	55	55	55	85	55
	2	50	50	50	50	50	50	50	50	50	60	50
	3	40	40	40	40	40	40	40	40	40	50	40
	4	15	15	15	15	15	15	15	15	15	60	15
	5	0	0	0	0	0	0	0	0	0	85	0
	6	5	5	5	5	5	5	5	10	5	100	5
	7	30	30	25	30	75	30	20	25	20	100	20
	8	70	60	40	55	100	55	25	25	25	100	25
	9	85	65	60	70	90	70	45	45	45	100	45
	10	55	55	55	55	55	55	55	55	55	100	55
	11	60	60	60	60	60	60	60	60	60	100	60
	12	60	60	60	60	60	60	60	60	60	95	60

Table D.4: Summary of Bi-Decadal Vulnerability (%) by HUC4 and Month (GFDL, RCP45)

Decadal Block	Month	1401	1402	1403	1404	1405	1406	1407	1408	1501	1502	1503
2020-2040	1	0	0	0	0	0	0	0	0	0	0	0
	2	0	0	0	0	0	0	0	0	0	0	0
	3	0	0	0	0	0	0	0	0	0	0	0
	4	0	0	0	0	0	0	0	0	0	10	0
	5	0	0	0	0	0	0	0	0	0	60	0
	6	0	0	0	0	0	0	0	0	0	100	0
	7	0	0	0	0	10	0	0	0	0	100	0
	8	0	0	0	0	50	0	0	0	0	100	0
	9	0	0	0	0	35	0	0	0	0	95	0
	10	0	0	0	0	0	0	0	0	0	45	0
	11	0	0	0	0	0	0	0	0	0	25	0
	12	0	0	0	0	0	0	0	0	0	0	0
2040-2060	1	0	0	0	0	0	0	0	0	0	10	0
	2	0	0	0	0	0	0	0	0	0	10	0
	3	0	0	0	0	0	0	0	0	0	10	0
	4	0	0	0	0	0	0	0	0	0	35	0
	5	0	0	0	0	0	0	0	0	0	55	0
	6	0	0	0	0	0	0	0	0	0	100	0
	7	0	0	0	0	30	0	0	0	0	100	0
	8	0	0	0	0	60	0	0	0	0	100	0
	9	0	0	0	0	70	0	0	0	0	100	0
	10	0	0	0	0	0	0	0	0	0	90	0
	11	0	0	0	0	0	0	0	0	0	65	0
	12	0	0	0	0	0	0	0	0	0	25	0
2060-2080	1	0	0	0	0	0	0	0	0	0	25	0
	2	0	0	0	0	0	0	0	0	0	20	0
	3	0	0	0	0	0	0	0	0	0	10	0
	4	0	0	0	0	0	0	0	0	0	30	0
	5	0	0	0	0	0	0	0	0	0	65	0
	6	0	0	0	0	0	0	0	0	0	100	0
	7	0	0	0	0	30	0	0	0	0	100	0
	8	0	0	0	0	85	0	0	0	0	90	0
	9	0	0	0	0	50	0	0	0	0	90	0
	10	0	0	0	0	0	0	0	0	0	90	0
	11	0	0	0	0	0	0	0	0	0	80	0
	12	0	0	0	0	0	0	0	0	0	45	0
2080-2100	1	0	0	0	0	0	0	0	0	0	45	0
	2	0	0	0	0	0	0	0	0	0	35	0
	3	0	0	0	0	0	0	0	0	0	25	0
	4	0	0	0	0	0	0	0	0	0	45	0
	5	0	0	0	0	0	0	0	0	0	75	0
	6	0	0	0	0	0	0	0	0	0	100	0
	7	10	0	0	0	35	0	0	0	0	100	0
	8	10	0	0	0	60	0	0	0	0	100	0
	9	0	0	0	0	50	0	0	0	0	95	0
	10	0	0	0	0	0	0	0	0	0	95	0
	11	0	0	0	0	0	0	0	0	0	75	0
	12	0	0	0	0	0	0	0	0	0	55	0

Table D.5: Summary of Bi-Decadal Vulnerability (%) by HUC4 and Month (IPSL, RCP45)

Decadal Block	Month	1401	1402	1403	1404	1405	1406	1407	1408	1501	1502	1503
2020-2040	1	0	0	0	0	0	0	0	0	0	0	0
	2	0	0	0	0	0	0	0	0	0	0	0
	3	0	0	0	0	0	0	0	0	0	0	0
	4	0	0	0	0	0	0	0	0	0	25	0
	5	0	0	0	0	0	0	0	0	0	60	0
	6	0	0	0	0	0	0	0	0	0	100	0
	7	5	0	0	0	40	0	0	0	0	100	0
	8	5	0	0	0	95	0	0	0	0	100	0
	9	0	0	0	0	75	0	0	0	0	100	0
	10	0	0	0	0	0	0	0	0	0	80	0
	11	0	0	0	0	0	0	0	0	0	25	0
	12	0	0	0	0	0	0	0	0	0	0	0
2040-2060	1	0	0	0	0	0	0	0	0	0	10	0
	2	0	0	0	0	0	0	0	0	0	15	0
	3	0	0	0	0	0	0	0	0	0	15	0
	4	0	0	0	0	0	0	0	0	0	30	0
	5	0	0	0	0	0	0	0	0	0	75	0
	6	0	0	0	0	0	0	0	0	0	100	0
	7	10	0	0	0	45	0	0	0	0	100	0
	8	30	0	0	0	95	0	0	0	0	100	0
	9	35	0	0	0	75	0	0	0	0	95	0
	10	0	0	0	0	0	0	0	0	0	90	0
	11	0	0	0	0	0	0	0	0	0	70	0
	12	0	0	0	0	0	0	0	0	0	25	0
2060-2080	1	25	25	25	25	25	25	25	25	25	40	25
	2	25	25	25	25	25	25	25	25	25	40	25
	3	10	10	10	10	10	10	10	10	10	15	10
	4	5	5	5	5	5	5	5	5	5	35	5
	5	5	5	5	5	5	5	5	5	5	90	5
	6	5	5	5	5	5	5	5	5	5	100	5
	7	20	20	15	15	60	15	5	10	5	100	5
	8	50	20	20	20	95	20	5	20	5	95	5
	9	70	20	20	25	85	25	20	20	20	100	20
	10	20	20	20	20	20	20	20	20	20	95	20
	11	20	20	20	20	20	20	20	20	20	80	20
	12	25	25	25	25	25	25	25	25	25	50	25
2080-2100	1	45	45	45	45	45	45	45	45	45	75	45
	2	45	45	45	45	45	45	45	45	45	70	45
	3	30	30	30	30	30	30	30	30	30	55	30
	4	15	15	15	15	15	15	15	15	15	75	15
	5	5	5	5	5	5	5	5	5	5	90	5
	6	10	10	10	10	10	10	10	10	10	100	10
	7	30	50	30	25	75	25	15	40	15	100	15
	8	70	50	40	50	95	50	40	40	40	100	40
	9	75	50	50	50	85	50	45	45	45	100	45
	10	45	45	45	45	45	45	45	45	45	100	45
	11	45	45	45	45	45	45	45	45	45	100	45
	12	45	45	45	45	45	45	45	45	45	90	45

Table D.6: Summary of Bi-Decadal Vulnerability (%) by HUC4 and Month (MIROC, RCP45)

Decadal Block	Month	1401	1402	1403	1404	1405	1406	1407	1408	1501	1502	1503
2020-2040	1	0	0	0	0	0	0	0	0	0	0	0
	2	0	0	0	0	0	0	0	0	0	0	0
	3	0	0	0	0	0	0	0	0	0	0	0
	4	0	0	0	0	0	0	0	0	0	45	0
	5	0	0	0	0	0	0	0	0	0	70	0
	6	0	0	0	0	0	0	0	0	0	100	0
	7	0	0	0	0	40	0	0	0	0	100	0
	8	0	0	0	0	100	0	0	0	0	100	0
	9	0	0	0	0	80	0	0	0	0	100	0
	10	0	0	0	0	0	0	0	0	0	85	0
	11	0	0	0	0	0	0	0	0	0	40	0
	12	0	0	0	0	0	0	0	0	0	0	0
2040-2060	1	20	20	20	20	20	20	20	20	20	30	20
	2	25	25	25	25	25	25	25	25	25	45	25
	3	20	20	20	20	20	20	20	20	20	35	20
	4	5	5	5	5	5	5	5	5	5	65	5
	5	0	0	0	0	0	0	0	0	0	85	0
	6	0	0	0	0	0	0	0	0	0	95	0
	7	0	5	0	5	55	5	0	0	0	100	0
	8	35	15	10	15	95	15	5	5	5	100	5
	9	20	10	10	30	75	30	10	10	10	100	10
	10	10	10	10	10	10	10	10	10	10	95	10
	11	10	10	10	10	10	10	10	10	10	90	10
	12	25	25	25	25	25	25	25	25	25	60	25
2060-2080	1	50	50	50	50	50	50	50	50	50	90	50
	2	55	55	55	55	55	55	55	55	55	85	55
	3	45	45	45	45	45	45	45	45	45	50	45
	4	15	15	15	15	15	15	15	15	15	70	15
	5	0	0	0	0	0	0	0	0	0	85	0
	6	5	5	5	5	5	5	5	5	5	100	5
	7	30	35	25	35	75	35	25	30	25	100	25
	8	50	40	35	40	95	40	35	35	35	100	35
	9	65	40	40	50	90	50	40	40	40	100	40
	10	40	40	40	40	40	40	40	40	40	100	40
	11	40	40	40	40	40	40	40	40	40	100	40
	12	45	45	45	45	45	45	45	45	45	90	45
2080-2100	1	65	65	65	65	65	65	65	65	65	90	65
	2	75	75	75	75	75	75	75	75	75	90	75
	3	50	50	50	50	50	50	50	50	50	50	50
	4	10	10	10	10	10	10	10	10	10	70	10
	5	5	5	5	5	5	5	5	5	5	100	5
	6	5	5	5	5	5	5	5	5	5	100	5
	7	5	35	5	30	85	30	5	25	5	100	5
	8	70	55	55	60	100	60	30	45	30	100	30
	9	85	55	50	80	100	80	50	50	50	100	50
	10	55	55	55	55	55	55	55	55	55	100	55
	11	60	60	60	60	60	60	60	60	60	100	60
	12	60	60	60	60	60	60	60	60	60	100	60

Table D.7: Summary of Bi-Decadal Vulnerability (%) by HUC4 and Month (MPI, RCP45)

Decadal Block	Month	1401	1402	1403	1404	1405	1406	1407	1408	1501	1502	1503
2020-2040	1	0	0	0	0	0	0	0	0	0	0	0
	2	0	0	0	0	0	0	0	0	0	0	0
	3	0	0	0	0	0	0	0	0	0	0	0
	4	0	0	0	0	0	0	0	0	0	25	0
	5	0	0	0	0	0	0	0	0	0	55	0
	6	0	0	0	0	0	0	0	0	0	95	0
	7	5	0	0	0	20	0	0	0	0	100	0
	8	10	0	0	0	70	0	0	0	0	100	0
	9	5	0	0	0	55	0	0	0	0	95	0
	10	0	0	0	0	0	0	0	0	0	75	0
	11	0	0	0	0	0	0	0	0	0	50	0
	12	0	0	0	0	0	0	0	0	0	0	0
2040-2060	1	0	0	0	0	0	0	0	0	0	5	0
	2	0	0	0	0	0	0	0	0	0	10	0
	3	0	0	0	0	0	0	0	0	0	0	0
	4	0	0	0	0	0	0	0	0	0	25	0
	5	0	0	0	0	0	0	0	0	0	50	0
	6	0	0	0	0	0	0	0	0	0	100	0
	7	0	0	0	0	25	0	0	0	0	100	0
	8	15	0	0	0	95	0	0	0	0	100	0
	9	0	0	0	0	50	0	0	0	0	100	0
	10	0	0	0	0	0	0	0	0	0	95	0
	11	0	0	0	0	0	0	0	0	0	75	0
	12	0	0	0	0	0	0	0	0	0	15	0
2060-2080	1	0	0	0	0	0	0	0	0	0	25	0
	2	0	0	0	0	0	0	0	0	0	15	0
	3	0	0	0	0	0	0	0	0	0	10	0
	4	0	0	0	0	0	0	0	0	0	40	0
	5	0	0	0	0	0	0	0	0	0	75	0
	6	0	0	0	0	0	0	0	0	0	100	0
	7	15	0	0	0	45	0	0	0	0	100	0
	8	45	0	0	0	85	0	0	0	0	100	0
	9	35	0	0	0	75	0	0	0	0	100	0
	10	0	0	0	0	0	0	0	0	0	100	0
	11	0	0	0	0	0	0	0	0	0	75	0
	12	0	0	0	0	0	0	0	0	0	50	0
2080-2100	1	0	0	0	0	0	0	0	0	0	60	0
	2	0	0	0	0	0	0	0	0	0	45	0
	3	0	0	0	0	0	0	0	0	0	30	0
	4	0	0	0	0	0	0	0	0	0	45	0
	5	0	0	0	0	0	0	0	0	0	75	0
	6	0	0	0	0	0	0	0	0	0	95	0
	7	0	0	0	0	25	0	0	0	0	100	0
	8	35	0	0	0	90	0	0	0	0	100	0
	9	55	0	0	0	60	0	0	0	0	100	0
	10	0	0	0	0	0	0	0	0	0	95	0
	11	0	0	0	0	0	0	0	0	0	95	0
	12	0	0	0	0	0	0	0	0	0	80	0

Table D.8: Summary of Bi-Decadal Vulnerability (%) by HUC4 and Month (BCC, RCP85)

Decadal Block	Month	1401	1402	1403	1404	1405	1406	1407	1408	1501	1502	1503
2020-2040	1	0	0	0	0	0	0	0	0	0	0	0
	2	0	0	0	0	0	0	0	0	0	0	0
	3	0	0	0	0	0	0	0	0	0	0	0
	4	0	0	0	0	0	0	0	0	0	15	0
	5	0	0	0	0	0	0	0	0	0	65	0
	6	0	0	0	0	0	0	0	0	0	100	0
	7	0	0	0	0	20	0	0	0	0	100	0
	8	0	0	0	0	90	0	0	0	0	100	0
	9	0	0	0	0	55	0	0	0	0	100	0
	10	0	0	0	0	0	0	0	0	0	70	0
	11	0	0	0	0	0	0	0	0	0	20	0
	12	0	0	0	0	0	0	0	0	0	0	0
2040-2060	1	0	0	0	0	0	0	0	0	0	15	0
	2	0	0	0	0	0	0	0	0	0	5	0
	3	0	0	0	0	0	0	0	0	0	5	0
	4	0	0	0	0	0	0	0	0	0	40	0
	5	0	0	0	0	0	0	0	0	0	80	0
	6	0	0	0	0	0	0	0	0	0	100	0
	7	0	0	0	0	40	0	0	0	0	100	0
	8	25	0	0	0	80	0	0	0	0	100	0
	9	25	0	0	0	60	0	0	0	0	95	0
	10	0	0	0	0	0	0	0	0	0	90	0
	11	0	0	0	0	0	0	0	0	0	75	0
	12	0	0	0	0	0	0	0	0	0	30	0
2060-2080	1	15	15	15	15	15	15	15	15	15	40	15
	2	15	15	15	15	15	15	15	15	15	40	15
	3	10	10	10	10	10	10	10	10	10	20	10
	4	10	10	10	10	10	10	10	10	10	45	10
	5	0	0	0	0	0	0	0	0	0	90	0
	6	0	0	0	0	0	0	0	0	0	100	0
	7	10	15	10	15	40	15	5	5	5	100	5
	8	50	30	30	25	100	25	5	15	5	100	5
	9	55	25	25	35	80	35	15	25	15	100	15
	10	20	20	20	20	20	20	20	20	20	100	20
	11	15	15	15	15	15	15	15	15	15	95	15
	12	20	20	20	20	20	20	20	20	20	70	20
2080-2100	1	35	35	35	35	35	35	35	35	35	60	35
	2	40	40	40	40	40	40	40	40	40	50	40
	3	30	30	30	30	30	30	30	30	30	40	30
	4	10	10	10	10	10	10	10	10	10	65	10
	5	5	5	5	5	5	5	5	5	5	100	5
	6	10	10	10	15	15	15	10	20	10	100	10
	7	50	40	40	35	90	35	30	30	30	100	30
	8	95	60	55	55	100	55	30	35	30	100	30
	9	80	60	45	60	85	60	35	45	35	100	35
	10	35	35	35	35	35	35	35	35	35	100	35
	11	30	30	30	30	30	30	30	30	30	85	30
	12	40	40	40	40	40	40	40	40	40	85	40

Table D.9: Summary of Bi-Decadal Vulnerability (%) by HUC4 and Month (CAN, RCP85)

Decadal Block	Month	1401	1402	1403	1404	1405	1406	1407	1408	1501	1502	1503
2020-2040	1	0	0	0	0	0	0	0	0	0	0	0
	2	0	0	0	0	0	0	0	0	0	0	0
	3	0	0	0	0	0	0	0	0	0	0	0
	4	0	0	0	0	0	0	0	0	0	20	0
	5	0	0	0	0	0	0	0	0	0	60	0
	6	0	0	0	0	0	0	0	0	0	95	0
	7	0	0	0	0	30	0	0	0	0	100	0
	8	0	0	0	0	85	0	0	0	0	100	0
	9	0	0	0	0	75	0	0	0	0	100	0
	10	0	0	0	0	0	0	0	0	0	65	0
	11	0	0	0	0	0	0	0	0	0	30	0
	12	0	0	0	0	0	0	0	0	0	0	0
2040-2060	1	0	0	0	0	0	0	0	0	0	15	0
	2	0	0	0	0	0	0	0	0	0	10	0
	3	0	0	0	0	0	0	0	0	0	15	0
	4	0	0	0	0	0	0	0	0	0	35	0
	5	0	0	0	0	0	0	0	0	0	80	0
	6	0	0	0	0	0	0	0	0	0	100	0
	7	0	0	0	0	60	0	0	0	0	100	0
	8	25	0	0	0	80	0	0	0	0	95	0
	9	5	0	0	0	25	0	0	0	0	80	0
	10	0	0	0	0	0	0	0	0	0	75	0
	11	0	0	0	0	0	0	0	0	0	65	0
	12	0	0	0	0	0	0	0	0	0	35	0
2060-2080	1	0	0	0	0	0	0	0	0	0	25	0
	2	0	0	0	0	0	0	0	0	0	15	0
	3	0	0	0	0	0	0	0	0	0	10	0
	4	0	0	0	0	0	0	0	0	0	40	0
	5	0	0	0	0	0	0	0	0	0	85	0
	6	0	0	0	0	0	0	0	0	0	100	0
	7	25	0	0	0	65	0	0	0	0	100	0
	8	30	0	0	0	75	0	0	0	0	100	0
	9	15	0	0	0	35	0	0	0	0	85	0
	10	0	0	0	0	0	0	0	0	0	70	0
	11	0	0	0	0	0	0	0	0	0	65	0
	12	0	0	0	0	0	0	0	0	0	30	0
2080-2100	1	0	0	0	0	0	0	0	0	0	20	0
	2	0	0	0	0	0	0	0	0	0	20	0
	3	0	0	0	0	0	0	0	0	0	20	0
	4	0	0	0	0	0	0	0	0	0	25	0
	5	0	0	0	0	0	0	0	0	0	80	0
	6	0	0	0	0	0	0	0	0	0	100	0
	7	30	0	0	0	70	0	0	0	0	100	0
	8	55	0	0	0	70	0	0	0	0	90	0
	9	35	0	0	0	15	0	0	0	0	65	0
	10	0	0	0	0	0	0	0	0	0	55	0
	11	0	0	0	0	0	0	0	0	0	60	0
	12	0	0	0	0	0	0	0	0	0	45	0

Table D.10: Summary of Bi-Decadal Vulnerability (%) by HUC4 and Month (CSIRO, RCP85)

Decadal Block	Month	1401	1402	1403	1404	1405	1406	1407	1408	1501	1502	1503
2020-2040	1	35	35	35	35	35	35	35	35	35	35	35
	2	35	35	35	35	35	35	35	35	35	35	35
	3	35	35	35	35	35	35	35	35	35	30	35
	4	25	25	25	25	25	25	25	25	25	40	25
	5	5	5	5	5	5	5	5	5	5	70	5
	6	5	5	5	5	5	5	5	5	5	100	5
	7	25	20	15	15	40	15	15	15	15	100	15
	8	35	25	15	30	90	30	15	20	15	100	15
	9	30	25	25	30	85	30	25	25	25	100	25
	10	20	20	20	20	20	20	20	20	20	75	20
	11	30	30	30	30	30	30	30	30	30	50	30
	12	30	30	30	30	30	30	30	30	30	30	30
2040-2060	1	20	20	20	20	20	20	20	20	20	25	20
	2	20	20	20	20	20	20	20	20	20	25	20
	3	15	15	15	15	15	15	15	15	15	15	15
	4	5	5	5	5	5	5	5	5	5	35	5
	5	0	0	0	0	0	0	0	0	0	60	0
	6	0	0	0	0	0	0	0	0	0	100	0
	7	5	0	0	0	40	0	0	0	0	100	0
	8	35	0	0	5	90	5	0	0	0	95	0
	9	30	0	0	10	75	10	0	0	0	95	0
	10	10	10	10	10	10	10	10	10	10	90	10
	11	10	10	10	10	10	10	10	10	10	70	10
	12	15	15	15	15	15	15	15	15	15	35	15
2060-2080	1	55	55	55	55	55	55	55	55	55	75	55
	2	50	50	50	50	50	50	50	50	50	70	50
	3	45	45	45	45	45	45	45	45	45	50	45
	4	20	20	20	20	20	20	20	20	20	55	20
	5	10	10	10	10	10	10	10	10	10	85	10
	6	15	15	15	15	15	15	15	15	15	100	15
	7	45	45	35	35	95	35	20	35	20	100	20
	8	90	60	50	55	100	55	30	35	30	100	30
	9	80	40	35	60	100	60	35	35	35	100	35
	10	35	35	35	35	35	35	35	35	35	85	35
	11	50	50	50	50	50	50	50	50	50	90	50
	12	50	50	50	50	50	50	50	50	50	90	50
2080-2100	1	50	50	50	50	50	50	50	50	50	75	50
	2	45	45	45	45	45	45	45	45	45	70	45
	3	10	10	10	10	10	10	10	10	10	25	10
	4	0	0	0	0	0	0	0	0	0	45	0
	5	0	0	0	0	0	0	0	0	0	85	0
	6	5	5	5	0	0	0	0	0	0	100	0
	7	60	50	45	30	95	30	5	25	5	100	5
	8	100	65	25	50	100	50	15	35	15	100	15
	9	95	50	25	55	90	55	25	25	25	95	25
	10	30	30	30	30	30	30	30	30	30	80	30
	11	40	40	40	40	40	40	40	40	40	80	40
	12	45	45	45	45	45	45	45	45	45	75	45

Table D.11: Summary of Bi-Decadal Vulnerability (%) by HUC4 and Month (GFDL, RCP85)

Decadal Block	Month	1401	1402	1403	1404	1405	1406	1407	1408	1501	1502	1503
2020-2040	1	0	0	0	0	0	0	0	0	0	0	0
	2	0	0	0	0	0	0	0	0	0	0	0
	3	0	0	0	0	0	0	0	0	0	0	0
	4	0	0	0	0	0	0	0	0	0	25	0
	5	0	0	0	0	0	0	0	0	0	70	0
	6	0	0	0	0	0	0	0	0	0	95	0
	7	0	0	0	0	20	0	0	0	0	100	0
	8	0	0	0	0	55	0	0	0	0	100	0
	9	0	0	0	0	50	0	0	0	0	100	0
	10	0	0	0	0	0	0	0	0	0	65	0
	11	0	0	0	0	0	0	0	0	0	25	0
	12	0	0	0	0	0	0	0	0	0	0	0
2040-2060	1	0	0	0	0	0	0	0	0	0	10	0
	2	0	0	0	0	0	0	0	0	0	10	0
	3	0	0	0	0	0	0	0	0	0	5	0
	4	0	0	0	0	0	0	0	0	0	25	0
	5	0	0	0	0	0	0	0	0	0	60	0
	6	0	0	0	0	0	0	0	0	0	90	0
	7	5	0	0	0	25	0	0	0	0	100	0
	8	0	0	0	0	65	0	0	0	0	95	0
	9	0	0	0	0	50	0	0	0	0	95	0
	10	0	0	0	0	0	0	0	0	0	80	0
	11	0	0	0	0	0	0	0	0	0	50	0
	12	0	0	0	0	0	0	0	0	0	15	0
2060-2080	1	0	0	0	0	0	0	0	0	0	45	0
	2	0	0	0	0	0	0	0	0	0	30	0
	3	0	0	0	0	0	0	0	0	0	20	0
	4	0	0	0	0	0	0	0	0	0	50	0
	5	0	0	0	0	0	0	0	0	0	85	0
	6	0	0	0	0	0	0	0	0	0	100	0
	7	15	0	0	0	40	0	0	0	0	100	0
	8	5	0	0	0	90	0	0	0	0	95	0
	9	0	0	0	0	80	0	0	0	0	100	0
	10	0	0	0	0	0	0	0	0	0	95	0
	11	0	0	0	0	0	0	0	0	0	80	0
	12	0	0	0	0	0	0	0	0	0	60	0
2080-2100	1	0	0	0	0	0	0	0	0	0	55	0
	2	0	0	0	0	0	0	0	0	0	30	0
	3	0	0	0	0	0	0	0	0	0	15	0
	4	0	0	0	0	0	0	0	0	0	35	0
	5	0	0	0	0	0	0	0	0	0	80	0
	6	0	0	0	0	0	0	0	0	0	100	0
	7	0	0	0	0	50	0	0	0	0	100	0
	8	35	0	0	0	90	0	0	0	0	100	0
	9	40	0	0	0	65	0	0	0	0	95	0
	10	0	0	0	0	0	0	0	0	0	90	0
	11	0	0	0	0	0	0	0	0	0	90	0
	12	0	0	0	0	0	0	0	0	0	75	0

Table D.12: Summary of Bi-Decadal Vulnerability (%) by HUC4 and Month (IPSL, RCP85)

Decadal Block	Month	1401	1402	1403	1404	1405	1406	1407	1408	1501	1502	1503
2020-2040	1	0	0	0	0	0	0	0	0	0	0	0
	2	0	0	0	0	0	0	0	0	0	0	0
	3	0	0	0	0	0	0	0	0	0	0	0
	4	0	0	0	0	0	0	0	0	0	30	0
	5	0	0	0	0	0	0	0	0	0	50	0
	6	0	0	0	0	0	0	0	0	0	90	0
	7	0	0	0	0	35	0	0	0	0	100	0
	8	10	0	0	0	95	0	0	0	0	100	0
	9	0	0	0	0	75	0	0	0	0	100	0
	10	0	0	0	0	0	0	0	0	0	75	0
	11	0	0	0	0	0	0	0	0	0	30	0
	12	0	0	0	0	0	0	0	0	0	0	0
2040-2060	1	0	0	0	0	0	0	0	0	0	5	0
	2	0	0	0	0	0	0	0	0	0	10	0
	3	0	0	0	0	0	0	0	0	0	10	0
	4	0	0	0	0	0	0	0	0	0	30	0
	5	0	0	0	0	0	0	0	0	0	60	0
	6	0	0	0	0	0	0	0	0	0	100	0
	7	15	0	0	0	65	0	0	0	0	100	0
	8	50	0	0	0	100	0	0	0	0	95	0
	9	40	0	0	0	70	0	0	0	0	95	0
	10	0	0	0	0	0	0	0	0	0	90	0
	11	0	0	0	0	0	0	0	0	0	65	0
	12	0	0	0	0	0	0	0	0	0	10	0
2060-2080	1	60	60	60	60	60	60	60	60	60	90	60
	2	55	55	55	55	55	55	55	55	55	70	55
	3	45	45	45	45	45	45	45	45	45	60	45
	4	20	20	20	20	20	20	20	20	20	85	20
	5	10	10	10	10	10	10	10	10	10	95	10
	6	20	20	20	20	20	20	20	30	20	100	20
	7	65	65	50	60	95	60	40	45	40	100	40
	8	95	70	60	65	100	65	50	55	50	100	50
	9	95	75	70	70	100	70	60	65	60	100	60
	10	60	60	60	60	60	60	60	60	60	100	60
	11	65	65	65	65	65	65	65	65	65	100	65
	12	65	65	65	65	65	65	65	65	65	100	65
2080-2100	1	45	45	45	45	45	45	45	45	45	75	45
	2	25	25	25	25	25	25	25	25	25	55	25
	3	15	15	15	15	15	15	15	15	15	40	15
	4	5	5	5	5	5	5	5	5	5	50	5
	5	5	5	5	5	5	5	5	5	5	100	5
	6	10	15	10	10	15	10	10	15	10	100	10
	7	70	50	40	40	95	40	20	40	20	100	20
	8	100	60	45	40	100	40	25	35	25	100	25
	9	95	60	35	50	90	50	35	35	35	100	35
	10	40	40	40	40	40	40	40	40	40	100	40
	11	40	40	40	40	40	40	40	40	40	90	40
	12	40	40	40	40	40	40	40	40	40	80	40

Table D.13: Summary of Bi-Decadal Vulnerability (%) by HUC4 and Month (MIROC, RCP85)

Decadal Block	Month	1401	1402	1403	1404	1405	1406	1407	1408	1501	1502	1503
2020-2040	1	0	0	0	0	0	0	0	0	0	0	0
	2	0	0	0	0	0	0	0	0	0	0	0
	3	0	0	0	0	0	0	0	0	0	0	0
	4	0	0	0	0	0	0	0	0	0	35	0
	5	0	0	0	0	0	0	0	0	0	75	0
	6	0	0	0	0	0	0	0	0	0	100	0
	7	0	0	0	0	20	0	0	0	0	100	0
	8	0	0	0	0	85	0	0	0	0	100	0
	9	0	0	0	0	75	0	0	0	0	100	0
	10	0	0	0	0	0	0	0	0	0	75	0
	11	0	0	0	0	0	0	0	0	0	40	0
	12	0	0	0	0	0	0	0	0	0	0	0
2040-2060	1	20	20	20	20	20	20	20	20	20	30	20
	2	20	20	20	20	20	20	20	20	20	55	20
	3	10	10	10	10	10	10	10	10	10	20	10
	4	0	0	0	0	0	0	0	0	0	50	0
	5	0	0	0	0	0	0	0	0	0	90	0
	6	0	0	0	0	0	0	0	0	0	100	0
	7	0	0	0	0	60	0	0	0	0	100	0
	8	20	10	0	5	100	5	0	0	0	100	0
	9	5	0	0	15	70	15	0	0	0	100	0
	10	5	5	5	5	5	5	5	5	5	100	5
	11	15	15	15	15	15	15	15	15	15	90	15
	12	15	15	15	15	15	15	15	15	15	55	15
2060-2080	1	50	50	50	50	50	50	50	50	50	75	50
	2	60	60	60	60	60	60	60	60	60	85	60
	3	35	35	35	35	35	35	35	35	35	55	35
	4	5	5	5	5	5	5	5	5	5	70	5
	5	0	0	0	0	0	0	0	0	0	95	0
	6	20	20	20	20	20	20	20	20	20	100	20
	7	55	45	45	40	75	40	35	35	35	100	35
	8	70	60	40	55	100	55	35	40	35	100	35
	9	70	55	50	70	95	70	40	40	40	100	40
	10	40	40	40	40	40	40	40	40	40	100	40
	11	50	50	50	50	50	50	50	50	50	100	50
	12	55	55	55	55	55	55	55	55	55	95	55
2080-2100	1	55	55	55	55	55	55	55	55	55	85	55
	2	55	55	55	55	55	55	55	55	55	70	55
	3	35	35	35	35	35	35	35	35	35	50	35
	4	5	5	5	5	5	5	5	5	5	65	5
	5	5	5	5	5	5	5	5	5	5	95	5
	6	15	15	15	15	15	15	15	15	15	100	15
	7	60	55	45	50	95	50	25	40	25	100	25
	8	95	70	55	65	100	65	35	50	35	100	35
	9	85	70	60	75	95	75	45	55	45	100	45
	10	45	45	45	45	45	45	45	45	45	100	45
	11	60	60	60	60	60	60	60	60	60	100	60
	12	65	65	65	65	65	65	65	65	65	100	65

Table D.14: Summary of Bi-Decadal Vulnerability (%) by HUC4 and Month (MPI, RCP85)

Decadal Block	Month	1401	1402	1403	1404	1405	1406	1407	1408	1501	1502	1503
2020-2040	1	0	0	0	0	0	0	0	0	0	0	0
	2	0	0	0	0	0	0	0	0	0	0	0
	3	0	0	0	0	0	0	0	0	0	0	0
	4	0	0	0	0	0	0	0	0	0	35	0
	5	0	0	0	0	0	0	0	0	0	70	0
	6	0	0	0	0	0	0	0	0	0	95	0
	7	0	0	0	0	15	0	0	0	0	100	0
	8	10	0	0	0	70	0	0	0	0	100	0
	9	0	0	0	0	55	0	0	0	0	100	0
	10	0	0	0	0	0	0	0	0	0	60	0
	11	0	0	0	0	0	0	0	0	0	45	0
	12	0	0	0	0	0	0	0	0	0	0	0
2040-2060	1	0	0	0	0	0	0	0	0	0	5	0
	2	0	0	0	0	0	0	0	0	0	10	0
	3	0	0	0	0	0	0	0	0	0	5	0
	4	0	0	0	0	0	0	0	0	0	35	0
	5	0	0	0	0	0	0	0	0	0	70	0
	6	0	0	0	0	0	0	0	0	0	100	0
	7	5	0	0	0	45	0	0	0	0	100	0
	8	25	0	0	0	95	0	0	0	0	100	0
	9	20	0	0	0	70	0	0	0	0	95	0
	10	0	0	0	0	0	0	0	0	0	90	0
	11	0	0	0	0	0	0	0	0	0	80	0
	12	0	0	0	0	0	0	0	0	0	35	0
2060-2080	1	35	35	35	35	35	35	35	35	35	65	35
	2	35	35	35	35	35	35	35	35	35	55	35
	3	25	25	25	25	25	25	25	25	25	40	25
	4	10	10	10	10	10	10	10	10	10	50	10
	5	5	5	5	5	5	5	5	5	5	90	5
	6	5	5	5	5	5	5	5	5	5	100	5
	7	25	35	25	20	80	20	10	20	10	100	10
	8	85	40	40	40	100	40	20	25	20	100	20
	9	85	45	35	60	100	60	25	30	25	100	25
	10	30	30	30	30	30	30	30	30	30	95	30
	11	30	30	30	30	30	30	30	30	30	90	30
	12	35	35	35	35	35	35	35	35	35	75	35
2080-2100	1	25	25	25	25	25	25	25	25	25	60	25
	2	25	25	25	25	25	25	25	25	25	50	25
	3	15	15	15	15	15	15	15	15	15	35	15
	4	5	5	5	5	5	5	5	5	5	40	5
	5	5	5	5	5	5	5	5	5	5	95	5
	6	5	5	5	5	5	5	5	10	5	100	5
	7	40	25	15	15	80	15	5	15	5	100	5
	8	90	45	40	35	100	35	15	20	15	100	15
	9	90	40	25	35	90	35	20	20	20	100	20
	10	20	20	20	20	20	20	20	20	20	95	20
	11	20	20	20	20	20	20	20	20	20	90	20
	12	20	20	20	20	20	20	20	20	20	85	20

D.3 Development of VIC-VEO

VIC-VEO (Vegetal Optimality) was developed through modifications of existing source code files. The development is based upon VIC-4.1.2m, a single layered big-leaf model. Several significant modifications to the code were made, and are detailed in the following sections, including several of the input files and data requirements.

D.3.1 Source Code Modifications

Modifications of the source code files is summarized here:

1. Vegetation Library - The vegetation library defines properties of plant functional types; the code was modified to read in additional parameters including: well-watered marginal water use efficiency (λ), maximum N_{org}, canopy light decay exponent (K_L), and marginal nitrogen use efficiency (η).

2. Climate Summaries - The leaf phenology is determined at the start of each year, looking back at the historic 20-year period, and determining annual averages, totals, or monthly statistics. Data stored in the forcing files, or derived variables during run-time and stored, are evaluated to create the required statistics for the LAI phenology regression. Shortened climate periods are assumed for initial model timesteps less than 20-years.

3. Monthly Summaries - At the start of each month, summaries of the previous month temperatures and irradiance are determined. This is used to update the biochemical properties through optimal resource allocation. Optimal allocation is found through a particle swarm optimization routine.

4. Stomatal Resistance - The stomatal resistance function has been updated to use an optimal stomatal response. This formulation requires the vapor pressure deficit, irradiance, photosynthetic system capacities, and leaf water potential.

5. Leaf Water Potential - A routine to estimate leaf water potential based on soil water potential, fluxes from soil to root, and then root to leaf, was added.

6. Multi-Layered Canopy - The canopy is divided into discrete integer layers (rounded up to next integer from current estimate of LAI), where calculations are performed separately for each layer. Transpiration and conductance of the fractional layer is then adjusted accordingly.

D.3.2 Running VIC-VEO

Implementation of the dynamic vegetation model significantly increases computational demand and model run-times. Further developments should focus on streamlining the code to further reduce computational burden.

Beyond additions to the vegetation library, the model is compiled and run exactly the same as previous versions of VIC. Monthly phenology specified in the vegetation library is used for the first year of run-time, and thus is still required even though the phenology is updated for subsequent years.

Routing Model

The available routing model based upon the St.Venant equations (simply named 'rout'), was used to determine the outflow hydrographs from each basin. Inputs to the routing model include the surface and groundwater runoff hydrographs for each cell covering the basin, in addition to several other controlling datasets. This includes:

- Direction Raster - a file indicating the flow direction for each grid cell,
- Area File - a file indicating the cell area for each grid cell,
- Fraction File - a file indicating the fraction of cell area contributing to the runoff for a given watershed.

Each of these items required additional setup for the CORB with subcatchment specific files. For example, a given calculation cell in VIC may cross a watershed boundary between two subcatchments; in this case, the cell requires a different flow direction value depending on the subcatchment being routed. In this case, ESRI ArcGIS and ArcPy were used to create hydrologically correct flow direction rasters for each subcatchment, resulting in unique files for each.

The VIC-VEO model utilizes a spatially distributed regular gridded layout in decimal degrees, here at 1/8th of a degree intervals. Although the decimal degrees are constant across the entire

CORB, the contributing area for each 1/8th degree cell changes with latitude. Therefore, an area raster specifying the cell contributing area is required.

Finally, the fraction file was developed by dividing the contributing cell area clipped to the subcatchment boundaries by the total cell area, resulting in a fraction in [0,1].

All of these files for each subcatchment are included on the Data CD.